The geological context of Lunar meteorites

https://eprints.bbk.ac.uk/id/eprint/40250/

Version: Full Version

Citation: Calzada-Diaz, Abigail (2017) The geological context of Lunar meteorites. [Thesis] (Unpublished)

THE GEOLOGICAL CONTEXT OF LUNAR METEORITES

By

Abigail Calzada-Diaz

A thesis submitted to Birkbeck College, University of London
for the degree of Doctor of Philosophy (PhD)

I, Abigail Calzada-Diaz confirm that the work presented in this thesis is my own. Where information has been derived from other sources, I confirm that this has been clearly indicated in the text.

Abstract

Meteorites are ejected from random areas of the lunar surface and therefore provide geological information about the Moon far from areas sampled during the Apollo and Luna programs. However, unlike those samples, the exact launch locations and geological setting of lunar meteorites are unknown, limiting greatly the knowledge we can obtain from them. During this project the launch location of lunar meteorites were studied using both laboratory analytical techniques and remote sensing instruments. This approach enabled me to provide meteorites with a geological context, increasing the geological knowledge it is possible to obtain from them.

The lunar feldspathic meteorites Miller Range (MIL) 90036 and MIL 090070 bulk-rock compositions and mineral chemistries were studied. MIL 090036 is a feldspathic immature regolith breccia (26.72 wt.% Al_2O_3, 5.27 wt.% FeO) that exhibits a Th-enrichment (1.89 ppm Th). This could be related to a high alkali component that has been observed in impact melt breccia clasts in this meteorite, but also it could be related to a KREEP component that, although it was not observed in the particular sample studied, it can be present in the bulk meteorite. Most of the provenance results show that the regolith from the surroundings of the Procellarum KREEP Terrane (PKT) in the nearside are the most similar to the composition of this meteorite and therefore the likely source location for MIL 090036. MIL 090070 is a feldspathic immature regolith breccia with bulk-rock compositions of 30.72 wt.% Al_2O_3, 3.77 wt.% FeO and a low Th abundance (0.44 ppm). The geochemistry of MIL 090070 may be formed by a mixture of ferroan and magnesian anorthositic rocks, although other possible explanation could be that they were all essentially ferroan-derived and that this rock types are more related to high-magnesium suite that previously thought. MIL 090070 was probably launched from the farside of the Moon as suggested by its compositional differences when compared to Apollo 16 regolith breccias, including the lack of KREEP.

The present work has studied the possible launch locations of 37 lunar meteorites (67 individual stones) using bulk-rock FeO, TiO_2 and Th compositions and the 2-degree LP-GRS dataset from Prettyman et al. 2006. My method compares the composition of both the analytical and the remote sensing measurements. The outcome is a shapefile that allows for a correct visualization in ArcGIS™. Results obtained suggest that differences in KREEP components between the PKT and other areas of the Moon are not the only indicator of a heterogeneous mantle.

This study also indicates that ferroan anorthosites are widely distributed with patches occurring within the central farside highlands. The large number of feldspathic meteorites that contain both magnesian and ferroan anorthosites compared to those that contain only one or the other, could indicate that these rock types are genetically related and that the wide Mg# distribution in FAN and MAN could be produced by serial magmatism. If this is correct, some of the ferroan anorthositic lithologies observed within lunar samples would not be the direct product of the magma ocean crystallization.

Acknowledgements

This thesis would not have been possible without the support of many people. I am extremely grateful to each of them.

First of all, I would like to thank Prof. Ian Crawford. He has been a patient and enthusiastic supervisor, he has supported and helped me during every stage of this thesis and made me feel as a valuable part of the planetary science community. Many thanks to the Sciences and Technology Facilities Council for funding this project.

I also thank Dr. Katherine Joy who has contributed to her extensive petrology knowledge and experience to this work. She has been a very supportive and thorough supervisor. The success of this work is in great part thanks to her.

I would like to thank Prof. Hilary Downes for trusting me to teach Magmatic Processes and Igneous Petrology to Birkbeck students. I enjoyed greatly her classes and our talks on Lanzarote’s nights.

Thanks to the CPS people: Jen, Louise, Chris, Huma, Roberto, Elliot, Pete, Indhu, Peter, and all those students who has been in our office from time to time during these years. It was a pleasure to enjoy lunch times, conversations and conferences with all of you. I would like to thank to Joel for all his kind words (and pints) every time I doubted about my own capabilities to finish this thesis. Also, thank you for showing me the nicest pubs of London!

A large part of these years were shared with Tom Nordheim. I would like to thank him very much his support, his friendship and his love. We shared long and profound conversations, many films, travels, some concerts and zombies. Thanks Tom for being by my side since the moment we met, for your encouragement and your unconditional love.

I would like to thanks to Dr. David Kring, NASA SSERVI, USRA and all the staff and interns from the Lunar and Planetary Institute for giving the opportunity to learn and to spend a wonderful summer during the Summer Graduate Internship at Houston, Texas.

Special thanks to the people from the Planetary Sciences and Astrobiology Group TITAN from the National University of Colombia, the Organization Cielos Despejados from the University of Oviedo and the Space Generation’s Space Exploration Working Group. I really admire your enthusiasm and hard work. I feel very grateful of working with all of you and hope to continue

doing it for many years to come. You are my inspiration and the future of the planetary sciences and the space exploration.

I would like to say thanks to Manu. Thanks for your support, friendship, care and long Skype conversations while writing this thesis. I am very happy and grateful of having met you during the Camino. I am looking forward to walk with you, we will be doing it soon.

My time in London would not have been the same without Arturo, Luis, Nikola, Alex and all my friends from Camden Town. Thank you for all the fun, concerts and beers! Also, thank you Houda for being such a nice and understanding flatmate.

Last but not least, thank you to my mum and my family for being so supportive and caring, and for teach me how important is to pursue my dreams. Thank you dad, Su, Rosaura, Marga, Lute, my two “güelitas”, “güelito”, Jaito (I am already missing you), Maria, Tania, Ani, Tim, Missy and all my friends in Asturias for being always there for me even when I was far. I missed you every day during these three years.

The Moon was but a Chin of Gold
A night or two ago,
And now she turns her perfect face
Upon the world below.

Her forehead is of amplest blonde,
Her cheek, a beryl hewn,
Her eye unto the Summer Dew
The likest I have known.

Her lips of amber never part,
But what must be the smile
Upon her friend she could confer
Were such her Silver will.

And what a privilege to be
But the remotest star,
For certainly she take her way
Beside your palace door.

Her bonnet is the Firmament,
The universe, her shoe,
The Stars, the trinkets at her belt,
Her dimities, of blue.

Emily Elizabeth Dickinson (1830-1886)

Contents

Table Contents

Figure Contents

Electronic Appendix

Appendix 3 Mineral chemistry of MIL 090036. (A) Plagioclases, (B) Pyroxenes, (C) Olivines.

Appendix 4 Mineral chemistry of MIL 090070. (A) Plagioclases. (B) Pyroxenes, (C) Olivines.

Websites

Randy Korotev's list of lunar meteorites: *http://meteorites.wustl.edu/lunar/moon_meteorites_list_alumina.htm* (accessed 17th of August 2016)

Meteoritical Bulletin Database: *http://www.lpi.usra.edu/meteor/metbull.php* (accessed 17th of August 2016)

Lunar and Planetary Institute: *http://www.lpi.usra.edu* (accessed 23rd of August 2016)

Chapter 1. Introduction

1.1. Introduction

During the past centuries, humanity has studied the lunar surface, first with the naked eye and from the early 17th century with the aid of telescopes. Early maps have depicted a heavily cratered surface and numerous morphological features. The ancient lunar surface, with areas over 3 billion years old (Ga), preserves a geological record of the history of the Earth-Moon system. The study of returned and meteoritic samples will lead to a better knowledge of the origin and evolution of the Earth-Moon system (e.g. Joy and Arai 2013) and by extension, of the terrestrial planets and the entire Solar System (Korotev 2005; Hiesinger and Head 2006).

The samples returned from the Apollo and Luna programs have provided new insights into the lunar lithologies (Taylor 1975). However, all those samples were collected from a relatively small region on the equatorial area in the nearside (Figure 1.1), so they do not give a complete view of lunar lithological compositions. Lunar meteorites are an additional source of samples, ejected from random localities of the surface. These materials have shown that lunar compositions are much more complex than previously has been thought. Unfortunately, the geographical launch locations of these samples are unknown, limiting the information we can obtain from their geological context (Joy and Arai 2013; Jolliff et al. 2014).

This thesis aims to connect lunar meteorites to their possible launch locations, to understand their geological context and therefore, to provide new insights into the crustal evolution of the Moon.

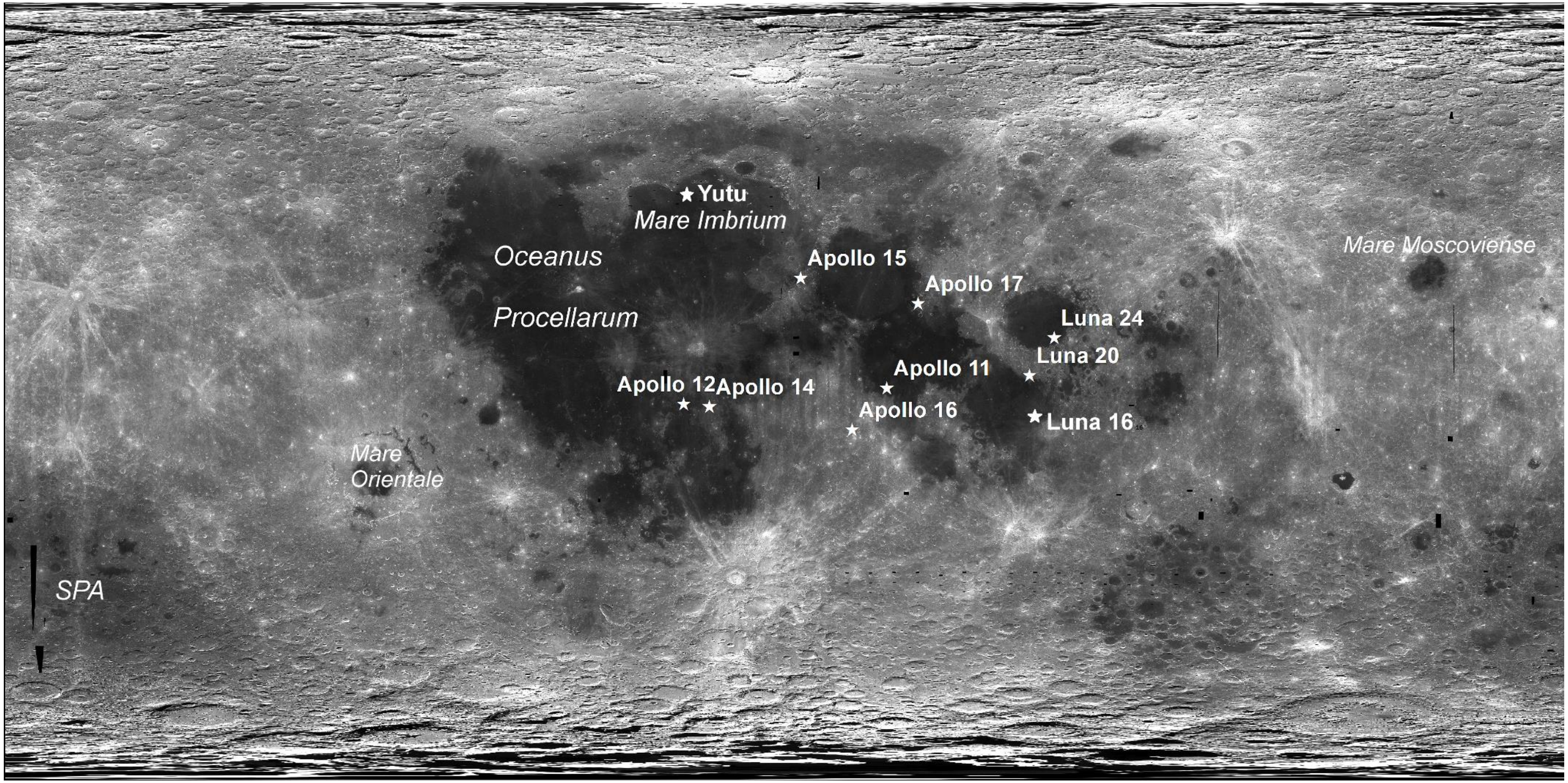

Figure 1.1 Apollo crewed missions, Luna robotic lander and Yutu rover landing sites. Underlying a Clementine albedo image in cylindrical projection with 0° latitude and 0° longitude in the centre.

1.2. Lunar Exploration

The first lunar exploration missions date back over 50 years when the Luna, Zond and Ranger Programs made their first attempts to investigate the Moon. Several missions followed as technological capabilities increased. The first successful controlled landings were performed by Luna 9 (USSR) and Surveyor 1 (US) landers in 1966. These accomplishments were followed by crewed orbital missions within the NASAs Apollo program (1968-1972) and the robotic soviet program Luna (1970-1976). Lunar exploration reached its peak with the sampling of lunar material carried out by astronauts during the Apollo missions to the surface (Figure 1.1; Vaniman et al. 1991).

With the end of the Apollo and Luna Programs, exploration activities decreased significantly until NASA’s probe Clementine was launched in 1994. This mission was followed by Lunar Prospector in 1998. With the new century, interest in the Moon was renewed as new countries showed interest in exploration challenges. The SMART-1 probe (2003) meant the entry of the European Space Agency (ESA) into lunar exploration and, although its main purpose was to test technological capabilities, it achieved a wide range of scientific outputs (e.g. Swinyard et al. 2009). Six missions were launched between 2007 and 2010 from several countries. The Japanese probe Kaguya-SELENE and the Chinese Chang’e 1 in 2007, the Indian orbiter Chandrayaan-1 (2008), NASA’s Lunar Reconnaissance Orbiter (LRO, 2009) and the Chinese Chang’e 2 and NASA’s GRAIL missions in 2010. China achieved a great success in 2013, when the lander platform and rover Yutu successfully landed on the lunar surface (see Figure 1.1 for landing site). The same year NASA sent the LADEE mission to investigate lunar atmosphere (Figure 1.2).

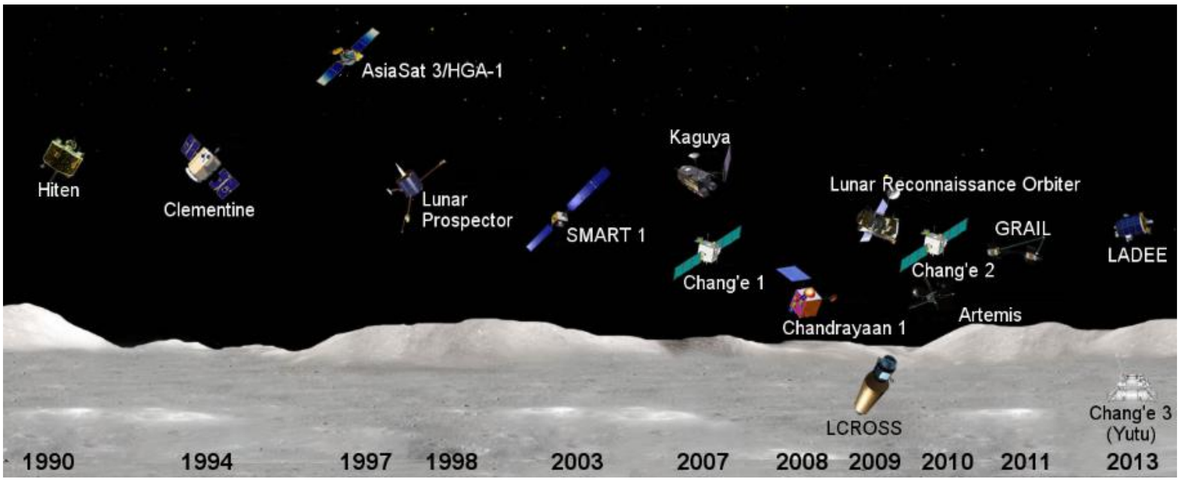

Figure 1.2 Lunar exploration missions after Apollo and Luna programs (modified from the LPI website *http://www.lpi.usra.edu*).

1.3. Lunar Mineralogy

Lunar rocks have a relatively simple mineralogy compared with rocks found on Earth. However, it is key to understand the physical and chemical conditions in which these rocks have been formed. The most common minerals in lunar rocks are plagioclase feldspar $(Ca,Na)(Al,Si)_4O_8$, pyroxene $(Ca,Fe,Mg)_2Si_2O_6$ and olivine $(Mg,Fe)_2SiO_4$. Oxides such as ilmenite $(Fe,Mg)TiO_3$ (carries most of the TiO_2 on lunar basalts) and spinel follow the silicates in abundance. Silica polymorphs (e.g. quartz, SiO_2) and potassium feldspar ($KAlSi_3O_8$) very common in terrestrial rocks are rare in lunar counterparts. Sulfides (troilite, FeS) and phosphates (e.g. merrillite, $Ca_9NaMg(PO_4)_7$) can appear as accessories (<3% modal of the rock) in some lunar rocks (e.g. Papike 1998; Shearer et al. 2006). Hydrous minerals such as clay, amphibole and mica phyllosilicates are absent in lunar rocks (McKay et al. 1991; Lucey et al. 2006).

1.4. Lunar Rocks

Much of what we know about lunar compositions and ages derives from the study of lunar samples. This material was obtained from two sources: (1) sampling conducted by US astronauts and soviet robotic collection, and (2) lunar meteorites (Vaniman et al. 1991; Shearer et al. 2006; Jaumann et al. 2012). Geological sampling carried out by the Apollo astronauts returned approximately 382 kg of rocks and soils from 6 landing sites from a restricted area in the nearside of the Moon (Figure 1.1). The soviet Luna missions brought back a total of 321 g of lunar material from 3 separate localities within the nearside (Figure 1.1).

Lunar rocks are generally grouped in three main groups: (1) Pristine non-mare rocks from the highlands, (2) Polymict impact breccias and (3) Basaltic volcanic rocks, including lava flows and pyroclastic deposits (Taylor et al. 1991).

1.4.1. Pristine non-mare rocks

Pristine rocks (Figure 1.3) are identified as part of the original lunar crust (Warren and Wasson 1977). They all share some common characteristics, they exhibit coarse-grained plutonic textures or they appear as monomict breccias. These rocks have not suffered from mixing with other rocks types, and they lack siderophile elements of meteoritic origin (Warren and Kallemeyn 1993).

Primary Crust: The Ferroan Anorthosite (FAN) suite encompasses rocks with >90% anorthitic plagioclase feldspar. Some may also contain pyroxene and in much lesser extent olivine. Pyroxene and olivine Mg# (atomic Mg/(Fe+Mg)) within these rocks are much more ferroan than any other types of non-mare igneous rocks. This suite is characterized for having low concentrations of FeO and low incompatible trace elements compared to other lunar rocks (e.g. Ryder 1982; Warren 1990). However, farside anorthosites appear to be distinct to the nearside FANs. Magnesian anorthosites (MAN) are a type or rock richer in magnesium. Compositionally, their Mg# fall between FAN and the Mg-suite samples (Korotev et al. 2003; Arai et al. 2008; Gross et al. 2014).

Secondary crust: The magnesian suite (Mg-suite or HMS) are formed mostly by norites, troctolites, some gabbros, gabbronorites and ultramafic rocks. They include all coarse-grained rocks that are distinguishable from the FAN group by having higher mafic mineral Mg# and/or lower plagioclase An# (atomic Ca/(Ca+Na+K)) content (Warner et al. 1976). Mg-suite rocks appear to have crystallized from magmas rich in incompatible elements (Korotev et al. 2003).

High alkali-suite (HAS) rocks have compositions from anorthositic to norite and gabbronorite. The plagioclase is more sodic (average An_{82}), than plagioclase in FAN (average An_{96}). These rocks tend to be enriched in incompatible elements suggesting that they are associated to KREEP (material rich in Potassium, Rare Earth elements and Phosphorus; Shervais and McGee

1998; Lucey et al. 2006).

KREEP lithologies often appear as small clasts in breccias and as fragments within the regolith (Jolliff 1991). They are highly enriched in incompatible minor and trace elements (Papike 1998). The only ‘pristine’ (i.e. non-impact) KREEP rocks are erupted basalts with 40-50% plagioclase and low-Ca pyroxene and they exhibit different geochemical signatures than the primordial urKREEP material from which it derives (Spudis and Hawke 1986; Jilly et al. 2011).

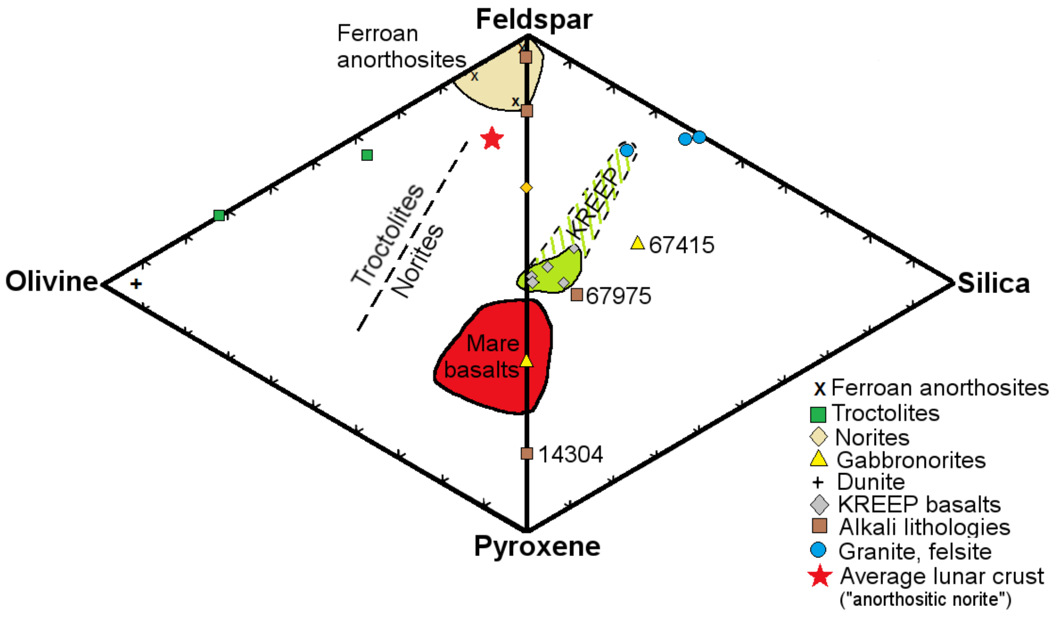

Figure 1.3 Modal volume proportions of feldspar, olivine, pyroxene and silica for lunar highland pristine igneous rocks and monomict breccias. (Modified from Taylor et al. 1991).

1.4.2. Breccias

Lunar breccias are rocks formed by fragments of older rocks (clasts) that have been broken, disaggregated, melted and lithified by meteoroid impacts (Warren et al. 1983; McKay et al. 1991). The material that binds the clasts together to form a coherent rock is called matrix. Most rocks consists of clasts of several lithologies (polymict), but also they can be dimict (clasts from two lithologies), and the clasts can even derive from a single precursor lithology (monomict; Stöffler et al. 1979).

Impact melt breccias consist of clasts or mineral fragments in an igneous-textured matrix (fine-grained or coarse-grained). The proportion of clasts may be variable raging from clast-poor to clast-rich (Stöffler et al. 1979).

Granulites and granulitic breccias are rocks that have experienced recrystallization as a consequence of impact metamorphism as it is indicated by the presence of siderophile elements contamination. They usually exhibit granoblastic (polygonal morphology with grain triple junctions) to poikiloblastic (crystals which are riddle with finer grained inclusions of other minerals) textures (Stöffler et al. 1979).

1.4.3. Mare volcanics

Mare basalts are formed by partial melting of the mantle of the Moon and the subsequent ascent and eruption to the lunar surface. Two types of volcanic materials have been observed on the lunar surface: (1) Basaltic lava flows with low viscosities erupted from fissures in the lunar surface and (2) pyroclastic deposits where magmas containing gasses where explosive released close to the surface of the Moon (Neal and Taylor 1992; Shearer and Papike 1993; Lucey et al. 2006). The extent and the characteristics of mare volcanism are discussed in section 1.8.

1.4.4. Lunar meteorites

Lunar meteorites provide with valuable information far from areas sampled during the Apollo and Luna programs. It is believed that they have been ejected from random locations in the lunar surface. Available cosmic-ray data measurements indicate that they were probably launched in the last 2 million years (Ma) from small shallow impact craters <2 km in diameter (Korotev 2005). Therefore, they sample the upper layer of the lunar surface (Warren 1994; Basilevsky et al. 2010).

According to the Meteoritical Bulletin Database, there are 261 classified lunar stones recovered up to the 17th of August 2016 (*http://www.lpi.usra.edu/meteor/metbull.php*), including launch and fall grouped stones.

Petrological and geochemical analyses show a wide range of meteoritic compositional variations (Korotev 2005; Joy and Arai 2013), although they can be broadly classified into three lithological types: (1) brecciated anorthosites (2) crystalline and brecciated basalts and

(3) impact-melt breccias (Korotev 2005, *http://meteorites.wustl.edu/lunar/moon_meteorites_list_alumina.htm*).

The interpretation of these samples, however, is limited by the fact that we do not know the source region of any individual sample. Providing these samples with a geological context will shed light into the distribution, origin and evolution of the lunar crust (Pieters et al. 1983; Gnos et al. 2004; Joy et al. 2010; Robinson et al. 2012; Joy and Arai 2013).

Several lines of evidence indicate the lunar provenance of these meteoritic samples. The presence of a fusion crust is indicative of melting by frictional heating during passage through Earth's upper atmosphere. The lack of hydrous phases and a mineralogy different to that found in terrestrial rocks (i.e. the presence of FeNi metal, Ti-rich ilmenite, etc.) indicates that the sample was formed in a highly reducing environment. Fe/Mn ratios of pyroxene and olivine phases vary between planetary bodies because of the original composition of accreted material, differentiation and oxygen fugacity conditions. Finally, other bulk elemental ratios similar to those observed on the Apollo and Luna samples, and an oxygen isotope ratio that matches the Earth-Moon fractionation trend, also indicate a lunar origin (Delaney et al. 1979; Kallemeyn and Warren 1983).

Anorthositic meteorites have bulk rock compositions with 26-31 wt.% Al_2O_3, 3-6 wt.% FeO and low concentrations of incompatible trace elements (e.g. <1 ppm Th). They are breccias composed by feldspathic fragments or/and impact melt breccias (Korotev et al. 2003; Korotev 2005; Warren et al. 2005) and are thought to have originated from areas far from the Apollo 16 samples, namely from regions that have not been influenced by the ejecta of the Imbrium basin formation. Before the lunar meteorite studies, all the information about the lunar crust had been extrapolated from the study of the Apollo 16 and the Luna 20 samples (Laul and Schmitt 1973; Wänke et al. 1973; McKay et al. 1986; Korotev 1996). Lunar anorthositic meteorites have shown the diversity of the lunar crust compositions (i.e. it was possible the identification of magnesian anorthosites unknown in the Apollo and Luna collection) and therefore provide with valuable information about the early lunar differentiation processes (Lucey et al. 2006; Arai et al. 2008; Gross et al. 2014).

Basaltic meteorites, with bulk rock compositions of 8-10 wt.% Al_2O_3, 18-22 wt.% FeO and low incompatible trace elements (0.4-2 ppm Th), can be either crystalline mare basalts or breccias formed by basaltic fragments or/and impact melt breccias (Korotev 2005). Some basaltic meteorites are very similar to many basaltic samples returned from the Apollo missions (e.g. Fagan et al. 2002; Righter et al. 2005), but others show characteristics not observed previously (e.g. Terada et al. 2007; Gaffney et al. 2008). Basaltic meteorites shed light into the age, extent, and properties of lunar volcanism and therefore, into the evolution of the lunar mantle (Dasch et al. 1987; Day and Taylor 2007; Borg et al. 2009).

Finally, the third lithological end member is formed by KREEP bearing material with noritic composition, however, most of the meteorites that fall in this category are polymict impact melt breccias, with bulk rock compositions of 11-25 wt.% Al_2O_3, 7-17 wt.% FeO and high concentration of incompatible elements (up to 3 ppm Th; Gnos et al. 2003; Al-Kathiri et al. 2007; Zeigler et al. 2011). They inherit the KREEP signature from melting and mixing with KREEP-bearing rocks in the impact event, HAS, Mg-suite, or KREEP basalts which in turn gain their KREEPy signature during magma ascent through the urKREEP layer. These samples have great significance in understanding the development and distribution of KREEP material (Warren and Wasson 1979; Korotev 2005).

1.5. Lunar Stratigraphy

The lunar stratigraphy arranges the geological units into a relative time sequence, mostly based on radiometric ages of Apollo and Luna samples, size-frequency distribution data and crater degradation (e.g. Hiesinger et al. 2000; Hiesinger et al. 2011). These methods also have allowed to understand the relationships among the different lunar geological periods (Hartmann et al. 1981; Wilhelms and John 1987; Neukum and Ivanov 1994; Stöffler and Ryder 2001; Figure 1.4).

Radiometric ages of impact melts of Apollo samples indicate ages older than 3.9 Ga, this has been interpreted as a period of intense bombardment that occurred on the Moon between 4.38-4.42 Ga (Tera et al. 1973, 1974; Ryder 1990, 2002; Kring and Cohen 2002; Morbidelli et al. 2012; Fernandes et al. 2013; Niihara et al. 2013; Hopkins and Mojzsis 2015). During this period, also known as Late Heavy Bombardment (LHB), most of the impact basins were created, with the exception of Orientale, and ended abruptly approximately after the formation of the Imbrium basin (~3.9 Ga; Chapman et al. 2007). However, other authors have argued the existence of a peak in the lunar impact flux (e.g. Hartmann 2003) suggesting that the absence of impact melts in the early history of the Moon does not mean a lack of impacts but it is caused because the high rate of early impacts that led to their pulverization.

1.5.1. Lunar timescale

The *Pre-Nectarian period* is the time span between the origin of the Moon (~4.4-4.5 Ga; McLeod et al. 2014; Boyet et al. 2015) and the formation of the Nectaris basin (between 3.91 and 4.2 Ga; Schaeffer and Shaeffer 1977; Korotev 2005). During this period around 30 multi-ring basins and samples from FAN and Mg-suite rocks with older ages than the Nectaris basin were identified (Papike 1998; Stöffler and Ryder 2001; Norman et al. 2011).

During the *Nectarian period*, twelve multiring basins were formed including Crisium and Serenitatis (Wilhelms and John 1987; Swindle et al. 1991; Stöffler and Ryder 2001). This period covers from an age from the Nectaris impact event and the Imbrium impact basin formation, which age (~3.91 Ga) was obtained from the Apollo 14, 15 and 16 samples (Hartmann et al. 1981; Neukum and Ivanov 1994; Snape et al. 2015).

The *Imbrian period* lasted approximately 0.7 Ga, until the Erasthostenes crater formation (~ 3.2 Ga; Stöffler and Ryder 2001). During this period, the formation of the Orientale basin took place, the youngest of the multiring basins, which absolute age cannot be determined because the lack of samples (Wilhelms and John 1987; Spudis et al. 1994). Also, Apollo 11, 15, 17, and Luna 24 basaltic surfaces were formed (Wilhelms and John 1987; Neukum and Ivanov 1994; Stöffler and Ryder 2001).

The Apollo 12 basalts are the youngest from the Apollo samples (~3.15 Ga; Stöffler and Ryder 2001). They have extruded during the *Eratosthenian period*, between the Eratosthenian crater formation and the Copernicus crater (~0.8 Ga; Eberhardt et al. 1973; Alexander et al. 1976; Bogard et al. 1994).

Finally the *Copernican period* covers a time span from ~0.8 Ga until these days (Wilhelms and John 1987; Stöffler and Ryder 2001). Tycho craters (~0.1 Ga; Wolfe et al. 1975; Drozd et al. 1977) and the North Ray (50 Ma), Cone (25 Ma) and South Ray (2 Ma) craters are the main events that took place during this period (Moore et al. 1980; Eugster 1999).

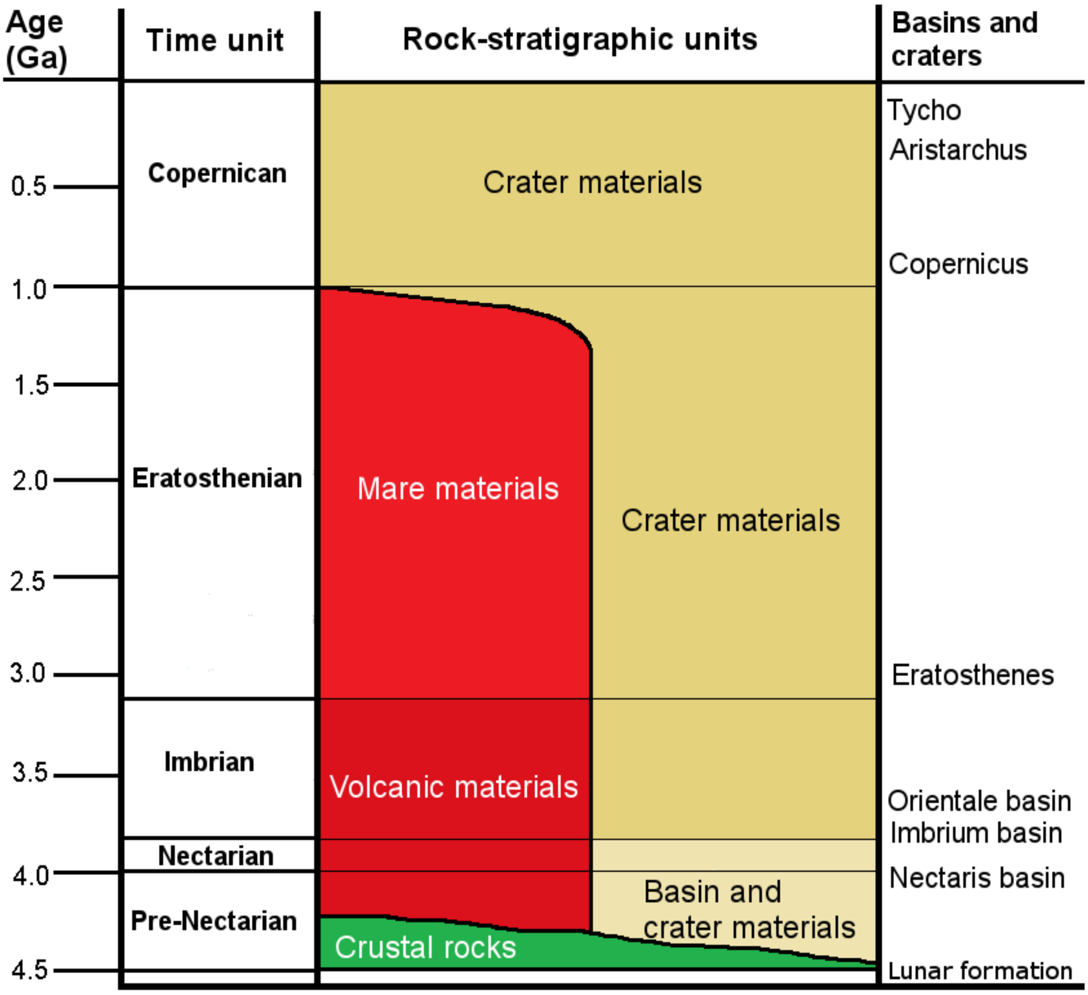

Figure 1.4 Lunar stratigraphic column with age (Ga), time units, rock-stratigraphic units and the main basin and crater events in lunar history. (Modified from USGS after Wilhelms and John, 1987).

1.6. Formation and Early Differentiation of the Moon

1.6.1. Formation of the Moon

There are several main models that aimed to explain the origin of the Moon (see Hartmann et al. 1984). These models include: the fission of equatorial material from a rapidly rotating Earth (Darwin 1879; Wise 1963); gravitational capture where the Moon, formed elsewhere in the Solar System and was captured by Earth's gravity into a stable orbit (e.g. Gerstenkorn 1955); and the co-accretion model which suggests that the Moon was formed along with the Earth from a proto-planetary disk (Schmidt et al. 1959). Currently, the giant impact hypothesis (Hartmann and Davis 1975; Cameron and Ward 1976) is widely accepted as the likely scenario for the formation of the Moon. This model proposes that the Moon is a consequence of a catastrophic impact event between the Earth and a Mars-sized planet (Figure 1.5). Earth's crust and upper mantle ejecta from this collision fell into orbit around the Earth where, during a relatively short period of time (from 1 month to 100 years depending on the model), it re-accreted to form the Moon (Canup and Asphaug 2001; Cuk and Stewart 2012; Canup 2012; Righter and Canup 2016).

Numerical models have shown that a giant impact can eject a sufficient amount of material to meet the Moon's orbital and geochemical characteristics. Also, the similar oxygen isotopes on both bodies support the model that the material from which the Moon was formed derives from a location within the solar nebula close to the Earth (Wiechert et al. 2010). Recently, it was suggested that the Moon was formed by the proto-Earth's mantle relocated after the giant impact event (Wang and Jacobsen 2016).

Radiogenic crystallization ages for lunar highland rocks support a formation age for the Moon between 4.44 and 4.51 Ga (McLeod et al. 2014; Boyet et al. 2015; Borg et al. 2015).

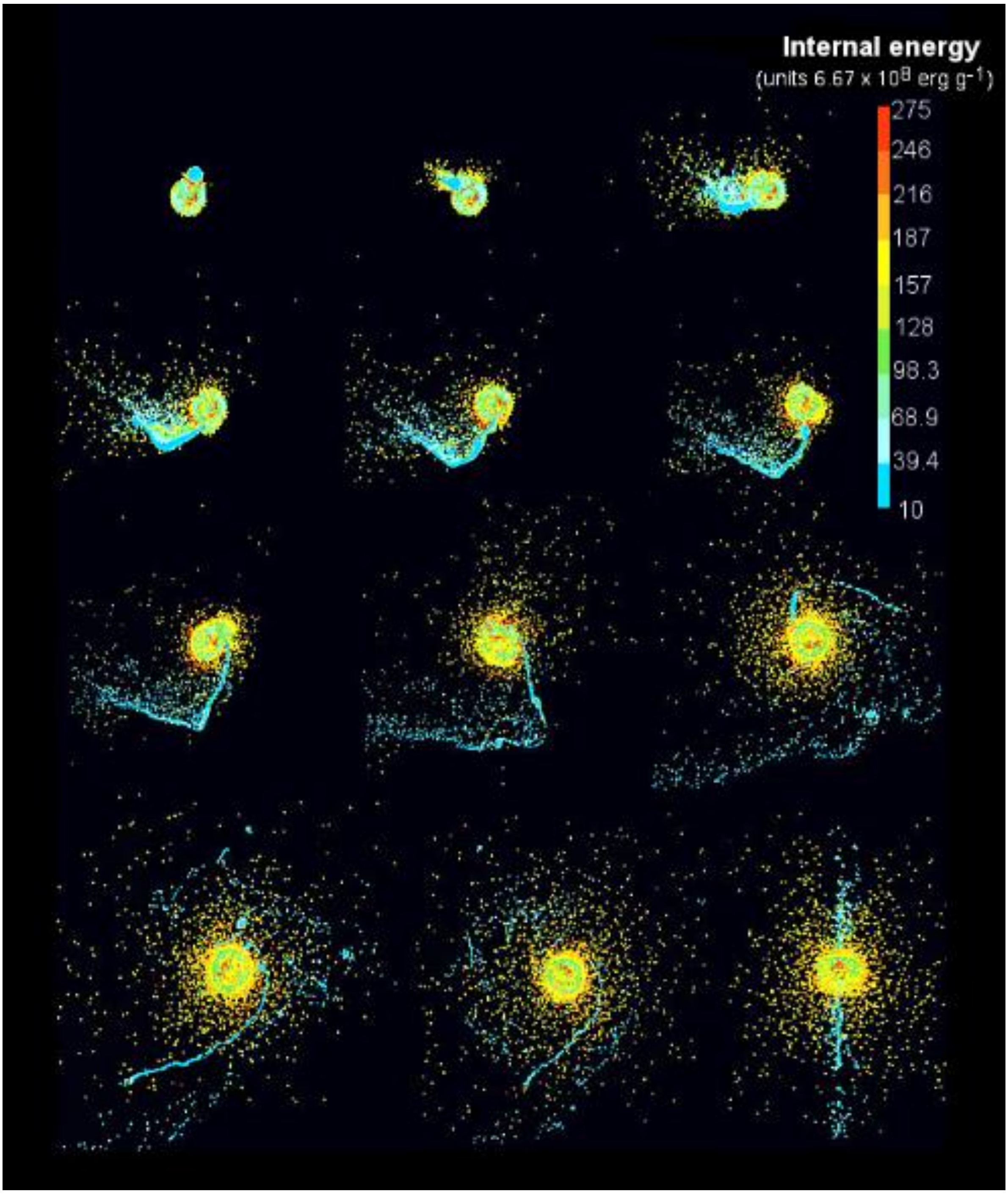

Figure 1.5 Computer simulation of the giant Moon forming impact. Colour scale represents internal energy and varies from blue and dark green that are condensed matter, to red particles representing either an expanded phase or a hot, high-pressure condensed phase. (Taken from Figure 1 in Canup and Asphaug 2001).

1.6.2. Early differentiation of the Moon

Following the giant impact, a rapid accretion happened causing the melt of a large fraction of the Moon, forming a global magma ocean. According to the Lunar Magma Ocean hypothesis (LMO; Warren 1990; Shearer and Papike 1999), Mg-rich minerals (olivine and to a lesser extent pyroxene) crystallised first and sank to form the Moon's mantle (Fig. 1.6). After approximately 75-80% of the LMO had solidified, the crystallization of plagioclase started (Snyder et al. 1995). Because the low oxygen fugacity conditions, europium was present in its divalent state (Eu^{2+}) and it was incorporated into the plagioclase feldspar structure replacing Ca^{2+} and removing it from the melt creating the positive-normalized Eu-anomaly observed in anorthositic samples (Warren 1990; Taylor et al. 1991; Shearer and Papike 1999; Shearer et al. 2006). Petrological studies suggest that the likely crystallisation sequence may have been as follows: olivine → orthopyroxene ± olivine → olivine + clinopyroxene ± plagioclase → clinopyroxene + plagioclase → clinopyroxene + plagioclase + ilmenite (Figure 1.6; Shearer and Papike 1999; Shearer et al. 2006).

The high contrast in density between plagioclase and the denser mafic phases resulted in the former buoyantly rising and migrating towards the lunar surface to form a global anorthositic crust composed of >90% calcic plagioclase (Figure 1.6). Incompatible trace elements encompassing elements as K, rare earth elements (REE), P, Th, U, Zr, Hf and Nb, are generally not included in the crystal structures of the silicates phases. These elements remained in the melt dregs forming a KREEPy residual material – often termed urKREEP (i.e., original KREEP) - that concentrated between the lower mafic cumulates and the upper anorthositic crust (Figure 1.6; Shearer and Papike 1999; Shearer et al. 2006).

However, the LMO hypothesis faces several problems. For example, granulites are re-crystallized polymict clastic breccias that can be either ferroan (mineralogically similar to ferroan anorthosites) or magnesian (mineralogically similar to magnesian anorthosites; Lindstrom et al. 1986). This last type of rock, magnesian granulite, appears to be widely distributed within the Moon and has no place within the LMO model as previously described, in which ferroan anorthosites (or granulites) are its main products (Gross et al. 2014). Heterogeneity of the distribution of some LMO products such as the KREEP, localized in the nearside, and Mg (higher abundances on the feldspathic farside terrane relative to the feldspathic nearside; Arai et al. 2008; Ohtake et al. 2009; Crites and Lucey 2015; Pernet-Fisher and Joy 2016) also challenges the global distribution of the rock types expected by a LMO model.

The crystallization ages of Apollo ferroan anorthosites span 200 million years (Shearer et al. 2006; Borg et al. 2011), while most of the LMO models suggest that the LMO would have solidified in tens of millions of years (Elkins-Tanton et al. 2011). Also, in the LMO hypothesis, magnesian suite plutons would have crystallized after the ferroan anorthosite was stabilized, but radiometric ages of magnesian suite rocks overlap with those of ferroan anorthosites (Shearer et al. 2006; Elkins-Tanton et al. 2011).

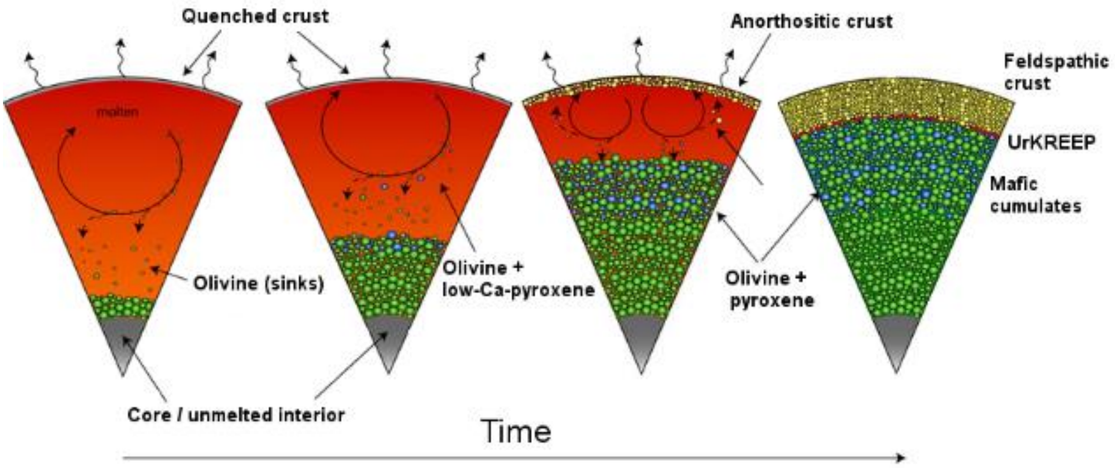

Figure 1.6 Diagram of the evolution of the lunar magma ocean from the formation (left) to the present (right). Olivine crystallized first within a turbulent convection magma, followed by pyroxene. These minerals cooled and sank forming the early-stage cumulates. Plagioclase started to crystallize and floated to the top to form an anorthositic cap. The latest melt dregs are enriched in elements not incorporated into the main minerals forming the KREEP. (Modified from Jennifer Rapp, LPI).

An alternative to the LMO hypothesis is serial magmatism, which suggests that the lunar crust may have been produced by multiple “massif-like” anorthosite bodies that have been differentiated upon their emplacement, to form anorthositic and mafic-ultramafic layers (Longhi and Ashwal 1985; Longhi 2003; Gross et al. 2014; Pernet-Fisher and Joy 2016). In this scenario, the magnesian or ferroan nature of the magma is controlled by the Mg# of the source mantle. Each diapir is expected to have an exclusive chemistry because each parental intrusion derives from a unique portion of the mantle with different history (age, chemical interactions with the pre-existing crust, etc.) and degree of fractionation. The differentiated anorthositic layer shows a relatively constant An and a range of Mg# (that increases by the circulation of mafic interstitial melt among the plagioclases; Gross et al. 2014). This trend is observed among anorthosites and anorthositic clasts within lunar feldspathic meteorites (Treiman et al. 2010).

1.7. Lunar Crustal Terranes

Remote sensing and sample geochemical data suggested the division of the lunar crust into three major geologic terranes (Jolliff et al. 2000): the Feldspathic Highlands Terrane (FHT and FHT-O), the Procellarum KREEP Terrane (PKT) and the South Pole-Aitken Terrane (SPA). A terrane or province is defined as "a group of rock formations that have some specific aspect of geologic history in common and that differ from adjacent groups of rock units" (Jolliff et al. 2000; Wieczorek et al. 2006) and have both spatial continuity and a depth dimension. Clementine UVVIS data and Th data from the Apollo gamma-ray-spectrometer (Lucey et al. 1998; Lawrence et al. 1998; Gillis and Jolliff 1999) were used by Jolliff et al. (2000) to define the boundaries of each terrane (Figure 1.7).

1.7.1. Feldspathic Highlands Terrane

The Feldspathic Highlands Terrane (Figure 1.7) represents the formation of the lunar primary crust formed by accumulation of plagioclase from the magma ocean and later modified by impact processes (Figure 1.8). It is characterised by its high albedo, elevated topography and feldspathic compositions. It covers more than 60% of the surface of the Moon and less than 10% of its material are mare basalts (Jolliff et al. 2000; Wieczorek et al. 2006).

There are two compositionally different regions within the FHT, an anorthositic portion centred on the farside (FHT) and a slightly more mafic outer portion situated in the eastern and western limbs (FHT-O; Figure 1.7).

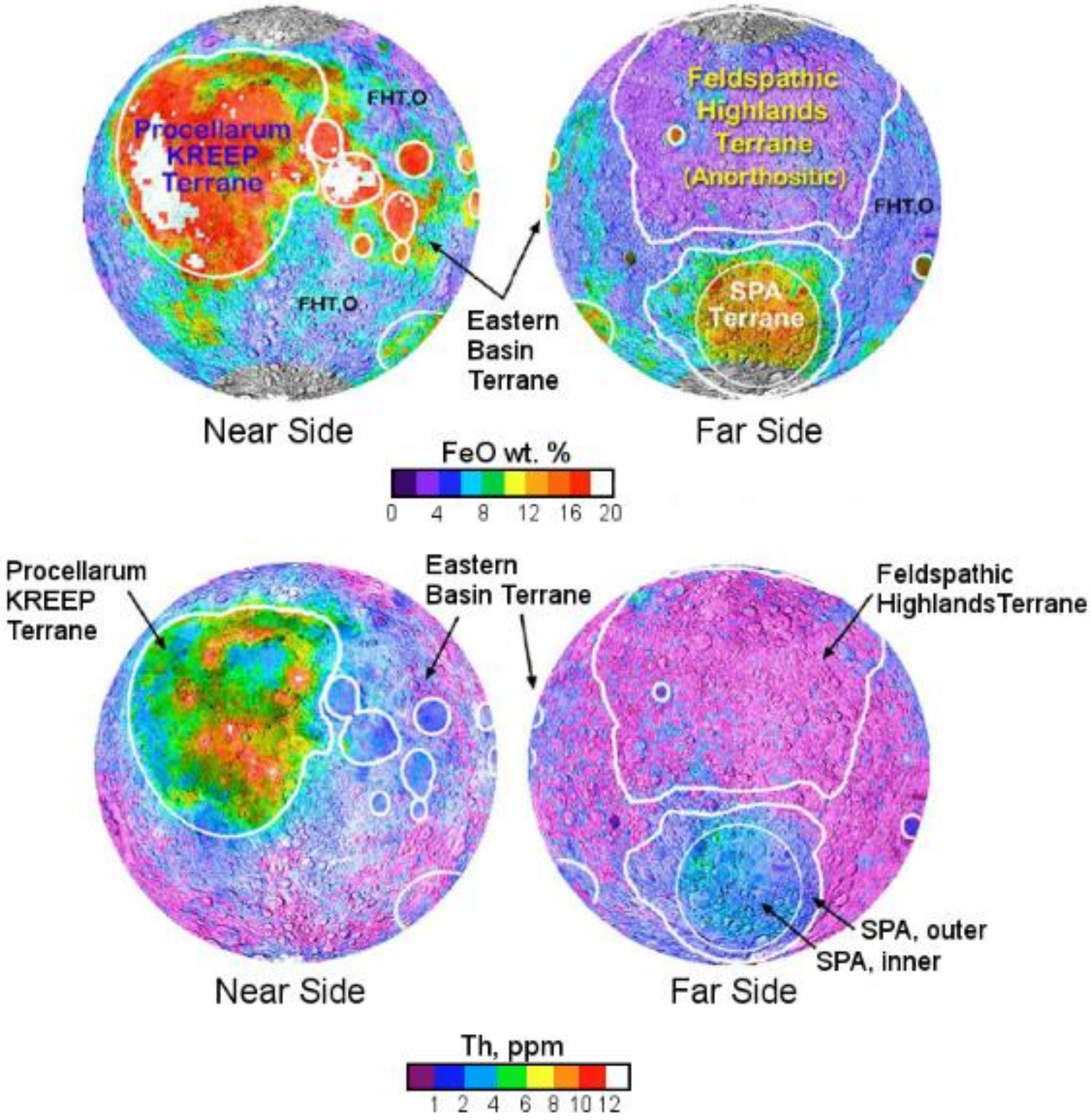

Figure 1.7 Major lunar terranes as inferred from the distribution of FeO derived from Clementine data (2 degree resolution, 60 × 60 km) and Th concentration from Lunar Prospector data on the lunar surface. (Modified after Jolliff et al. 2000; Gillis and Spudis 2000).

The central anorthositic portion (FHT; Figure 1.7 and Figure 1.8) is considered to be the thickest part of the crust with thicknesses between 50 and 60 km (Zuber et al. 1994; Jolliff et al. 2000; Wieczorek et al. 2013; Besserer et al. 2014). The FHT has an average FeO content of ~4.2 wt.% and an estimated Al_2O_3 content of ~29 wt.%. This estimation is based on empirical correlations between FeO and Al_2O_3 observed in the Apollo sample collection (Korotev 1999). With the exception of Mare Moscoviense (Figure 1.1), there are no observations of elevated FeO concentrations on the FHT, neither evidence of exposures of mafic compositions on central peaks. This indicates that the composition of this crust is dominated by a mixture of materials with an average composition similar to noritic anorthosite (80-90% plagioclase; Jolliff et al. 2000).

The FHT-O (Figure 1.7) is feldspathic and shows FeO abundances of ~6 wt.%. The possible explanation for this slightly more mafic signature is that the crust of this region is thinner compared to the central portion and therefore, it contains greater quantities of lower crust material (more mafic) from ejecta blankets of large impact basins. The lower crust is thought to be dominated by ferroan anorthosites and granulites, this is supported by feldspathic lunar meteorites (Korotev 1999; Jolliff et al. 2000; Wieczorek et al. 2006).

There is evidence suggesting that the feldspathic crust becomes more mafic with depth, and this could be considered the result of cumulate flotation in a chemically evolving LMO (Wieczorek and Zuber 2001; Wieczorek et al. 2006). As the LMO crystallised, the residual magma became enriched in FeO and, therefore, denser (Warren 1990). Because of the increasing density of the residual magma, the crust grew downward and the proportion of mafic cumulates were incorporated into the floating crust (Figure 1.8). The observed chemical zonation may be the result of the mechanical separation of feldspathic and mafic phases after the crust was largely formed (Wieczorek et al. 2006).

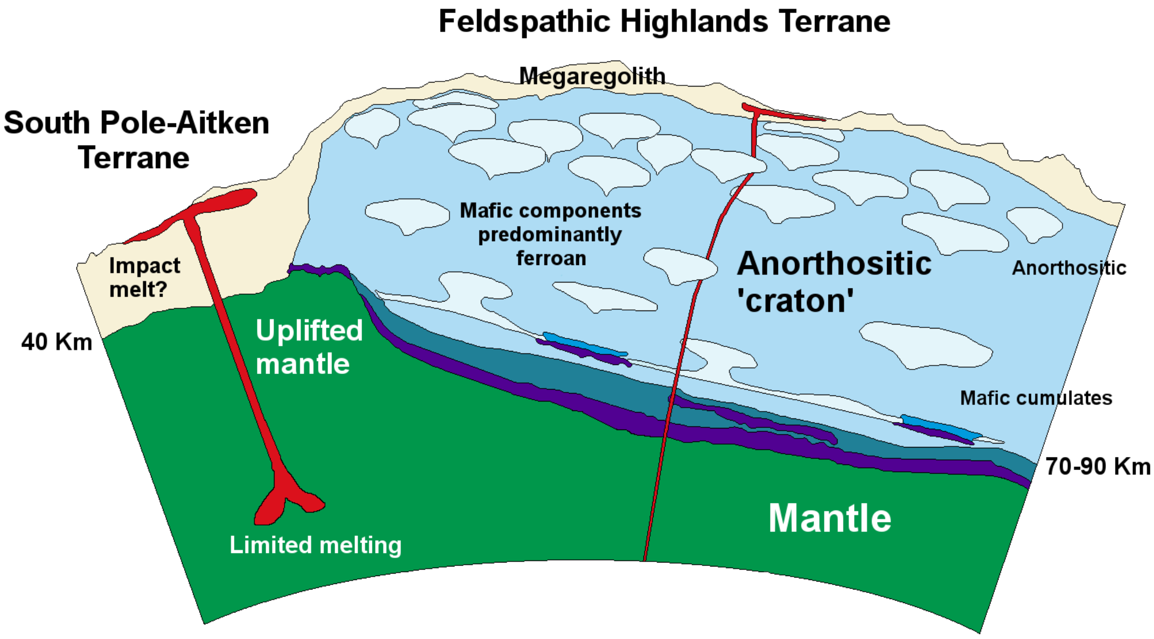

Figure 1.8 Cross section of the Feldspathic Highlands Terrane (FHT) and South Pole-Aitken Terrane (SPA). The thickest part of the lunar crust is the central anorthositic region of the FHT. It is composed of ferroan-anorthositic rocks and covered by a thick megaregolith partly consisting of basin ejecta. More mafic rocks such as anorthositic norite or gabbro occurred when bodies of residual may occur throughout the terrane. Basin ejecta suggests that the terrane is more mafic at depth. The SPA could be simply the excavation of typical FHT. (Modified from Jolliff et al. 2000).

Remote sensing observations suggest, however, that the crust formation scenario was much more complex than suggested (see discussion in Pernet-Fisher and Joy 2016), since FHT in the far side appears to be more magnesian that the highlands in the nearside (Ohtake et al. 2009; Crites and Lucey 2015). The causes of this compositional dichotomy are not well understood yet, although several models address this issue. The asymmetrical plagioclase flotation within the LMO model (Loper and Werner 2002; Ohtake et al. 2013) proposes that during the LMO crystallization, the nearside was hotter than the farside because of shielding by the Earth (Arai et al. 2008). As a result, plagioclase crystals float first on the farside, from a more Mg-rich parental magma. Gravity measurements from NASA's GRAIL and other gravity missions show that farside crust is thicker relative to the nearside crust (Wieczorek et al. 2013), this observation is seen by some authors as supportive of this model (Ohtake et al. 2013).

1.7.2. South Pole-Aitken basin

The South Pole-Aitken basin (SPA) is distinguished in the southern far side of the Moon by its circular shape and low albedo. It is considered to be the largest impact basin in the Solar System with a diameter between 2400 and 2500 km and reaching depths of up to 12 km below the surrounding highlands (Jolliff et al. 2000; Garrick-Bethell and Zuber 2009; Potter et al. 2012; Figure 1.7). The area has higher FeO abundances compared with the feldspathic lunar crust (7-14 wt.%) and, although impact-crater-scaling laws predict that the impact should have excavated into the mantle, crustal thickness modelling and remote sensing data indicate that the floor of the basin is composed of lower crustal crust (Spudis et al. 1994; Wieczorek and Phillips 2000; Jolliff et al. 2000).

Two regions are distinguished within the SPA: an inner central region (~1000 km of diameter) with thinner crust that may represent a mixture of lower crust and upper mantle, and an outer region along the topographic rim and the proximal exterior that could represent ejected lower and mid-crustal materials mixed with the ancient surface (Jolliff et al. 2000). The inner region shows FeO average abundances of ~10 wt.%, Th concentrations of ~2 ppm, lower to those observed within the PKT (~5 ppm), although slightly higher than those observed in the FHT (< ppm; Figure 1.7). Thus, the Th content is less than expected if the lower crust were KREEP-rich. Despite the thinner crust, there is no significant resurfacing by mare basalt flows, although basalt patches, predominantly of Imbrian age, were observed on the floor (Pieters et al. 2001).

The lithology of the mafic floor of the SPA still remains unknown. Although the possibility that the basin has excavated into the mantle could not be dismissed, crustal thickness modelling suggests the basin is situated over a significant thickness of crustal and not mantle material (Figure 1.8). However, it is not totally unreasonable that part of the underlying mantle melted as a consequence of the impact (Potter et al. 2012, 2015; Miljkovic et al. 2015). The SPA basin is a high-priority target for future investigations because of the lack of knowledge of its crust/mantle components (Wieczorek and Phillips 2000; Jolliff et al. 2000; Wieczorek et al. 2006).

1.7.3. Procellarum KREEP Terrane

The Procellarum KREEP Terrane (PKT) covers up to 16% of the lunar surface and encompasses nearside Oceanus Procellarum, Mare Imbrium and the adjacent mare and highlands (Figure 1.7). This region is defined by large concentrations of incompatible trace elements such as Th, K, P and REE. Its limits are defined by the Th concentrations derived from Lunar Prospector measurements that lie within a range between ~3 to ~12 ppm (Figure 1.7), whereas, the concentrations of this element outside the area are less than 2 ppm (Wieczorek and Phillips 2000; Jolliff et al. 2000; Wieczorek et al. 2006).

Despite its relatively small extent, 60% of the lunar basalts are concentrated in this terrane. These basalts occur as smooth lava plains, occasionally disrupted by impact craters. The PKT material shows higher concentrations of FeO (up to ~22 wt.%) in these basalts than in the surrounding PKT highlands, however, Th concentrations within these basalts and surrounding highlands have similar concentrations (average ~5 ppm). Over 50% of the PKT basalts also have abundances of TiO_2 higher than 5 wt.%, in contrast with the 20% of the basalts outside this region (Haskin et al. 2000; Wieczorek and Phillips 2000; Wieczorek et al. 2006).

Remotely sensing data indicate that KREEP-rich material on the Moon is mostly confined to this region, although there are some KREEP-rich patches in SPA and in the Compton area on the farside (Lawrence et al. 2003; Jolliff et al. 2011). According to the LMO model, a KREEP-rich residual melt accumulated between the crust and the mantle (Figure 1.9; Wieczorek et al. 2006). KREEP-bearing mafic impact-melt breccias from the Apollo program provide the best estimates for the bulk composition of the PKT. Korotev (2000) proposed a mixing model where the composition of these samples corresponds to mixtures of three components: approximately 30% of the crust would be formed by anorthositic upper crust materials, about 60% would have norite compositions similar to those of the Apollo 15 basalts, and the remainder 10% would be Fo_{90} dunite derived from the upper mantle. The crust in this area is suspected to be thinner, making easier to KREEP material reach the surface (Korotev 2000; Wieczorek and Phillips 2000; Wieczorek et al. 2006).

The voluminous volcanism of the PKT may be explained by the high abundance of radioactive elements that would produce enough heat to partially melt the underlying mantle causing the mare volcanism (Wieczorek and Phillips 2000; Parmentier et al. 2002; Wieczorek et al. 2006). This extensive melting of the mantle may have altered its composition leaving a residuum formed mainly by olivine. This agrees with the observations made by Korotev (2000) of a highly forsteritic dunite component. Hess and Parmentier (1995) alternatively suggested that the high magnesium dunite could be consequence of a possible overturn of the magma-ocean cumulates. The underlying mafic minerals were stratified with denser, more Fe-rich compositions on their top causing the instability that produced the overturn. However, not all mare basalts exhibit the isotopic signature of the presence of KREEP in their source regions, suggesting the presence of alternative magma generation models (Hess and Parmentier 1995; Parmentier and Hess 1998).

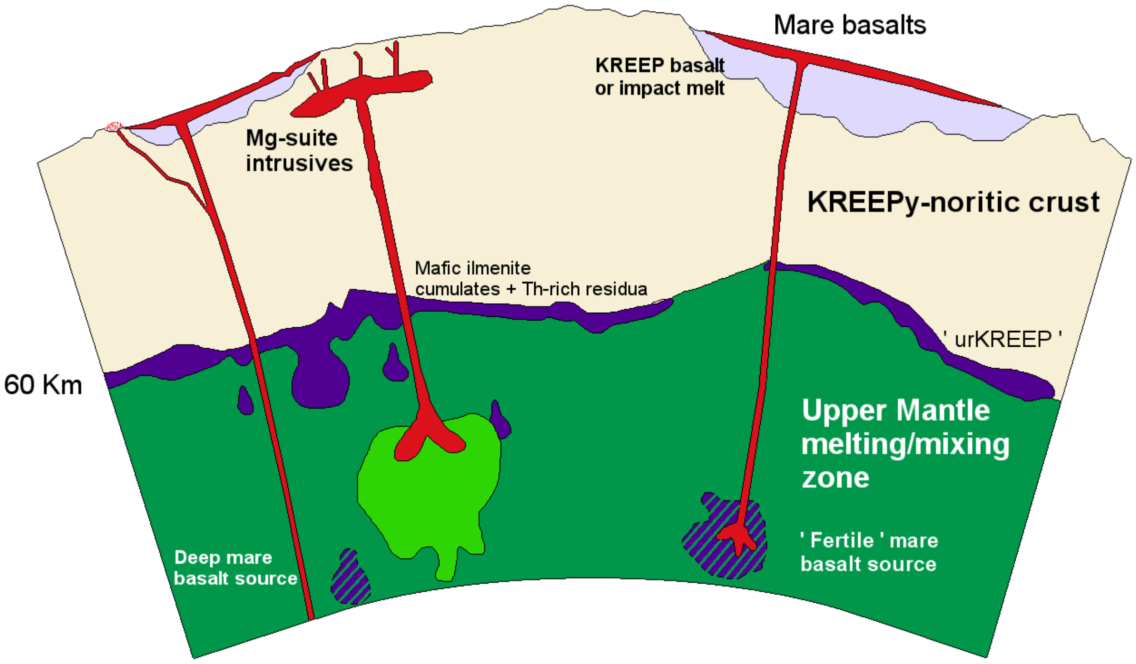

Figure 1.9 Cross section of the Procellarum KREEP Terrane (PKT). The entire crust (60 km depth) is considered to be formed by relatively mafic, Th-rich material. The urKREEP residue is concentrated between the mantle and the crust and associated to mafic ilmenite cumulates and Th-rich residua that sank interacting with the underlying mantle and providing with fertile melting zones for mare basalts or reacted with magnesian olivine-rich cumulates. Additional heating zone could have been provided by Th-bearing residua, helping to melt mantle cumulates. Isolated bodies of urKREEP and Mg-suite intrusives derived from KREEP-like parent magmas produced the alkali suite of rocks in this terrane. (Modified from Jolliff et al. 2000).

1.7.4. Cryptomaria

The term cryptomaria is used to describe mare basalt deposits that are hidden or obscured by a variable thickness (a few kilometres to metres) of superposed higher albedo material (Figure 1.10) These deposits are identified by the presence of a dark halo surrounding craters that excavate through the higher albedo ejecta reaching the underlying mare, and by the observation of spectral or geochemical anomalies (Antonenko et al. 1995). It is believed that this mare material is formed by extrusive magmatic rocks and represents an early phase of mare magmatism predating the late heavy bombardment (LHB; 3.8-4.1 Ga). Therefore, cryptomaria record the earliest mare volcanism undergone by the Moon, lasting from ~4.2 to ~3.2 Ga (Shearer et al. 2006). The nature of these deposits are not still fully understood, mainly due to the limited amount of samples recovered from these areas (Shearer et al. 2006). So far, just the basaltic meteorite Kalahari 009 and its feldspathic paired stone Kalahari 008, has been considered of cryptomare origin (Terada et al. 2007; Sokol et al. 2008).

Antonenko (1999) estimated that cryptomare materials cover a surface area approximately half of the area covered by maria, and represent a volume equal to 30% of the mare volume. These hidden mafic materials are a significant contribution to lunar volcanism, although it also could be possible that some of these deposits are, in fact, shallow magnesian plutons and not extrusive volcanism (Shearer et al. 2006).

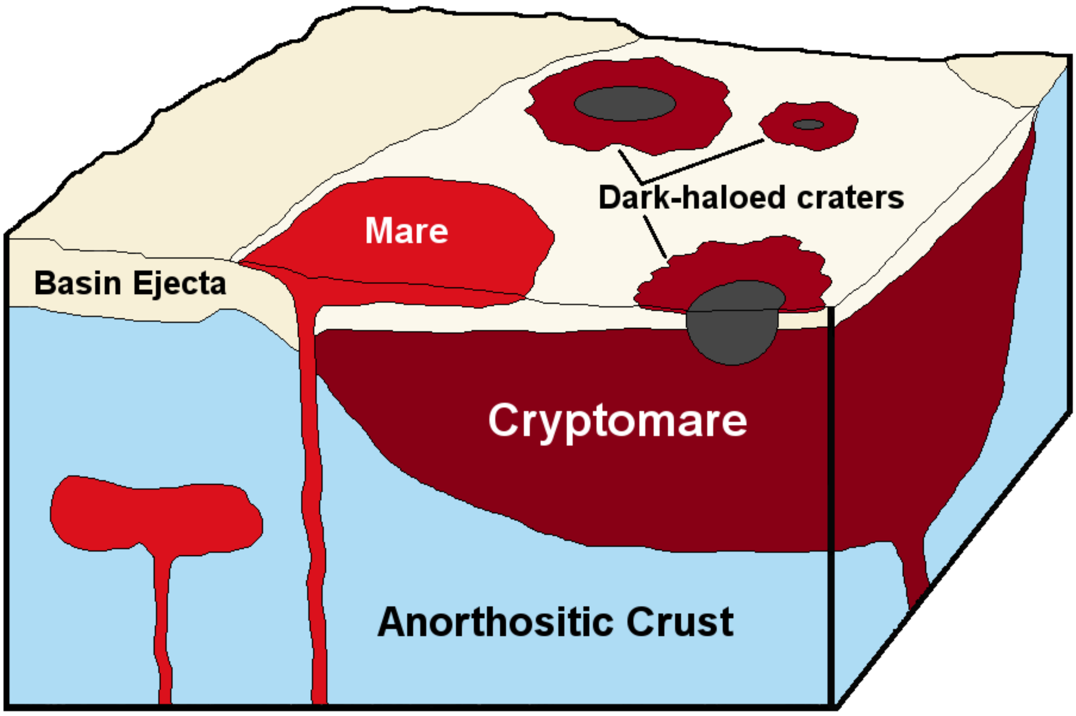

Figure 1.10 Diagram representing the formation of a cryptomare by emplacement of basin ejecta of higher albedo over a pre-existing low albedo mare deposit. The dark halo impact craters (DHC) penetrates the regional ejecta to excavate mare material. (Modified from Shearer et al. 2006).

1.8. Lunar Maria

Secondary crusts are created as a result of the partial melting of planetary mantles, as opposed to primary crusts that are formed as a result of accretional heating like the ferroan anorthosite suite (Taylor 1988; Taylor and McLennan 2009). Mare basalts cover approximately 17% of the lunar surface (Taylor and McLennan 2009), mostly filling low topographic areas on the nearside with limited occurrences in the far side (i.e. Mare Moscoviense or patches within SPA; Figure 1.11). This observed asymmetry between maria from the nearside and the farside has been interpreted as variations between crustal thickness. The farside crust is considered to be thicker (between 50-60 km) than the nearside crust (between 25-35 km; Wieczorek et al. 2013).

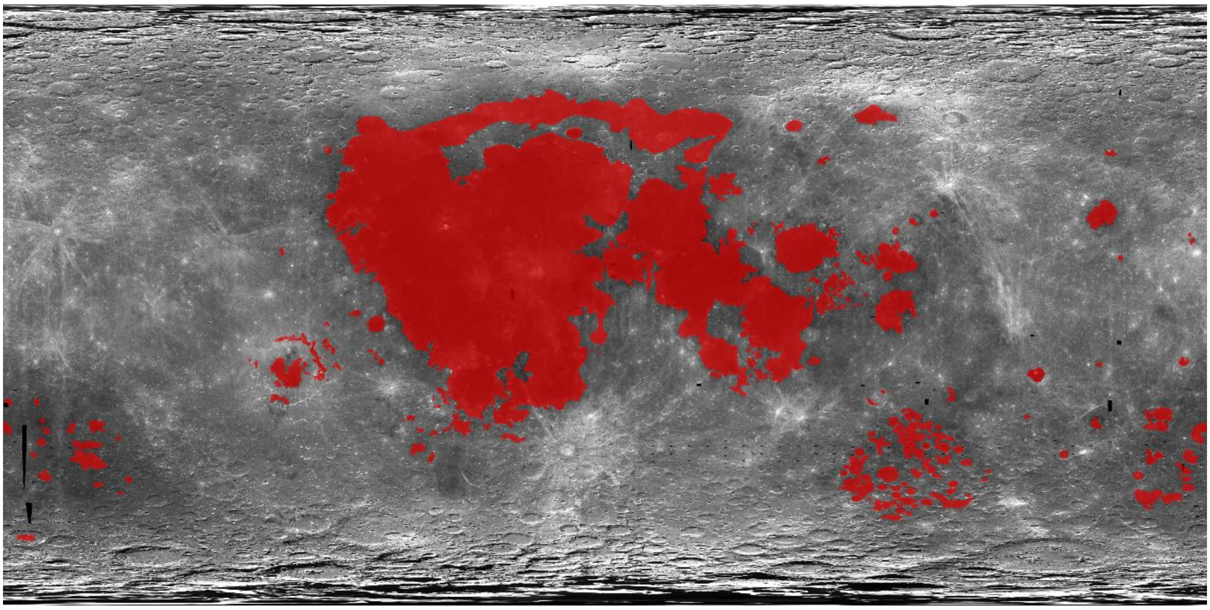

Figure 1.11 Approximate distribution of maria basalts on the Moon based on their albedo, shown in red.

Mare basalts show low albedo and smoother surfaces in contrast to the rugged and older feldspathic highlands. The characteristics of the mare basalts are observed on effusive, flood-type eruptions. The average thickness of the basalt deposits are ~0.74 km, with lava flows of ~10 m thick (Robinson et al. 2012; Gong et al. 2016). Based on stratigraphic evidence, the volume of these basalts has been estimated in 1×10^7 km^3 (Head and Wilson 1992; Shearer et al. 2006; Taylor and McLennan 2009). In addition to the basalts, beds of picritic and coloured volcanic glasses probably generated by fire-fountaining, has been detected (Head and Wilson 1992).

The major-element compositions of the mare suite have a wide range of compositions. They have been summarized by several authors (Neal and Taylor 1992; Shearer and Papike 1993, 1999; Shearer et al. 2006). Mare basalts and picritic glasses have lower CaO, Al_2O_3, and Na_2O contents, and higher FeO and MgO than terrestrial ocean floor and ocean islands basalts. The lower Na_2O is a signature of the depletion in volatile elements on the Moon (Taylor 1982). In basalts formed in equilibrium with the terrestrial lherzolite mantle the CaO and Al_2O_3 content is higher than those observed in the lunar maria basalts. Bulk compositions of picritic glasses are similar to komatiites, thus the mare basalts are products of ultramafic magmas (Shearer et al. 2006).

Bulk rock Ti content in mare basalts varies between very low to high content (0.22-17 wt.% TiO_2), while primitive terrestrial MORB and magnesian alkali lavas have narrower TiO_2 values (0.5-1.2 wt.% and 4-6 wt.% respectively; Papike 1998; Giguere et al. 2000; Shearer et al. 2006). Basalts derived from small degrees of fertile lherzolite do not have more than 2 wt.% TiO_2, depleted mantle close to harzburgite has even smaller TiO_2 values. The higher TiO_2 concentrations on terrestrial highly alkaline primitive basalts is probably because the effect of the CO_2 in the melting process. Therefore, in a volatile-depleted environment such as the Moon, the high TiO_2 must be originated from a mantle that is differentiated and TiO_2 enriched (Shearer et al. 2006).

Bulk rock TiO_2 content is used to classify mare materials, with additional divisions based on their Al_2O_3 content and K_2O (Neal and Taylor 1992). This classification distinguishes three groups: Very low-Ti basalts, high-Ti basalts and low to intermediate-Ti basalts (Neal and Taylor 1992; Taylor and McLennan 2009).

Very-low-Ti basalts (VLT) have bulk rock chemical compositions with <1 wt.% TiO_2. Basalts within this suite contain Mg# molar up to 0.6, which indicates either that the VLT basalts were produced by higher degrees of partial melting or derived from a magnesian source. It is also observed than TiO_2, CaO and Al_2O_3 increases with decreasing MgO in VLT basalts. This is because the olivine and pigeonite compositions higher in Mg, are in the liquidus phase (Papike 1998).

High-Ti basalts have bulk rock chemical compositions between 9-14 wt.% TiO_2. In high-Mg mare basalts where olivine is the only liquidus phase, it is observed than TiO_2 increases as MgO decreases (Green et al. 1975; Walker et al. 1975; Longhi 1992). However, in lower magnesian basalts, armacolite and spinel join the olivine as the liquidus phase and it produces that the TiO_2 content decreases as MgO decreases. The increase of Al_2O_3 and CaO as MgO decreases is caused by the fractional crystallization sequence (Papike 1998).

The low to intermediate-Ti basalts group is formed by basalts with bulk rock TiO_2 compositions between 1 and 5 wt.%. This type of basalts was unknown in the Apollo, Luna and meteoritic samples, however, it was found within the Chang'e 3 landing site (Neal et al. 2015).

The chondrite-normalized REE patterns of what shows a characteristic Eu depletion within the basalts (Figure 1.12). This is evidence of an origin from a previously differentiated interior where the plagioclase has been already removed from the source. The depth of the Eu-anomaly usually increases with increasing REE concentration from VLT to high-Ti basalts. This anomaly is a consequence of the fractionation of Eu^{2+} from the REE under low Oxygen fugacity conditions during plagioclase flotation in the magma ocean (Taylor 1982; Papike 1998; Taylor and McLennan 2009; Shearer et al. 2006).

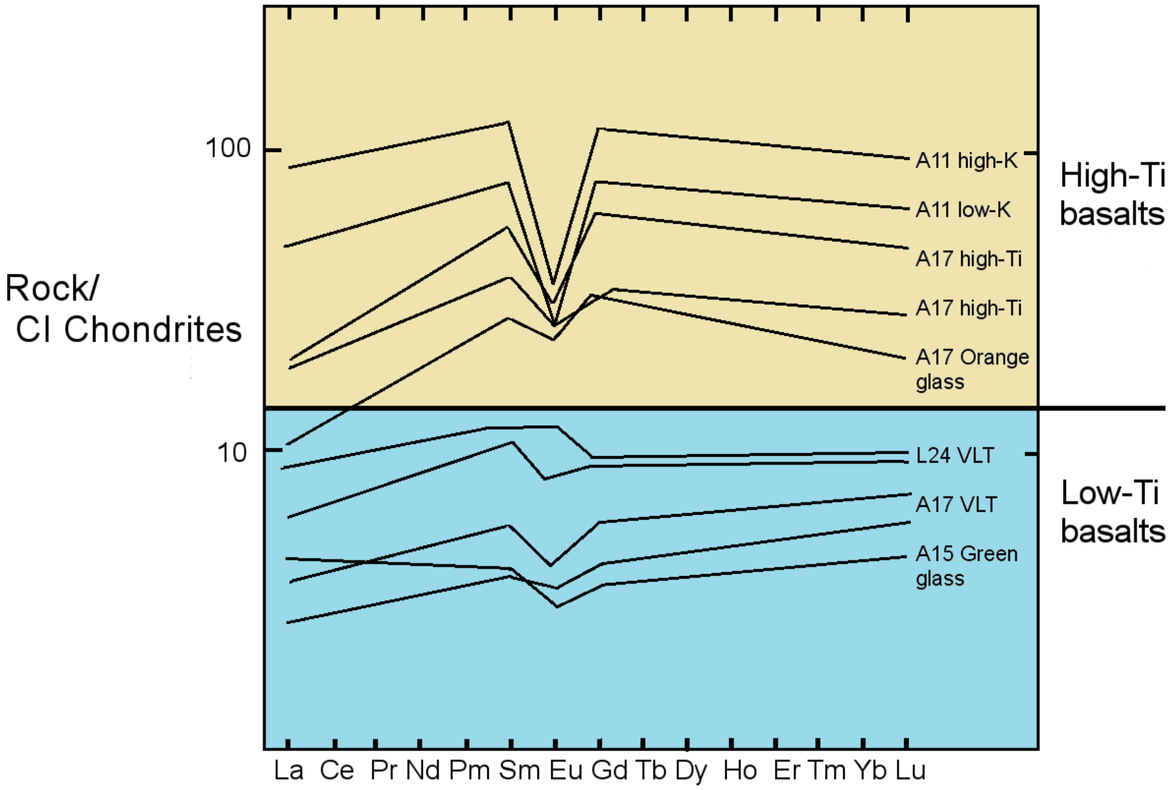

Figure 1.12 Chondrite-normalized REE bulk rock concentrations in a series of mare high-Ti and low-Ti basalt samples. The REE are in order of increasing atomic number in the horizontal axis. The vertical axis shows the REE concentration in the samples normalised to the chondritic average compositions. (Modified from Papike 1998).

Radiometric ages and photogeology crater counting indicate that the ages of mare basalts ages range from 3.8 to ~1.0 Ga (Taylor 1982; Nyquist and Shih 1992; Shearer et al. 2006) and the youngest basaltic units could have been extruded between 0.9 and 2.0 Ga (Schultz and Spudis 1983). Early and intermediate extrusive events within a basin were probably dominated by high-Ti basalts, followed by low-Ti basalts in subsequent periods of eruption (Head and Wilson 1992).

1.9. The Lunar Regolith

The regolith is the layer that is nearly everywhere on the lunar surface", it overlies the bedrock and is formed by fragmental and unconsolidated rock material of varied character, whether residual or transported (Figure 1.13; McKay et al. 1991; Lucey et al. 2006). The term regolith is not exclusively a lunar term, it may be applied to any layer with these characteristics that covers any planetary surface, including the Earth (Spray 2016). However, the processes that create and influence this layer on the Moon are very different of those that develop the Earth's counterpart. Because the lack of atmosphere on the Moon, the regolith is the result of large and small meteoroids and space weathering. It represents the actual boundary between the lunar surface and the outer space environment, and it preserves information from both of these regions (McKay et al. 1991; Papike 1998).

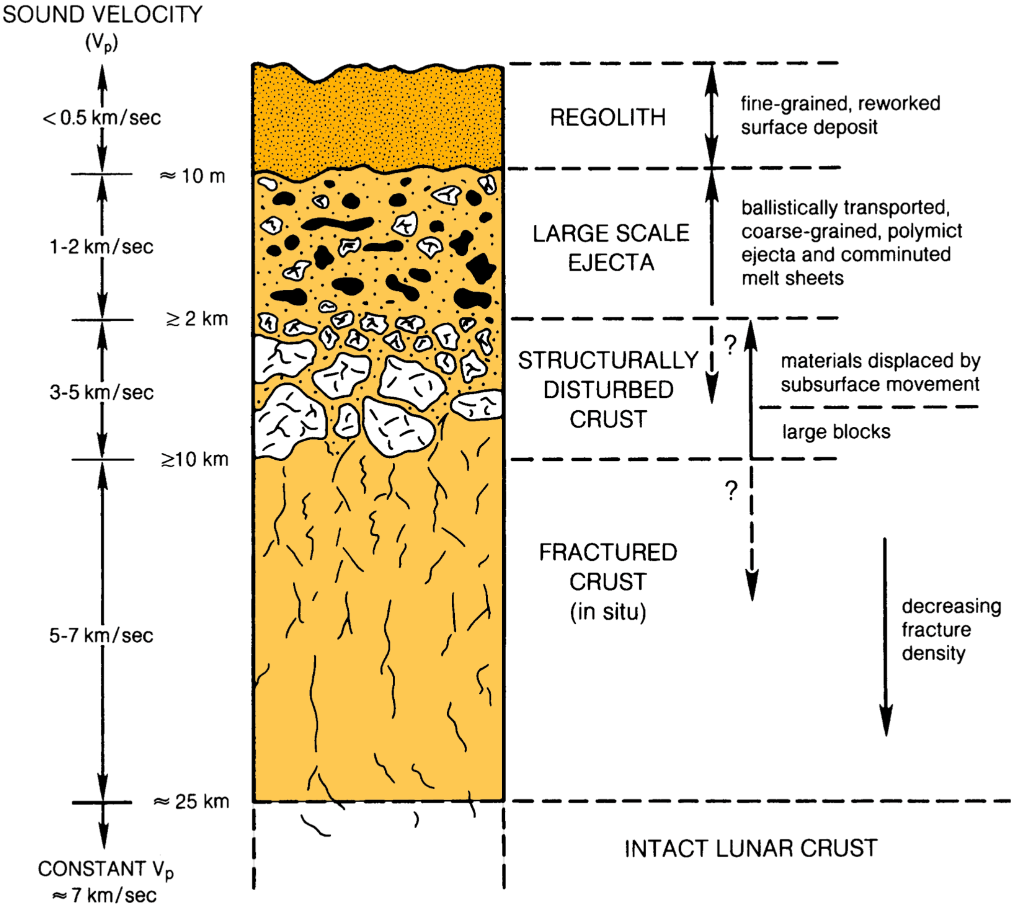

Figure 1.13 Idealized cross-section of the upper lunar crust. The scale is uncertain and based on observations at the Apollo landing sites and inferred from impact cratering models (from Friedrich Hörz, Lunar and Planetary Institute).

1.9.1. Space weathering

Space weathering is a set of processes, caused by external forces that modify in situ the material on the upper layer of the lunar surface. Because of the lack of atmosphere and hydrosphere, the major weathering forces on the Moon are external to the planet and operate at smaller scales. These processes include the impacts of micrometeoroids, the implantation of solar-wind gases, and products of solar and galactic-cosmic-ray interactions (Lucey et al. 2006). They are of great importance for understanding the lunar exposure ages and burial depths of lunar meteorites.

Micrometeoroids are interplanetary material of <1 mm of diameter that impact a planetary surface. During the impact, the micrometeoroids vaporise but cause erosion, melt and vaporisation of the lunar regolith. Studies suggest that the erosion rates caused by micrometeoroids are of ~1-2 mm per million years (Nishiizumi 1995; Fink et al. 1998). This process creates agglutinates that are lithic, mostly glassy, highly vesicular components and the main carrier of the nanophase iron (^{0}Fe) on lunar materials (McKay et al. 1991; Lucey et al. 2006).

Lunar regolith contains solar-wind isotopes that were implanted while exposed on the surface. The Sun creates isotopes that are carried out by solar winds to be finally implanted in the regolith (e.g. He and Ne). These isotopes allow us to trace the processes that occurred in the outer regions of the Sun (Wieler 2016). Other isotopes escape the Moon to the interplanetary environment, became ionized and finally are accelerated and implanted in the Moon. Decay of ^{40}Ar into ^{36}Ar makes it possible to date the samples where they were implanted (Eugster et al. 2001; Lucey et al. 2006; Joy et al. 2011; Fagan et al. 2014).

Neutron-capture reactions are function on depth and are used to determine the depth at which a lunar sample was exposed. These isotopic anomalies include ^{14}Ca and ^{10}Be (Nishiizumi et al. 1997; Hidaka et al. 2000; Sands et al. 2001). Cosmic ray spallation creates new elements expelling from the impact of cosmic rays on the lunar surface. They have been used to determine the formation age of many impact craters (Eugster 1999; Lucey et al. 2006).

Maturation is the result of the processes described above, which decreases the mean grain size of the regolith particles with time. Despite the fact that maturation works at the very surface, turnover of the regolith by impacts (also known as in situ reworking) mixes and buries mature soil. Apollo cores have shown that units of mature regolith exist to depths of at least a few metres (Morris et al. 1983; Lucey et al. 2006).

1.9.2. Regolith composition

The vast majority of the lunar samples returned from the Apollo and Luna missions are regolith samples. Study of this material has shown that it mainly consists of particles ranging from 40 to 800 µm in size, with averages from 60 to 80 µm, poorly to very poorly sorted (Spray 2016). Compositionally, the lunar regolith is a mixture of three lithological end-members: (1) rocks and breccias of feldspathic composition, (2) KREEP material and (3) mare basalts or volcanic glass (Figure 1.14), plus impact products (glasses and agglutinates) and a minor exogenous meteoritic/cometary component (Lucey et al. 2006; Joy et al. 2012). However, although most of the possible mixtures are found within Apollo and Luna samples, other mixtures are not seen in those samples although it was observed in some lunar meteorites, such as 50:50 feldspathic and basaltic material on Queen Alexandra Range (QUE) 94281 and Yamato 793274 (Jolliff et al. 1998; Arai and Warren 1999). Other lithology types that are not included in the mixing triangles, such as the Mg-rich suite or the high-alkali suite that would plot outside the mixing triangle (Spudis and Davis 1987; Lucey et al. 2006).

Within each Apollo and Luna site it is common local variations that suggest changes in the regional geology as well as variations with depth as a result of overlapping ejecta deposits from different craters (Lucey et al. 2006).

Shock compression during impact events lithifies the unconsolidated regolith forming regolith breccias (McKay et al. 1986). Like the regolith from which they derive, they represent complex mixtures of different mineral and rock fragments derived from a range of different protolith environments. They provide information about the regolith formation in different periods of lunar history (McKay et al. 1986; Joy et al. 2011; Fagan et al. 2014). Regolith breccias also provide insights into the composition of different regions of the Moon giving an estimate of the composition of the upper crust (Palme et al. 1991; Warren 1994; Korotev et al. 2003; Warren et al. 2005; Joy et al. 2010; Korotev and Zeigler 2015).

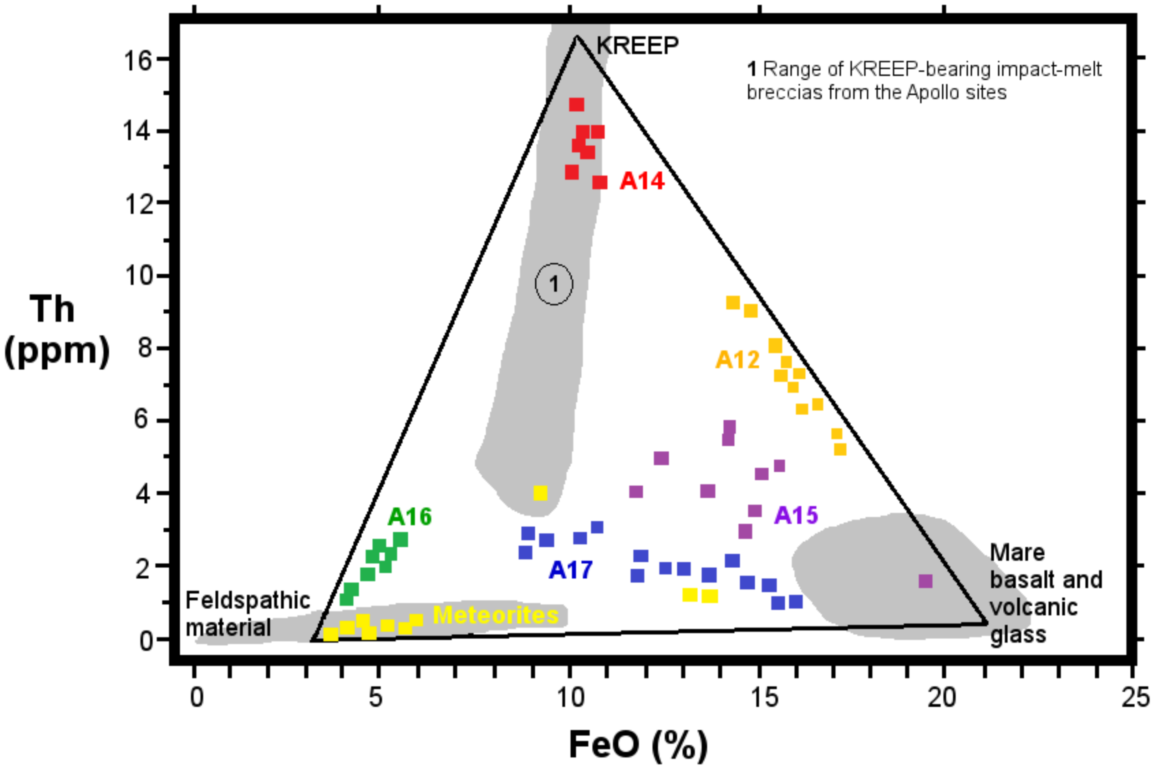

Figure 1.14 The Apollo lithological rock composition mixing triangle using the bulk rock Th ppm and FeO wt.% contents. Regolith compositions are mainly mixture of three components: Feldspathic material, mare basalt and volcanic glass and KREEP material represented on the corners of the triangle. Regolith samples for Apollo missions and meteorites are plotted as a mixture of those three materials. Grey areas represent the compositional range of these classes among Apollo samples. (Modified from Korotev et al. 2003 and data sources listed therein).

1.10. Lunar Remote Sensing

Remote sensing missions have provided key insights into the chemical, mineralogical and geophysical diversity of the Moon. For example, the Lunar Prospector gamma ray spectrometer (LP-GRS) data have enabled the estimation of global concentrations of rock-forming elements, which differentiate the major lunar crustal terranes (Figure 1.7; Elphic et al. 1998; Lawrence et al. 1998; Jolliff et al. 2000; Gillis et al. 2004). Other instruments have been used to understand the mineralogy of the Moon. As examples, the Moon Mineralogical Mapper (M^3) on board the Indian spacecraft Chandrayaan-1 revealed the distribution and composition of low-Ca pyroxene exposures on lunar highlands terrane (Klima et al. 2011). Also, it allowed the discovery of Mg-spinel lithologies on the lunar farside showing that this type or rock plays an important role in the crustal structure (Pieters et al. 2011). Diviner Lunar Radiometer on NASA’s LRO was used to discover locations with highly silicic compositions, it helped to shed light into the global distribution of silicate mineralogy and evolved (high-alkali suite-style) magmatism and KREEP-rich volcanism on the Moon (Glotch et al. 2010; Greenhagen et al. 2010).

1.10.1. Lunar Prospector gamma-ray spectrometer

Gamma-rays are an electromagnetic radiation of very high frequency ($>10^{19}$ Hz) and short wavelengths ($<10^{-11}$ m) generated during the decay of an atomic nucleus from a high energy state to a lower energy state. This radiation can be produced naturally by the decay of radioisotopes such as Th, K and U, and as a secondary radiation from the bombardment of high-energy cosmic rays between cosmic ray particles and matter (Figure 1.15). When a cosmic ray nuclei (CR) hits the lunar surface, the nucleus of the matter gets excited generating a fast neutron by a process called beta-decay. The inelastic collision produced by the emitted fast neutron and the matter emits gamma ray in the process of returning to the previous non-excited state. The gamma-rays can be detected by spectrometers in orbit (Feldman et al. 1999; Scott Hubbard et al. 2002).

The Lunar Prospector mission gamma-ray spectrometer (LP-GRS) measured the abundances of 10 elements (Th, K, U, Fe, O, Si, Al, Ca, Mg and Ti) of the Moon’s regolith up to a depth of 20 cm (Feldman et al. 1999). It orbited in polar and circular orbits at an altitude between 80 and 120 km. The footprint of the instrument’s spatial response function is approximately 1.5

times the altitude of the spacecraft (Prettyman et al. 2006). The instrument consisted of a bismuth germanate cylinder (BGO) crystal of 7.1 cm of diameter by 7.6 cm long that measures gamma-rays at energies from 0.5 to 9 MeV. The BGO was placed within a borated-plastic scintillator anticoincidence shield that actively rejected galactic cosmic ray and other charged interactions in the BGO (Feldman et al. 1999; Lawrence et al. 2004).

The raw data directly received from the spacecraft were converted to time series gamma-way spectra that were used to derive composition measurements of the lunar surface. Several articles (e.g. Lawrence et al. 2004; Prettyman et al. 2006) describe the set of corrections and processing techniques applied to the gamma-ray spectra to create resultant spatially resolved elemental maps (Figure 1.16).

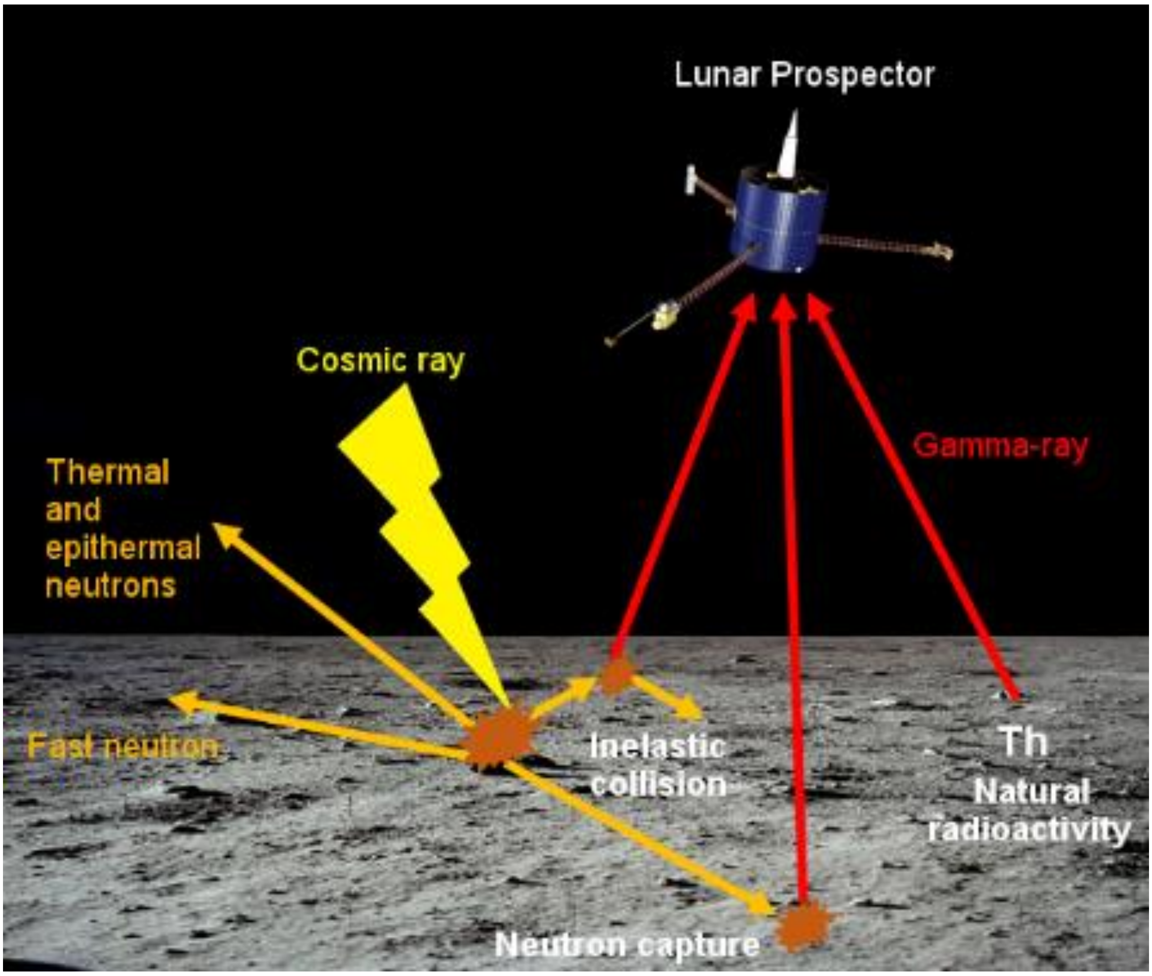

Figure 1.15 Interactions between cosmic rays and the lunar surface and nuclear gamma-ray emissions.

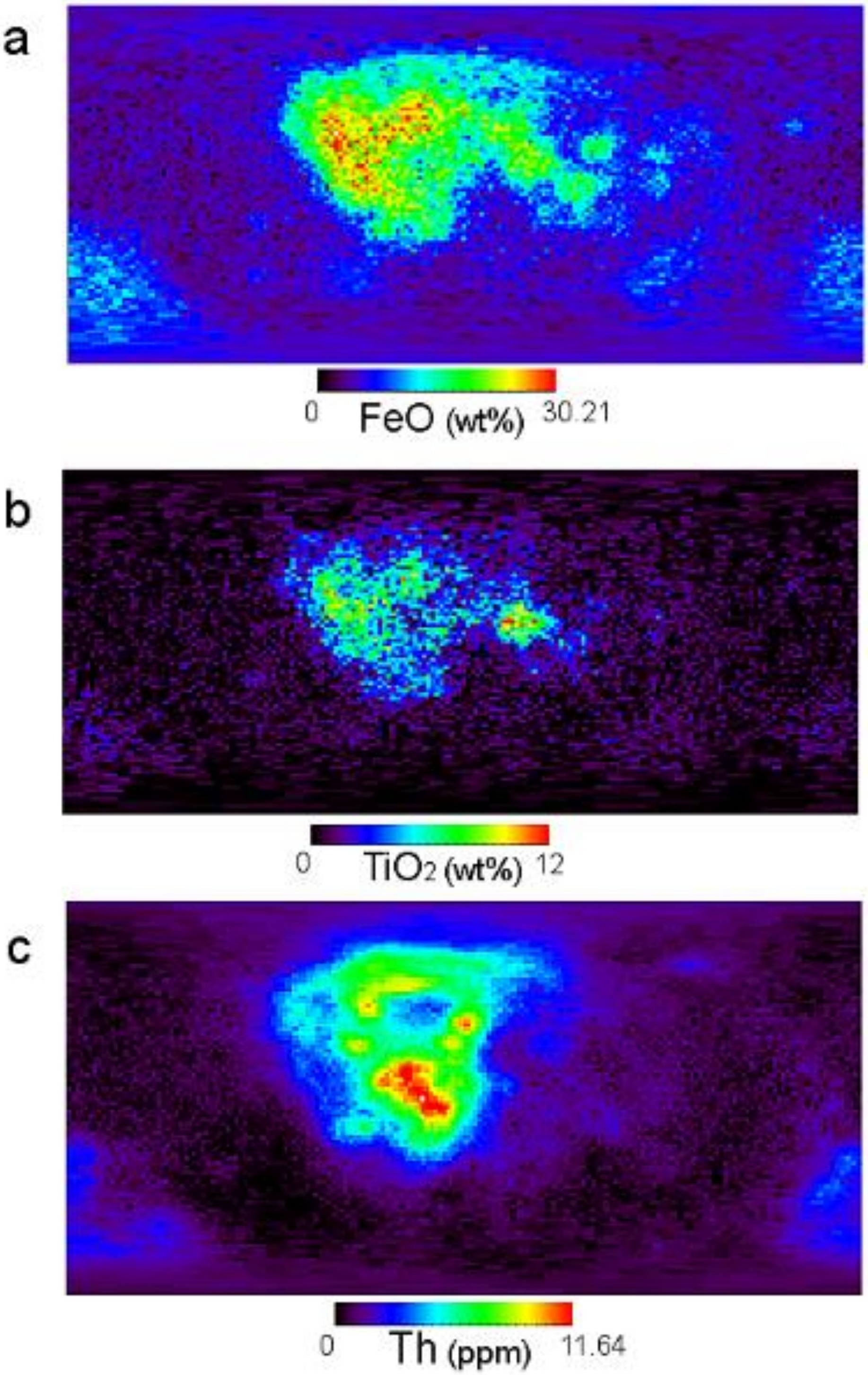

Figure 1.16 Global FeO (a), TiO_2 (b) and Th (c) abundance maps derived from LP-GRS measurements. The images are in cylindrical projection with 0° longitude and 0° latitude in the center. The spatial resolution is 60×60 km per pixel (2×2 degree). (Image produced by K. Joy using data from the Prettyman et al. 2006 LP calibration).

1.11. Aim and Thesis Structure

1.11.1. Aim of the project

Meteorites are ejected from random areas of the lunar surface and therefore provide information far from areas sampled during Apollo and Luna programs. But unlike these samples, the exact launch location and geological setting of meteorites are unknown, limiting greatly the knowledge we can obtain from them (Korotev 2005; Joy et al. 2008; Joy et al. 2010; Joy and Arai 2013b; Jolliff et al. 2014). This project intends to study the precedence of lunar meteorites, providing it with geological context and so, increasing the information that is possible to obtain from them.

Two major objectives are addressed during this thesis: (1) to provide lunar meteorites with a possible launch location to understand their geological setting using laboratory geochemical compositions of lunar meteorites both from the existing literature and own analysis, and global lunar data obtained using orbital remote sensing instruments. (2) To characterize geochemically and petrologically two unpaired lunar anorthositic meteorites, Miller Range (MIL) 090036 and 090070. Both stones were found during the 2009-2010 field season in Antarctica (Righter 2010; Korotev and Zeigler 2015). These meteorites were selected based on their novelty and lack of previous studies. Bulk elemental composition, mineral chemistry analysis and petrography of both meteorites are studied during this project and their possible launch origin identified in order to provide insights into their geological evolution.

Finally, data obtained during this study is used to refine geochemical models of lunar evolution as they relate to particular geographical and geological settings.

1.11.2. Thesis structure

This thesis is divided in 7 chapters. This chapter is an introduction to the lunar geology and a project outline. Chapter 2 describes the laboratory techniques and methodology followed to characterize the two feldspathic meteoritic samples Miller Range (MIL) 090036 and 090070. The results and data from the petrological and geochemical investigations are presented in Chapter 3 (MIL 090036) and Chapter 4 (MIL 090070). Chapter 5 presents the implications that possible launch locations of basaltic and high-Th meteorites have for the understanding of composition and evolution of the lunar crust. Chapter 6 describes the results and implications of possible launch locations of feldspathic meteorites. Finally, in Chapter 7 I summarize the results of this project, I also present some conclusions and suggest some recommendations for future research opportunities.

Chapter 2. Samples and Methods

2.1. Meteorite Samples

Miller Range (MIL) 090036 and 090070 are two lunar meteorites, classified as feldspathic regolith breccias (Figure 2.1). Both stones were found during the 2009-2010 Antarctic Search for Meteorites (ANSMET) field season in Antarctica (Righter 2010; Korotev and Zeigler 2015).

The Meteoritic Working Group (MWG) awarded allocation of the samples and the curation lab at NASA Johnson Space Center provided me with two chips: MIL 090036,32 weighing 217 mg, and MIL 090070,33 with a weight of 275 mg. I was also provided with two polished thick (100 µm thick) sections mounted in epoxy resin blocks: MIL 090036,34 and 090070,35.

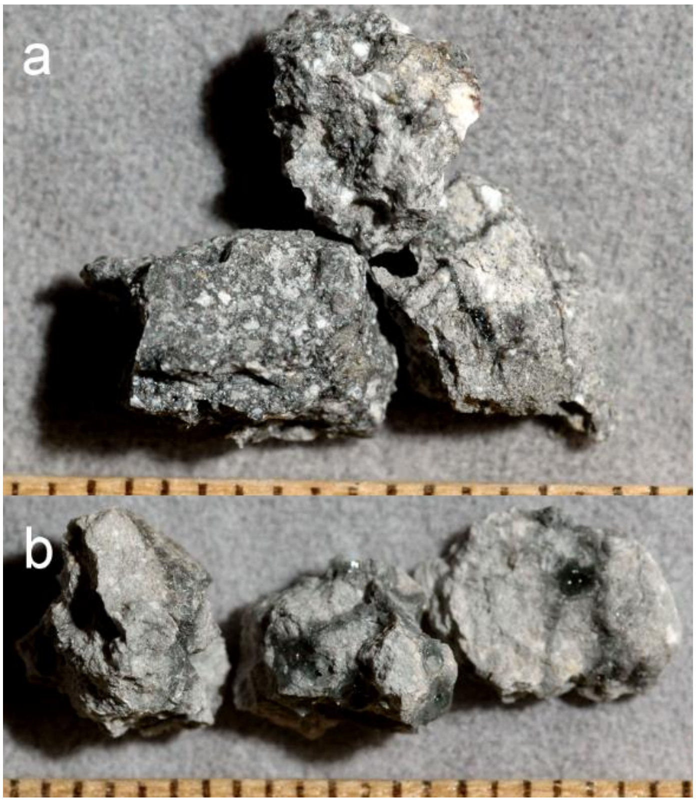

Figure 2.1 Chips of MIL 090036 (a) and MIL 090070 (b). Millimetre ticks for scale. (Courtesy of Randy Korotev *http://meteorites.wustl.edu/lunar/stones/mil0900xx.htm*).

2.2. Sample Preparation

A split of 150 mg of MIL 090036,32 and 090070,33 was powdered by myself using an agate pestle and mortar in a class 1000 clean room environment to avoid external contamination, at the University of Manchester. The splits were processed further at the Natural History Museum (NHM) in London, using a standard procedure, by Dr. Stanislav Strekopytov, in order to analyse their bulk chemistry. The samples were first dried at 105 °C and a 40 mg sub-split of each homogenized sample powder was pre-treated with 0.5 ml concentrated HNO_3 (SpA™ grade, ROMIL Ltd) and fused with 120 mg of $LiBO_2$ (Spectroflux™ 100A, Alfa Aesar®) in a Pt/Au crucible. The fused beads were dissolved in 40 ml 10% HNO_3 and made up to 100 ml with Milli-Q water.

An aliquot of 40 mg of each sample was pre-treated with 1 ml of concentrated HNO_3 and dissolved in a mixture of 4 ml HF and 1 ml $HClO_4$ (all acids were SPA™ grade, ROMIL Ltd) in a closed 60 m-l Savillex™ vial at 100 °C. This solution was dried down at 150°C and the residue re-dissolved at 150°C using 1 ml $HClO_4$. The solution was again dried down and then, re-dissolved in a mixture of 2 ml concentrated HNO_3 + 5 ml H_2O + 0.1 ml H_2O_2 (Suprapur® Merck) at 70 °C and afterwards made up to 40 ml with water.

The thick polished sections MIL 090036,34 and 090070,35 (Figure 2.2) were carbon coated at the NHM.

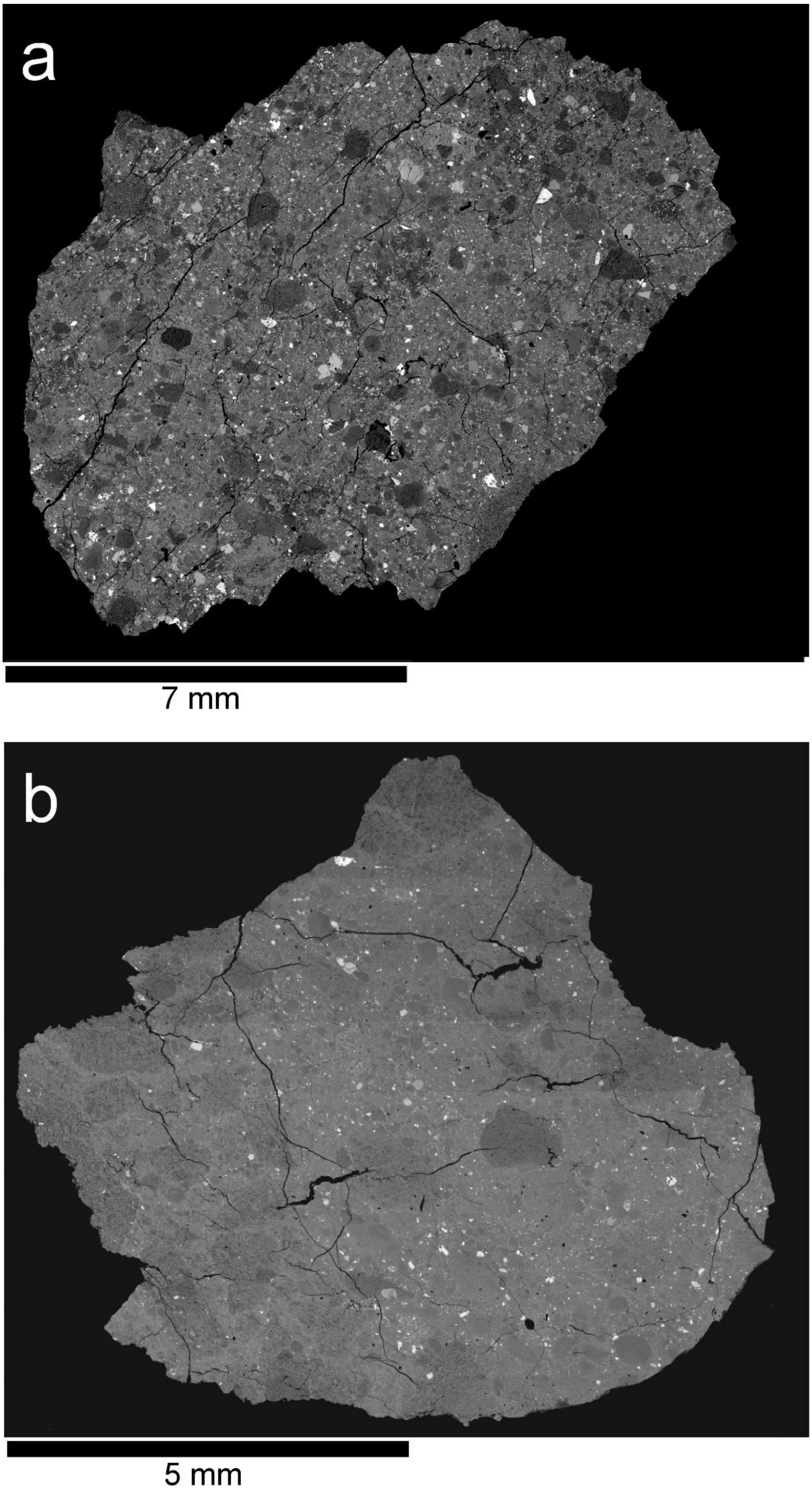

Figure 2.2 Back scattered electron image of (a) MIL 090036,34 and (b) MIL 090070,35

2.3. Analytical Techniques

2.3.1. Bulk-sample major, minor and trace compositions

Bulk-rock concentrations of major and minor elements (except Mn and K) were determined by inductively coupled plasma atomic emission spectrometry (ICP-AES). ICP-AES is a type of emission spectroscopy in which plasma produced by electric currents caused by electromagnetic induction (i.e. inductively coupled plasma) is used to produce excited atoms and ions that then emit electromagnetic radiation. The wavelengths emitted are characteristics of a particular element and the intensity of the emission indicative of the concentration of the element (Lichte et al. 1987; Manning and Grow 1997).

The analysis was performed by Dr. Stanislav Strekopytov at the NHM using a Thermo Scientific iCap 6500 Duo ICP Spectrometer. Calibration was performed using certified reference materials (CRM) prepared in the same way (see appendix 2A): AGV-2, BCR-2, DTS-1, GSP-2 and STM-1 (andesite, basalt, dunite, granodiorite and syenite, USGS); JG-1 and JDo-1 (granodiorite and dolomite; GSJ, Japan), NIM-G, NIM-S and NIM-P (granite, syenite and pyroxenite; NIM, South Africa), MGR-1 (gabbro; CCRMP, Canada), AC-E (granite, GIT-IWG); and a candidate reference material DBC-1 (Ball Clay, IAG). Calibration curves were calculated using up to 13 points for each element. Each sample was analysed in triplicate and the reproducibility for each major element was always better than 0.7%, and for P_2O_5 better than 3%. Accuracy was checked by the analysis of a CRM BHVO-2 (basalt, USGS) and a candidate reference material TML-1 (tonalite, IAG) and was within 1.1% of recommended values for all major elements and within 1.5% for P_2O_5.

Bulk-rock concentrations of trace elements, Mn and K were determined by inductively coupled plasma mass spectrometry (ICP-MS). This technique is very useful to determine trace elements because of its high precision and low detection limits. It uses inductively coupled plasma (usually Ar) to ionize the sample, the mass spectrum is then measured by a mass spectrometer (Beauchemin et al. 2002; Holliday and Beauchemin 2004; Beauchemin 2010).

In this work, I used an Agilent 7700x ICP-MS at the NHM. Samples were analysed in triplicate for most elements; the reproducibility being better than 1% for about half of the trace elements and better than 5% for all other elements apart from Cd, Cs and Tl. The analytical accuracy was checked using CRMs JLs-1 and JLk-1 (limestone and lake sediment, GSJ), and BCR-2 and

DNC-1 (basalt and dolerite, USGS; see Appendix 2A). For most elements the concentrations found in the CRMs were within the uncertainty of the recommended values.

Reference standards are very important for verification of the accuracy of the technique. Because dissolution of the minerals is important and the ICP-AES technique only analyses the final solution, the reference material must match the mineral content and the major and minor elemental concentrations

2.3.2. Mineral chemistry

Back scattered electron (BSE) images and major and minor element concentrations of the samples were obtained by myself using an electron microprobe (EMP). EMP is a non-destructive technique where the sample is bombarded with an electron beam which causes elements in the sample to emit characteristics X-rays lines. The intensity of the emitted X-rays enables the abundances of the elements to be determined. The interaction of the sample with an accelerated electron beam produces elastic and inelastic collisions between electrons and atoms within the sample. Atoms with greater atomic number (Z) have higher probabilities of producing elastic collision because of their bigger size, thus the amount of BSE is proportional to the mean atomic weight of the sample. These interactions produce images that allow us to differentiate between phases (Lloyd 1987; Lyman et al. 1994).

The instrument used were a Cameca SX100 at the NHM and a Jeol8100 Superprobe with an Oxford Instrument INCA microanalytical system (EDS) using INCA software (Oxford Instruments 2006) at UCL/Birkbeck. Both instruments were operated at 20 keV accelerating voltage with a 20 nA bean current, 1µm diameter beam and a focused beam analysis for 10 to 30 s count time per element. Only mineral grains in which the sum of the major elements is between 97.8-101.99 wt.% were accepted as valid.

Qualitative element concentration maps and BSE images were also collected at a 260 × 256 pixels resolution using a Zeiss EVO EDX SEM at the NHM. All the instruments were calibrated using well-characterized standards (see Appendix 2A).

2.3.3. X-ray element map and modal mineralogy

Elemental concentrations within the samples were determined to provide a series of maps to represent of the concentration of each element. The images were processed using the GNU

Image Manipulation Program (GIMP). The element maps were colourised, imported as individual layers and combined using the program's function "Addition" tool to create false-colour element map (Joy et al. 2011; Snape et al. 2011; Figure 2.3).

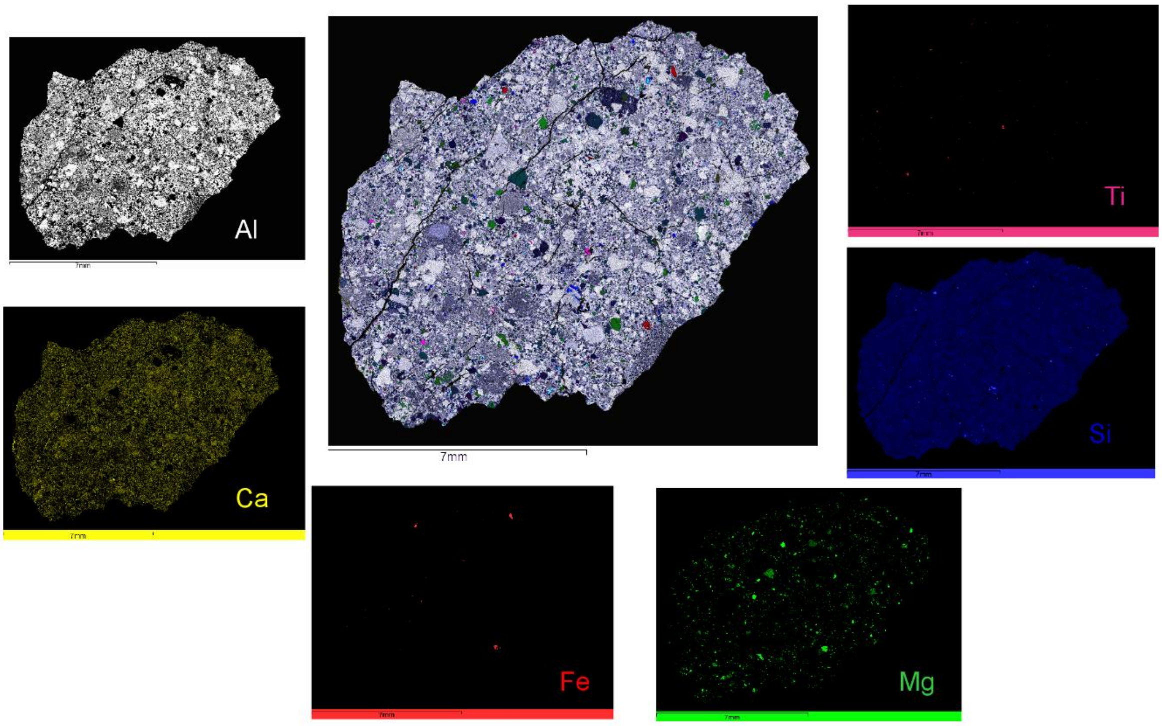

Figure 2.3 The individual colourised elements maps were used to generate the false colour element map of MIL 090036,34 where individual colours correspond to the distribution and qualitative concentration of different elements.

Modal mineralogy of clasts was determined from BSE and element map images using GIMP (Snape et al. 2011). Individual phases within each clast were automatically identified based on the greyscale tone in the BSE images. Modal abundances by area were calculated by counting pixels associated with each mineral phase within each clast. The major source of uncertainties in this method of calculating modal mineralogy occurs in distinguishing phases with similar greyscale tones in cases, it was necessary to then also use the elemental maps to refine the selection (see Snape et al. 2011).

2.4. Lunar Origin of the Samples

The meteorites have been determined to have an extraterrestrial origin based on several lines of evidence:

Fusion crust: The MIL 090036 bulk rock shows a thin ochre film on two surfaces that probably is a weathered fusion crust. The macroscopic description of MIL 090070 reports an olive-green glassy fusion crust (Righter 2010). The fusion crust is originated by the frictional heating during passage though Earth's upper atmosphere.

Mineralogy: Both rocks show a mineralogy different to that found in terrestrial rocks. They both present FeNi metal and Ti-rich ilmenite. Also both rocks of hydrous phases and ferric iron that indicate that the samples were formed in a highly reducing environment. These phases have been observed in Apollo and Luna sample collections (Papike 1998).

Fe/Mn ratios of pyroxenes and olivines vary between planetary bodies, reflecting the original composition of accreted material, subsequent differentiation, and oxygen fugacity conditions, making them a useful tool to determine planetary origin (Delaney et al. 1979; Kallemeyn and Warren 1983; Papike 1998). Lunar pyroxenes and olivines show a Fe/Mn ratio strongly differentiated compared with the Earth, Mars, Vesta and chondrites. This may be caused by the volatile loss during the formation of the Moon (Papike 1998). Average Fe/Mn (atoms per formula unit) values measured on pyroxenes are 54.81 ± 0.51 (1 standard deviation, sd) for MIL 090036 and 62.67 ± 0.52 (1 sd) for MIL 090070; those for olivine are 97.48 ± 0.38 (1 sd) on MIL 090036 and 85.93 ± 0.62 (1sd) on MIL 090070, all these measurements support a lunar origin for these samples (Delaney et al. 1979; Kallemeyn and Warren 1983).

2.5. Identification of Possible Launch Localities of Lunar Meteorites

Bulk-rock elemental compositions were matched with elemental remote sensing datasets in order to provide to the meteorites with a possible launch location. This techniques has been attempted by several previous authors for a range of lunar meteorites (e.g., Gnos et al. 2004; Joy et al. 2008, 2010, 2011; Corrigan et al. 2009; Jolliff et al. 2009; Jolliff et al. 2014). Adapting a method of Joy et al. (2010, 2011), a new software application was developed using Python programming language (Calzada-Diaz et al. 2015; Figure 2.4).

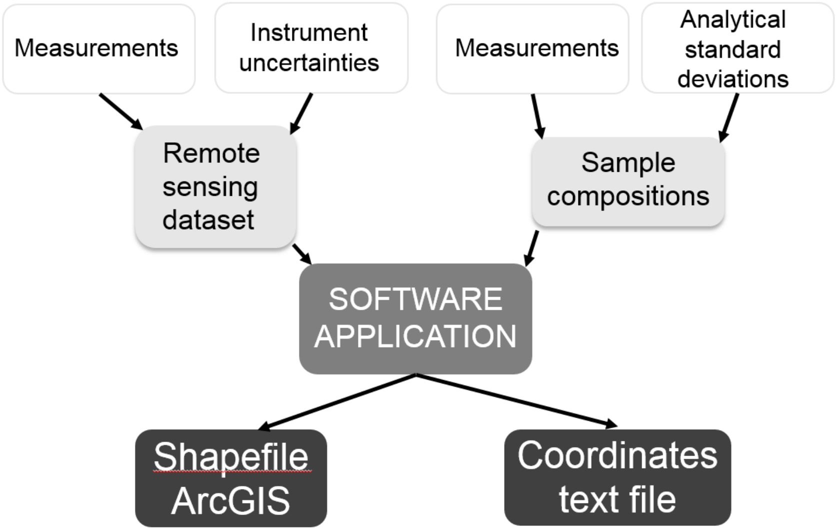

Figure 2.4 Schematic diagram of the method developed for this thesis to compare remote sensing datasets with analytical meteoritic compositions.

2.5.1. Remote sensing dataset and software application

The LP-GRS data set (Prettyman et al. 2006) provide global FeO, TiO_2 and Th compositions with a spatial resolution of 2 × 2 degree (i.e. 60 × 60 km) across the lunar surface. This data set was chosen because it provided a combination of an adequate compositional accuracy and an acceptable spatial resolution. Prettyman et al. 2006 modeled the observed gamma ray spectrum for each pixel using linear spectral mixing model. This was accomplished by scaling the spectral shapes with lunar surface parameters determined by neutron spectroscopy, including the number density of neutrons slowing down within the surface and the effective atomic mass of the surface materials. The spectral shape for each elemental constituent was determined by a Monte Carlo radiation transport calculation. The association of the highlands with the feldspathic lunar meteorites is used to calibrate the mixing model and to determine backgrounds. LP abundance data compared to the lunar sample data for soils have shown that the propagated statistical uncertainty increases with an increase of the spatial resolution (Figure 2.4). Latitude variations in the LP-GRS dataset occurs because the efficiency of the instrument depends of the incident angle of the gamma rays into the detector. An empirical latitude correction was carried out to minimize this latitude error (Lawrence et al. 2004, Prettyman et al. 2006). The 2-degree sampling of the surface is close to the limit for which surface spatial variations can be resolved from 100 km because the spatial response of the spectrometer is approximately 2.2° (Prettyman et al. 2006).

FeO distinguishes between basalts and highland rocks, TiO_2 discriminates between types of mare basalts and Th differentiates KREEP material (see Figure 1.16).

The code was developed using the Python programming language because of the existence of extensive libraries containing built-in modules that allowed me to work with geographic information systems (GIS) platforms such as ArcGIS™. The code is described in Calzada-Diaz et al. (2015). The LP-GRS dataset used in this approach also includes the statistical uncertainties derived from the instrument (appendix 2B). The analytical elemental measurements of the meteorites were obtained from the existing literature. Where several values were reported for the same stone, these values were averaged together, and the standard deviation of all the averaged values was used to indicate the compositional diversity of that sample. For example, samples with larger standard deviations may reflect highly heterogeneous samples (i.e., soil, regolith breccias) compared with more homogenous samples (i.e., impact melt breccias or mare basalts).

The software identifies a match between the sample and surface compositions when the LP-GRS values for all the three elements (FeO, TiO_2 and Th) lies within two or more standard deviations (2σ) of the average 'input' sample composition. However, for some meteorites the 2σ 'threshold' defines a very narrow range of values and the software did not report any matches that fell into this range. In these cases, I increased consistently the number of σ on the sample compositions until the first pixel matches (for all the three elements) with the GRS dataset appear (Figure 2.5). The rationale behind this increase is to obtain the first results that are closer to the reported composition of the sample using the standard deviation for consistency. This increase was done consistently through all the sample composition in which the 2σ deviation do not show any results. The level of standard deviations vary among the different meteorites depending of their heterogeneity. For example, regolith breccias from the highlands are relatively heterogeneous and so the measured compositions have quite large standard deviations (Table 6.1) at the 2σ level as expressed as a percentage of the mean value; the opposite is true of the more homogeneous basalts (Table 5.1). It is important to note that the standard deviation expressed as a percentage of the mean value (hereafter referred to as the '% error') for each element is similar between the meteorite searches (Table 5.1 and Table 6.1) and the Apollo and Luna landing sites search validation exercise (see Section 2.5.2, Table 2.1), with FeO always having the smallest % errors and Th always having the greatest errors.

The software outputs a text file with the matching coordinates and a shapefile layer compatible with most of the GIS systems that allow for convenient visualization of the outcome overlain on a map of the Moon.

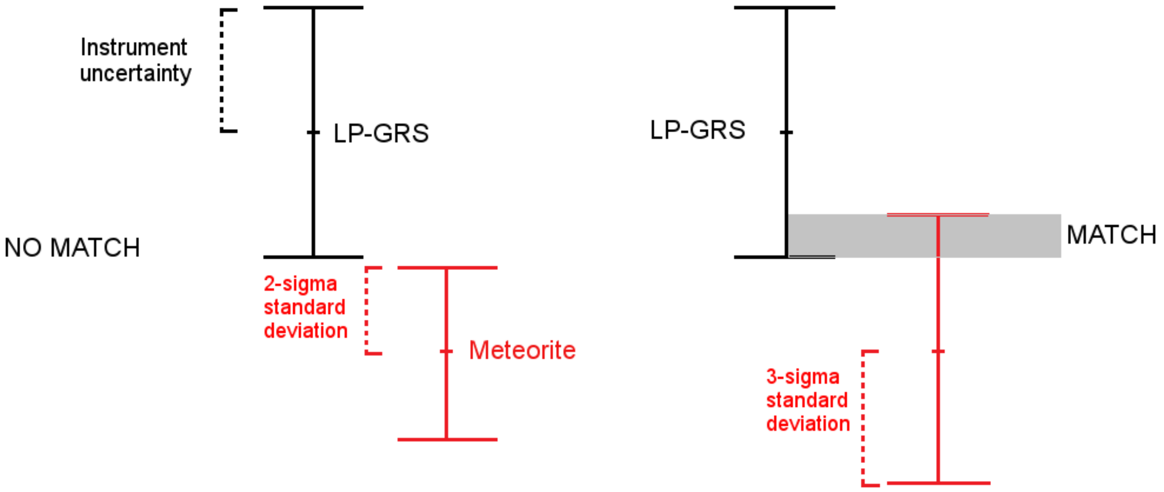

Figure 2.5 Diagram showing LP-GRS ± instrument uncertainty range in black, and meteorite composition (average measurement) ± standard deviations range in red, when there is not a match (left) and when there is a match (right). The grey shadowed area represents the match overlap. This is repeated for all the three of the elements of interest (FeO, TiO_2 and Th) until there is a match for all three.

2.5.2. Validation

The approach was validated by comparing the compositions of the Apollo and Luna bulk regolith samples (Table 2.1; Rhodes and Blanchard 1981; Morris et al. 1983; Simon et al. 1985; McKay et al. 1986; Jerde et al. 1987, 1990; Korotev 1997) with the abundances of FeO, TiO_2 and Th reported by the LP-GRS dataset (Prettyman et al. 2006).

Most of the samples (± 2 standard deviation bulk-rock compositions; Table 2.1) were well allocated to their respective landing site (Figure 2.6). In particular, for Apollo 11, 12, 17 and Luna 24, the method correctly matches the landing site location average regolith sample compositions with the corresponding LP-GRS pixels, although unsurprisingly other areas of the lunar surface are also found to have similar compositions.

For Apollo 15, the software matches areas approximately 60 km (1 pixel) away from the actual landing site. The matches for Apollo 16 and Luna 20 are in the general vicinity of the landing sites (i.e. <120 km, 2 pixels), however, not at the exact landing sites. For Luna 16, the closest matches are considered as being too far from the landing site (>500 km) to be accepted as a valid result. This possibly is because the difference between the small amounts of sample collected from this site and the larger footprint of the LP-GRS instrument.

In the case of the Apollo 14 landing site, the average Th compositions are larger (up to 13.72 ppm) than those measured by the remote sensing instrument (the highest measurement is 11.64 ppm), so a direct match was not obtained.

	Number of samples (n)	**FeO (wt.%)**	**% error**	**TiO_2 (wt.%)**	**% error**	**Th (ppm)**	**% error**
Apollo 11	24	16.31 ± 1.42	9	8.02 ±1.04	13	2.12 ± 1.52	72
Apollo 12	25	14.63 ± 7.32	50	2.44 ± 2.12	87	7.01 ± 7.64	109
Apollo 14	18	10.43 ± 1.84	18	1.64 ± 0.5	30	13.72 ± 2.26	16
Apollo 15	34	14.98 ± 6.6	44	1.46 ± 0.68	47	3.35 ± 3.1	93
Apollo 16	56	4.95 ± 1.38	28	0.52 ± 0.22	42	2.36 ± 5.3	225
Apollo 17	10	13.01 ± 6.94	53	4.96 ± 6.32	127	1.77 ± 2.12	120
Luna 16	6	16.75 ± 0.18	1	3.3 ± 0.2	6	nr	nr
Luna 20	6	7.46 ± 0.94	13	0.5 ± 0.12	24	0.97 ± 0.03	6
Luna 24	6	19.55 ± 1.24	6	1.04 ± 0.30	29	0.4 ± 0.18	45
		Average % error	***25***		***45***		***86***

Table 2.1 Average Apollo and Luna landing site bulk soil and regolith breccia compositions used for the software validation exercise including the 2 standard deviations of the reported values. % error is an indication of the magnitude of the level 2 standard deviation compared with the averaged value. See text for references.

When σ number is increased, the number of matches for each sample increases exponentially until it covers all the area with similar compositions. For example, covering all the highlands terrane or an entire mare basin.

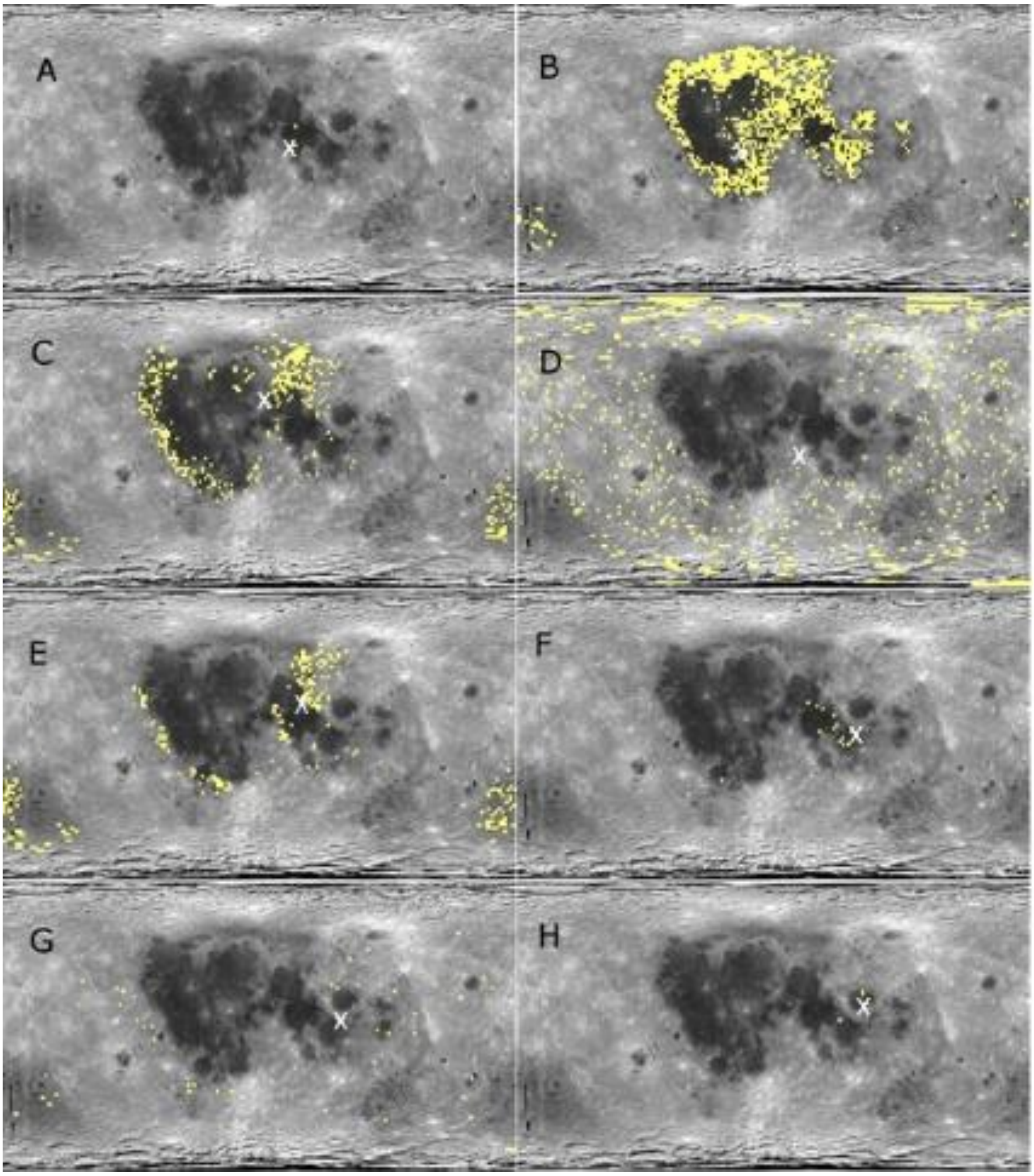

Figure 2.6 Apollo and Luna returned samples method validation using the 2 degree LP-GRS (Prettyman et al. 2006). Identification of lunar regolith with similar composition to the input ± 2σ (Table 2.1) Apollo 11 (A), Apollo 12 (B), Apollo 15 (C), Apollo 16 (D), Apollo 17 (E), Luna 16 (F), Luna 20 (G), and Luna 24 (H) soils and regolith breccias. Matching compositions to the inputs ± 2σ in Table 1 are shown in yellow. Apollo and Luna landing sites locations are denoted as white crosses. The underlying image is a global Clementine albedo image in a cylindrical projection with 0° longitude and 0° latitude in the center.

2.5.3. Limitations

The lunar surface has not suffered large-scale disturbance in the last 2-3 Ga, and so the present day surface composition represents mostly the composition of the underlying rocks (Heiken et al. 1991). However, the lithologies of an area may vary over short distances and with depth, so the regolith compositions measured by the GRS may be a lithological mixture of several types of rock and soil. Moreover, unavoidable errors occur owing to the large difference in spatial scale from lunar meteorites (cm in scale) to GRS data (60 × 60 km per pixel). The limiting effect of spatial resolution is especially clear in the case of the Th for which small spatial scale variations are known to occur (Lawrence et al. 1998, 2003, 2007; Hagerty et al. 2006).

The comparison with the GRS is most straightforward when using soil samples and regolith breccias because they derive from the upper layer of the lunar surface, however, it becomes more uncertain applied to other types of material such as pristine basalts, magmatic rocks or impact melt breccias. These lithologies may lie beneath the lunar surface and therefore out of the detection range of the LP-GRS. It is also possible that they represent more localised geological material covering areas smaller than the spatial resolution of the remote sensing instrument.

Chapter 3. Miller Range 090036[1]

3.1. Introduction

Miller Range (MIL) 090036 is an anorthositic regolith breccia lunar meteorite (Korotev et al. 2011; Liu et al. 2011; Shirai et al. 2012; Zeigler et al. 2012; Lanfang et al. 2014; Figure 3.1). It was found in Antarctica during the 2009-2010 Antarctic Search for Meteorites (ANSMET) field season (Righter 2010; Korotev and Zeigler 2015) with an original mass of approximately 245 g.

The sample does not show an obvious fusion crust, however, it does show a thin ochre film on two surfaces that may be a fusion crust subsequently weathered by Earth's atmosphere. It also has penetrating fractures in one side (Righter 2010). The interior of the stone is formed by dark gray coloured impact melt breccias and white coloured feldspathic clasts of variable sizes (from mm to cm) within a greenish fine-grained matrix (Righter 2010).

This study presents the petrography of a polished thick (100 µm) section (MIL 090036,34) and the bulk-rock composition of a 217 mg chip (MIL 090036,32). Both the chip and the thick section were kindly allocated by the Meteoritic Working Group and provided by the curatorial team at NASA's Johnson Space Center. I aim to investigate the bulk-rock composition and the mineralogy of the individual components and conduct a provenance study of the lithologies that were included in the original regolith environment.

---

[1] The work presented in this chapter was published in [**The petrology, geochemistry and age of lunar regolith breccias Miller Range 090036 and 090070: insights to the crustal history of the Moon**. Calzada-Diaz A, Joy K.H., Crawford I.A. and Strekopytov S. *Meteoritics and Planetary Sciences, 2016*].

Figure 3.1 Hand specimen of MIL 090036. Dark grey impact melt breccias and lighter coloured feldspathic clasts are observed within the dark matrix. (Randy Korotev's website *http://meteorites.wustl.edu/lunar/stones/mil090036.htm*).

3.2. Petrography and Clast Inventory

MIL 090036,34 is a polymict regolith breccia with a fine-grained to glassy matrix. The section studied has clasts of different lithologies and sizes, ranging from <0.1 mm to 2 mm (Figure 3.2). The majority of these clasts fall in two lithologies: monomict plagioclase grains and clast-rich impact melt breccias, although it also contains clasts of granulitic breccias with olivine, annealed granulitic breccias with ilmenite and rare fine-grained granulitic breccias are also present. Sparse clasts of poikiloblastic impact melt clasts are also observed. The impact melt breccias are the clasts with largest sizes (up to 3 mm). However, there are much variation in size within the different clasts types. All of them are embedded in a matrix which is dark-greenish in hand specimen, and formed by small (<1 mm) lithic clasts, individual mineral grains and glass (Figure 3.2).

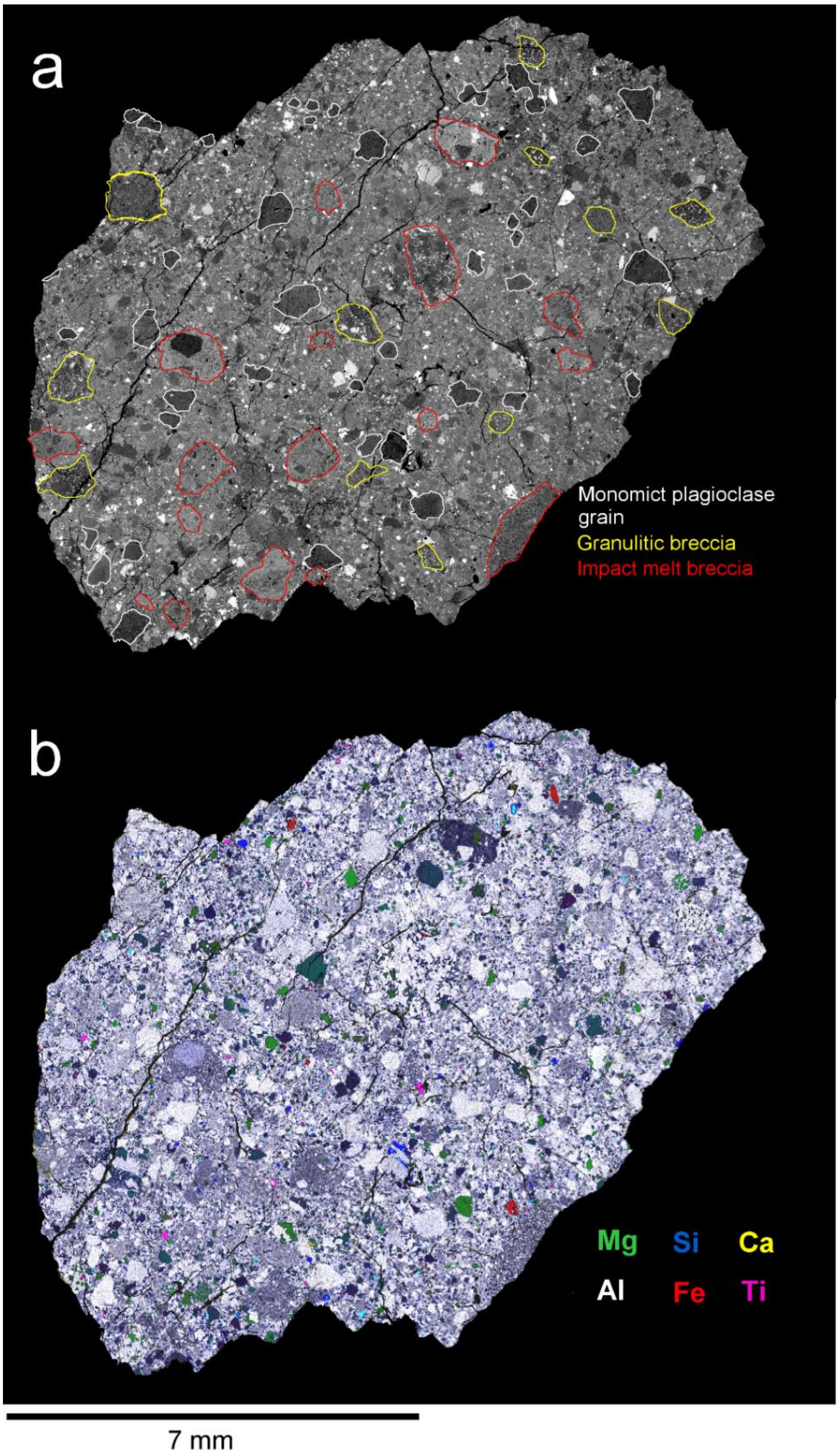

Figure 3.2 (a) Back scattered electron (BSE) image of MIL 090036,34 section with monomict plagioclase grain outlined in white, granulitic breccias in yellow and impact melt breccias outlined in red. (b) False colour elemental map of MIL 090036,34 where colours represent element concentrations and distribution: Mg – green (probably pyroxene or olivine), Si – blue, Ca – yellow, Al – white (the predominance of those colors represent the plagioclase), Fe – red (probably iron from meteoritic material) and Ti – pink (representing the ilmenite grains).

3.2.1. Monomict plagioclase clasts

Monomict plagioclase grains (Figure 3.3) are poorly sorted with fragments of different sizes, ranging from <0.1 mm to ~1 mm. They are angular (visual estimation), with well-defined borders and strongly affected by microfractures.

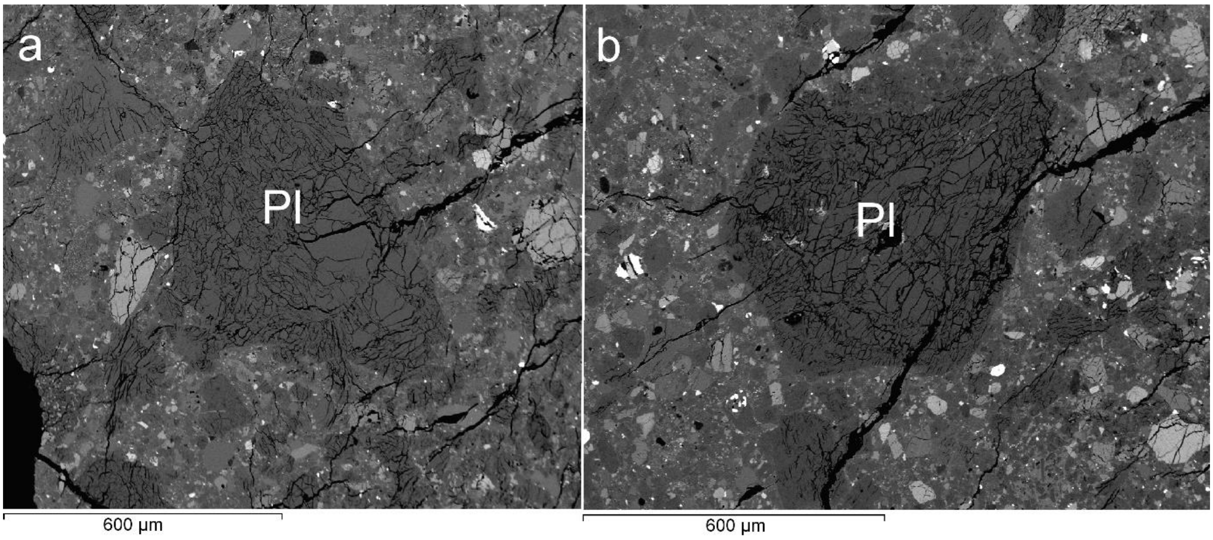

Figure 3.3 Close up of two BSE images (a and b) of monomict plagioclase (Pl) grains observed within MIL 090036,34 surrounded by a matrix formed by small lithic and mineral fragments and glass.

3.2.2. Granulitic breccias

Granulitic breccias are rocks that have experienced metamorphism and recrystallization. Usually they exhibit granoblastic to poikiloblastic textures (Stöffler, Knöll, Marvin, Simonds, and Warren 1980).

I have observed three different types of granulitic breccias in this sample section based in their mineral constituents and grain size: (1) gabbroic granulitic breccias with olivine (Figure 3.4a), (2) recrystallized or annealed granulitic breccias with ilmenite (Figure 3.4b-c), and (3) fine-grained granulites (Figure 3.4d). They do not appear in the same proportion, with the fine-grained granulites being very rare within MIL 090036,34.

Gabbroic granulitic breccias (Figure 3.4a) are formed mainly of calcic plagioclase (~85% modal area), clinopyroxene (~10% modal area) and olivine (~5% modal area). They have irregular shapes and vary significantly in size, reaching up to 1 mm.

Commonly, plagioclase crystals within these clasts are highly fractured and they may exhibit re-melting in some regions, and possible maskelynitization (glassy impact phase with plagioclase composition, see also Martin et al. 2016). This usually occurs in the border of the clasts (Figure 3.4a). Olivine crystals have subhedral textures and present sizes of ~8 µm.

Annealed granulitic breccias with ilmenite are heavily recrystallized breccias. They are composed of calcic plagioclase (~80% modal area), clinopyroxene (~20% modal area) and variable amounts of ilmenite, usually no more than approximately 1 % modal (Figure 3.4b-c). These clasts have irregular shapes and sizes between ~0.8 mm and ~2 mm.

Plagioclase crystals reach up to 400 µm in length. They are highly fractured and in some clasts, they have been transformed into maskelynite (see also Martin et al. 2016). Pyroxenes are poorly sorted, with sizes from sub-micron to 165 µm. They are anhedral to lath-like in form. Ilmenite crystals have sizes from sub-micron to ~60 µm and blocky shapes.

*Fine-grained granulite*s (Figure 3.4d) are scarce within this subsample, however, some angular clasts with sizes up to 1 m, have been observed. They are formed of >90% modal area calcic plagioclase, which encases small (<5 µm) grains of pyroxene.

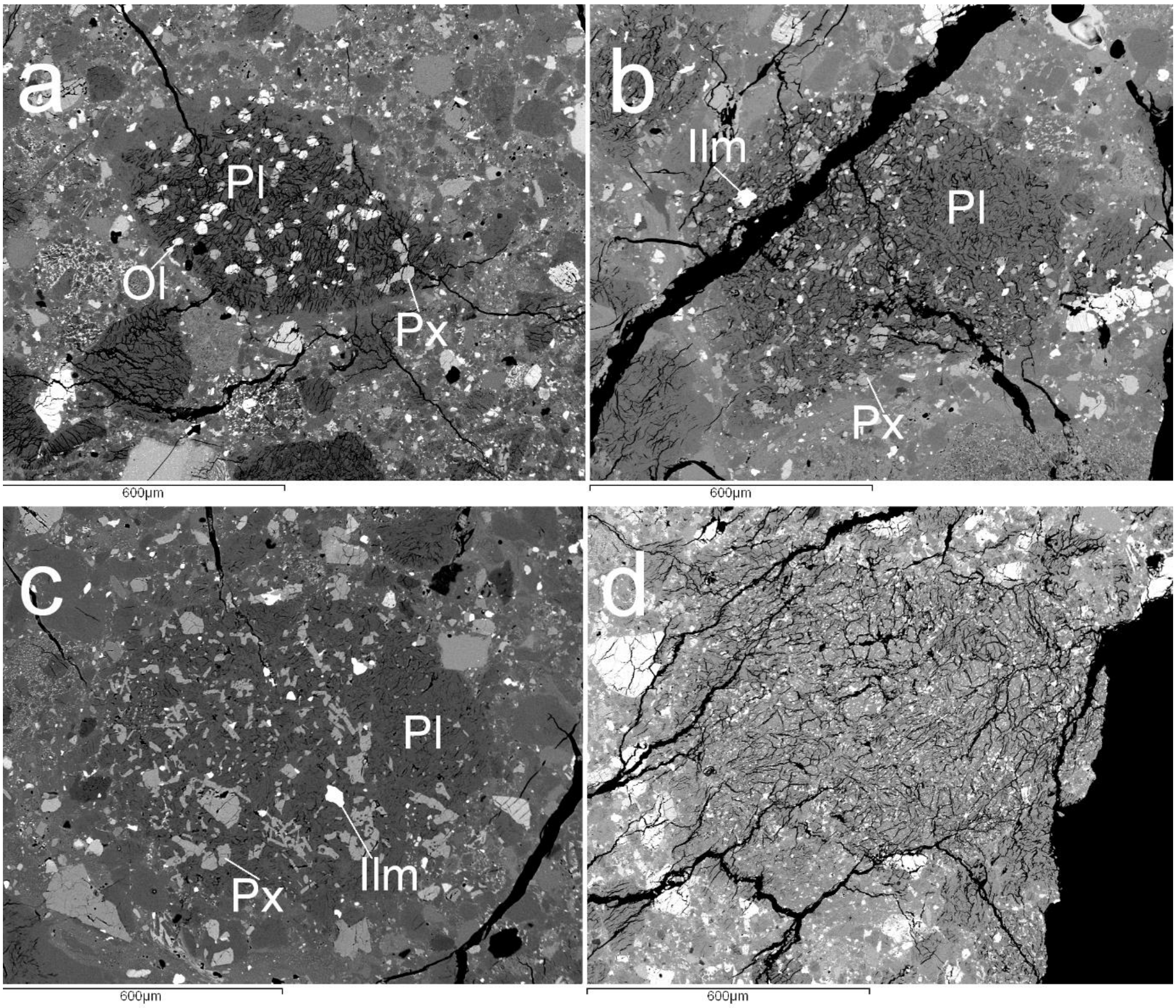

Figure 3.4 Close up BSE images of granulitic breccias in MIL 090036,34. (a) Gabbroic granulitic breccia formed by plagioclase (Pl), pyroxene (Px) and olivine (Ol); (b-c) annealed granulitic breccias with ilmenite (Ilm); (d) fine-grained granulite clast.

3.2.3. Impact melt breccias

Impact breccias are classified according to their components, texture and shock metamorphism into 3 groups: (1) shocked rocks, (2) clast-free impact melt rocks, including holocrystalline impact melt rocks, and (3) impact breccias. This last group can also be classified into monomict impact breccias, polymict clastic impact breccias and clast-bearing impact melt breccias (Stöffler and Grieve 2007). Impact rock clasts found in MIL 090036,34 are clast-bearing impact melt breccias and holocrystalline impact melt rocks.

Clast-bearing impact melt breccias are abundant within MIL 090036,34. They all show similar textures, although they have different makeup of mineral and clast components. They are clast-rich, with a recrystallized matrix composed of quenched plagioclase laths in a mafic glass (Figure 3.5a-b) or a feldspathic glass matrix (Figure 3.5c-d). The clasts within these impact melt breccias are mainly fragments of poorly sorted plagioclase (>50% modal area) with sizes up to 600 µm, and showing a range of shock states.

Poikiloblastic (holocrystalline) impact melt clasts have been observed in MIL 090036,34 (Figure 3.6). They are formed by plagioclase (~90% modal area), clinopyroxene (~10% modal area) and rare grains of FeNi metal (<1% modal area). This metal indicates that the clasts were probably derived from an impact melt precursor, as it was likely added by a meteoritic component. Clinopyroxenes are large, from ~100 µm to ~400 µm, anhedral with poikiloblastic texture. Anhedral to subhedral plagioclase grains of medium size (approximately from ~20 µm to ~75 µm) are included into the clinopyroxene crystals. Enclosing these phases are larger crystals of plagioclase (up to ~220 µm) with some regions transformed into glass. These glassy phases have been analysed and have shown compositions similar to those measured in the plagioclase grains, so this glass could be considered to be maskelynite.

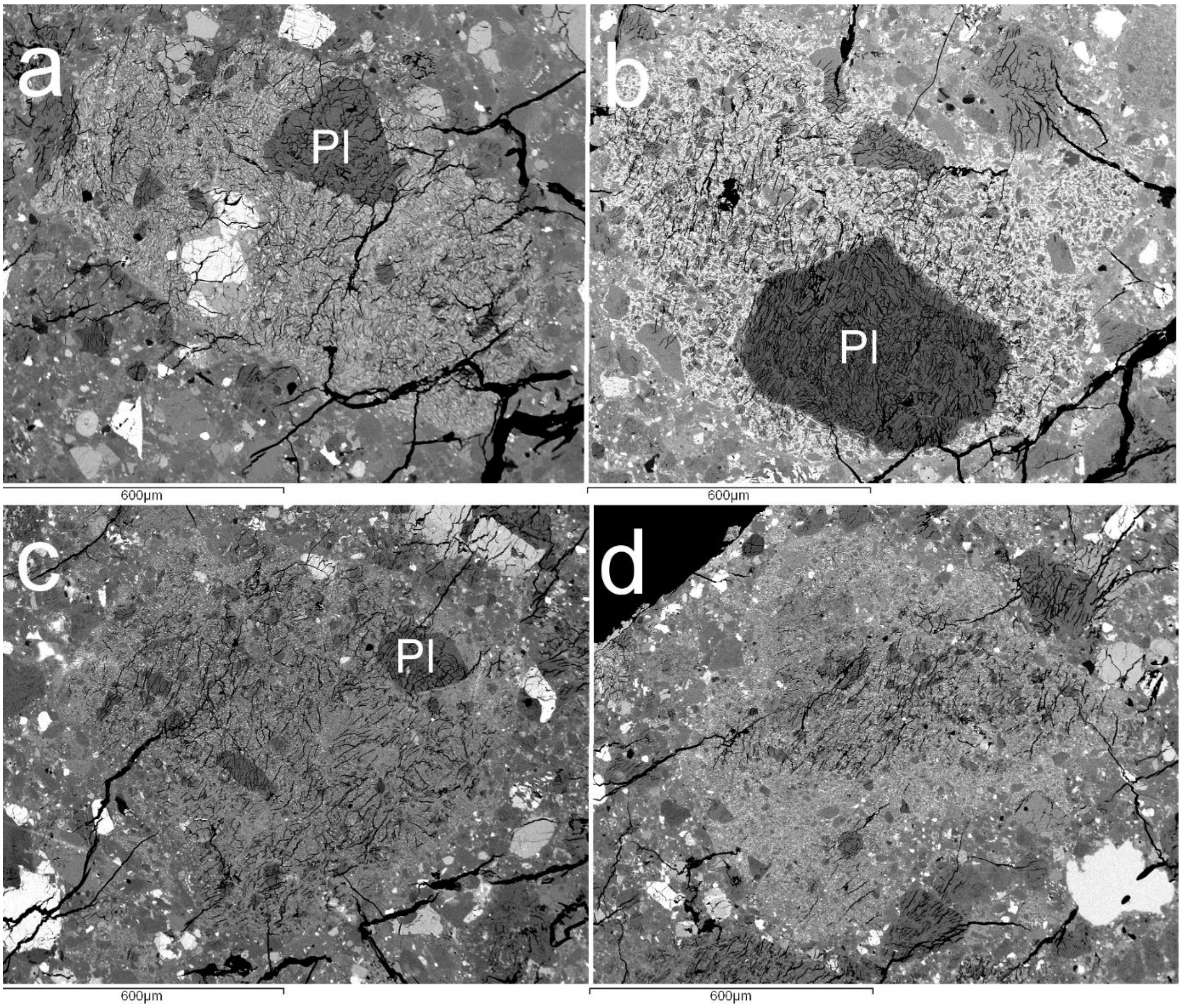

Figure 3.5 Close up BSE images of clast-bearing impact melt breccias in MIL 090036,34, in a mafic glass matrix (a,b), and containing a feldspathic glass matrix (c,d). Large plagioclase grains are observed in most of them (labelled Pl).

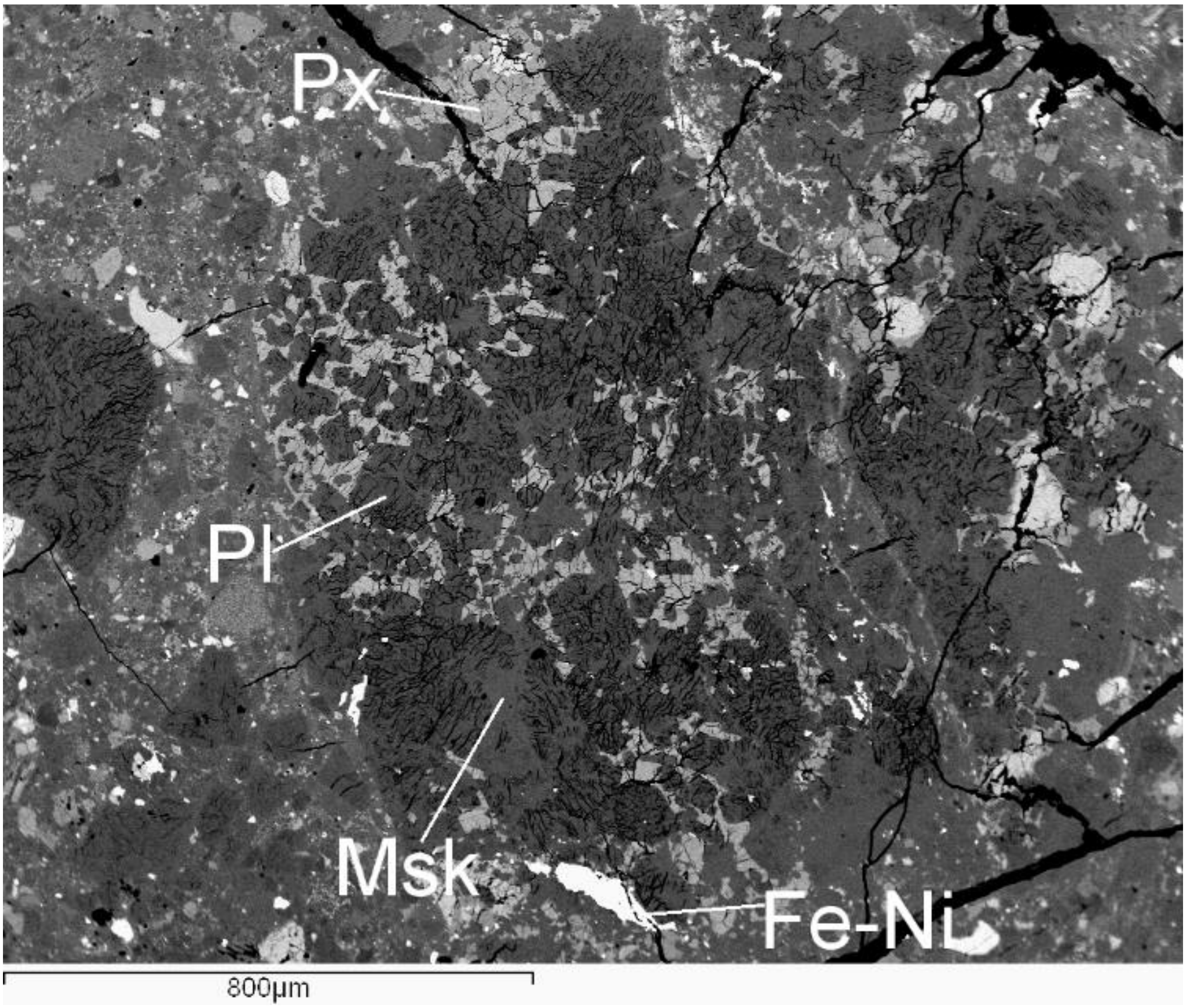

Figure 3.6 Close up BSE image of one poikiloblastic impact melt clast found in MIL 090036,34. The phases observed are plagioclase (Pl), pyroxene (Px), maskelynite (Msk) and FeNi metal (Fe-Ni).

3.2.4. Matrix

The matrix of the MIL 090036,34 section comprises fine-grained individual mineral grains (<150 µm). The silicate phases include plagioclase and pyroxene. Oxide phases such as ilmenite and minor amounts of chromite also appear within the matrix. In addition to the silicate and oxides, a minor metallic component is present. These are Fe-Ni metal grains showing sizes from <1 µm up to 4 µm.

3.2.5. Mineral chemistry

Plagioclase: Monomict plagioclase grains, granulitic breccias and most of the impact melt breccias have calcic plagioclase with anorthite content varying between An_{78} to An_{98} (Figure 3.7; electronic appendix 3A). However, one of the impact melt clasts has been found to contain alkali-rich plagioclase clasts (labeled Pl in Figure Figure 3.5b) with a composition more albitic (An_{59-63}). This suggests a different type of parent lithology.

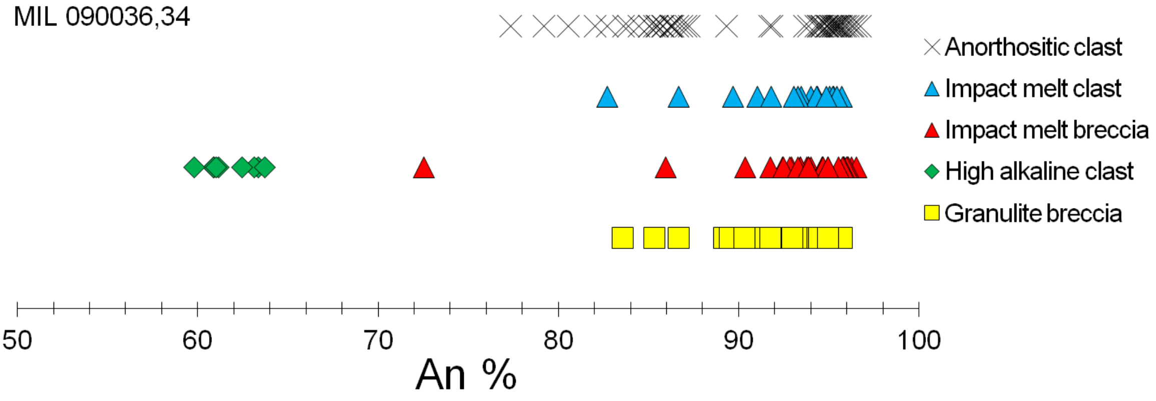

Figure 3.7 Plagioclase anorthite content (atomic Ca/(Ca+K+Na) × 100) diagram for MIL 090036,34 averaged plagioclases compositions from anorthositic clasts (black crosses), impact melt clasts (blue triangles), impact melt breccias (red triangles), including the high-alkali clasts compositions (green diamonds), and finally granulite breccias (yellow squares).

Pyroxene: Augite and pigeonite crystals can be found in all the types of lithic clasts. They present a bimodal composition in gabbroic granulitic breccias (En_{46-49} Fs_{13-15} Wo_{36-41} and En_{63-64} Fs_{26-29} Wo_{5-11}) and in annealed granulitic clasts (En_{35-49} Fs_{15-25} Wo_{33-40} and En_{59-61} Fs_{27-31} Wo_{6-13}). Compositions show a narrow range in impact melt breccias (En_{61-72} Fs_{25-30} Wo_{4-9}). Enstatite (En_{56-69} Fs_{27-39} Wo_{4-5}) appear in annealed granulitic breccias, impact melt breccias and poikiloblastic impact melt but not in gabbroic granulitic breccias (Figure 3.8, electronic appendix 3B).

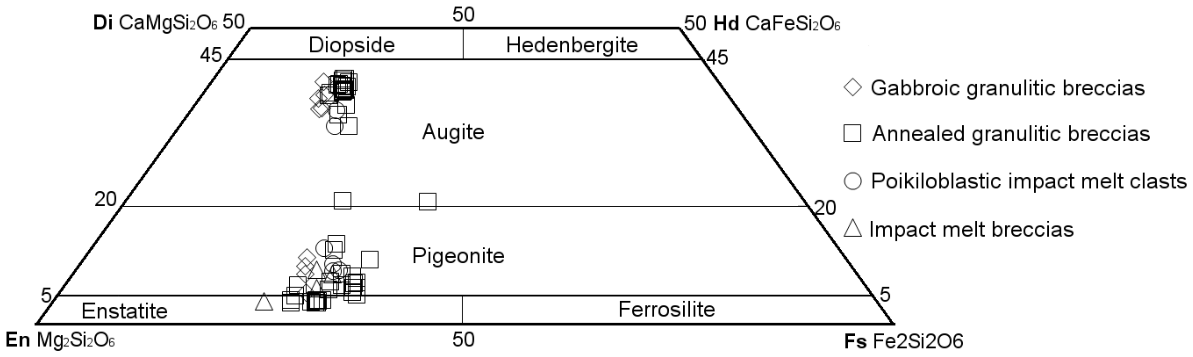

Figure 3.8 Pyroxene quadrilateral diagram showing compositions of pyroxenes in different clasts of MIL 090036,34.

Olivine is only observed in gabbroic granulitic breccia clasts (Figure 3.4a; electronic appendix 3C). These crystals appear to have homogenous compositions of Fo_{66-67}.

Mineral compositions for the different clast types in MIL 090036,34 are shown in Table 3.1. A complete list of mineral compositions can be found in the electronic appendix 3A-D.

	Pyroxene			**Plagioclase**	**Olivine**
Clast	**Wo-range**	**En-range**	**Fs-range**	**An-range**	**Fo-range**
Monomict plagioclase clasts	nm	nm	nm	79-98	nm
Gabbroic granulitic breccias	5-41	46-64	13-29	83-96	66-67
Annealed granulitic breccias	4-40	35-69	15-39	84-94	nm
Impact melt breccias	6-9	61-64	28-30	92-98	62-63
High-alkali impact melt breccias	nm	nm	nm	59-63	nm

Table 3.1 Inventory table of pyroxene, plagioclase and olivine clast compositions within MIL 090036,34 (nm: not measured). Pyroxene wollastonite (Wo) value was calculated as atomic Ca/(Ca+Fe+Mg) × 100, Pyroxene enstatite (En) value was calculated as atomic Mg/(Ca+Fe+Mg) × 100 and Pyroxene ferrosilite (Fs) value was calculated as atomic Fe/(Ca+Fe+Mg) × 100. Plagioclase anorthite (An) range was calculated as atomic Ca/(Ca+K+Na) × 100. Olivine forsterite (Fo) value was calculated as atomic Mg/(Mg+Fe) × 100.

3.3. Bulk Composition

Bulk compositions (wt.%) and trace element (ppm) compositions for MIL 090036,32 obtained during this study (Table 3.2 Bulk-rock (wt.%) and trace element (ppm) compositions for MIL 090036,32 obtained during this study. Previous analysis on this meteorite (Korotev and Zeigler 2015) and average Apollo 16 highland regolith and NWA 4936 lunar meteorites (Korotev 1996; Korotev et al. 2009) are also shown for comparison. MIL 090036,34 results are similar to those obtained previously by other authors using electron microprobre (EPMA) and instrumental neutral activation analysis (INAA), in several chips (e.g. Korotev and Zeigler 2015). All the analysis performed in this sample by this and other authors, show a slight enrichment in Th and others ITE elements. This ITE enrichment could be related to a KREEP component within the sample, although KREEP clasts were not found in the sample.

	MIL 090036 ,32 (this work)	**MIL 090036 (Korotev and Zeigler 2015)**	**Average A16 highland regolith (Korotev 1996)**	**NWA 4936 (Korotev et al. 2009)**
SiO_2	46.24 ± 0.12	45.40		44.5
TiO_2	0.478 ± 0.002	0.57	0.38	0.75
Al_2O_3	26.72 ± 0.071	27.10	28.4	24.7
FeO	5.27 ± 0.015	5.01	4.18	5.94
MnO	0.0731 ± 0.0007	0.07		0.08
MgO	5.92 ± 0.036	5.18	4.53	8.60
CaO	15.45 ± 0.029	15.50	16.4	14.4
Na_2O	0.567 ± 0.004	0.62	0.45	0.51
K_2O	0.0828 ± 0.0006	0.10	0.12	0.13
P_2O_5	0.0845 ± 0.0002	0.10		0.15
Total	100.88	99.75		
Mg#	66.68	64.80		
Li	7.08 ± 0.13			
Be	0.893 ± 0.016			
Sc	11.8 ± 0.11	9.77	7.46	8.96 ± 0.09
V	25.7 ± 0.34			
Co	22.62 ± 0.08	17.80	17.8	39.5 ± 0.4
Cr	761 ± 10.2		561	774 ± 8
Ni	381 ± 4.0	218.00	212	572 ± 15
Cu	3.80 ± 0.07			
Zn	14.8 ± 0.13			
Ga	4.32 ± 0.024			
Rb	2.06 ± 0.05			<4
Sr	197 ± 1.5	198.00	181	198 ± 10
Y	29.7 ± 0.24			
Zr	129 ± 0.4	153.00	168	187 ± 12
Nb	8.55 ± 0.022			
Mo	0.125 ± 0.004			
Sb	1.20 ± 0.032			
Cs	0.0909 ± 0.005		0.126	0.13 ± 0.02
Ba	117 ± 0.4	131.00	81.9	167 ± 6
La	10.6 ± 0.03	11.11	6.64	13.4 ± 0.13
Ce	26.7 ± 0.05	29.00	30.9	35.2 ± 0.4
Pr	3.62 ± 0.05			
Nd	16.5 ± 0.06	17.20	18.4	20.9 ± 1.5
Sm	4.65 ± 0.04	5.04	3.10	6.22 ± 0.06
Eu	1.47 ± 0.002	1.38	1.04	1.41 ± 0.02
Gd	5.57 ± 0.013			
Tb	0.96 ± 0.008	0.98	1.12	1.20 ± 0.014
Dy	6.20 ± 0.013			
Ho	1.29 ± 0.006			
Er	3.69 ± 0.031			
Tm	0.528 ± 0.003			
Yb	3.30 ± 0.03	3.25	2.28	4.03 ± 0.04
Lu	0.475 ± 0.014	0.45	0.321	0.557 ± 0.006
Hf	3.74 ± 0.04	3.86		4.79 ± 0.05
Ta	0.486 ± 0.003	0.44		0.60 ± 0.02
W	0.244 ± 0.0031			
Tl	0.0102 ± 0.0004			
Pb	1.40 ± 0.012			
Th	1.89 ± 0.002	1.65	1.095	1.95 ± 0.03
U	0.52 ± 0.0005	0.46	0.526	0.49 ± 0.05

Table 3.2 Bulk-rock (wt.%) and trace element (ppm) compositions for MIL 090036,32 obtained during this study. Previous analysis on this meteorite (Korotev and Zeigler 2015) and average Apollo 16 highland regolith and NWA 4936 lunar meteorites (Korotev 1996; Korotev et al. 2009) are also shown for comparison.

3.4. Discussion

3.4.1. Similarities to other lunar lithologies

MIL 090036 is unusual among Al-rich feldspathic lunar meteorites because of its bulk rock incompatible trace elements enrichment. Previously it was suggested that the most compositionally similar materials are the lunar meteorite North West Africa (NWA) 4936 and regolith from the Apollo 16 landing site (Shirai et al. 2012; Lanfang et al. 2014). The similarities and differences previously reported were revised during this work using the new data obtained.

NWA 4936 is a feldspathic glassy impact-melt breccia formed by mineral clasts that includes anorthitic plagioclase, pyroxenes (both pigeonite and augite), limited olivine, and ilmenite. These fragments are included in a fine-grained matrix with heterogeneous glass and grains of kamacitic metal and troilite. This meteorite differs from other feldspathic meteorites in having higher concentrations of incompatible elements, and for being one of the most compositionally similar to the Apollo 16 regolith (Korotev et al. 2009).

The Apollo 16 landing site is the only one from the Apollo mission that took place in the lunar highlands (Figure 1.1). However, all the Apollo sites regolith, including A16, have shown a high proportion of Th-rich material likely originated as a result of the proximity of the anomalous Th-rich Procellarum KREEP Terrain (PKT), so the Apollo 16 site does not represent the average highland composition (Korotev et al. 2003, 2009).

Despite similarities, NWA 4936 and A16 regolith samples also have shown some differences. Among these differences are the higher concentrations of Sc and lower abundances of MgO in the Apollo 16 regolith compared to NWA 4936 (Figure 3.9), suggesting minor amount of mare material and the existence of a magnesian anorthosite (MAN) component in the meteorite (Korotev 1997; Korotev et al. 2003, 2006, 2009; Takeda et al. 2006).

Bulk rock FeO values for the A16 regolith and the two meteoritic samples are very similar: 5.27 wt.% for MIL 090036,32 compared with 5.9 wt.% and 4.18 wt.% for NWA 4936 and Apollo 16 regolith samples respectively. MIL 090036,32 and Apollo 16 regolith samples are less magnesian (5.9 wt.% and 4.16 wt.% MgO respectively) than the NWA 4936 meteorite (8.6 wt.% MgO; Figure 3.9). Therefore, Mg# values are very similar in the case of MIL 090036,34

(66.7) and Apollo 16 regolith samples (66.5) but significantly lower than NWA 4936 stones (average for both stones 72.1; Korotev et al. 2009). This agrees with the possibility of an additional type of magnesian anorthosite (MAN) component in NWA 4936, not observed in either MIL 090036 nor dominant at the Apollo 16 site where FAN rocks are more common (Korotev et al. 2003; Korotev 2008; Takeda et al. 2006).

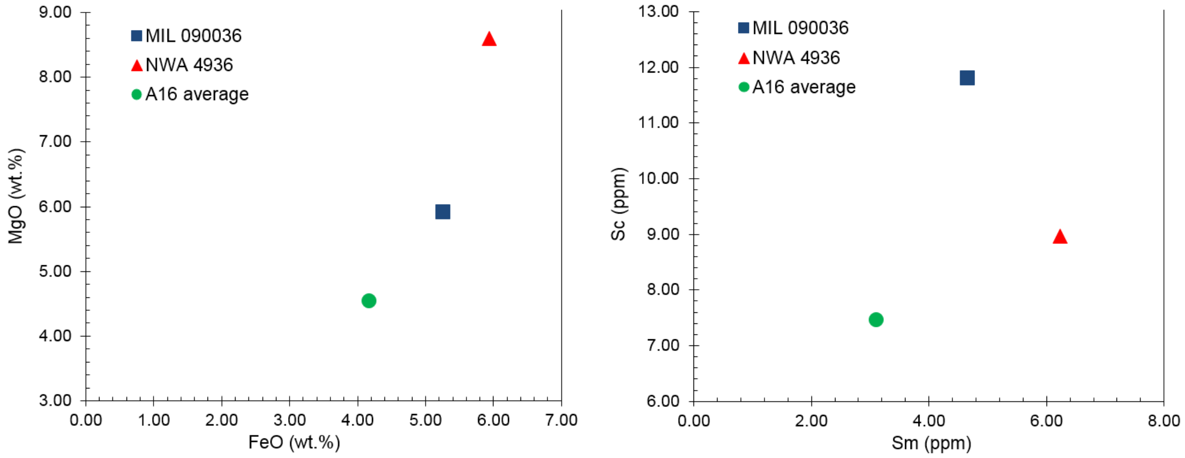

Figure 3.9 FeO vs MgO and Sm vs Sc compositional diagrams for MIL 090036, NWA 4936 lunar meteorite and the average Apollo 16 regolith. The errors are smaller than the size symbol (Korotev 1996; Korotev et al. 2009).

Perhaps, the main shared characteristic among these three samples are their content in incompatible elements. Their REE abundances are similar, although slightly lower for MIL 090036 compared to NWA 4936 and Apollo 16 (Figure 3.10). Negative Eu-anomalies, however, are significantly different. The Eu anomaly is calculated using the formula

$$Eu / Eu^{*} = \frac{Eu_{CN}}{\sqrt{Sm_{CN} \times Gd_{CN}}}$$

Equation 1

where CN = chondrite-normalized (using the values of Anders and Grevesse 1989). A larger negative Eu-anomaly (Eu/Eu* = 0.52) is observed on the Apollo 16 bulk soils and NWA 4936 REE pattern diagram, compared to the anomaly of MIL 090036,32 (Eu/Eu* = 0.8) being the anomaly larger as farther Eu/Eu* value is from the value 1 (Rollison 1993). This discrepancy may result from the difference in mare basalt or KREEP components found at the Apollo 16 site and MIL 090036: our study and that of Lanfang et al. (2014) did not identify any mare basalt lithological debris, whereas mafic impact melt rocks are common in samples from all stations within the Apollo 16 landing site (McKay et al. 1986; Jerde et al. 1987; Lucey et al. 2006). Small sample size (150 mg) of the chips used in the bulk-rock analysis in this study (typical for modern meteorite research) makes, however, direct comparison with average composition difficult.

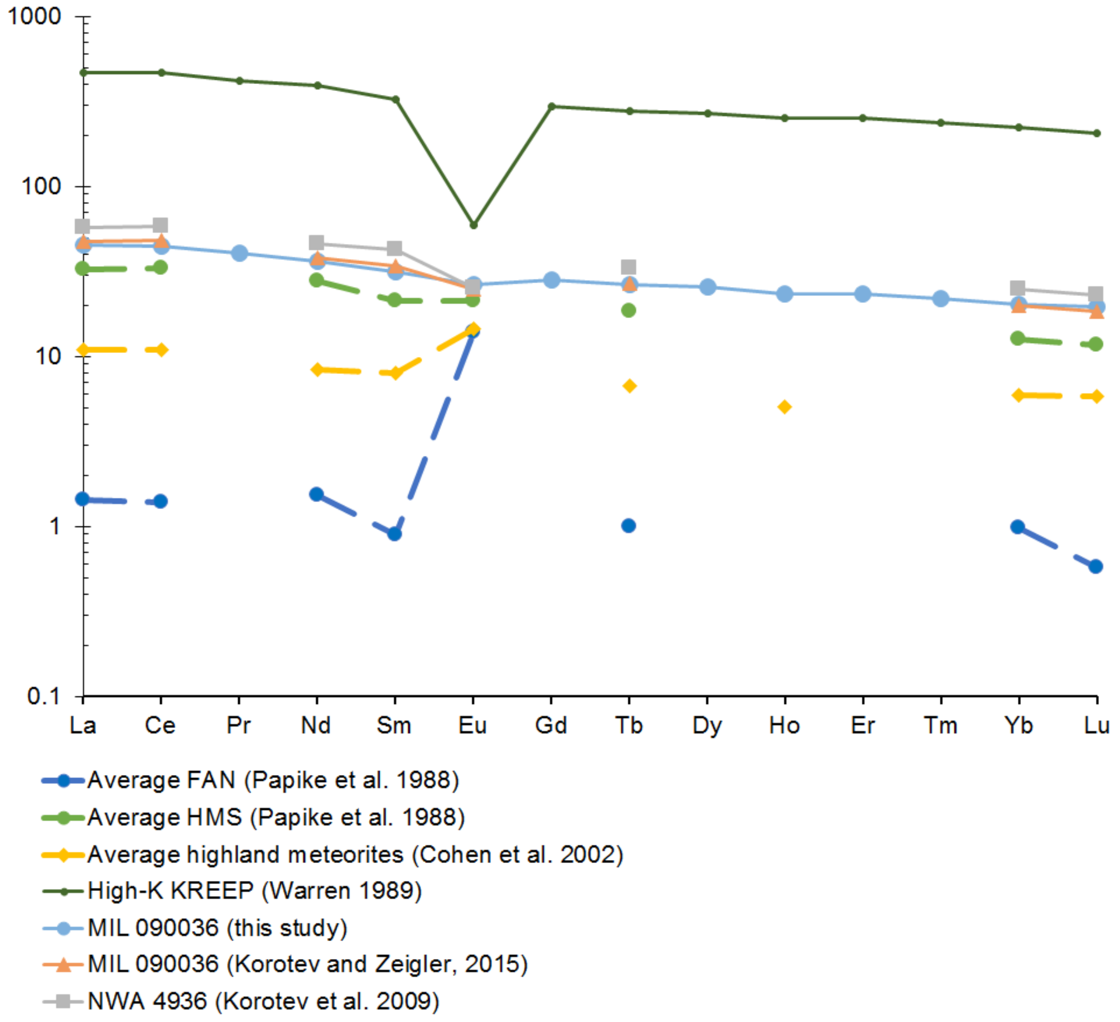

Figure 3.10 CI-normalized (Anders and Grevesse 1989) rare earth elements abundances for MIL 090036,32 (This study and Korotev and Zeigler 2015), Apollo 16 regolith (Korotev 1996) and NWA 4936 (Korotev et al. 2009). Also, the average highland meteorites (Cohen et al. 2002), the average FAN and HMS (Papike et al. 1998) and the average high-K KREEP (Warren 1989) abundances are shown.

The slightly higher abundances of Na_2O and Eu in both meteorites (Na_2O: 0.56 wt.% MIL 090036,32 and 0.52 wt.% NWA 4936; Eu: 1.47 ppm MIL 090036 and 1.41 ppm NWA 4936), compared to the bulk average Apollo 16 regolith composition (Na_2O: 0.45 wt.%; Eu: 1.04 ppm), may indicate that plagioclase in both meteorites is more albitic than that observed on the Apollo 16 soil samples. This agrees with the presence of high-alkali suite clasts within MIL 090036 (Figure 3.11).

MIL 090036 contains plagioclase with more albitic compositions than those plagioclase in NWA 4936 and the Apollo 16 FANs. This has been observed in MIL 090036,34 and in other The higher Mg# calculated in NWA 4936 that it could have a MAN component that is not present in MIL 090036 (Figure 3.12).

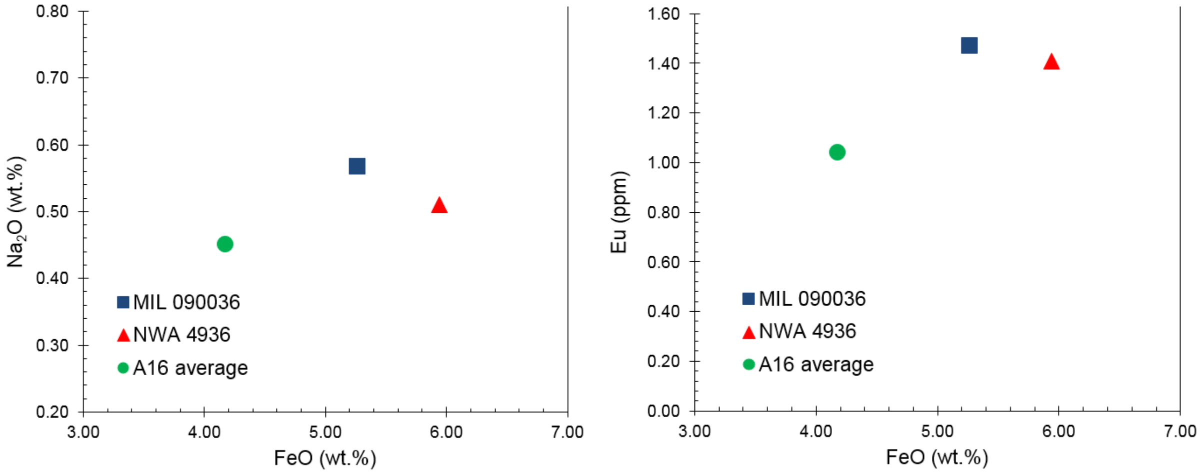

Figure 3.11 FeO vs Na_2O and FeO vs Eu compositional diagrams for MIL 090036, NWA 4936 and the average Apollo 16 regolith (NWA 4936 and Apollo 16 average regolith from Korotev 1996; Korotev et al. 2009). Error bars are too small to be observed in the diagram.

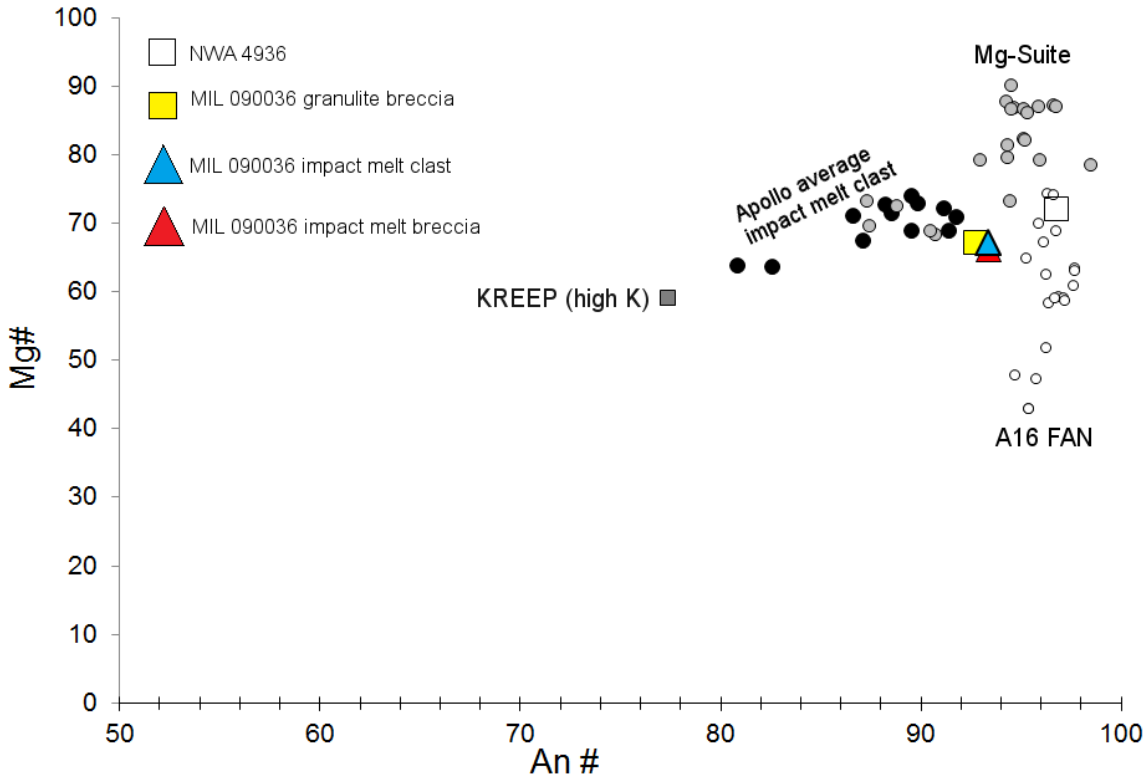

Figure 3.12 Diagram for averaged normative bulk rock An# and Mg# of the different lithologies observed in MIL 090036: granulite breccias, poikilitic impact melt clasts and clast-rich impact melt breccias compared with the Apollo rock suites (Korotev 1996; Jolliff et al. 1998; Wieczorek et al. 2006; Warren and Wasson 1977). NWA 4936 normative bulk-rock An# and Mg# is also plotted for comparison (Korotev et al. 2009). Error bars are too small to be observed in the diagram.

3.4.2. Petrogenesis

As described in previous sections, the clasts present in MIL 090036 exhibit a number of different lithologies with no gradation among them. Most of these lithic clasts are breccias, formed by fragments of rocks that were fragmented and later lithified by impact processes. In many cases, these fragments have been affected by thermal annealing and re-equilibration as consequence of impact metamorphism, forming granulites. As they are not pristine rocks, fully understanding the origin and history of the different clasts is challenging. Some observations and interpretations however, can be done.

Momomict plagioclase grains contain a relatively large range of anorthite content (An_{78-98}) but clearly they fall in two separate groups: one with ~ An_{95} and a second one with ~An_{78-88} (Figure 3.7). This suggests different types of source, on one hand ferroan anorthosites with more calcic compositions, and another component similar to Mg-bearing lithologies rocks with less content in anorthite (Papike 1998). The proportion of each component is difficult to assess because of the reported heterogeneity of the meteorite (Korotev and Zeigler 2015).

Granulites are polymict clastic breccias that could have been recrystallized from igneous rocks, impact-melts breccias and clast-bearing impact melts that underwent metamorphism by high-temperature events (1050 ± 50°C), forming granoblastic textures (Warner et al. 1976; Lindstrom et al. 1986; Çushing et al. 1999; Hudgins et al. 2008, 2011). Some of the granulite breccias show partial maskelynization (Martin et al. 2016) indicating shock pressures between 28-34 GPa (Hudgins et al. 2011; Rubin 2015). Maskelynite is uncommon in the Apollo granulitic breccias indicating that the pressures they underwent were lower (5-22 GPa; Hudgins et al. 2011).

The compositions of the monomict plagioclase grains, granulites and impact melt clasts suggest that they derive from two different types of parent lithologies: FAN and Mg-rich rock and that those lithologies experimented several degrees of shock effects, from fracturation to total recrystallization of the clast. The shock effects observed on MIL 090036, particularly the maskelynization of plagioclase grains, are probably the result of the clasts being excavated from depth (Hudgins et al. 2008, 2011).

One of the more intriguing things about this sample is the existence of two more alkaline plagioclase fragments (An_{59-63}) found in one of the impact melt breccias. These fragments (Figure 3.5b) are unusually alkali-rich compared with lithologies from the FANs and the Mg-suite, being more similar to plagioclase found in the ancient high-alkali magmatic rock suite (HAS). However, these plagioclase grains in MIL 090036 show greater Na_2O content (~4.3 wt.%) than those compiled for anorthositic alkaline rocks from the Apollo 12 and 14 landing sites by Papike (1998; Na_2O <2.14 wt.%). Also, they have slightly lower CaO content than in anorthositic alkaline rocks from the Apollo collection, ~15.8 wt.% in contrast with ~12.4 wt.% obtained during this analysis. This may indicate an origin outside of the Apollo sampled sites (Figure 3.13).

Alkaline rocks are known to have high concentration of incompatible trace elements compared to Apollo FAN rocks (Snyder et al. 1995). The presence of high alkali anorthositic clasts could be the cause of the enhanced KREEPy signature within this sample. In the thick section I was able to find only two of these clasts that is definitely insufficient to be considered the cause of the KREEPy signature. However, it shouldn't be totally dismissed either, since the heterogeneity of the bulk meteorite in terms of clast compositions have been previously described (Korotev and Zeigler 2015).

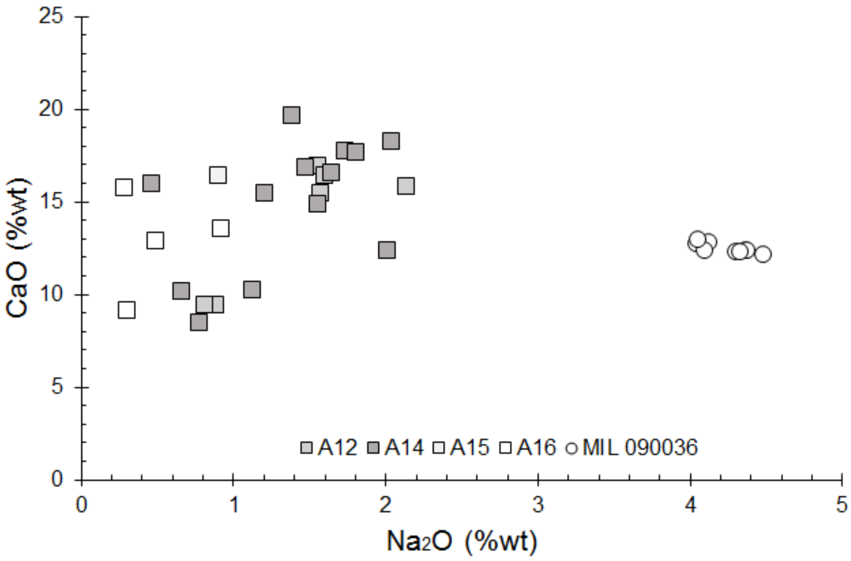

Figure 3.13 Na_2O vs CaO diagram of plagioclase grains from alkali anorthositic clasts from MIL 090036 in circles and from plagioclases from the Apollo regolith breccias and soils in squares (Apollo samples data from Papike 1998). Error bars too small to be shown in the image.

Reported $^{39}Ar/^{40}Ar$ ages suggest that the last major argon isotope re-setting event in the meteorite took place at ~3.54 Ga (Park et al. 2013), likely the event that created the breccia from which the meteorite finally was derived. The granulites and impact melt breccias within the sample likely have been formed from FAN and Mg-suite lithologies that have been uplifted from deeper layers, probably at some point during the intense period of bombardment that took place before 3.9 Ga (Chapman et al. 2007).

MIL 090036 has a cosmic ray exposure of ~50±10 Ma (Park et al. 2013; Nishiizumi and Caffee 2013), indicating that this sample was ejected from the lunar near-subsurface (depths ~100 cm) and it had a short transit time, arriving on the Earth as a meteorite 0.1-0.2 Ma ago.

3.5. Possible Launch Origin

The possible provenance of this sample was investigated using the averaged bulk-rock FeO, TiO_2 and Th compositions from the literature and this study ± 2σ standard deviation of the averaged measurements (Table 3.3), the 2-degree LP-GRS dataset (Prettyman et al. 2006) and the procedure developed by myself (Calzada-Diaz et al. 2015). The 2σ standard deviation was chosen, because 1σ standard deviation is often too small to obtain any values.

	Average	Standard deviation (2σ)
FeO	5.14 wt.%	0.36
TiO_2	0.52 wt.%	0.14
Th	1.77 ppm	0.34

Table 3.3 Averaged FeO, TiO_2 and Th ± 2σ standard deviation of the averaged bulk-rock compositions used to determine the possible launch site of MIL 090036. The averages were calculated from data published by Korotev and Zeigler (2015) and the bulk-rock analysis performed during this study (2n).

The results obtained suggest an origin for MIL 090036 in the surroundings of the PKT, although also a couple of results appear in the vicinity of the SPA basin and in the north area of the Compton crater (Figure 3.14). All these results are consistent with the enrichment on Th observed in this sample and although most of them are located in the nearside of the Moon, some areas are in the farside (SPA and Compton crater).

Because the area of similar regolith composition to the sample in the nearside is larger, I suggest that the likely launch region for this meteorite is the surroundings of the PKT in the nearside. But differences described in previous sections between the meteorite and the Apollo 16 regolith samples, also suggest that the origin of MIL 090036 is outside the area sampled by the Apollo missions.

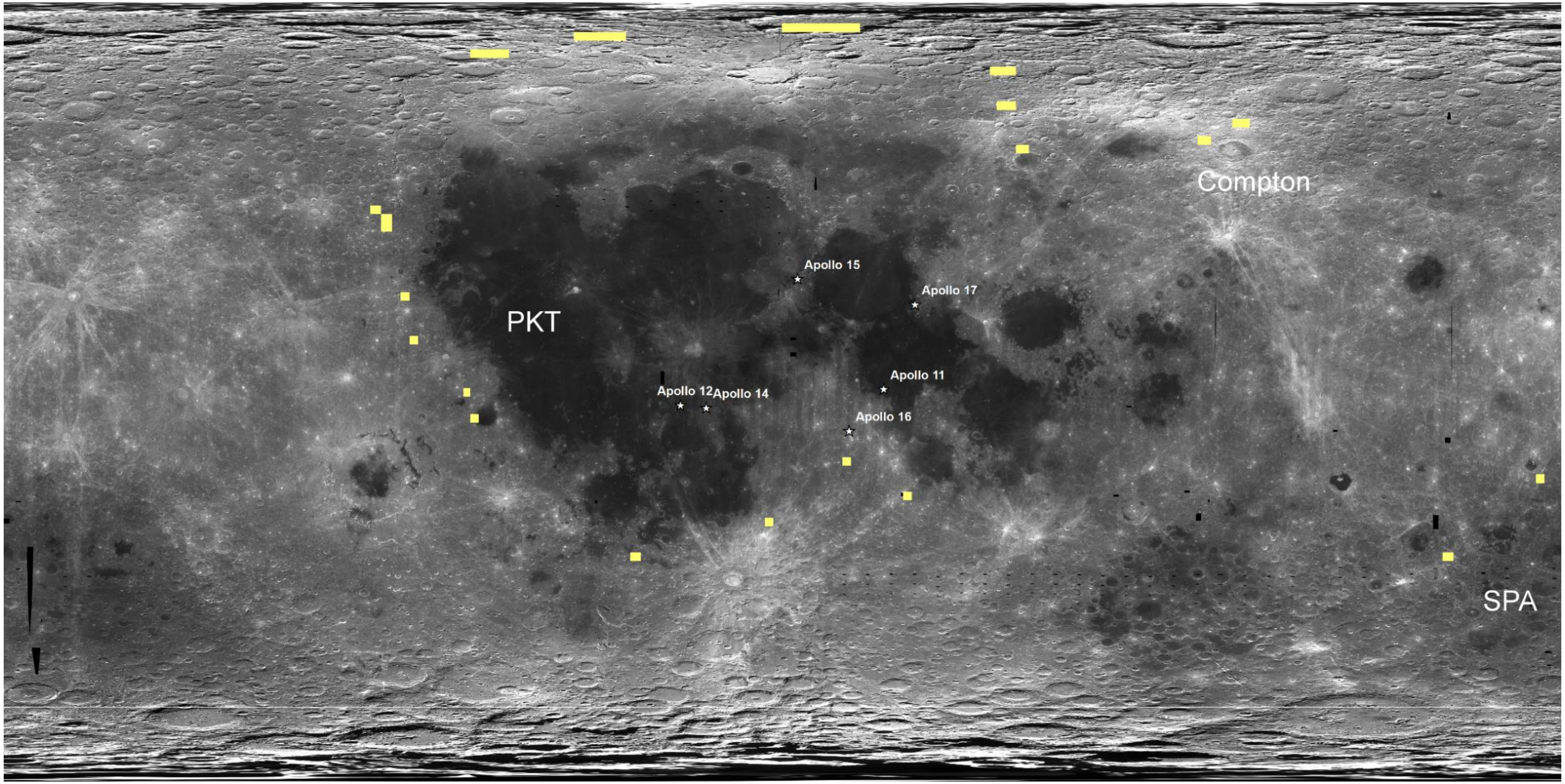

Figure 3.14 Identification of lunar regolith with similar FeO, TiO_2 and Th compositions to MIL 090036 in yellow. Search location are overlain on a Clementine mission albedo map of the Moon.

3.6. Summary

MIL 090036 is a feldspathic immature regolith breccia (26.72 wt.% Al_2O_3, 5.27 wt.% FeO) that exhibits a Th-enrichment (1.89 ppm Th). This could be related to a high alkali component that have been observed in impact melt breccia clasts, but also it could be related to a KREEP component that, although not observed in this sample, it cannot be precluded. The clasts of the sample have suffered shock metamorphism as indicated by the presence of recrystallized breccias and plagioclase transformed into maskelynite.

Petrography and bulk-rock major element composition show some similarities with regolith and soils from the Apollo 16 site and lunar feldspathic meteorite NWA 4936. However, also there are differences among the three samples in major elements, mainly MgO and Na_2O, as well as in REE, that suggest that Apollo 16 and NWA 4936 have different source regions. FeO, TiO_2 and Th, have been used to investigate possible launch location of the MIL 090036 sample. Most of the results shows that the regolith from the surroundings of the PKT in the nearside are the most similar to the composition of the meteorite and therefore the likely source location for MIL 090036. However, because the differences mentioned above, it is also highly probable that this sample were launched from an area not sampled previously by any Apollo mission.

Chapter 4. Miller Range 090070[2]

4.1. Introduction

MIL 090070 is an anorthositic regolith breccia (Figure 4.1) not paired with MIL 090036. It was found in Antarctica during the 2009-2010 ANSMET field season (Righter 2010; Korotev and Zeigler 2015) with an original mass of approximately 137 g. It was found together with MIL 090075 so both stones are considered to be paired. MIL 090070 is covered by a shiny green fusion crust in about 40% of its surface. The interior of the sample is formed by 3-5 mm white clasts in a dark, fine-grained or glassy matrix. This meteorite is grouped with MIL 090034 and MIL 090075 (Righter 2010).

This study presents the petrography of a polished thick (100 µm) section (MIL 090070,35) and the bulk-rock composition of a 275 mg chip (MIL 090070,33). Both the chip and the thick section were kindly allocated by the Meteoritic Working Group and provided by the curatorial team at NASA's Johnson Space Center. I aim to investigate the bulk-rock composition and the mineralogy of the individual components of the sample, as well as to conduct a study to investigate its possible launch origin to understand its original regolith environment.

---

[2] The work presented in this chapter published in [**The petrology, geochemistry and age of lunar regolith breccias Miller Range 090036 and 090070: insights to the crustal history of the Moon**. Calzada-Diaz A, Joy K.H., Crawford I.A. and Strekopytov S. *Meteoritics and Planetary Sciences, 2016*].

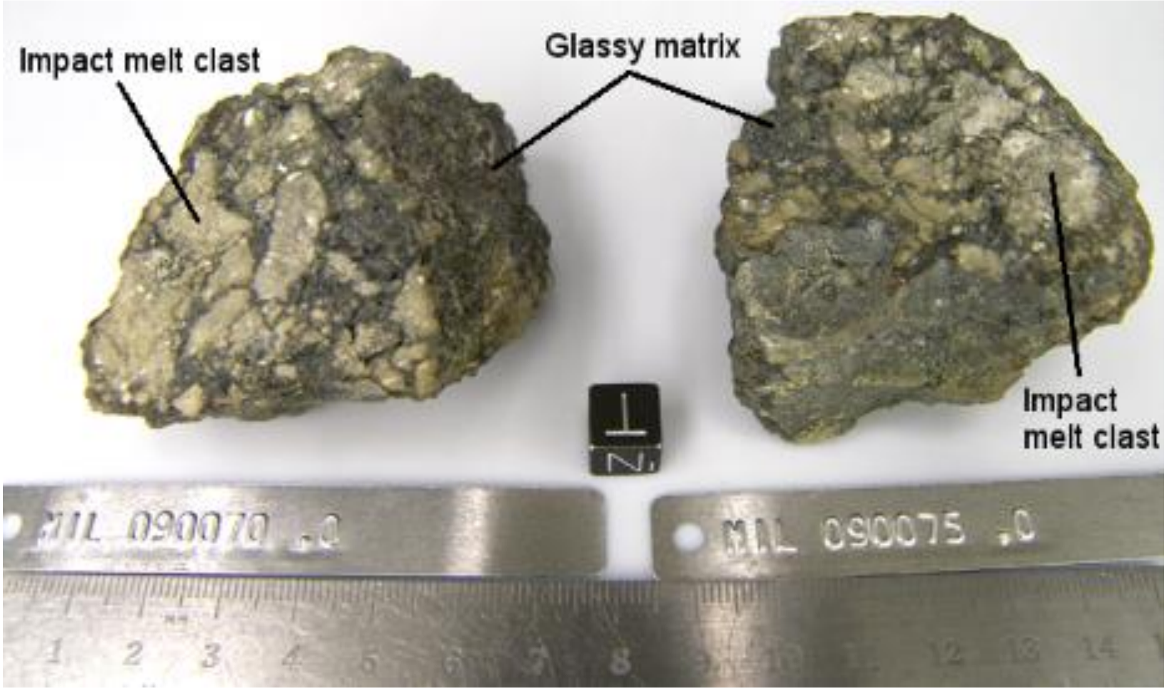

Figure 4.1 Hand specimen of MIL 090070 and its paired stone 090075. Lighter impact melt clasts are included in a dark glassy matrix. (Credit: Randy Korotev's webpage *http://meteorites.wustl.edu/lunar/stones/mil0900xx.htm*).

4.2. Petrography and Clast Inventory

MIL 090070,35 is an anorthositic regolith breccia with a dark, glassy matrix (Figure 4.2). The sample contains several lithologies with a large range of sizes (from <0.1 mm to 3 mm). This section is dominated by clast-rich impact melt breccias following the classification of Stöffler and Grieve (2007) described in Chapter 3, and monomict plagioclase grains. Scarce annealed impact melt clasts are also observed. Larger clasts corresponding to the clast-rich impact melt breccias. Fined-grained (<0.1 mm) mineral fragments of plagioclase, pyroxene and olivine are included in a dark glassy matrix. No mare basaltic or KREEP-rich clasts were found within MIL 090070,35.

Plagioclase fragments within impact melt breccias and monomict plagioclase clasts appear heavily fractured. Also, maskelynite is present in the borders of many monomict plagioclase grains. Some fractures cross the sample not showing any preferred orientation. Silica-rich areas are observed, especially in the borders of the sample, suggesting it could be a product of terrestrial alteration.

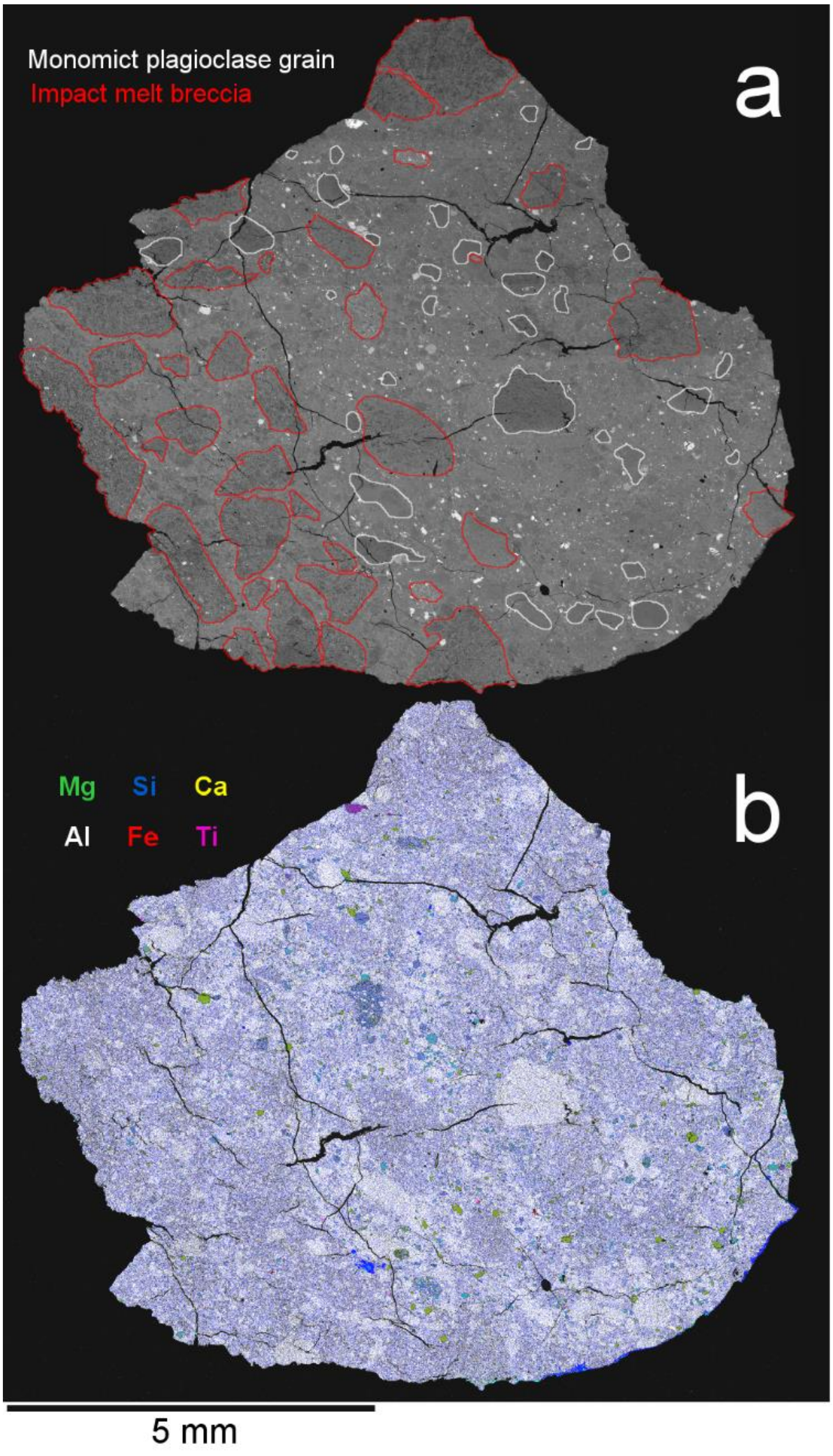

Figure 4.2 (a) BSE image of MIL 090034,35 section with monomict plagioclase grain denoted outlined in white and impact melt breccias in red. Other types of clasts have not been noted because their small size and scarce presence. (b) False colour elemental map of MIL 090034,35 where colours represent element concentrations and distribution: Mg – green (probably pyroxene or olivine), Si – blue, Ca – yellow, Al – white (the predominance of those colors represent the plagioclase), Fe – red (probably iron from meteoritic material) and Ti – pink (representing the ilmenite grains).

4.2.1. Impact melt breccias

Impact melt breccias are clast-rich, most of them containing fragments of plagioclase grains (~70-90% modal) and glass. They are variable in size, from <1 mm to up to 3 mm. They exhibit angular shapes and poorly defined borders that merge into the meteorite matrix (Figure 4.3a-c). These impact-melt breccia clasts contain poorly-sorted plagioclase (90% modal) fragments up to 500 μm in size.

Occasionally, other impact melt breccia clasts contain a more mafic assemblage of pigeonite and augite (~20% modal) and plagioclase (~80% modal; Figure 4.3d).

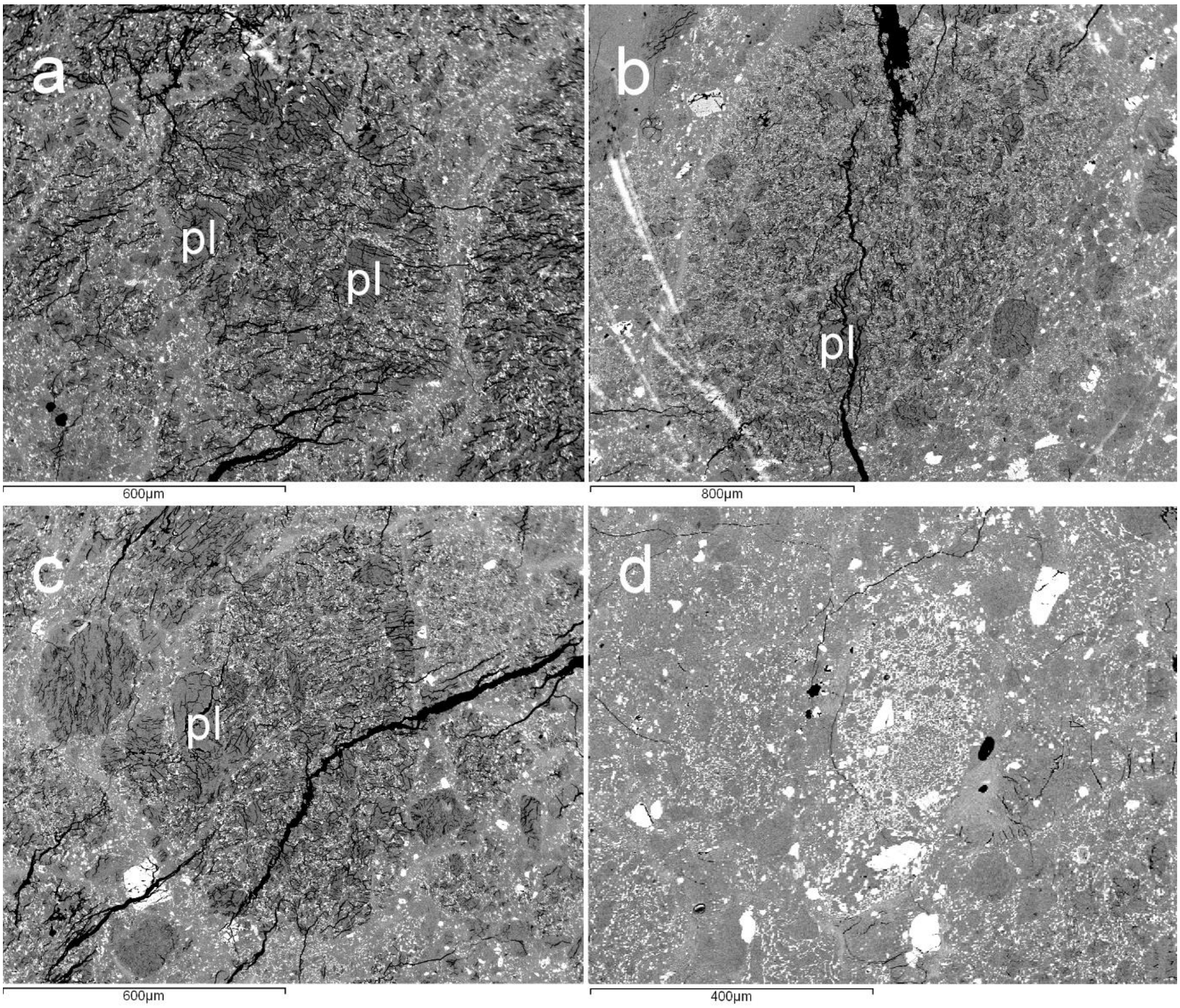

Figure 4.3 Close up BSE images of impact melt breccias in MIL 090070,35. (a,b,c) Clast-rich impact melt breccias with highly fractured plagioclase, pl. (d) Clast-rich impact melt-breccia bearing more mafic components.

4.2.2. Monomict plagioclase clasts

Monomict plagioclase fragments occur within the matrix in variable sizes up to 1 mm. They often appear highly fractured and transformed into maskelynite, especially in the borders of the clasts (Figure 4.4). This maskelynitization have been confirmed by the chemical analysis of the glassy areas during this study but also by their Fourier Transform Infrared (FTIR) spectra and cathodoluminescence images by Martin et al. (2016).

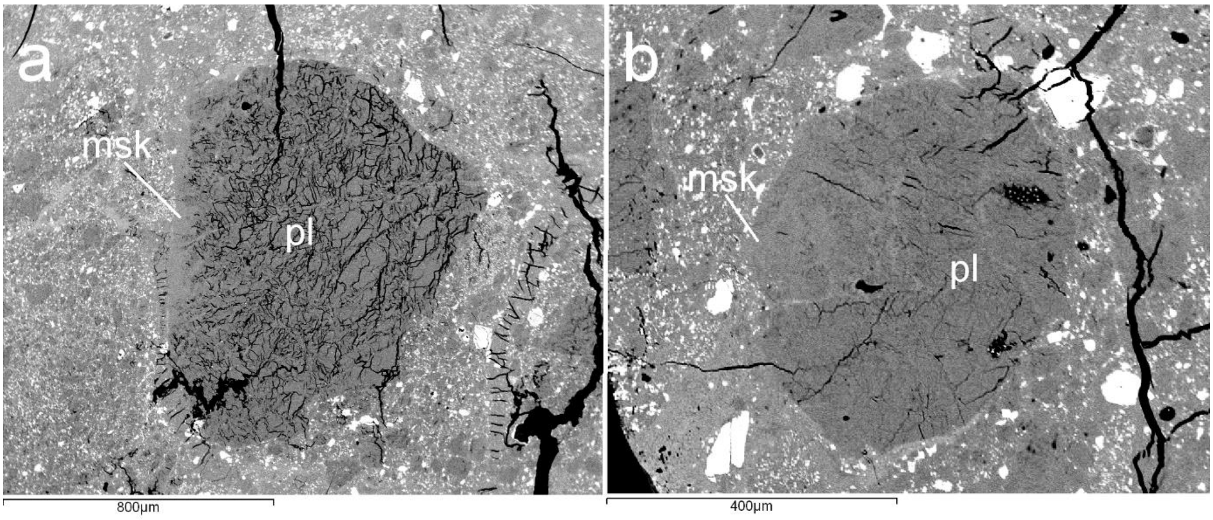

Figure 4.4 Close up BSE images of monomict plagioclase grains (pl) observed within MIL 090070,35. Maskelynitized areas (msk) can be observed in the rims of the clasts.

4.2.3. Annealed impact melt clasts

Annealed impact melt clasts (Figure 4.5) are clasts that have suffered a large degree of melting and slow cooling (e.g. Joy et al. 2011). They are scarce within the sample and usually of sizes <500 µm. They contain plagioclase (~70 % modal) and pyroxene (~30 % modal). A small amount of Fe-Ni meteoritic component occasionally can be found in these samples.

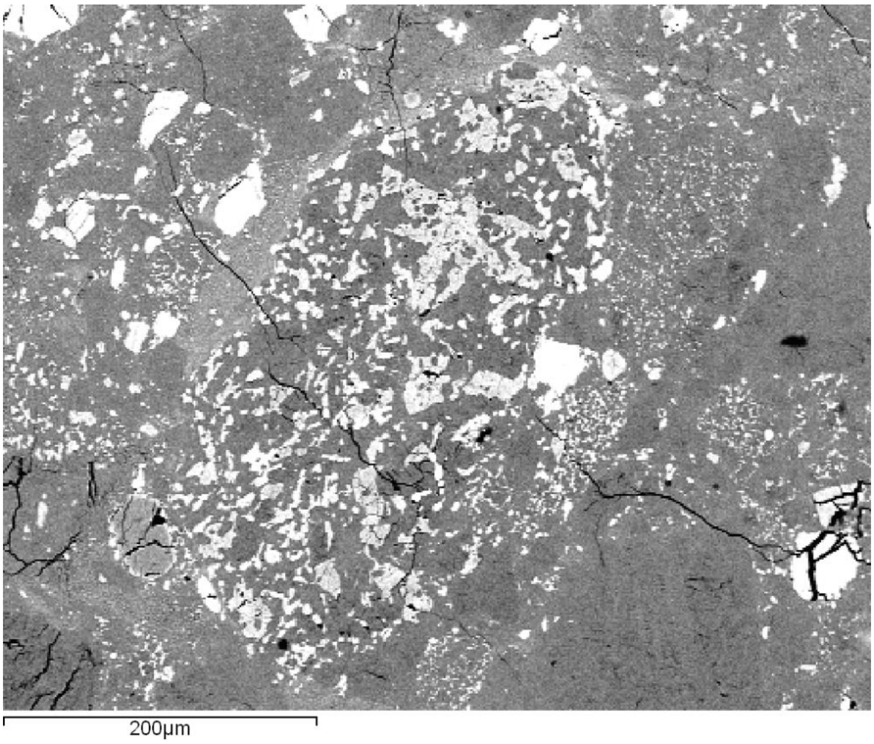

Figure 4.5 Close up BSE image of an annealed clast found in MIL 090070,35.

4.2.4. Matrix

The matrix of MIL 090070,35 hosts plagioclase, pyroxene, scarce olivine crystals and glass. Mineral fragments usually are anhedral, occasionally subhedral, and with small sizes, not larger than 0.2 mm. In addition, a minor small (<0.1 mm) FeNi metallic grain component also is present.

4.2.5. Mineral chemistry

Plagioclase: Plagioclase in monomict plagioclase clasts are similar in composition (An_{93-97}) to most of those found in the impact melt breccias (An_{91-98}). This suggests a similarity of parent lithology. Highly anorthitic plagioclase grains (An_{99}) were also found within some impact melt breccias. Plagioclase crystals in annealed impact melt clasts has a very narrow composition variability ranging from An_{91} to An_{95} (Figure 4.6). Crystals of plagioclase were found in the matrix with compositions ranging from An_{92} to very calcic An_{99}.

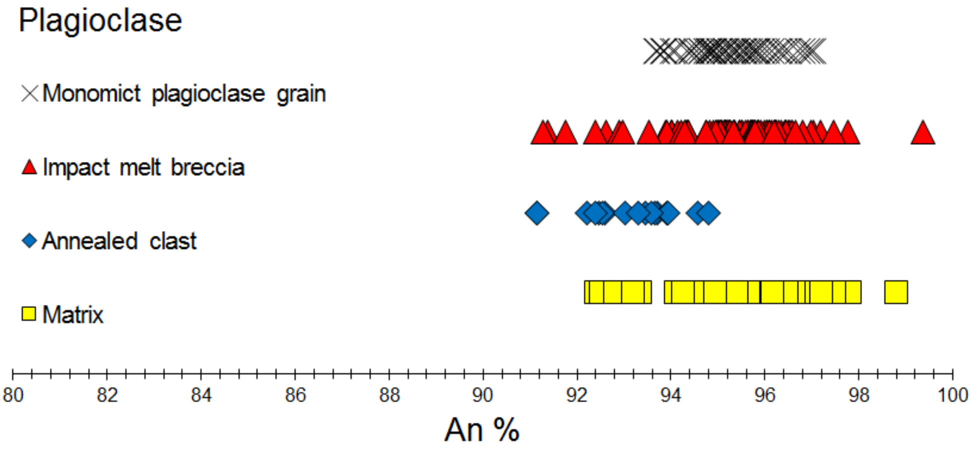

Figure 4.6 Anorthite content diagram of averaged plagioclases from MIL 090070,35: Anorthositic clasts (black cross), impact melt breccia (red triangle), annealed impact melt clasts (blue diamond) and matrix (yellow square).

Pyroxene: The only type of pyroxene observed in impact melt breccias are pigeonite ($En_{50-64}Wo_{6-19}Fs_{25-32}$; Figure 4.7, triangle). Annealed impact melt clasts have two types of pyroxenes: enstatite with Ca compositions very close to the lower end of the pigeonite field (En_{28-29} Wo_{4-5} Fs_{28-29}) and augite (En_{37-42} Wo_{36-41} Fe_{16-26}; Figure 4.7, square). Pyroxene fragments in the matrix are highly variable in composition, ranging from enstatite to pigeonite to augite with more FeO rich compositions (En_{22-75} Wo_{3-42} Fs_{16-59}; Figure 4.7, cross).

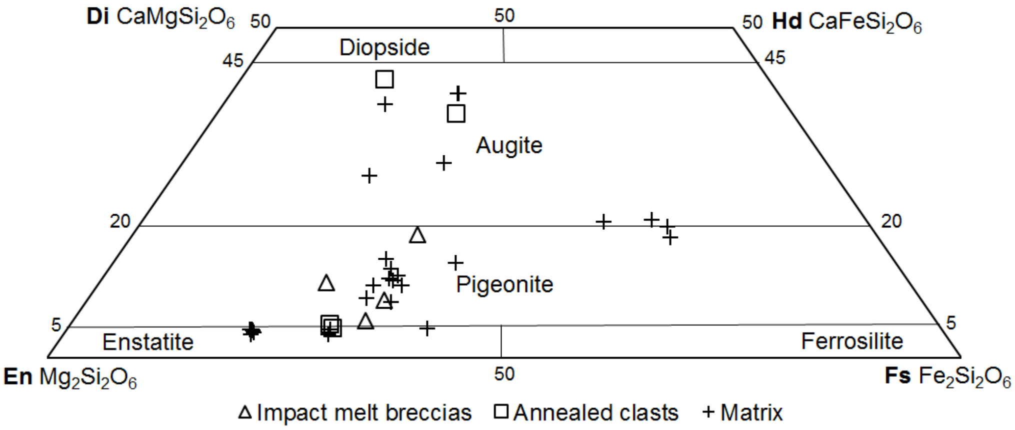

Figure 4.7 Pyroxene quadrilateral diagram showing compositions of pyroxenes observed in clasts and matrix from MIL 090070,35.

The sparse olivine grains that were found within the sample have variable compositions, ranging between Fo_{49} and Fo_{70}.

Mineral compositions for the different clast types in MIL 090070,35 are shown in Table 4.1. A complete list of mineral compositions can be seen in the electronic appendix 4A-C.

	Pyroxene			Plagioclase	Olivine
Clast	Wo-range	En-range	Fs-range	An-range	Fo-range
MPG	nm	nm	nm	93-97	nm
IMB	6-19	50-64	25-32	91-98	nm
AC	4-5 36-41	28-29 37-42	28-29 16-26	91-95	nm
Matrix	3-42	22-75	16-59	92-99	49-70

Table 4.1 Inventory table of the pyroxene, plagioclase and olivine clast composition within MIL 090070,35 (nm: not measured). MGP: Monomict plagioclase grain; IMB: Impact melt breccia; AC: annealed clast and Matrix. Pyroxene wollastonite (Wo) value was calculated as atomic Ca/(Ca+Fe+Mg) × 100, Pyroxene enstatite (En) value was calculated as atomic Mg/(Ca+Fe+Mg) × 100 and pyroxene ferrosilite (Fs) value was calculated as atomic Fe/(Ca+Fe+Mg) × 100. Plagioclase anorthite (An) range was calculated as atomic Ca/(Ca+K+Na) × 100. Olivine forsterite (Fo) value was calculated as atomic Mg/(Mg+Fe) × 100.

4.3. Bulk Composition

Bulk compositions for MIL 090070,34 are very similar to those obtained by previous authors (e.g. Korotev and Zeigler 2015). Both are shown in Table 4.2 together with analysis of the paired stones MIL 090075 and 090034, FAN, feldspathic crust and highland meteorites bulk-rock averages for comparison.

Abundances in Al_2O_3 and CaO are very similar between the MIL 090070,34,75 and the average FAN, feldspathic and highland meteorite bulk-rock averages. FeO, MgO and ITE's concentrations are however, lower in FAN averages than in the meteorites studied (Table 4.2).

	MIL 090070,33 (this work)	MIL 090070 (Korotev and Zeigler 2015)	MIL 090075 (Korotev and Zeigler 2015)	MIL 090034 (Korotev and Zeigler 2015)	Average FAN (Papike et al. 1988)	Feldspathic crust (Korotev et al. 2003)	Average highland meteorites (Cohen et al. 2002)
SiO_2	45.16 ± 0.19	44.50	45.20	44.30	44.7	44.9	
TiO_2	0.164 ± 0.001	0.14	0.21	0.15	0.09	0.22	0.27
Al_2O_3	30.72 ± 0.16	31.30	29.80	31.00	32.9	28.5	26.3
FeO	3.77 ± 0.014	3.26	3.70	3.40	1.71	4.0	5.24
MnO	0.0493 ± 0.0002	0.05	0.05	0.05	0.03	0.060	0.07
MgO	2.984 ± 0.019	2.75	3.85	2.84	1.62	5.3	6.10
CaO	17.45 ± 0.045	17.00	16.60	17.10	18.6	16.4	15.4
Na_2O	0.375 ± 0.002	0.37	0.39	0.37	0.33	0.34	0.33
K_2O	0.0257 ± 0.0004	0.04	0.06	0.04	0.03	0.026	0.02
P_2O_5	<0.02	0.02	0.06	0.02	0.02	0.023	0.02
Total	100.69	99.49	100.00	99.33	100.03	99.77	
Mg#	61.07	60.10	65.00	59.60		70	
Li	2.99 ± 0.069						
Be	0.28 ± 0.0093						
Sc	6.81 ± 0.093	6.29	11.90	6.62	3.77	8.0	9.06
V	14.8 ± 0.04						
Co	9.39 ± 0.014	8.10	11.10	8.10	4.16	10	17.0
Cr	463 ± 1.6				207	630	699
Ni	52.0 ± 0.12				9.56	~16	
Cu	2.77 ± 0.026						177
Zn	5.85 ± 0.07						
Ga	3.27 ± 0.011						3.43
Rb	0.558 ± 0.031					0.7	
Sr	168 ± 1.7	161.00	162.00	159	159	151	251
Y	9.02 ± 0.1					9	
Zr	33.4 ± 0.25	27.00	94.00	24.00	31	35	35.4
Nb	2.10 ± 0.004						
Mo	0.0436 ± 0.0019						
Sb	0.111 ± 0.0055						
Cs	0.0169 ± 0.0022				0.019		0.142
Ba	32.5 ± 0.26	27.00	78.00	26.00	9.59	33	65.5
La	2.99 ± 0.016	2.15	6.78	1.80	0.334	2.4	2.58
Ce	6.24 ± 0.053	5.38	17.20	4.72	0.838	6.0	6.60
Pr	0.978 ± 0.0049					0.8	
Nd	4.41 ± 0.063	3.31	10.40	2.99	0.691	3.7	3.80
Sm	1.28 ± 0.035	0.98	3.02	0.86	0.131	1.1	1.17
Eu	0.986 ±0.0034	0.86	0.94	0.84	0.769	0.79	0.810
Gd	1.55 ± 0.008					1.3	
Tb	0.263 ± 0.0024	0.20	0.61	0.18	0.036	0.23	0.243
Dy	1.77 ± 0.034					1.5	
Ho	0.371 ± 0.0043					0.33	0.282
Er	1.06 ± 0.008					0.9	
Tm	0.156 ± 0.0014					0.14	
Yb	0.99 ± 0.0081	0.78	2.22	0.70	0.16	0.90	0.966
Lu	0.142 ± 0.0019	0.11	0.30	0.10	0.014	0.13	0.142
Hf	0.949 ± 0.03	0.66	2.31	0.62	0.126	0.8	0.874
Ta	0.121 ± 0.002	0.08	0.26	0.08		0.11	0.130
W	0.0559 ± 0.0025						
Tl	0.0077 ± 0.0009						
Pb	0.348 ± 0.0036						
Th	0.441 ± 0.0036	0.32	1.11	0.28	0.0364	0.38	0.411
U	0.13 ± 0.0046	0.13	0.33	0.07	0.07	0.16	0.132

Table 4.2 Bulk-rock and trace element compositions for MIL 090070.35 obtained during this study. Previous analysis on this meteorite and paired stones MIL 090075 and 090034 (Korotev and Zeigler 2015), FAN (Papike 1998), feldspathic crust (Korotev et al. 2003) and highland meteorites (Cohen et al. 2005) average compositions are also shown for comparison.

4.4. Discussion

4.4.1. Similarities to other lunar meteorites

Based on bulk-rock compositions, petrography and radiogenic isotopes, MIL 09070 is paired with MIL 090075 and with MIL 090034 (Korotev 1999; Liu et al. 2011; Shirai et al. 2012; Zeigler et al. 2012; Nishiizumi and Caffee 2013).

MIL 090070 have the highest bulk rock concentrations of Al_2O_3 (30.72 wt.%) of all the lunar highland meteorites found to date, although its concentration is close to NWA 2200 (30.1 wt.%), Dho 081 (30.5 wt.%), DaG 400 (28.6 wt.%) and DaG 262 (27.5 wt.%) MIL 090070, NWA 2200 and Dho 081 also have similar FeO/MgO values, in these cases >1 whereas the DaG meteorites have FeO/MgO very close to, but less than, 1 (Bischoff et al. 1998; Semenova et al. 2000; Warren 2001; Nagaoka et al. 2013).

Incompatible element concentrations are very similar among most of these meteorites (Figure 4.8) although there are some exceptions: Dho 081 and MIL 090075. Dho 081 shows lower content in REE, although having a similar pattern with a positive Eu-anomaly. In the case of the MIL 090075, paired stone of MIL 090070, the concentration of incompatible elements are considerably higher. In this case, the REE pattern as well as the concentrations are very similar to the average HMS (Papike 1998; Semenova et al. 2000; Warren 2001; Cahill et al. 2004; Nagaoka et al. 2013; Korotev and Zeigler 2015).

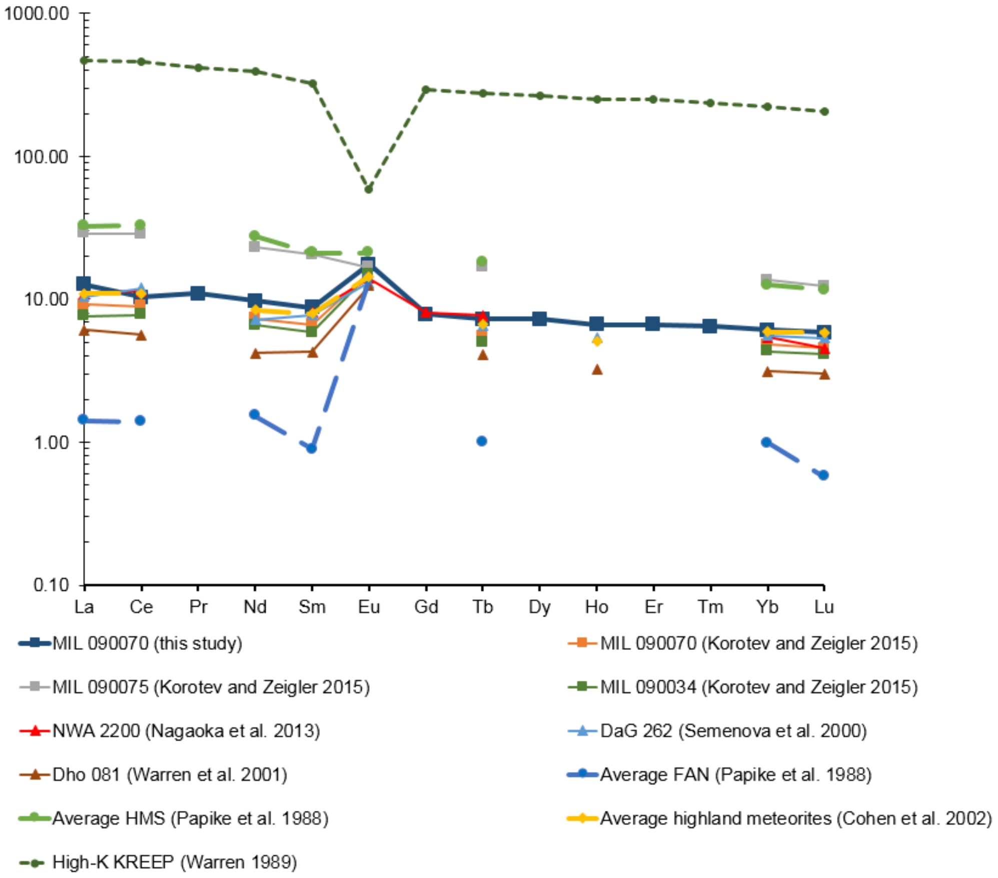

Figure 4.8 CI-normalized (Anders and Grevesse 1989) REE abundances for MIL 090070,33 (this study and (Korotev and Zeigler 2015), paired stones MIL 090075 and 090034 (Korotev and Zeigler 2015), NWA 2200 (Nagaoka et al. 2013), Dho 081 (Warren 2001), DaG 262 (Semenova et al. 2000). Also, the average FAN, HMS, average highland meteorites and high-K KREEP REE abundances are shown (Papike 1998; Cohen et al. 2002).

Sc is carried mainly by pyroxenes, thus Sc abundance is larger as the mafic component of the sample increases as it does FeO abundances. So, it is expected that feldspathic meteorites have lower FeO-Sc ratios than its basaltic counterparts. In the case of MIL 090070, this ratio falls very close to the average Fe-Sc ratio for highlands material (Figure 4.9). The exception is MIL 090075 that has a larger Sc content compared to the rest of the samples. The difference in Sc abundances in MIL 090075 suggests that this sample is more pyroxene-rich that its paired stones, this difference in Sc abundances among the paired samples could be caused by the size of the sample and the heterogeneity nature of the breccias.

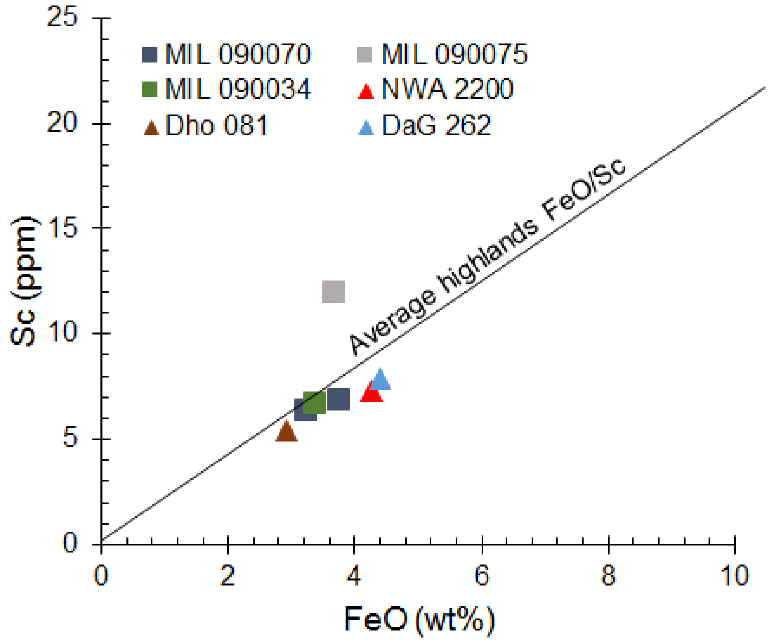

Figure 4.9 Bulk-rock FeO vs Sc for MIL 090070 (this study and Korotev and Zeigler 2015), paired stones MIL 090075 and 090034 (Korotev and Zeigler 2015), NWA 2200 (Nagaoka et al. 2013), Dho 081 (Warren 2001), DaG 262 (Semenova, Nazarov, Kononkova, Patchen, and Taylor 2000). Also are shown the average FAN, HMS and average highland meteorites (Papike 1998; Cahill et al. 2004). Error bars are smaller than the symbols.

Sc and Sm concentrations are related to the ITEs and mafic phases. For example, FAN lithologies exhibit low Sc and Sm and high Al_2O_3 abundances (Figure 4.10). MIL 090070 shows lower Sc and Sm, and higher Al_2O_3 abundances than the Apollo 16 regolith breccias (Korotev 1997) indicating that the KREEP and mafic component in the meteorite are lower than those found in the Apollo 16 regolith breccias (Figure 4.10). These differences suggest that the meteorites are formed by highlands material that differs compositionally to the materials found at the Apollo 16 landing site.

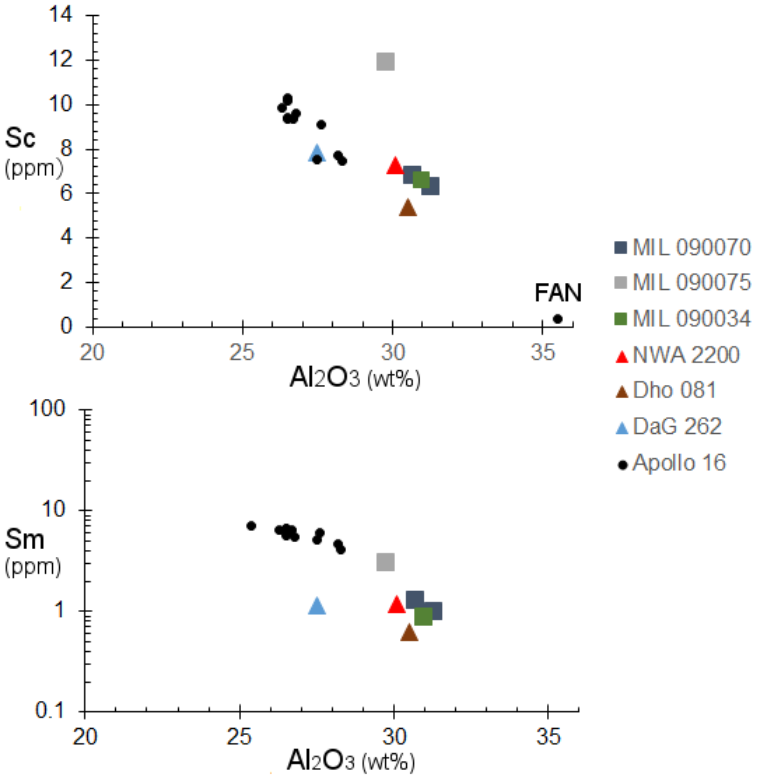

Figure 4.10 Bulk-rock Sc and Sm abundances versus Al_2O_3 for MIL 090070, 090075, 090034, NWA 2200, Dho 081 and DaG 262 and Apollo 16 regolith breccias (Papike 1998; Korotev 1997; Semenova et al. 2000; Warren 2001; Cahill et al. 2004; Nagaoka et al. 2013; Korotev and Zeigler 2015). Error bars are smaller than symbols.

4.4.2. Petrogenesis

Most impact melt breccia clasts and the matrix in the studied sample of MIL 090070, have mineral compositions that are similar to samples from the FAN suite (Figure 4.11). However, some poikiloblastic impact melt clasts plot in the gap between the FAN and the HMS, indicating that either the parent rocks were mixed together during the impact melting event or the parent rock were distinct and different from these two suites such as MAN. This is similar to what was previously observed in other feldspathic impact melt breccias lunar meteorites (Cahill et al. 2004).

Mineral chemistry from plagioclase (electronic appendix 4A) also indicates a FAN protolith as the most likely parent lithology of the mineral clast component within the feldspathic impact melt breccias. The FAN protolith likely originated during crust formation in early lunar history (Taylor and McLennan 2009; Elkins-Tanton et al. 2011). This protolith was highly disrupted by impact bombardment and extensively reworked, although still preserving compositionally evidence of a FAN parent rock affinity.

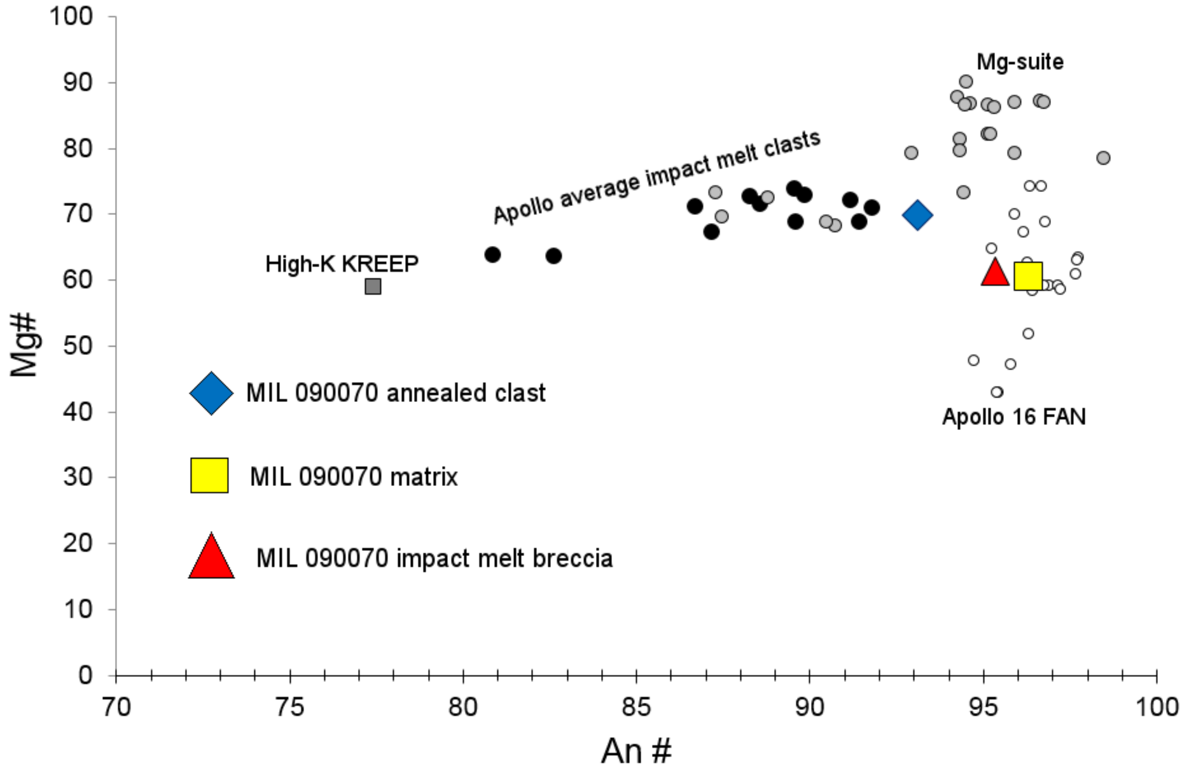

Figure 4.11 Diagram for averaged bulk-clast Mg# and An# for MIL 090070 impact melt breccia, annealed clast and matrix, compared to the main Apollo rock suites (Warren and Wasson 1979; Korotev 1996; Jolliff et al. 1998). Error bars are smaller than symbols.

Bulk-rock REE abundances in MIL 090070 plot very close to the average bulk-rock abundances for highlands rocks. These abundances fall between FAN and HMS averaged concentrations, suggesting that some magnesian component is present in the sample. This is supported by the fact that the REE content in paired stone MIL 090075 is very similar to the average HMS (Figure 4.8).

The lack of KREEP components in MIL 090070 indicates that this meteorite is not derived from material related to the Apollo 16 regolith, as the Sc vs Al_2O_3 and Sm vs Al_2O_3 diagrams also show (Figure 4.10), indicating that the meteorite derives from an area far from PKT and is not-affected by Imbrium ejecta. These observations are consistent with an origin in the lunar farside, suggesting that FAN and HMS lithologies are globally distributed and that they are more related than previously thought.

I suggest that MIL 090070 is part of a group formed by the feldspathic lunar meteorites Dho

025, Dho 081, DaG 262 and DaG 400. These samples represent a different type of highland terrain not recognized previously in the KREEP-enhanced lunar impact breccia database (Cahill et al. 2004). Furthermore, my results are consistent with the observations made in other lunar meteorites (e.g. Joy et al. 2010) that indicate that the lunar crust has Mg lateral variations and that it is ferroan noritic anorthosite normative.

Some studies on radiogenic isotopes have been performed in this sample by other authors, providing an age frame. A major impact event occurred to the MIL 090070 parent crust at ~3.9 Ga that was preserved by the Pb isotope (Bouvier et al. 2013) and Ar isotope reset systems (K. Joy in Calzada-Diaz et al. 2016). This age is similar to the estimated timing of the nearside Imbrium impact event at ~3.9 Ga (Hartmann et al. 1981; Neukum and Ivanov 1994; Snape et al. 2015) at the end of the basin-forming era (Stöffler et al. 2006). The argon isotope resetting event at 3.9 Ga could represent the time of the impact that excavated into the protolith crust, shocking the mineral debris (Martin et al. 2016) and assembling the feldspathic impact melt breccias that can be seen in the sample. It also could represent the final assembly of the whole sample into a breccia.

Secondary impact events are recorded in the argon isotope system from 3.9 to ~3 Ga and induced preferential degassing of the heavily fractured rock components, as the shocked impact melt breccia have more grain boundaries and therefore are more likely to be affected (Park et al. 2013; Calzada-Diaz et al. 2016, in review). These ages are consistent with the $^{39}Ar/^{40}Ar$ dates recorded in impact melts in other feldspathic lunar meteorites, which show a range of resetting ages between 2.76 and 3.92 Ga (Cohen et al. 2000; Cohen et al. 2004; Nyquist et al. 2006; Fernandes et al. 2013 and refs. therein) after the timing of major basin-formation events (Joy and Arai 2013).

The sample does not contain solar wind implanted isotopes, indicating that it remained in the lunar subsurface (i.e. below the upper few meters of the surface) and underwent a short transit time since it was ejected, arriving to the Earth approximately 0.7 Ma ago (Nishiizumi and Caffee 2013).

4.5. Possible Launch Origin

The possible provenance of the MIL 090070 was investigated using the averaged bulk-rock FeO, TiO_2 and Th compositions from this study and the literature ± 2σ standard deviation of the averaged measurements (Table 4.3), the 2-degree LP-GRS dataset from Prettyman et al. (2006) and the software developed by myself (Calzada-Diaz et al. 2015).

	Average	Standard deviation (2σ)
FeO	3.52 wt.%	0.72
TiO_2	0.15 wt.%	0.02
Th	0.38 ppm	0.16

Table 4.3 Averaged FeO, TiO_2 and Th ± 2σ standard deviation of the averaged bulk-rock compositions used to determine the possible launch site of MIL 090070. The averaged were calculated from data published by Korotev and Zeigler (2015) and the bulk-rock analysis performed during this study (2n).

All the results supports a launch origin for MIL 090070 in the farside highlands (Figure 4.12) as it was proposed in the previous section, an area far from the PKT and the Apollo 16 landing site and therefore, not affected by Imbrium basin ejecta.

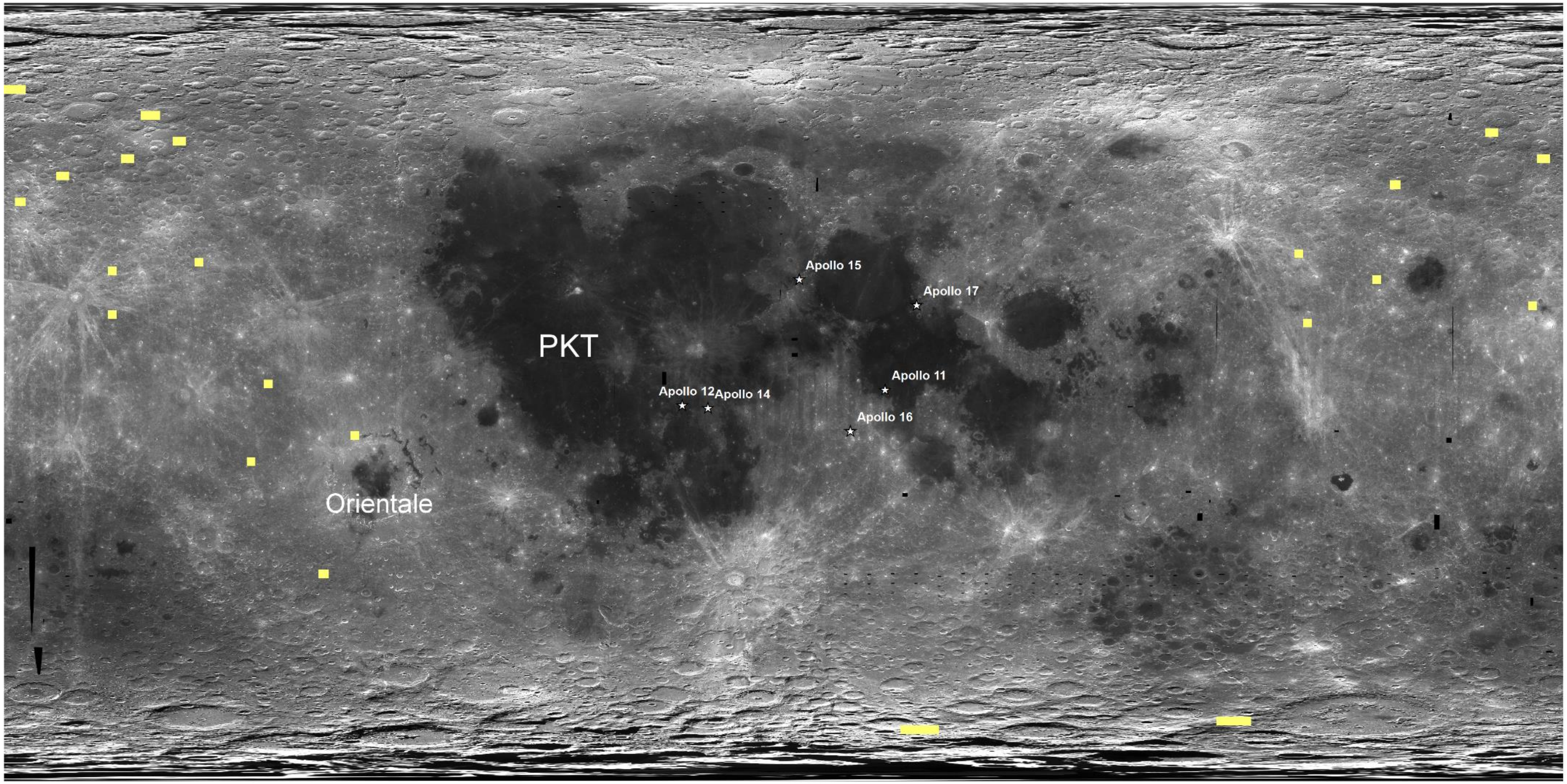

Figure 4.12 Identification of lunar regolith with similar FeO, TiO_2 and Th compositions for MIL 090070 in yellow. Search location are overlain on a Clementine mission albedo map of the Moon.

4.6. Summary

MIL 090070 is a feldspathic immature regolith breccia with bulk-rock compositions of 30.72 wt.% Al_2O_3, 3.77 wt.% FeO and a low Th abundance (0.44 ppm). It is formed mainly by impact melt-breccias and heavily fractured monomict plagioclase grains, all embedded in a glassy feldspathic matrix with small fragments of plagioclases, pyroxenes and scarce olivines. A small Fe-Ni meteoritic component is present too. This meteorite is paired with MIL 090075 and possibly with MIL 09034.

Petrography, bulk-rock and trace element compositions shows similarities with feldspathic meteorites NWA 2200, Dho 081, DaG 400 and DaG 262. The geochemistry of all these meteorites and MIL 090070 may be formed by a mixture of FAN and MAN rocks, although other possible explanation could be that they were all essentially FAN-derived and that this rock type is are more related to HMS that previously thought.

MIL 090070 was probably launched from the farside of the Moon as suggested by the differences among the Apollo 16 regolith breccia samples and the meteorites, including the lack of KREEP. If this is correct, it would mean that FAN and HMS are globally distributed, the Mg shows lateral variations within the lunar highlands and that the crust is ferroan noritic anorthosite normative.

Chapter 5. Investigating the Source Regions of Basaltic and Th-rich Lunar Meteorites[3]

5.1. Introduction

Basaltic (>17 FeO wt.%), intermediate (12-17 FeO wt.%) and Th-rich (>4 Th ppm) lunar meteorites analysis addresses important questions about the planetary processes that created the diversity of rocks observed in the Moon. Lunar volcanism is a window into the thermal and compositional evolution of the moon, and it provides valuable information of the evolution of a differentiated planetary body.

This chapter aims to shed light into the heat-source mechanisms that worked to create the lunar basalts and the time framework in which those materials were created. Furthermore, the compositional analysis of the Th-rich lunar meteorites and the knowledge of their possible launch location will help to address the compositional heterogeneity of the lunar mantle. Regolith breccia meteorites with intermediate compositions, those whose bulk rock compositions are between basaltic and feldspathic, are formed by impact processes that reworked the regolith. These two types of material that probably were situated close to each other were mixing forming intermediate rocks. Analysis of their petrography and the re-setting events that they may have suffered, as well as studying their possible launch origin provide with information about impact processes that mixed them up and the time frame when those processes happened. This could help to delimitate the time at where some basin-forming impacts took place.

---

[3] Aspects of the work presented in this chapter were published in [**Constraining the source regions of lunar meteorites using orbital geochemical data.** Calzada-Diaz A, Joy K. H., Crawford I.A, and Nordheim T. A. *Meteoritics and Planetary Sciences* 50, 214-229. 2015.].

I have investigated the possible launch locations of 15 lunar meteorites (21 individual stones) with bulk rock basaltic compositions with FeO contents >12 wt.%, Th abundances <2 ppm and variable TiO_2 content from ~0.2 to ~3 wt.% (Table 5.1).

The basaltic meteorites presented here are both unbrecciated and crystalline basalts, and brecciated rocks that sometimes may contain feldspathic fragments (<10%). Bulk rock FeO, TiO_2 and Th abundances were used to assess their possible launch location using 2-degree LP-GRS (Prettyman et al. 2006), bulk rock FeO, TiO_2 and Th compositions obtained from the literature (Table 5.1) and implementing the software described in Chapter 2. This software matches bulk rock compositions from the meteorites and the abundances observed by the remote sensing instrument.

Meteorite	**Meteorite type**	**No. of literature bulk rock analyses used**	**Std. Dev. (σ)**	**Referemces**	**FeO (wt.%)**	**% error**	**TiO_2 (wt.%)**	**% error**	**Th (ppm)**	**% error**
MET 01210	Regolith breccia	2	±9σ	Korotev et al. 2009, Joy et al. 2010	15.25 ± 2.79	18	1.48 ± 0.9	61	0.86 ± 0.2	23
LAP Group	Mare basalt	21	±4σ	Joy et al. 2005, Zeigler et al. 2005, Anand et al. 2005, 2006, Righter et al. 2005, Day et al. 2006	22.05 ± 4.2	19	3.18 ± 1.2	38	2.03 ± 0.92	45
NWA 032	Mare basalt	4	±3σ	Grossman et al. 2000, Fagan et al. 2002, Jolliff et al. 2003	22.2 ± 1.92	9	2.98 ± 0.57	19	1.88 ± 0.39	21
NWA 4898	Mare basalt	2	±8σ	Greshake et al. 2008, Korotev 2008	17.27 ± 0.8	5	2.39 ± 1.5	63	0.44 ± 0.80	182
NEA 003	Mare basalt	4	±7σ	Haloda et al. 2006[a], 2006b, 2009	21.83 ± 1.47	7	1.34 ± 2.91	217	0.43 ± 1.19	277
Dho 287	Mare basalt	14	±2σ	Taylor et al. 2001, Anand et al. 2003, Demidova et al. 2003, Korotev 2012	18.95 ± 4.49	24	2.48 ± 1.33	54	nr	
Yamato 793169	Mare basalt	5	±2σ	Korotev et al. 2003,	22.29 ± 3.34	15	1.94 ± 0.74	38	0.71 ± 0.08	11
EET 87521/96008	Regolith breccia	10	±2σ	Warren et al. 1991, Korotev et al. 2003, Anand et al. 2003	17.12 ± 2.54	15	0.61 ± 0.48	79	0.85 ± 0.48	56
NWA 773	Fragmental breccia	2	±5σ	Yanai and Kojima 1991, Jolliff et al. 1993, Warren et al. 1993, Koeberl et al. 2003, Fagan et al. 2003	19.67 ± 5.1	26	0.62 ± 0.62	100	1.63 ± 2.25	138
NWA 3136	Regolith breccia	1	±4σ	Korotev et al. 2009	15.36 ± 5.64	37	1.23 ± 1.0	81	1.29 ± 1.2	93
NWA 5153	Fragmental to impact-melt breccia	1	±2σ	Korotev et al. 2009	12.72 ± 2.34	18	0.73 ± 0.3	41	1.54 ± 0.72	47
Kalahari 008	Regolith breccia	2	±2σ	Sokol et al. 2008,Korotev et al. 2009	4.87 ± 0.56	11	0.4 ± 0.32	80	0.02 ± 0.02	100
NWA 4472	Regolith breccia	4	±5σ	Kuehner et al. 2007, Korotev et al. 2009	9.26 ± 0.45	5	1.28 ± 1.3	102	6.99 ± 0.4	6

Meteorite	Meteorite type	No. of literature bulk rock analyses used	Std. Dev. (σ)	Referemces	FeO (wt.%)	% error	TiO_2 (wt.%)	% error	Th (ppm)	% error
SaU 169	Regolith breccia with impact-melt clast	7	±3σ	Gnos et al. 2004 Korotev et al. 2009	10.87 ± 3.8	35	2.2 ± 1.72	78	20.38 ± 19.4	95
Calcalong Creek	Basalt-bearing breccia	7	±3σ	Hill and Boyton 2003, Korotev et al. 2009	9.52 ± 2.07	22	0.78 ± 0.36	46	3.92 ± 0.43	11
					Average % error	***18***		***73***		***79***

Table 5.1 Average bulk composition of basaltic meteorites ± the corresponding σ standard deviation for each element of averaged measurements that have been taken from that reported in the literature (nr: not reported).

5.2. Crystallline Basaltic Rocks

5.2.1. YAMM group

Due to compositional and mineralogical similarities, it is considered that meteorites Asuka (A) 881757, Miller Range (MIL) 05035, Yamato (Y) 793169 and Meteorite Hills (MET) 01210 are grouped (Arai et al. 2007; Zeigler et al. 2007; Joy et al. 2008). It is thought to depict a stratigraphic section of a basaltic lava flow from the surface, represented by the regolith breccia (MET 01210) in the upper layer, to the inner sections of the flow (Y-793169, A-881757 and MIL 05035). MET 01210 includes mineral fragments and basaltic clasts but also it contains feldspathic clasts and impact melt breccias (Joy et al. 2008; Arai et al. 2010). These could have been added by lateral mixing caused by impacts from deposits in its vicinity (Figure 5.1).

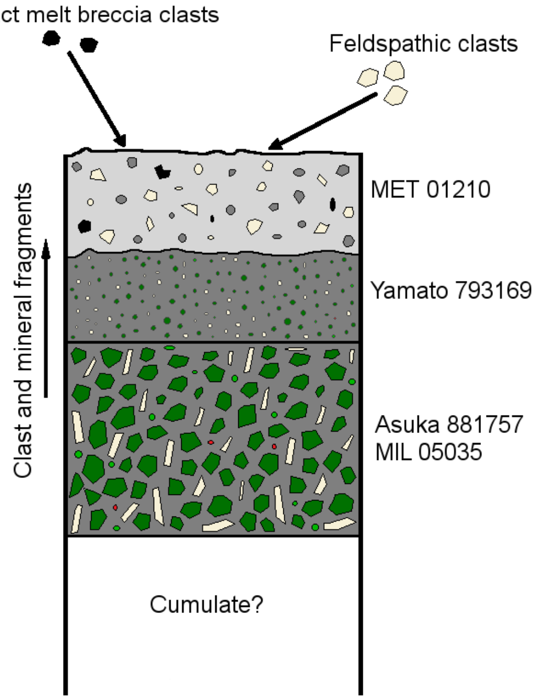

Figure 5.1 Not scaled diagram of the possible source environment of MET 01210, Yamato 793169, Asuka 881757 and MIL 05035. Basaltic clasts and mineral fragments are introduced into the regolith breccia by vertical mixing caused by impact processes in the area, meanwhile, feldspathic clasts and impact melt breccia fragments are added by lateral mixing from nearby deposits derived by impact processes. (Modified from Joy et al. 2008).

5.2.1.1. Inner section of the basalt flow: Asuka 881757 and MIL 05035

Asuka (A-) 881757 is a gabbroic basalt with coarse-grained, subophitic texture. It is formed of pyroxenes (En_{7-43} Fs_{7-68} Wo_{11-41}), plagioclase (An_{74-90}) and ilmenite. It also contains some troilite, apatite, Ni-Fe metal and traces of iron-rich olivine ($Fa_{85-95;}$ Yanai and Kojima 1991; Koeberl et al. 1993; Warren and Kallemeyn 1993; Arai et al. 1996). Bulk trace incompatible elements and REE in this meteorite resembles the patterns observed in Luna 24 VLT basalts (Koeberl et al. 1993; Warren and Kallemeyn 1993). Because of the coarse-grained texture (pyroxenes can reach up to 4 mm in size) of A-881757, it has been suggested that it could be a cumulate, however, the low-Mg, the moderate concentration of incompatible elements and the lack of detectable exsolution in pyroxene indicates that A-881757 is not the product of a high degree of crystal accumulation. In the Moon, coarse grained rocks could have been formed in shallow, relatively fast-cooling environments as in lava ponds, although deeper in the lava unit (Warren and Kallemeyn 1993).

Radiometric age dating using the ^{39}Ar-^{40}Ar system shows an impact resetting age of 3.763 ± 0.046 Ga (Fernandes et al. 2009) and cosmic-ray exposures indicates that the sample was launched from the Moon 0.8 ± 0.2 Ma ago (Nishiizumi et al. 1992; Eugster et al. 1992; Thalmann et al. 1996). The scarcity of solar-wind components suggest that the rock was buried several metres beneath the lunar surface (Arai et al. 2010), this is also supported by the depletion in Ni, Ir, and Au that indicates the absence of significant regolith component (Koeberl et al. 1993).

MIL 05035 is a crystalline basalt with a coarse-grained gabbroic texture. It is formed by large crystals (1 to 4.5 mm) of pyroxene (En_{2-42} Fs_{29-68} Wo_{13-43}), plagioclase with relict igneous zoning ($An_{76(rim)-95(core)}$), symplectite (intergrowth between two minerals) and rare ilmenite in a mesostasis formed by fayalitic olivine, troilite, silica, apatite and glass (Joy et al. 2008; Arai et al. 2010). Symplectitic assemblages and zoning pyroxenes suggests that the meteorites was crystallized in a shallow cooling environment rather than from magma cumulates (Arai et al. 2010).

The bulk rock REE pattern is very similar to the pattern observed in A-881757. Unlike Apollo low-Ti basalts, it does not show an extensive negative Eu- anomaly indicating that the source melt derives from a region dominated by early cumulates of the magma ocean, before plagioclase was removed to form the crust and KREEP precipitated (Joy et al. 2008)

Sm-Nd isotope analysis has dated this sample as 3.80 ± 0.05 Ga and Rb-Sr analysis has dated it in 3.90 ± 0.04 Ga (Nyquist et al. 2007). Cosmic-ray exposure shows that this sample could have been ejected from the lunar surface at 0.9 ± 0.2 Ma, very similar to the ejection age reported for A-881757 (Nishiizumi et al. 1992; Eugster et al. 1992; Thalmann et al. 1996). The scarcity of solar wind derived nuclides indicates that this sample was buried more than several metres beneath the surface (Figure 5.1; Arai et al. 2010).

5.2.1.2. Upper part of the basaltic flow: Yamato 793169

Y-793169 is a crystalline, subophitic basalt formed of pyroxene ($En_{1.9-53.5}$ $Fs_{22.2-84.3}$ $Wo_{9.7-40.7}$), plagioclase ($An_{88-97.5}$), ilmenite, spinel and glass. It also contains scarce crystals of olivine with high iron content ($Fa_{98.5}$). This meteorite is very similar to A-881757 and MIL 05035 in their bulk rock low-Ti compositions and extremely low Mg# (Yanai and Kojima 1991; Fukuoka 1992; Koeberl et al. 1993; Warren and Kallemeyn 1993). In terms of bulk-rock REE concentration levels, this meteorite is similar to low-Ti mare basalts but based on Tb/Lu ratios it is more similar to VLT mare basalts (Warren and Kallemeyn 1993).

The crystallization age of Y-793169 is estimated to be 3.811 ± 0.098 Ga. It also has higher amount of cosmic-ray implanted elements compared to A-881757 and MIL 05035. This suggests that Y-793169 has been crystallized from the near-surface under disequilibrium growth conditions (Fernandes et al. 2009).

5.2.1.3. Regolith breccia: Meteorite Hills 01210

Meteorite Hills (MET) 01210 is a polymict regolith breccia formed by lithic and mineral clasts within a glass matrix. Mineral and clasts are both mare and anorthositic (Arai et al. 2005; Righter and Bussey 2006). Lithic clasts in the sample are mostly coarse-grained VLT basalts and fine-grained granulite clasts. The coarse-grained basalts are formed by pyroxenes (Fs_{12-61} Wo_{3-39}) and plagioclase (An_{90-97}) with lower amounts of olivine (Fo_{37-76}). The granulitic clasts are highly feldspathic formed by >80 % modal plagioclase (An_{93-98}; Zeigler et al. 2005). The presence of coarse-grained gabbros and symplectites indicates an origin from deeper units. The fine-grained feldspathic clasts indicates an origin in highland material close to the launch place of this sample (Righter and Bussey 2006).

Studies of cosmogenic nuclides indicates an exposure age of 0.95 ± 0.13 Ma (^{10}Be) and 0.90 ± 0.18 M (^{36}Cl) and the ejection depth was >1000 g/cm^2 (>5 m, Nishiizumi et al. 2006).

MET 01210 is a regolith breccia, therefore, it represents the uppermost layer of the lunar crust, making this sample a better option to compare to the LP-GRS datasets to find the possible launch origin of the YAMM group (see Chapter 2).

The first results were obtained when the averaged analytical measurements of FeO, TiO_2 and Th ± 9 standard deviation was compared with the remote sensing dataset (Table 5.1). A couple of matches were found in Mare Fecunditatis, one match in Mare Crisium and one pixel was found in Mare Serenitatis (Figure 5.2). The three areas contain low TiO_2 according to the LP data and they are consistent with the VLT nature observed in the basaltic meteorites of YAMM as well as the basaltic clasts within the MET 01210 regolith breccia. Bulk trace incompatible elements and REE in A 881757 resembles the patterns observed in Luna 24 VLT basalts recovered from Mare Crisium.

Ages obtained by crater degradation and size-frequency distribution data indicates that most of the lava flows that formed the maria, were extruded in a period between 3.3-3.8 Ga (Hiesinger et al. 2003, 2011). This is consistent with the crystallization ages obtained for the meteorite Y-793269, A-881757 and MIL 05035. Ages observed in Mare Fecunditatis (3.2-3.65 Ga) and Crisium (2.5-3.65 Ga) appear to be younger than those obtained in the meteorites (~3.8 Ga) but it is within the range observed for Mare Serenitatis (2.94-3.81 Ga). However, it is important to bear in mind that numbers of mare basalts with ages over 3.8 Ga could be covered by younger basalts (Hiesinger et al. 2011).

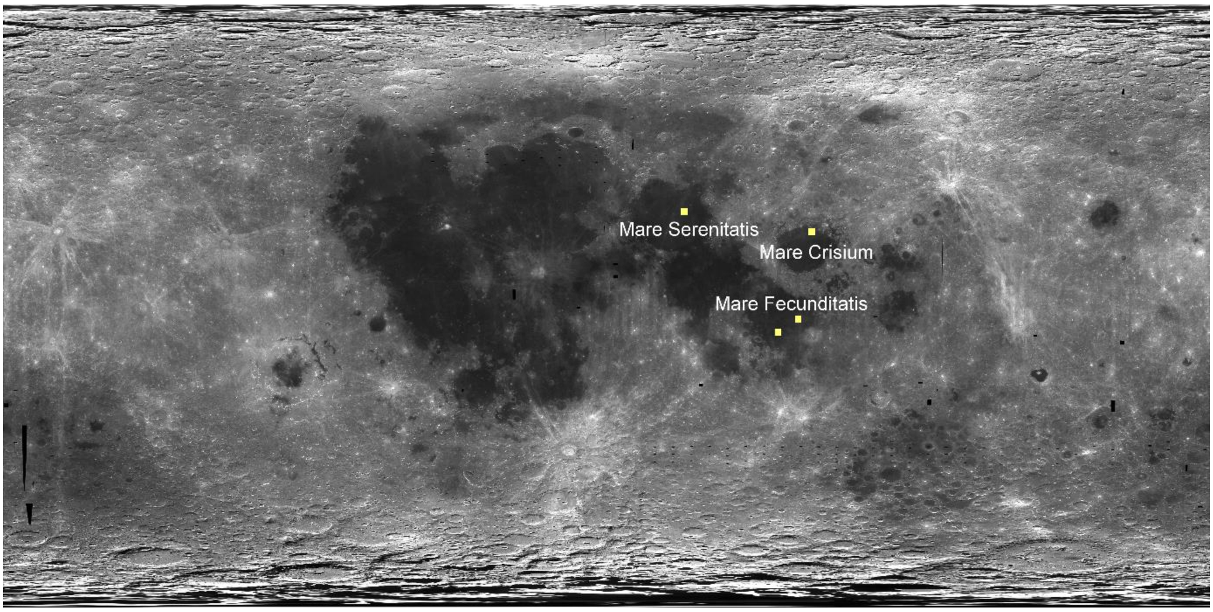

Figure 5.2 Identification of lunar regolith with similarities in composition to the regolith breccia MET 01210 ± 9σ standard deviation for each FeO, TiO_2 and Th bulk rock compositions (yellow).

5.2.2. LaPaz Icefield Group

Meteorites from the LaPaz Icefield (LAP) Group are considered to be launch-paired, based on their whole-rock, mineralogy, age and texture (Righter et al. 2005; Day et al. 2006; Day and Taylor 2007). LAP Group and NWA 032/479 petrography and crystal size distribution (CSD) show different cooling histories, accumulation and fractionation. $^{147}Sm/^{144}Nd$ indicates similar, but different source material, so it is possible that they derive from different lava flows from the same volcanic complex (Elardo et al. 2014).

LAP 02205, 02224, 02226, 02436, 03632 and 04841, are a group of coarse-grained, holocrystalline, low-Ti basalts (3.1 wt.% TiO_2). They are formed of pyroxenes, plagioclases, minor amounts of ilmenite, spinel and large sparse crystals of olivine in a groundmass of fayalite and cristobalite (Zeigler et al. 2005; Righter et al. 2005; Anand et al. 2006; Joy et al. 2006).

The pyroxenes are large grains up to 1 mm, strongly zoned from augite to pigeonite cores to rims highly enriched in Fe and show substantial variations among samples (LAP 02205 En_{0-58} Fs_{21-90} Wo_{9-41}; LAP 02224 En_{1-59} Fs_{23-86} Wo_{8-39}; LAP 02226 En_{0-55} Fs_{22-87} Wo_{8-40}). A small fraction of these crystals appear heavily fractured, showing mosaic extinction and some of them with parallel internal planar features (Joy et al. 2006). Plagioclase crystals vary compositionally from An_{89} in the cores to An_{85} in rims. Some of the plagioclase (20-30%) is maskelynitized (Righter et al. 2005; Joy et al. 2006). The most common opaque mineral in these meteorites is ilmenite followed by spinel. Ilmenite appears with lath-like to skeletal textures. They have lower MgO (0.02-0.24 wt.%) than ilmenite from other lunar basalts (1-9 wt.%; El Goresy et al. 1976; Righter et al. 2005) but are similar to Apollo 12 pigeonite and olivine basalts (Joy et al. 2006). Sparse large subhedral crystals of olivine (up to 300 μm in size) are observed within the group. These crystals have Fe compositions increasing towards the rims of the grains (Fo_{53-62} in the cores to Fo_{46-57} in the rims). Some olivines have melt inclusions (Righter et al. 2005). Melt veins with similar composition to the bulk rock cross the samples. This, together with the presence of maskelynite and cristobalite, indicates that the sample experienced shock pressures between 28 to 34 GPa (Righter et al. 2005; Zeigler et al. 2005).

^{40}Ar-^{39}Ar age dating suggests a crystallization age of 2.95 ± 0.02 Ga (Nyquist et al. 2005) and 2.92 ± 0.01 Ga (Fernandes et al. 2009) and based on cosmogenic radionuclides their ejection age is estimated to be 55 ± 5 Kyr (Nishiizumi et al. 2006).

The LAP group show similarities to Apollo 12 low-Ti, low-Al basalts. However, the group appears enriched in REE, and also exhibits different major element compositions and lower Mg# than the Apollo 12 samples. LAP is a product of fractional crystallization from a source enriched in Fe that experienced high fractionation with late-stage liquid immiscibility and REE enrichment (Joy et al. 2006). However, the geochemical characteristics could also be explained by a low-degree of partial melting or by melting of a late-stage LMO cumulate source (Borg et al. 2009; Elardo et al. 2014).

Results for the LAP group were obtained using bulk-rock data from Table 5.1 and the averaged measurements of all the meteorites were plotted together. The first results appeared using ± 4 standard deviations and, the matches are in two clearly different areas of the Moon: Mare Serenitatis and the western area of Oceanus Procellarum (Figure 5.3).

The ages of these meteorites (~2.9 Ga) are within the range of ages obtained in Oceanus Procellarum (1.20-3.93 Ga) and Mare Serenitatis (2.94-3.81 Ga; Hiesinger et al. 2003, 2011) but the aforementioned similarities with Apollo 12 basalts may indicate a relatively close origin. Furthermore, the REE enrichment observed in these meteorites compared to Apollo 12 basalts also suggest an origin within Oceanus Procellarum rather than in Mare Serenitatis. Joy et al. (2006) already has suggested an area within Procellarum as possible launch location for this sample, these results are consistent with that.

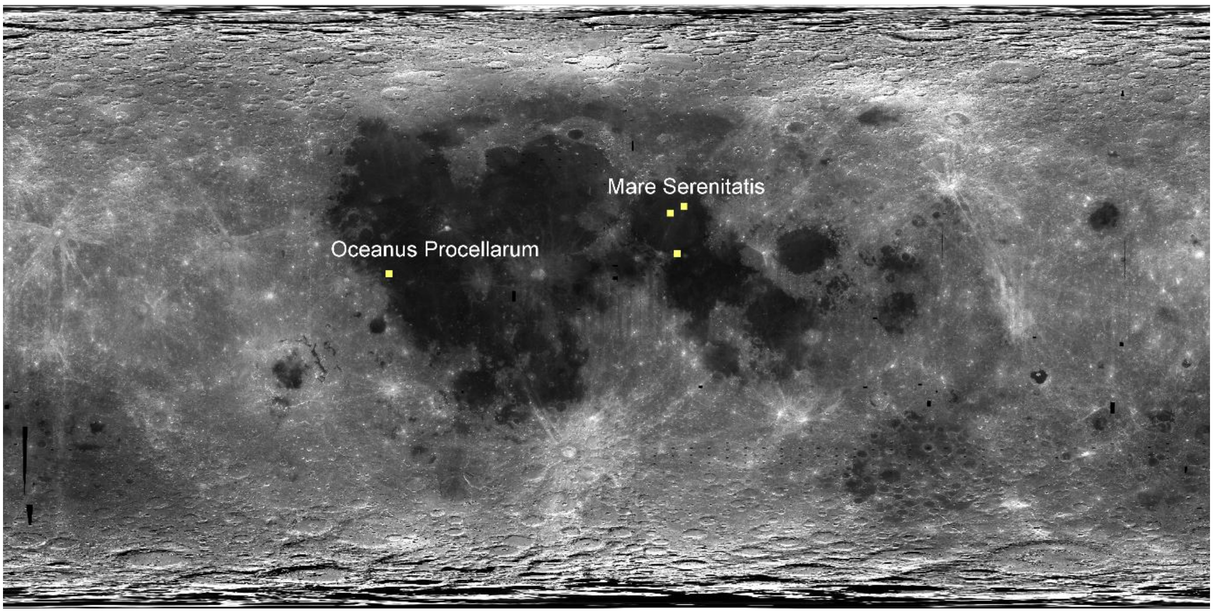

Figure 5.3 Identification of lunar regolith with similar compositions to LAP group ± 4σ standard deviation.

5.2.3. Northwest Africa 032

Northwest Africa 032 is a crystalline, very fine-grained, low-Ti (~3 wt.%) basaltic rock, formed of phenocrysts of olivine, pyroxene and spinel, in a groundmass of plagioclase, zoned pyroxene, ilmenite, troilite and traces of FeNi metal (Borg et al. 2009). Olivine phenocrysts are zoned, from Fo_{65} in the cores to Fo_{60} and surrounded by a Fe-rich quenched margin (~Fo_{30}). Pyroxenes phenocrysts are also zoned (En_{40-50} Wo_{20-40} and En_{15-25} Wo_{10-20}) and they are also surrounded by Fe-rich margins (En_{5-25} Wo_{15-30}; Fagan et al. 2002; Elardo et al. 2014). The groundmass is formed by zoned pyroxenes (En_{1-25} Wo_{15-25}) and plagioclase (An_{80-90}) crystals. Opaque phases also occur as elongated and skeletal ilmenite, troilite and FeNi metal (Fagan et al. 2000, 2002). Shock melt veins, maskelynite, the undulatory extinction in olivine and pyroxenes crystals and fracturation within phenocrysts and groundmass indicate shock pressure however, the scarcity of these effects suggests that probably they were created by the impact event that eject the sample from the lunar surface (Fagan et al. 2002).

^{40}Ar-^{39}Ar measurements indicate a crystallization age of 2.78 ± 0.01 Ga (Fagan et al. 2002; Fernandes et al. 2003) and cosmogenic radionuclide data shows an ejection age of 47 ± 10 Kyr (Nishiizumi and Caffee 2001).

Bulk rock TiO_2, Al_2O_3 and K_2O in NWA 032 are similar to those reported for Apollo 12 and Apollo 15 basalts but enriched in REE and high Th/Sm. This meteorite could have formed from a plagioclase-free source that have experienced high degrees of partial melting (Borg et al. 2009).

The results obtained using FeO, TiO_2 and Th bulk rock compositions ± 4σ standard deviation (Table 5.1) show a couple of matches in the western lava flows of the central Oceanus Procellarum, one match in Mare Serenitatis and another in Mare Imbrium (Figure 5.4).

The age of the meteorite is younger that the range of ages obtained for Serenitatis (2.94-3.91 Ga; Hiesinger et al. 2003) suggests than this mare probably is not the source for NWA 032. However, it could be derived from Oceanus Procellarum (1.20-3.93 Ga) and Mare Imbrium (2.01-3.57 Ga, Hiesinger et al. 2000) both of them spanning a wider range of lava flow ages

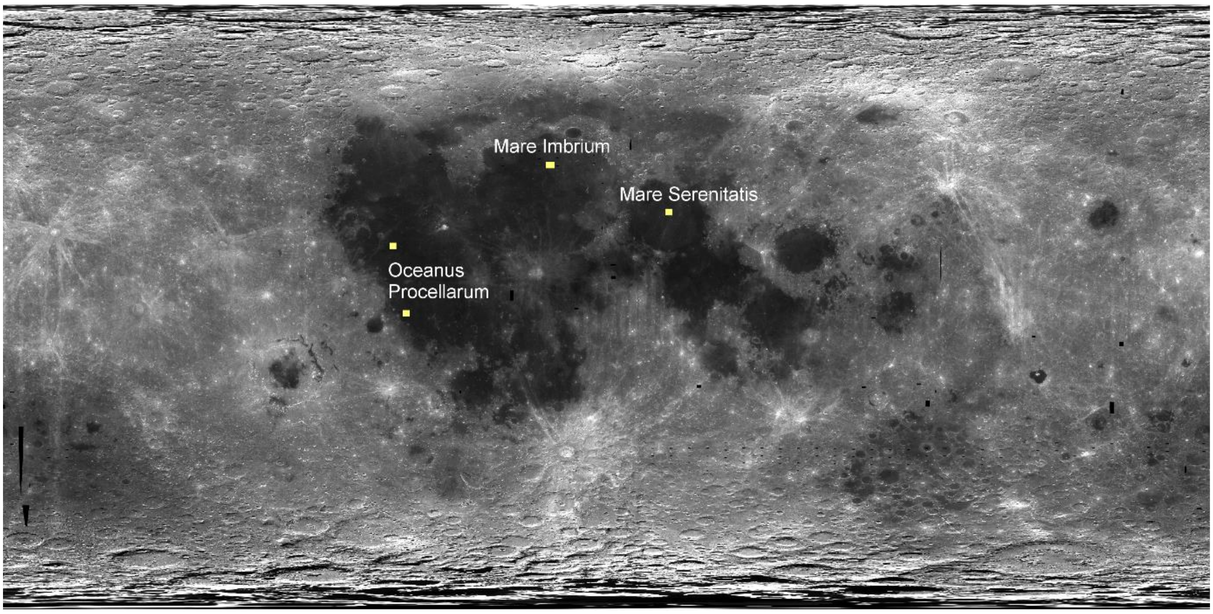

Figure 5.4 Image showing areas from the lunar surface where the regolith composition measurements match the analytical composition of crystalline basalt NWA 032 ± 3σ standard deviation.

5.2.4. Northwest Africa 4898

Northwest Africa (NWA) 4898 is an intergranular, fine-grained basalt with large euhedral to subhedral olivine grains set into a groundmass formed by zoned clinopyroxenes, maskelynite laths, needle-shaped ilmenite, Ti-rich chromite, occasional troilite and FeNi metal (Greshake et al. 2008).

Olivine crystals are zoned, from Fe-poor cores (Fa_{26}) to Fe-rich rims (Fa_{44}). Often, these olivines have chromite and melt inclusions. Sometimes, the crystals form clusters with glomerophyric appearances. Clinopyroxenes are subhedral to prismatic and are both pigeonite (Fs_{25-45} Wo_{10-20}) and augite (Fs_{25-59} Wo_{20-38}). Plagioclase grains appears as laths or blocky crystals and appear completely transformed into maskelynite of $An_{92-96.5}$ composition. Sprays of clinopyroxenes and plagioclases cause spherulitic appearances in some areas (Greshake et al. 2008). Rb-Sr and ^{40}Ar-^{39}Ar radiometric systems give crystallization ages of 3.58 ± 0.040 Ga (Gaffney et al. 2008; Fernandes et al. 2009).

Bulk chemistry of NWA 4898 is similar to that of Apollo 14 and Luna 16 high-alumina basalts, however, Mg# indicates that NWA 4898 is more evolved (Heiken et al. 1991; Greshake et al. 2008). The rock possibly derives from a mantle already depleted of incompatible elements, indicating the presence of a previously unidentified lunar mantle source (Gaffney et al. 2008). Probably this sample crystallized in a thick lava flow or a shallow magma chamber. The spherulitic texture was formed during the cooling when the residual melt came in contact with colder neighbouring rocks (Greshake et al. 2008).

The results based on bulk rock FeO, TiO_2 and Th ± 8 standard deviation (Table 5.1) show Mare Serenitatis and Mare Fecunditatis as possible source regions for this sample (Figure 5.5). Ages obtained by crater size-frequency measurements for Mare Fecunditatis show lava flows between 3.2 and 3.71 Ga (Hiesinger et al. 2006, 2011), and for Mare Serenitatis are between 2.94-3.81 Ga (Hiesinger et al. 2003), that does not appear to be very helpful to discriminate among the two possible origins. However, the incompatible elements depletion reported in the meteorites could indicate that NWA 4898 was launched from an area far from the PKT. From the two possibilities, I suggest Mare Fecunditatis as origin both because of the ages reported and the largest distance to PKT.

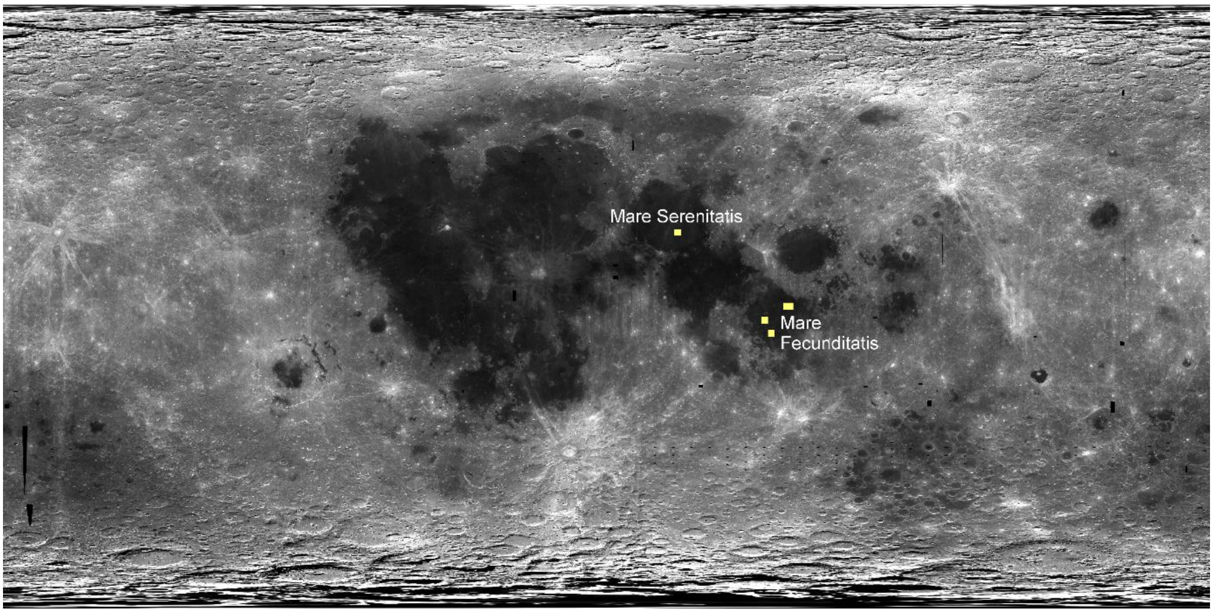

Figure 5.5 Identification of lunar regolith with similar compositions to NWA 4898 ± 8σ standard deviation.

5.2.5. Northwest Africa 003

Northeast Africa (NEA) 003 is a meteorite composed by two portions: an unbrecciated coarse-grained low-Ti olivine-rich basalt (~75% modal volume), and a basaltic breccia with glassy impact melt matrix. The contact between both portions is very sharp (Haloda et al. 2006a).

The main portion has olivine with porphyric texture and compositions Fo_{19-73}, zoned pyroxenes (En_{5-71} Wo_{6-38}) and plagioclase (An_{84-92}) with mesostasis of Fe-rich pyroxene, plagioclase, silica, ilmenite, troilite and apatite. Opaques include spinel (chromite, Ti-rich chromite and ulvöspinel), troilite, whitlockite, and traces of FeNi metal. Plagioclase crystals appear maskelynitized (Haloda et al. 2006a).

The bulk rock MgO abundance is one of the highest and the bulk rock TiO_2 one of the lowest of all the samples in the lunar meteoritic collection. This portion also exhibits one of the lowest and flattest chondrite-normalised REE pattern, it is not depleted in LREE and with a slightly Eu negative anomaly, indicating a primitive character of the parental magma (Korotev 2005; Haloda et al. 2006, 2009).

The basaltic breccia portion consists of two basalt clasts surrounded by a glassy impact melt matrix. The basaltic clasts consist in low-Ti olivine mare basalt with porphyritic texture of olivine (Fo_{32-71}), zoned pyroxene (En_{6-57} Wo_{9-41}) and plagioclase (An_{85-94}) converted into maskelynite. In one of the clasts the mesostasis is formed by Fe-rich pyroxene and piroxferroite, silica, plagioclase, ilmenite, troilite, apatite, fayalitic olivine and glass, suggesting a late-stage mesostasis. In the second clast, the mesostasis is formed by Fe-rich pyroxene, silica, plagioclase, ilmenite and troilite (Haloda et al. 2006b).

^{40}Ar-^{39}Ar dating reveals a crystallization age for the basaltic portion of the sample, of 2.38 ± 0.04 Ga (Fernandes et al. 2007). Sm-Nd, however, gives an older age of 3.09 ± 0.06 Ga suggesting that the ^{40}Ar-^{39}Ar system could represent a resetting event (Haloda et al. 2009). The exposure age based in cosmogenic Ar is 179 ± 5 Ma (Fernandes et al. 2007).

The averaged bulk-rock FeO, TiO_2 and Th abundances ± 7 standard deviation, of the bulk rock breccia portion was used to investigate its launch site (Table 5.1). Two possible locations were obtained for NEA 003: Mare Crisium and Mare Fecunditatis (Figure 5.6).

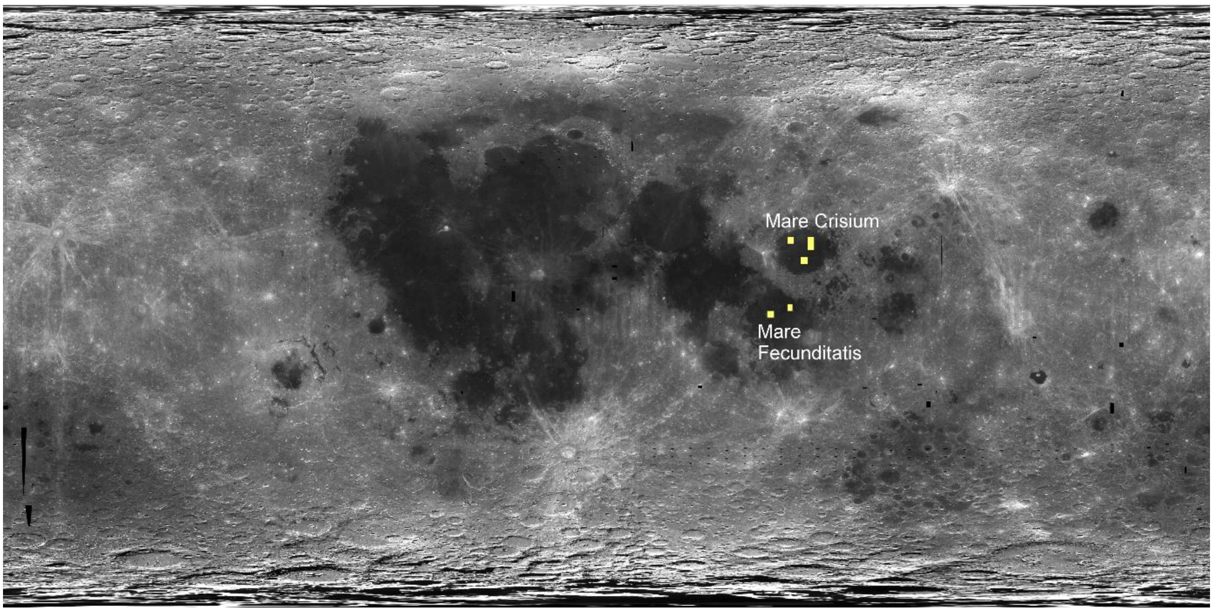

Figure 5.6 Image showing areas where surface regolith compositions match the bulk-rock analytical composition of NEA 003 ± 7σ standard deviation.

The crystallization age of the main clast (~3.09 Ga) of the sample is younger than the ages of most of the lava flows within Mare Fecunditatis (3.2-3.71 Ga; Hiesinger et al. 2006). Crater degradation and size-frequency distribution for Mare Crisium does exhibit units with ages ranging from 2.5 to 3.6 Ga Hiesinger et al. 2011). Also, the ages are in good concordance with crystallization ages (~2.52-3.45 Ga; Fernandes and Burgess 2005) as well as the low-Ti compositions observed in Luna 24 basalts (Head et al. 1978). However, REE abundances in

Luna 24 basalts show that they derive from a fractionated source (Ma et al. 1978), in contrast to the primitive character of the meteorite ruling out that Luna 24 and NEA 003 derives from the same source. This does not invalidate Mare Crisium as possible launch origin but it could indicate different basalt sources within the region.

5.2.6. Dhofar 287

Dhofar (Dho) 287 is a crystalline basalt with a minor portion of regolith breccia attached to it with a sharp contact between them. This sample could be interpreted as being a regolith breccia with a very large basaltic clast.

The crystalline basalt portion is formed by phenocrysts of pyroxene, maskelynite, olivine, and opaque minerals in late-stage mesostasis (Anand et al. 2003). Pyroxene shows elongated shapes and occur as phenocrysts (>0.5 mm) and within the groundmass. The crystals exhibit the typical mare basalt fractionation trend with high variations in Mg-Fe-Ca contents. All the plagioclase in the basalt is transformed into maskelynite suggesting pressures ~30 GPa (Stöffler et al. 1991). Olivine crystals appear as phenocrysts with sizes varying between 1-2 mm, some of them with asymmetrical compositional zoning with extreme iron enrichment (up to Fo_{40}) close to the rims. The most common opaque crystal is lath-shaped ilmenite with lamellar structures, followed by Al-rich chromite with ulvöspinel in their rims (Anand et al. 2003).

The basaltic portion has a large content of late-stage metastasis (>3% modal area). It contains fayalite with two types of glass blebs. These glasses are different both in size as in composition: Si-rich and K-rich. Also, it contains ilmenite, apatite and whitlockite (Anand et al. 2003). The bulk rock composition of this portion resembles that found in Apollo 12 and Apollo 15 low-Ti basalts although it would be required KREEP assimilation to account for its REE abundances (Anand et al. 2003).

The lunar regolith breccia portion is formed by lithic clasts and mineral fragments inside a fine-grained matrix with minor impact melt. Lithic clasts are crystalline rocks, vitrophyric rocks and impact melt breccias and vary in size from 0.1 to 3.2 mm. Crystalline rocks are low-Ti, VLT and picritic composition. Mineral grains range from 0.1 to 1 mm in size and are mainly pyroxene, olivine and plagioclase (An_{66-98}) completely converted into maskelynite. Traces of chromite, ilmenite, apatite, silica, troilite and Fe-Ni metal are also observed (Demidova et al. 2003). There could be lithologies from two distinct basaltic melts in the breccia: A highlysaturated basalt with olivine and also includes picritic lithologies, the low-Ti, low-Na glasses and the main basaltic clast. The second type is a basaltic melt very close to co-saturation with olivine, plagioclase and pyroxene. This includes the VLT and the low-Ti, high-Na basaltic lithologies (Demidova et al. 2003). The presence of maskelynite, lamellar structure in pyroxenes, fractures in pyroxenes and olivines as well as impact melt veins, indicate that the sample underwent shock processes of about ~30 GPa (Stöffler et al. 1991; Anand et al. 2003; Demidova et al. 2003).

The Sm-Nd system yields a crystallization age of 3.46 ± 0.03 Ga that lies within the range of the Apollo 15 low-Ti mare basalts (Shih et al. 2002).

Investigation of the provenance of this meteorite is quite difficult because of its heterogeneity. As it was mentioned in Chapter 2, regolith breccias are more adequate when using this approach, so the bulk-rock FeO and TiO_2 composition of the regolith breccia portion ± 2 standard deviation, was introduced into the software (Table 5.1). The results obtained cover most of the mare areas of the nearside (Figure 5.7). Th bulk rock abundance was not included because the lack of measurements of this element in the literature for the regolith breccia component. The inclusion of Th would allow to discriminate a possible origin within the Oceanus Procellarum.

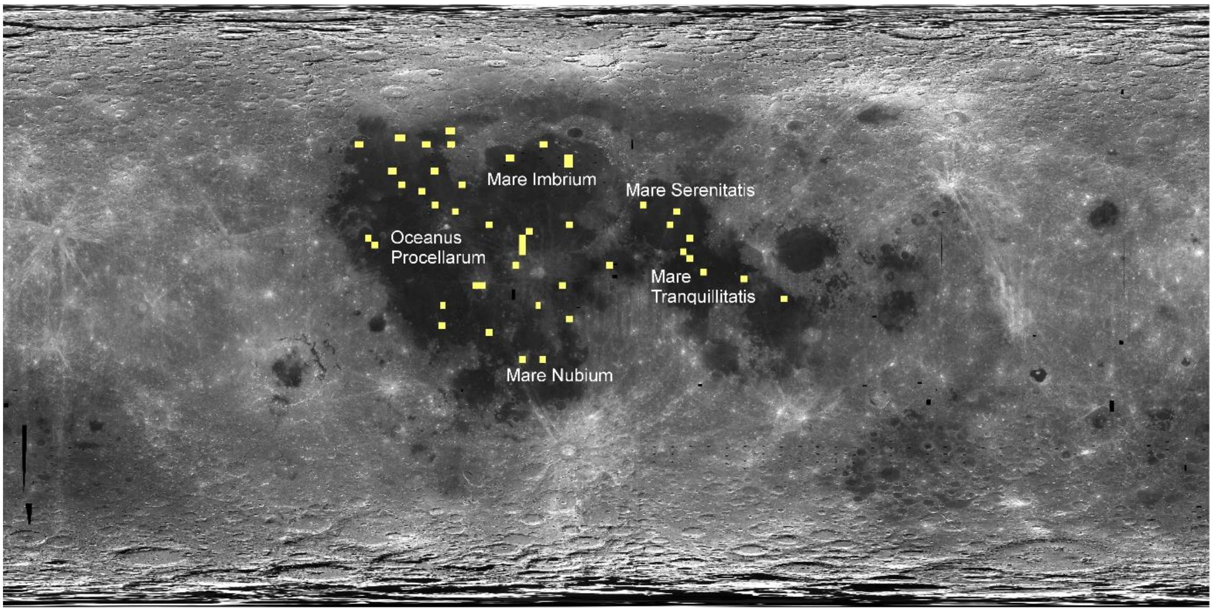

Figure 5.7 Identification of lunar regolith with similar bulk rock FeO and TiO_2 compositions to the regolith breccia component of Dho 287 ± 2σ standard deviation.

The age of the sample represents a period of extensive volcanism in the Moon. I have compared these results to the ages obtained by crater degradation and size-frequency analysis (Hiesinger et al. 2000) to discriminate some areas which ages does not coincide with the age of the sample (Figure 5.8). Ages of western Oceanus Procellarum, Mare Imbrium and Serenitatis in the Hiesinger map match the ages measured in the Dho 287 meteorite. Areas from Mare Tranquillitatis appears to be older than the ages reported in the meteorites, on the opposite side, some eastern areas of Oceanus Procellarum with ages < 2.0 Ga seems to be too young to be related to this sample. This comparison between the reported age and the Hiesinger et al. 2000 work suggests that areas of Oceanus Procellarum, Mare Imbrium and Serenitatis appear as possible launch origins for the meteorite.

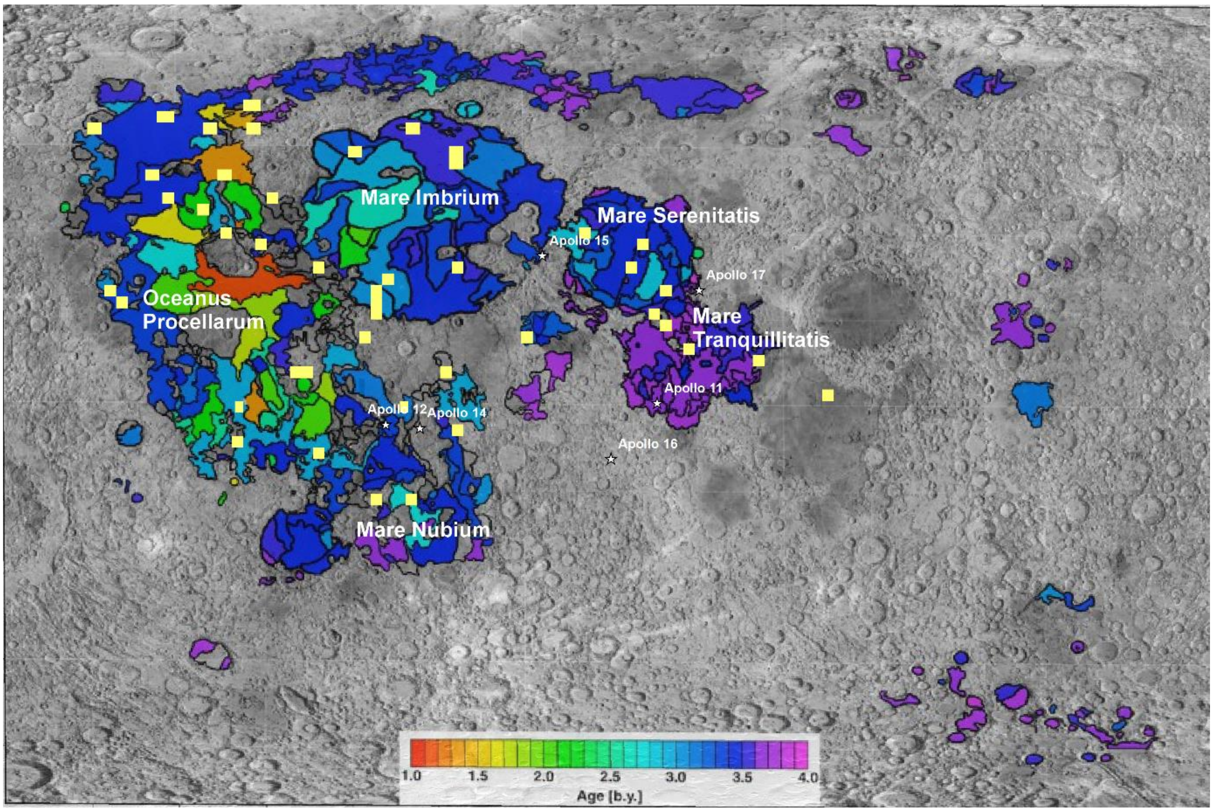

Figure 5.8 Lunar regolith with similar bulk rock FeO and TiO_2 compositions to the regolith breccia component of Dho 287 ± 2σ standard deviation overlying a Clementine albedo map with lava flows and their ages as studied by Hiesinger et al. 2000.

5.3. Brecciated Basalts

In this section, I discuss brecciated meteorites that are predominantly basaltic in composition (>11 wt.% FeO), although some of them contain clasts of other lithologies, including some feldspathic material. I include in this section also the feldspathic meteorite Kalahari 008 because of its relationship with the basaltic breccia Kalahari 009, and the interest that these have for understanding the earliest period of lunar magmatism.

5.3.1. YQN group and Elephant Moraine 87521/96008 pair

The YQN Group is formed by Queen Alexandra Range (QUE) 94281, Yamato (Y) 793274/981031 and Northwest Africa (NWA) 4884 (Arai and Warren 1999). These meteorites appear to be grouped on the basis of their similar bulk rock composition and petrology. It is also suspected that the meteorite Elephant Moraine 87521/9608 could be a launch paired stone to the group based on general compositional and mineralogical similarities (Warren and Kallemeyn 1989; Jolliff et al. 1998; Warren and Ulff-Møller 1999; Arai and Warren 1999; Korotev et al. 2003).

5.3.1.1.Queen Alexandra Range 94281

Queen Alexandra Range (QUE) 94281 is an immature, basaltic, regolith breccia with irregular shape. It has a heterogeneous texture, with chaotic aphanitic material in the middle, a clast-rich breccia (up to 3 mm), and a vesicular glass vein (Jolliff et al. 1998). The breccia contains mineral grains (e.g. coarse-grained pyroxene and plagioclase), glass and lithic clasts, in a glassy matrix. Components include mafic clastic materials probably from mare lithologies as well as impact melt breccias (1-2 mm of size) and feldspathic glasses from the highlands. This may be an indication of a possible source within the mare-highlands boundary (Jolliff et al. 1998). Clasts possibly deriving from mare lithologies include coarse-grained clasts with laths of plagioclase (An_{90-94}) and anhedral pyroxenes (En_{29-48} Wo_{6-35}) and very low Ti# (~57 mol %). Volcanic ferroan glass clasts are also found in this meteorite. Both the gabbroic and the glassy clasts show VLT affinities (Arai et al. 1996; Arai and Warren 1999). Anorthositic clasts include fine-grained impact melt with Al_2O_3 contents >28 wt.% and quite high TiO_2 (1.5 wt.%) compared to typical highland bulk-rock composition. Plagioclases grains show compositions of An_{89-98}, pyroxenes are ~En_{61} Wo_{10} and their olivine compositions are Fa_{32-37} (Arai and Warren 1999).

The substantial amount of highland materials of high FeO concentrations of this meteorites differs from regolith from the Apollo sites. The coarse-grained clasts are similar to those of

VLT basalts and the volcanic glass composition suggest that they can be derived from a common picritic parent composition (Jolliff et al. 1998).

Studies on cosmogenic radionuclides show that the material was exposed to the cosmic rays in the lunar surface ~400 ± 60 Ma, and ejected between 0.15 and 0.45 Ma to Earth (Nishiizumi et al. 1996; Polnau and Eugster 1998).

5.3.1.2.Yamato 793274/981031

Yamato (Y-) 793274/981031 are paired immature regolith breccias, consisting of clast-rich breccia. Lithic clasts include anorthositic, gabbroic rocks, impact melt rocks and fine-grained granulites. These clasts are in a matrix formed by mineral grains of large size, including clinopyroxene, Ca-rich plagioclase (An_{88-99}), olivine (Fo_{46-72}) and ilmenite. Rare glass spherules are present (Takeda et al. 1990; Koeberl et al. 1991).

Major and trace element analyses show similarities to other basaltic lunar meteorites and VLT mare basalts. However, different analysis by several authors indicate that this meteorite is highly heterogeneous (Fukuoka 1990; Koeberl et al. 1991; Warren and Kallemeyn 1991; Lindstrom et al. 1991). Compared to other meteorites, Y-793274 has slightly higher bulk-rock Al_2O_3 content (12-17 wt.%) than basaltic meteorites (11-13 wt.%) but much lower than that observed in anorthositic meteorites (25-30 wt.%). FeO bulk-rock content (12-17 wt.%) is also between the basaltic (19-21 wt.%) and the anorthositic meteorites (4-6 wt.%). REE abundances are high and the pattern is similar to the KREEP pattern and distinct from REE-poor anorthositic lunar meteorites (Lindstrom et al. 1991).

Y-793274 contains high abundance of solar wind gases and cosmic-ray produced nuclei suggesting it is mature regolith material exposed to the lunar surface. ^{40}Ar-^{39}Ar indicates the breccia was formed 500-1000 Ma ago. Most of the exposure to the cosmic rays took place before the breccia formation and it lasted for 700 ± 200 Ma (Eugster et al. 1992).

5.3.1.3.Northwest Africa 4884

Northwest Africa (NWA) is a regolith basalt-rich breccia formed by lithic and mineral clasts in a vesicular and glassy matrix. Lithic clasts are formed by coarse-grained mare basalts and dunitic or troctolitic rock, and a large breccia within a breccia clast. Mineral fragments include calcic plagioclase, clinopyroxene, Ti-chromite, ilmenite and silica polymorph. This rock appear to be a mixture of FHT material and VLT basalts in a proportion of 2:3, with no KREEP component (Korotev et al. 2009).

5.3.1.4.Elephant Moraine 87521/98008

Elephant Moraine (ETT) 87521 (and paired stone 96008) is a VLT basaltic breccia with lithic clasts and crystals of pyroxene, feldspar, olivine and ilmenite. Traces of chromite, spinel, silica, FeNi metal and glass with similar composition to the bulk-rock are also present. The pyroxene is iron-rich pigeonite, subcalcic augite and augite with compositional ranges from En_{65} Wo_{5-10} to En_{20} Wo_{15-40}. Most feldspar is plagioclase with composition from An_{93} to An_{97}, but some sodic feldspar is present. Olivine shows bimodal compositions with Fo_{5-15} and Fo_{57-65} (Delaney 1989). Mafic lithic clasts are VLT, coarse-grained compared to mare basalts and resemble samples from Apollo 17 or Luna 24 sites. There are also fined-grained feldspathic impact-melt breccia with metal probably a meteoritic component (Delaney 1989; Warren and Kallemeyn 1989; Anand et al. 2003; Korotev et al. 2003; Warren et al. 2005).

Age studies suggest that the basalt crystallized 3.53 Ga ± 110 Ma ago (Terada et al. 2005). The material was exposed to cosmogenic and trapped noble gas in the lunar surface about ~500 Ma (Eugster et al. 1996). The fragmental breccia portion indicates an impact event 631 ± 20 Ma ago (Fernandes et al. 2009).

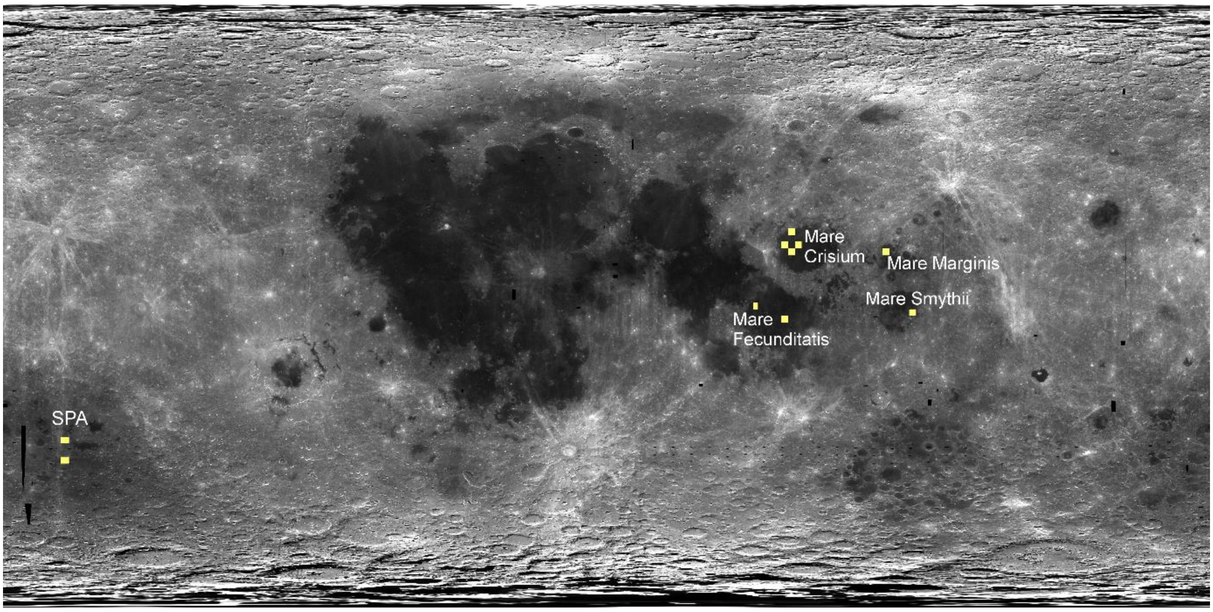

Figure 5.9 Identification of lunar regolith with similar compositions to YQN Group and EET87521/96008 ± 2σ standard deviation.

I assume that the composition of the source location is an average from the composition of all the grouped meteorites. I investigated the matches when all the meteorites are averaged to take all the compositions into account. I calculated the average FeO, TiO_2 and Th bulk-rock compositions and standard deviations of averaged measurements (Table 5.1). Most of the results show Mare Crisium as a possible source for this meteorite, with two pixels in Mare Fecunditatis, another two in SPA, and one pixel in Mare Marginis and Smythii (Figure 5.9). The VLT nature of the meteorites agrees with the VLT nature of the Luna 24 samples studied from Mare Crisium.

Age analysis of the basaltic clasts have shown a crystallization age of 2.65 Ga ± 0.086 that is significantly younger than the Imbrian lava flows in Mare Fecunditatis, Marginis and Smythii (Hiesinger et al. 2011). But, the younger lava flows at Mare Crisium (~2.7 Ga; Hiesinger et al. 2011), are within the error of the basaltic clasts ages in ETT 97521.

5.3.2. Northwest Africa 773

Northwest Africa (NWA) 773 has two different lithologies: a two-pyroxene olivine gabbro and a regolith breccia. The gabbro has a cumulate texture and is formed by olivine, clinopyroxene, feldspar, troilite, chromite and Fe-metal (probably from a meteoritic origin). The regolith breccia part is dominated by fragments of the cumulate portion, silica glass, pyroxene, volcanic rocks and fayalitic clasts, K-rich feldspar, silica and plagioclase (Fagan et al. 2003).

The olivine in the olivine gabbro has compositions between Fo_{64} and Fo_{70}. Clinopyroxenes are both pigeonite (En_{60-67} Fs_{24-27} Wo_{6-16}) and augite (En_{47-50} Fs_{13-17} Wo_{33-40}). Plagioclase compositions range between An_{80} and An_{94} and there are minor K-feldspar grains with An_3 Ab_4 Or_{93} composition. Olivine and pyroxenes in the regolith breccia have slightly higher compositional variation indicating a Fe-enrichment that led to the crystallization of symplectites of fayalite, silica and hedenbergite. Both lithologies have major element composition similar to VLT volcanic compositions but it also shows a LREE enrichment and a significant depletion in Eu. The REE pattern is similar to KREEP-like rocks but at lower abundances (Fagan et al. 2003; Jolliff et al. 2003).

The parent melt from where the olivine gabbro seems to derive could be similar to the Apollo 14 VLT picritic glasses, generated at depths ~400 km, and mixed with a KREEP component in the upper mantle. The differentiation and solidification of this magma in a shallow body could have produced other more chemically evolved components that were incorporated into the overlying regolith (Jolliff et al. 2003).

^{207}Pb-^{206}Pb analyses suggest similar ages for the two portions of this rock: 3.131 ± 0.032 Ga for the gabbro and 3.114 ± 0.32 Ga for the breccia (Shaulis et al. 2013).

FeO, TiO_2 and Th bulk-rock compositions ± 5σ standard deviations (Table 5.1) of the regolith breccia portion of the sample, were used to identify the possible launch locations of the regolith breccia portion. The results indicate several matches in mare-highlands boundaries (Serenitatis, Tranquillitatis, and Fecunditatis) and many of them fall within the SPA basin (Figure 5.10). Basalts from Tranquillitatis have a high-Ti nature (e.g. James and Jackson 1970; The Lunar Sample Preliminay Examination Team 1971; Walker et al. 1975) in contrast with the VLT of the meteorite so it is unlikely that this area or its vicinity is its launch origin. Crater degradation and cater size-distribution studies indicates that ages in Mare Fecunditatis (3.2-3.71 Ga) and basalts within SPA (3.2-3.8 Ga) are older than the ages reported for the sample (~3.1 Ga; Yingst and Head III 1999; Hiesinger et al. 2011; Shaulis et al. 2013). The possible source location for this sample could not be determined.

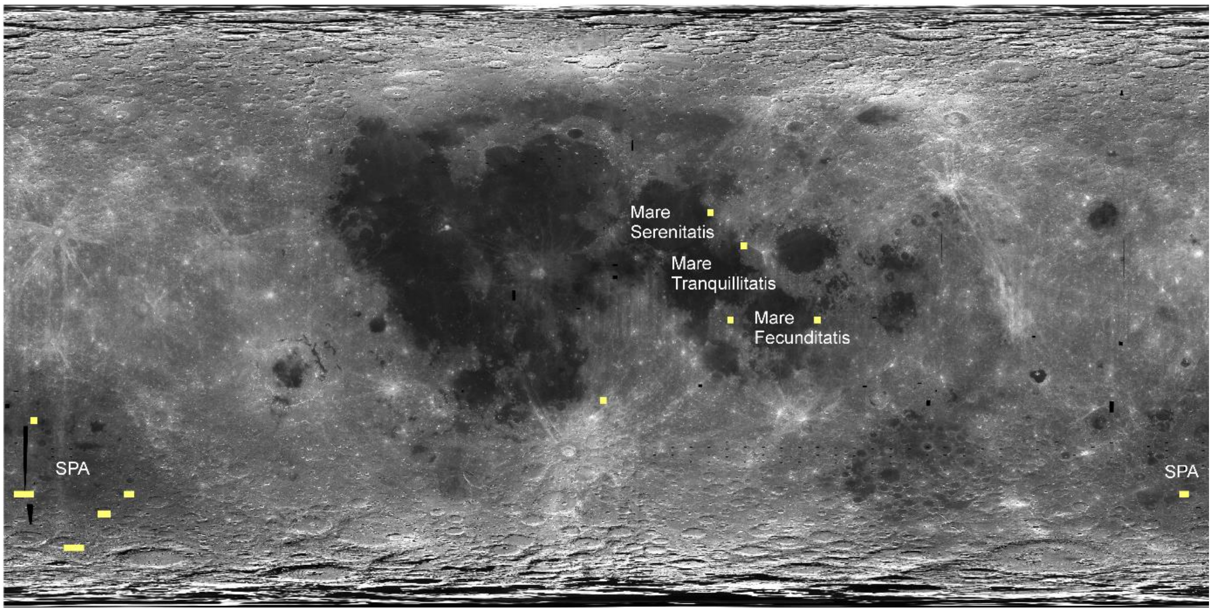

Figure 5.10 Identification of lunar regolith with similarities in composition to the regolith portion of NWA 773 ±5σ standard deviation.

5.3.3. Northwest Africa 3136

Northwest Africa (NWA 3136) is a polymict, clast-rich regolith breccia. It contains lithic and mineral clasts, glass and agglutinates from <1 µm to 1000 µm, in a fined-grain matrix (Kuehner et al. 2005; Korotev and Irving 2005; O'Donnell et al. 2008; Korotev et al. 2009). The lithic clasts are mostly VLT to low-Ti mare basalt, although one clast of high-Ti basalt has been reported (Korotev et al. 2009) and micrograbbro. Non-mare lithologies comprise olivine-bearing norite and gabbronorite, and orthopyroxene-olivine-bearing anorthosite (Kuehner et al. 2005). Impact-melt breccia of gabbronorite composition, feldspathic basalts, shocked anorthosite norite and shocked gabbronorite clasts were also reported (O'Donnell et al. 2008). High-feldspathic material is uncommon (Korotev et al. 2009). It has not been reported ages for this meteorite.

The bulk rock FeO, TiO_2 and Th compositions (Table 5.1) ± 4 standard deviation were used to investigate the possible launch region of this regolith. The results are localised in the southeast area of Mare Fecunditatis (Figure 5.11) that is consistent with the VLT to low-Ti basalt clasts reported (Kuehner et al. 2005). The proximity of Mare Tranquillitatis could account for the presence of basaltic clast of high-Ti affinity.

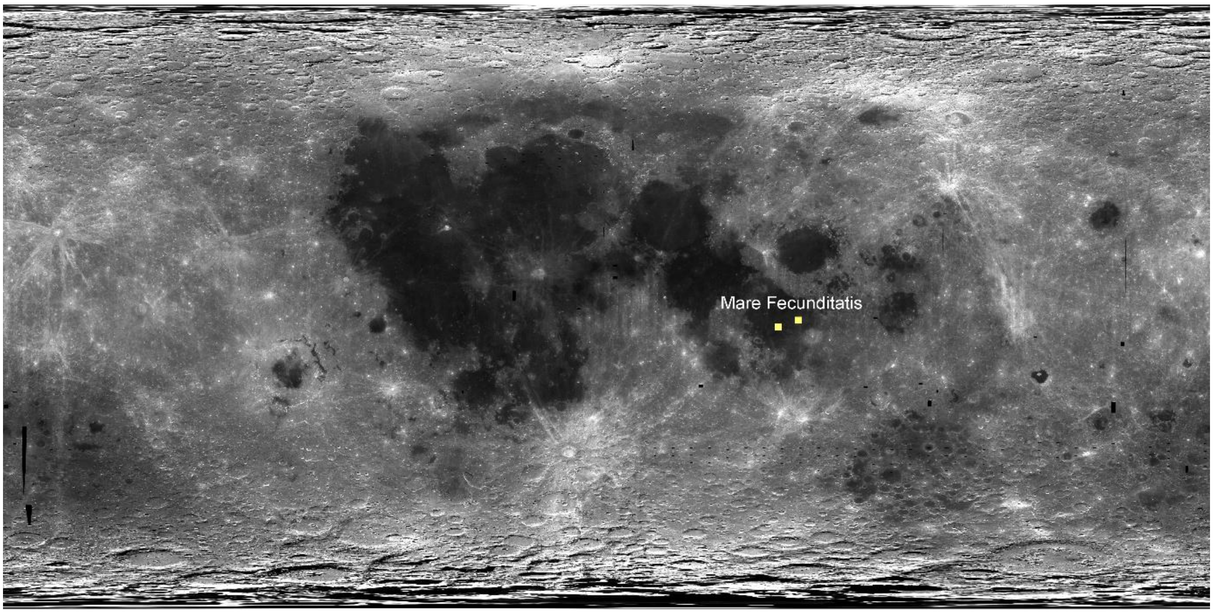

Figure 5.11 Image showing regolith composition that matches the composition of the regolith breccia NWA 3136 ± 4σ standard deviation.

5.3.4. Northwest Africa 5153

Northwest Africa (NWA 5153) is a fragmental breccia with clasts of highland lithologies (fragmented gabbro, troctolite, granophyric intergrowths of K-feldspar), mare basalts (ophitic pigeonite basalt and olivine basalt) and glasses of felsic nature (Korotev et al. 2009).

Olivine in gabbro is ~Fa_{32} and pigeonite has compositions of ~Wo_9 Fs_{26}. In troctolite clasts the olivine is slightly less ferric (~Fa_{22}) and Ca-pyroxene compositions are ~Wo_{14} Fs_{22}. Ophitic pigeonite basalts contains olivine of ~Fa_{37} and pigeonite with compositions of ~Wo_{13} Fs_7, these basalts also contained ilmenite (MgO ~5.2 wt.%). The basalts contains olivine (~Fa_{36}) and Ca-poor pyroxene with ~Wo_{13} Fs_{32} compositions (Korotev et al. 2009). Ages for this meteorite have not been reported.

Bulk-rock FeO, TiO_2 and Th compositions ± 2σ standard deviation (Table 5.1) of this meteorite matches regolith compositions measured in SPA and Endymion crater (Figure 5.12). It is not possible to constrain further the provenance of this meteorite with the limited information reported by the literature.

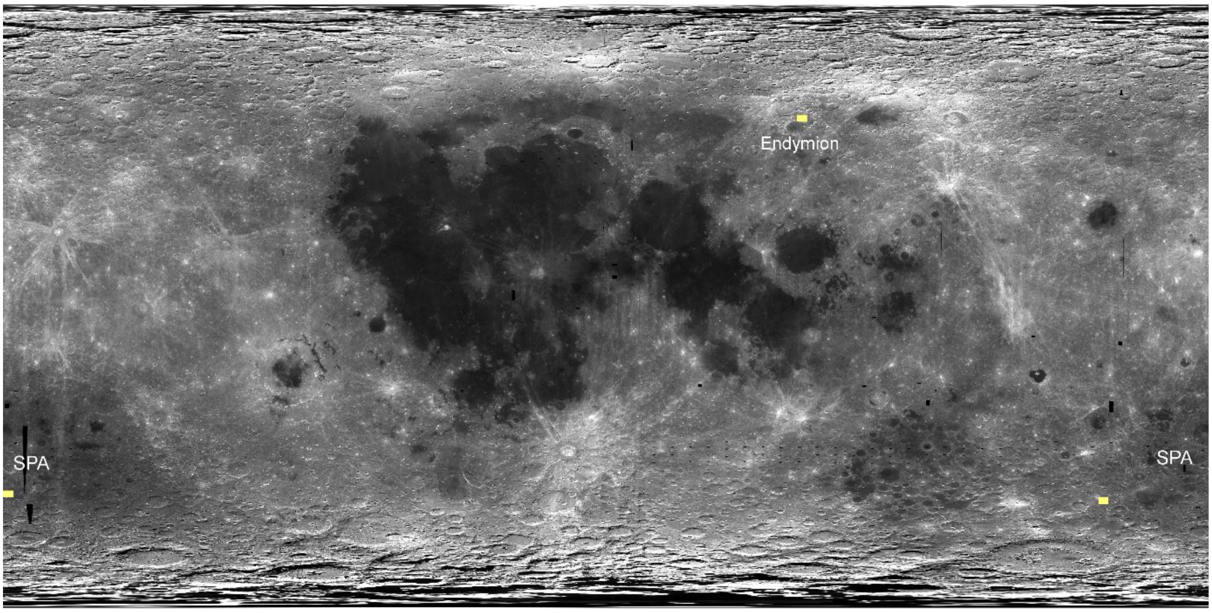

Figure 5.12 Identification of lunar regolith with similar compositions to fragmental breccia NWA 5153 ± 2σ standard deviation.

5.3.5. Kalahari 008/009

Kalahari 009 is a monomict fragmental breccia formed by clasts of basaltic lithologies in a fine-grained matrix. It has a low FeO content compared to other basalts (~16 wt.%; see Table 5.1). The clasts are basaltic, with sizes up 4 mm, and showing a coarse-grained subophitic texture. The matrix has similar composition and it is formed by fine to coarse-grained mineral debris and occasionally impact melt. The most common mineral both in clasts and in the matrix is pyroxene (pigeonite and augite with compositions from En_{22-67} Wo_{6-41} Fs_{22-67}) followed by plagioclase ($An_{>90}$) and to a minor extent, Fe-rich olivine ($Fa_{46-99.9}$). The main opaque grain is ilmenite appearing as rounded grains. Other accessories are chromite, troilite, Cr-rich spinel, baddeleyite, phosphates and Fe-Ni metal (Sokol and Bischoff 2005; Sokol et al. 2008).

Analysis of U-Pb in phosphates of Kalahari 009 has given a crystallization age of 4.35 ± 0.15 Ga. This is the oldest age of a basaltic lunar sample suggesting that this represents a cryptomare rock (Terada et al. 2008).

Kalahari 008 is an anorthositic breccia formed by mineral fragments and lithic clasts in a fine-grained clastic matrix. Plagioclase (An_{92-99}) is the most abundant mineral fragment with sizes reaching up to 1.5 mm. Pyroxene with wide range of compositions (En_{8-76} $Wo_{0.5-39}$ Fs_{14-77}) and olivine with a bimodal distribution (Fa_{42-72} and Fa_{78-98}), are also present. Lithic clasts are mostly impact melt breccias with crystalline to glassy matrix. These clasts are both feldspar-rich and mafic breccias with great variety of textures (from very fine-grained to microporphyric). Also some granulitic clasts and fragments of primary igneous clasts are present, they have plagioclase and different amounts of olivine, pyroxene and traces of Fe, Ti-oxides (Sokol et al. 2008).

Kalahari 008/009 exhibit petrographic evidence of impact-induced shock effects such as mosaicism and planar fracturing in feldspar and olivine. Some maskelynite transformation of plagioclase is observed. All consistent with shock pressures over 30-35 GPa (Stöffler et al. 1991; Sokol et al. 2008).

Despite their different nature, these samples are considered paired based on similar fayalite content in olivine, initial Hf isotope compositions, and the proximity of the locations where they were collected in Botswana. This could mean that the samples were originally launched as one rock and at some point during the Moon-Earth transfer or during Earth fall, it broke into two or more parts (Sokol et al. 2008).

I assumed that these meteorites represent a cryptomare basalt, covered by feldspathic ejecta. Cosmogenic radionuclides and noble gases are low in both meteorites, however Kalahari 008 has slightly higher concentrations than Kalahari 009, probably because the basaltic portion has never been exposed to the solar wind but at least some parts of the anorthositic portion have been exposed at the lunar surface prior to lithification (Sokol et al. 2008). If this is correct, the anorthositic clasts of Kalahari 008 could represent the highland rock covering Kalahari 009 and therefore, it is the most adequate to use this sample to determine their provenance. I plotted the bulk-rock FeO, TiO_2 and Th compositions ± 2 standard deviation for Kalahari 008. Two of the matches are in the Mendel-Rydberg cryptomare region, with only one match in the surroundings of Tycho crater (Figure 5.13). Mendel-Ryberg area is considered to be a cryptomare region covered by Orientale ejecta (Whitten and Head 2015a).

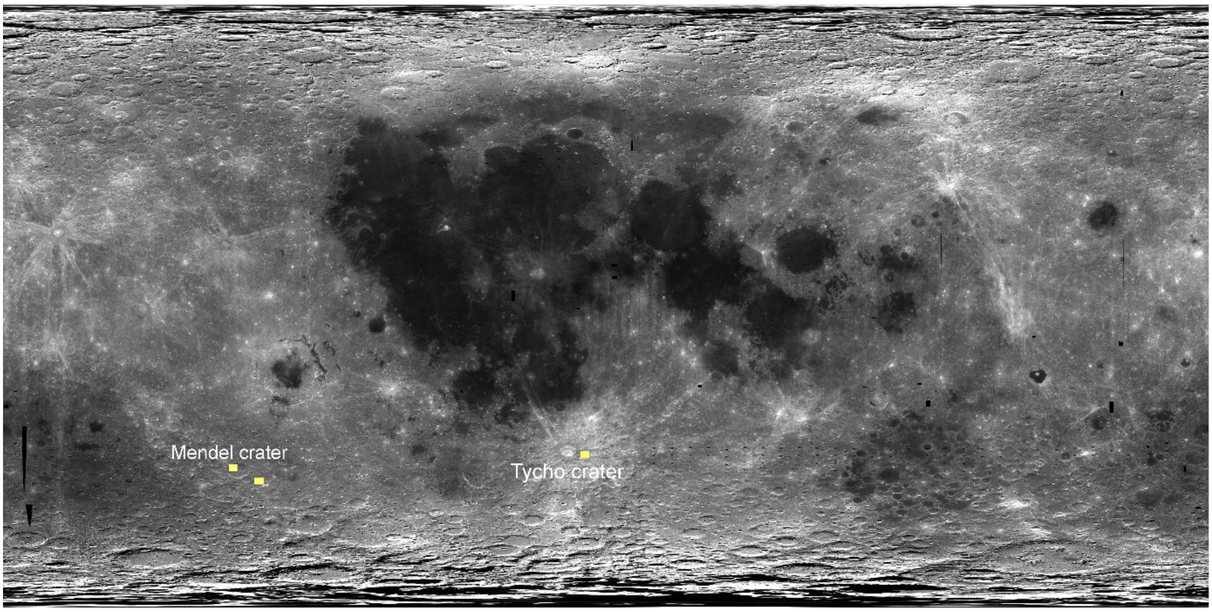

Figure 5.13 Identification of lunar regolith with similarities in composition to Kalahari 008 $\pm 2\sigma$ standard deviation.

5.4. Th-rich Breccias

Th-rich meteorites are those containing high bulk-rock abundances of incompatible trace elements. I include in this section meteorites whose bulk-rock Th concentrations are > 3.5 ppm.

KREEP basalts with high Th abundances were returned by the Apollo 15 and Apollo 17 missions, as small fragments, particles and clasts in breccias (Jolliff 1991; Nyquist and Shih 1992). Higher plagioclase abundances and enriched concentrations of incompatible trace elements are characteristics of this material (Papike 1998). Ages of Apollo 15 and 17 KREEP basalts range between 3.8 and 4.08 Ga (Nyquist and Shih 1992), although KREEP basalts analysed in lunar meteorites have shown ages much younger (~2.9 Ga), indicating that the duration of the KREEP volcanism lasted for more than 1 Ga (Borg et al. 2004).

5.4.1. Northwest Africa 4472

Northwest Africa (NWA) 4472 is a KREEP-rich regolith breccia formed by polymict lithic clasts (<5 mm) in a dark grey matrix of glass (feldspathic and Fe-rich), clasts and mineral fragments. Some impact melt breads can be found within the sample (Kuehner et al. 2007; Joy et al. 2008, 2011; Korotev et al. 2009). Lithic clasts comprise impact melts, impact melt breccias, basalts, granulitic feldspathic basalts, Mg-suite breccias, high-alkali suite (HAS) fragments. Basaltic clasts exhibit a variety of textures from subophitic to coarse-grained intersertal. They have low-Ti to VLT compositions (<3.5 wt.% Ti), they are moderately rich in K_2O and their plagioclases are more sodic that those in Apollo 12 and Apollo 15 low-Ti basalts. NWA 4472 basalts are more similar to low-K aluminous Apollo 14 and Luna 16 samples. Impact melts and impact melt breccias also show a very large range of textures and compositions appearing to be sourced from different lithologies ranging from feldspathic to a mixture of feldspathic and KREEP-rich lithologies. Mg-suite impact melt breccias are formed by orthopyroxene (En_{67-83} Wo_{2-9} Fs_{15-30}) and anorthite (An_{92-94}), feldspathic impact melt areas, rare pigeonite (En_{25-41} Wo_{18-39} Fs_{20-51}), ilmenite and siliceous clasts, Granulites are formed mainly by plagioclases ranging from Ca-rich (An_{83-97}) to more K-rich (An_{73-83}) enclosing Ca-rich (En_{37-44} Wo_{33-36} Fs_{21-27}) and Ca-poor (En_{42-55} Wo_{8-16} Fs_{33-42}) pyroxenes. Evolved lithologies such as alkali anorthosite and quartz monzodiorite clasts with a range of textures can be found within the matrix (Joy et al. 2011).

The matrix contains anhedral mineral fragments (<1 mm) of pyroxene (En_{16-92} Wo_{2-41} Fs_{6-68}) plagioclase (An_{69-97}) and olivine (Fo_{9-90}). The wide range of compositions within the minerals in the matrix indicates that they derive from similar rock types (Arai et al. 2010; Joy et al. 2011). U-Pb and Pb-Pb analyses performed in phosphates suggest crystallization ages of ~ 4.352 ± 0.01 Ga (Arai, Yoshitake, et al. 2010) and ~4.344 ± 0.014 Ga (Joy et al. 2011). An impact event took place ~4.07 ± 0.036 Ga, re-setting the systems. Age analyses on KREEP assemblages indicate a set of magmatism pulses or impact events associated with the formation of the Imbrium basin that took place between ~3.93-3.99 Ga (Joy et al. 2011).

The bulk rock FeO, TiO_2 and Th compositions ± 5σ standard deviation (Table 5.1) show matches with regolith compositions in the northeastern area of Sinus Roris (Figure 5.14). High-Al basalts has been found using remote sensing data within the Mare Frigoris area (Kramer et al. 2015) being consistent with our results. Furthermore, the crystallization ages are consistent with the cryptomare areas reported by Kramer et al. 2015, and lies within the ejecta blanket of the Imbrium event. During this work it has been possible to restrict the possible launch origin that were proposed previously (e.g. Joy et al. 2011) to 10 possible areas (Sinus Roris, Mons Alpes, Mons Caucasus, Gruitsen Domes, northern Procellarum, Apollo 15 landing site, Lassell Massif and Copernicus, Lalande and Prolemaeus Craters) to only Sinus Roris.

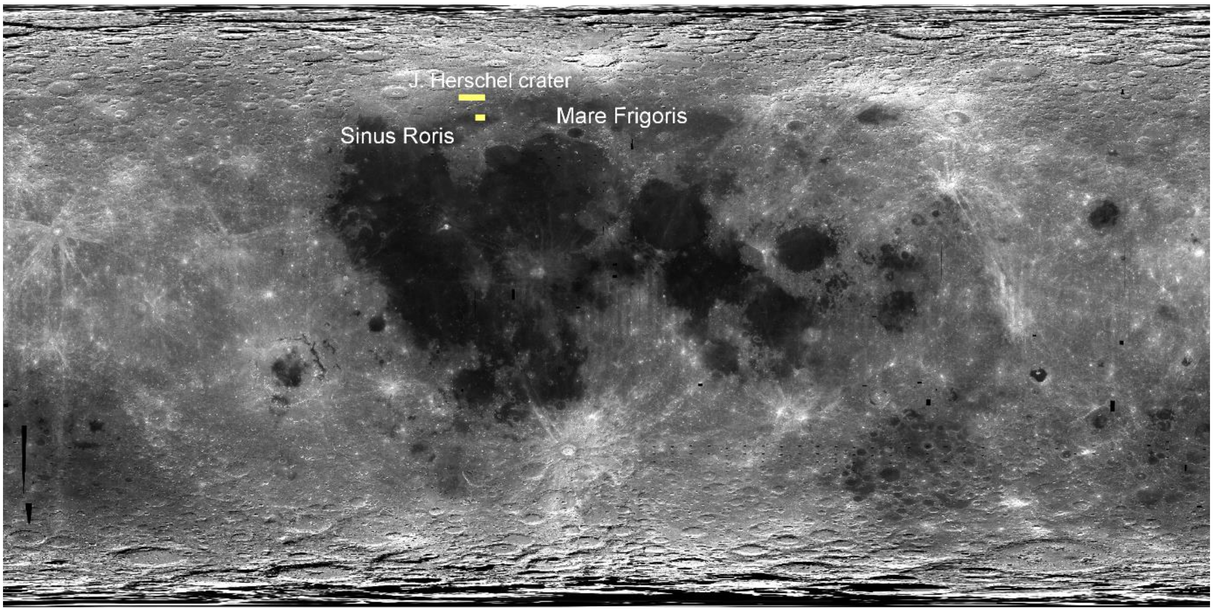

Figure 5.14 Image showing the area where surface regolith composition measurements match the analytical composition of NWA 4472 ± 5σ standard deviation.

5.4.2. Sayh al Uhaymir 169

Sayh al Uhaymir (SaU) 169 is formed by two types of lithologies: an impact melt breccia (~85% modal vol.) and a regolith breccia.

The impact melt breccia portion has gabbronoritic to noritic composition and lacks anorthositic components. The plagioclases are albitic (An_{57}) and it also contain low-Ca pyroxene, plagioclase intergrown with K-feldspar and smaller amounts of merrillite, zircon, olivine, troilite and kamacite. It also exhibits a strong enrichment in incompatible elements with Th abundances up to 32.7 ppm Th (Gnos et al. 2003, 2006). The impact melt breccia fraction has larger Na_2O and Eu bulk clast compositions than Apollo 14 samples, and Cr, Co and Ni also show a wide range of concentrations between Apollo 14 and this sample. This could indicate variable amounts of alkali anorthosite and metallic meteoritic components (Zeigler et al. 2006).

The regolith breccia portion comprises clasts of crystalline and glassy volcanic rocks, breccia clasts, granulites and crystal fragments. The volcanic rocks ranges from Ti-poor to Ti-rich basaltic clasts formed by plagioclase, pyroxene, olivine and ilmenite. Fine-grained olivine picrobasalts formed by olivine (~70% modal vol.) and glass, and aluminous medium-Ti basalt are also present. Among the regolith breccia clasts, there is a large KREEP-rich regolith breccia (~1 cm) formed by very fine-grained matrix enclosing mineral clasts of Ca-rich plagioclase (An_{78-97}), olivine and grains of silica. Mineral fragments in the regolith breccia portion includes plagioclase with An_{74} to An_{94} compositions (<1mm size), Mg and Fe-rich pyroxenes, Ca-poor to Ca-rich pyroxene, Mg-rich (Fo_{66-73}) olivine (<600 µm) and ilmenite (100-400 µm). Yellow and orange elongated glass beads from <1 mm to 2 mm with irregular boundaries. The composition of these glasses are similar to the average regolith composition. The regolith portion exhibit Th abundances up to 8.44 ppm and neither the regolith breccia nor the impact melt clast appear to be depleted in alkalis (Gnos et al. 2003; Al-Kathiri et al. 2007).

Zircon ^{207}Pb-^{206}Pb analyses in the impact melt breccia shown an age of 3.909 ± 0.013 Ga (Gnos et al. 2004), very similar to the 3.916 ± 0.015 Ga reported for the Apollo 12 high-Th impact melt breccia group (Liu et al. 2012).

The FeO, TiO_2 and Th bulk-rock compositions ± 3 standard deviation (Table 5.1) of the regolith breccia portion sample matches regolith compositions measured in the centre of PKT, between the Kepler and Copernicus craters (Figure 5.15).

Previous attempts to locate the launch origin of this sample have also shown areas localized in high Th spots within PKT, suggesting Lalande Crater as its most likely source (Gnos et al. 2004). My results suggest that the surrounding of Mts. Carpathus that was also suggested by (Gnos et al. 2004), match better the compositions of this sample and the elevated Th abundances observed in the central PKT (Lawrence et al. 2000; Lawrence et al. 2003).

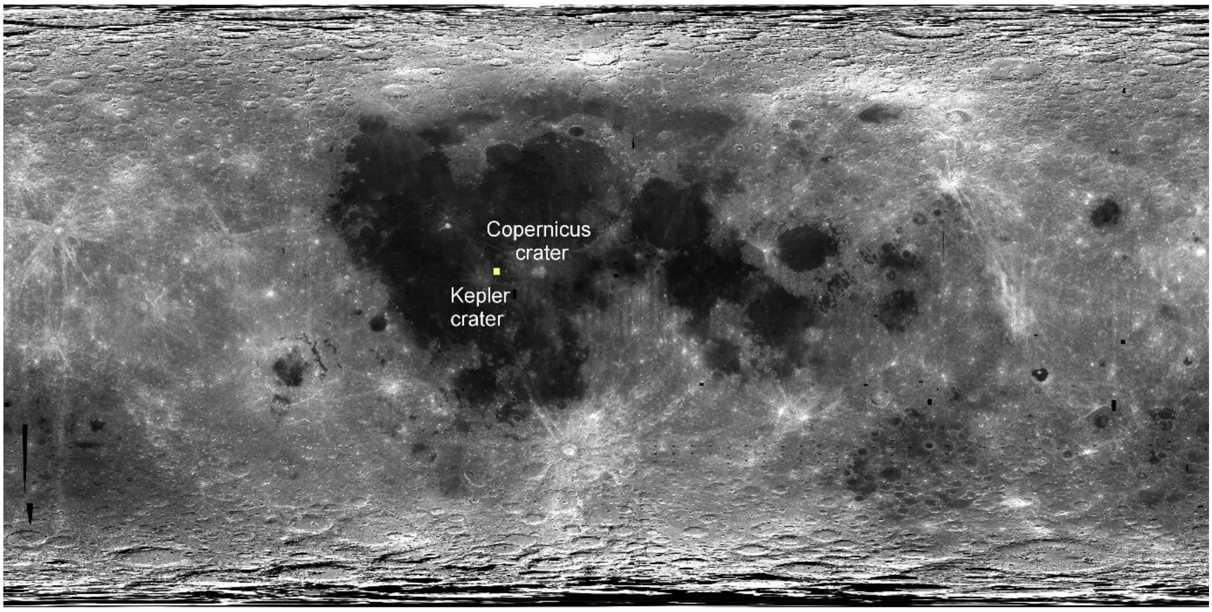

Figure 5.15 Identification of lunar regolith with similarities in composition to the regolith portion of SaU 169 ± 3σ standard deviation.

5.4.3. Calcalong Creek

Calcalong Creek is a regolith breccia with polymict clasts and mineral fragments of both highlands and mare compositions. The clasts are of small sizes (<1 mm) and included in a fine-grained and glassy matrix.

Mare basaltic clasts have Fe-rich assemblages typical of late-stage residual melts. Mare clasts are formed from any of all of the following phases: ilmenite (<0.3 wt.% MgO), ferroaugite (En_6 Wo_{24} Fs_{70}). Pyroxferroite (En_2 Wo_{16} Fs_{82}), low-Ca pigeonite (En_{66} Wo_7 Fs_{27}), olivine (Fa_{90}), silica, troilite and glass. It is probable that the parent materials of these clasts were VLT basalts. Highland clasts include fragments of plagioclase (An_{95-97}), ferroan anorthosites formed mainly by plagioclase (An_{95-97}) and small grains of pyroxenes (En_{62} Wo_6 Fs_{32}) and olivine (Fo_{61}), gabbroic anorthosite with plagioclase (An_{97}) and pyroxene (En_{62} Wo_4 Fs_{34} and En_{41} Wo_{44} Fs_{16}) with no shock evidence, and spinel troctolite formed by plagioclase (An_{96}) and olivine (Fo_{90-92}; Marvin and Holmberg 1992).

Compositionally, it is rich in incompatible elements (Th ~3.92 ppm), but there is no correlation between them and FeO or Sc compositions, suggesting that the incompatible elements are carried by a third component. The low bulk-rock concentration of Eu (~1 ppm; Korotev et al., 2009), also is not consistent with an anorthositic-mare-KREEP mixture. This is also reinforced by the fact that Calcalong Creek does not contain any lithic component of KREEP basalt or norite (Korotev et al. 2009).

^{40}Ar-^{39}Ar analyses indicated that the sample was exposed to the lunar surface within the last 1.5-2 Ga (Cohen et al. 2005). There is no formation age reported for this sample.

Bulk rock FeO, TiO_2 and Th ± 3 standard deviation (Table 5.1) indicates as possible launch locations for these sample several locations. These are mainly the surroundings of PKT, including the Apollo 16 area, and the western part of SPA (Figure 5.16). However, the lack of a KREEP component in the sample (Korotev et al. 2009) suggests that the vicinity of PKT or other close areas of the nearside are not the probable launch location for this sample, reinforcing a possible origin within the SPA. A possible provenance from the SPA for this sample was proposed previously (Hill and Boynton 2003).

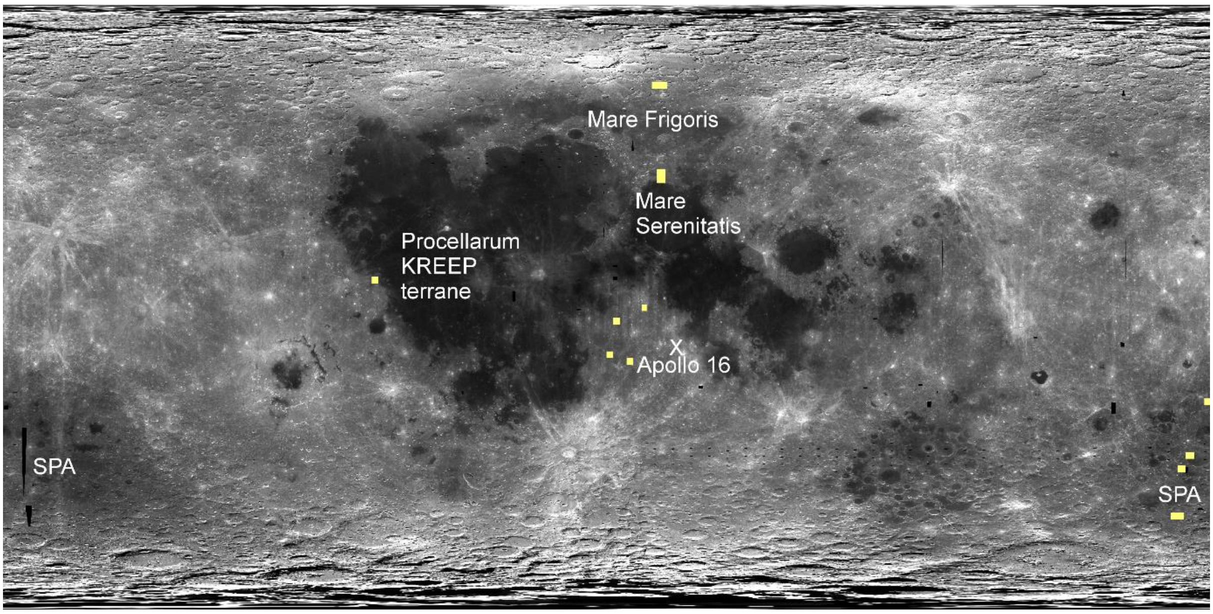

Figure 5.16 Image showing the area where surface regolith composition measurements match the analytical composition of regolith breccia Calcalong Creek ± 3σ standard deviation.

5.5. Discussion

5.5.1. Ancient >4.0 Ga magmatism

Crystallization ages obtained from Apollo samples (e.g. Taylor et al. 1983), meteorites such as Kalahari 009 and basaltic clasts from NWA 4472, remote sensing observations (e.g. Bell and Hawke 1984) and crater degradation and size-frequency distributions studies (Hiesinger et al. 2011) all suggest that magmatism and volcanism on the Moon was initiated prior to 4 Ga. This magmatism seems not to be localized in one specific area, but from several different mantle reservoirs with different chemical and isotopic characteristics (Taylor et al. 1983; Jennifer Whitten and Head 2015b). Such magmatic rocks comprise a wide range of petrologic groups: KREEP basalts, high-K basalts, high-Al basalts, alkali-rich plutonic rocks, Mg-suite plutonic rocks and highly evolved highland plutonic rocks (Warren and Kallemeyn 1989; Head and Wilson 1992; Borg et al. 2004).

The low REE abundances in 4.3 Ga basalt Kalahari 009 indicate a formation for the sample far from the PKT so, the radioactivity of KREEP elements could not have been the heat mechanism for the formation of the meteorite’s parent magma. The proposed Mendel-Rydberg source region is an ancient multi-ring basin detected by the Clementine Laser altimeter (Spudis et al. 1994) and more recently assessed by the Gravity Recovery and Interior Laboratory (GRAIL; Neumann et al. 2015). This basin is filled by basaltic materials and covered by Orientale ejecta (Whitten and Head 2015a, 2015b). A possible origin in Mendel-Rydberg for Kalahari 009 would indicate a maximum age for the impact event formation of ~4.3 Ga. The possible location of the sample within an impact basin agrees with the previous findings by Terada et al (2007) that suggest this basalt was formed as a result of decompression melting triggered by the basin-formation event

Very low-Fe, low-Ti volcanism could have happened in the Mendel-Rydberg region at ages ~ 4.3 Ga (Head III and Wilson 1992). Kalahari 009 could be a sample from this region, it is unique in having the lowest bulk-rock to REE ratio and Th abundances (0.1 ppm) of all basaltic meteorites, indicating a relatively depleted parent magma source. It also did not assimilate any KREEP material during the ascent to the surface.

KREEP driven magmatism: The source launch sites and crystallization ages of basaltic clasts analysed in NWA 4472 (4.352 ± 0.01 Ga; Joy et al. 2011) as well as zircons ages from all the

Apollo landing sites (3.90-4.35 Ga; Nemchin et al. 2008), suggest that early episodes of high-KREEP driven magmatism have also occurred in the Procellarum area approximately during the same period.. The basaltic clasts in NWA 4472 and Kalahari 009 share a VLT nature, but they significantly differ in their incompatible elements abundances, suggesting either that the KREEP layer could not be globally distributed or that they derive from different depths of melting. Kalahari 009 has previously been compared to HMS parent magmas and Apollo 14 KREEP-enriched mare basalts, and the results suggest that the meteorite probably derived from a depleted source (e.g. Terada et al. 2007).

The possible launch location obtained for NWA 4472 in the northeastern area of Sinus Roris (Figure 5.14) samples high-Al cryptomare basalts and Imbrium ejected material. High-Al cryptomare basalts derive from sources formed from late stage cumulates of the LMO that contain significant quantities of plagioclase (Neal and Taylor 1992; Kramer et al. 2015). The surroundings of the PKT are formed by a pattern of linear anomalies (rifts) formed by extensional tectonics as revealed by Grail gravity data (Andrews-Hanna et al. 2014). The high heat flux because radioactive elements associated with KREEP, together with passive mantle upwelling during rifting could have caused partial melting of the underlying mantle creating dyke intrusions and volcanism (White and McKenzie 1989; Andrews-Hanna et al. 2014; Kramer et al. 2015).

The localized nature of this model of magma generation also could indicate that the KREEP layer was not globally distributed (Snyder et al. 1997; Wieczorek and Phillips 2000; Borg et al. 2004; Nemchin et al. 2008). My results appear to indicate that pre-mare magmatism was caused by several mechanisms in different areas of the Moon occurring a similar time.

5.5.2. Younger <4 Ga mare volcanism

Mare basalts are represented by the smooth low albedo basalts that infill the large impact basins of the Moon between 4.0 to ~ 1 Ga, as a consequence of highly effusive, flood-type eruptions (Head and Wilson 1992). This type of magmatism occurred mainly in the nearside of the Moon, with very limited mare volcanism within the farside (e.g. Mare Moscoviense; Petro and Pieters 2004). This difference has been attributed to the thicker anorthosite crust in the far side that may have acted as a low density barrier preventing the eruption of the denser magmas (Zuber et al. 1994).

5.5.2.1. Mare Fecunditatis and Mare Crisium

Most of the volcanism in Mare Fecunditatis happened during the late Imbrian (3.34-3.71 Ga) according to crater size-frequency distribution studies (Hiesinger et al. 2006). Three meteorites could be considered to be derived from this area based in their major FeO, TiO_2 compositions, Th abundances and crystallization ages: the YAMM group, NWA 4898 and NWA 3136. It is possible that the source for Fecunditatis basalts was a depleted (i.e., the YAMM group) to very depleted mantle source (e.g. NWA 4898). NWA 3136 is a regolith breccia that contains both mare and non-mare components. The mare clasts present in this meteorite are olivine and pigeonite/olivine basalts (O'Donnell et al. 2008) that support the model of a depleted mantle that underwent a high degree of batch melting and melt extraction prior to the melting event that created the meteorite. NWA 3136 also contains material that could be either feldspathic material from the highlands or a different type of basalt not represented by the lunar mare-basalt suite (O'Donnell et al. 2008).

Meteorites that could be launched from Mare Crisium (the YQN group, EET 87521/96008 and NEA 003) seem to have been formed by fractional crystallization in a closed-system, of a primitive, VLT, slightly enriched mantle source (Jolliff et al. 1998; Haloda et al. 2009). This parent melt could itself originated from magmatic differentiation processes from a picritic magma (Haloda et al. 2009). They all are VLT, but also are highly heterogeneous in terms of REE content; i.e. among the YQN paired group primitive components with low REE (QUE 94281) were observed, as well as an evolved component with KREEPy signatures (EET 87521/96008). Petrographic and major element compositional similarities between EET 87521 and the VLT-gabbro found in QUE 94281 suggest that the differences in the incompatible element abundances could be caused by different degrees of fractionation of similar VLT parent magmas. Alternatively, VLT basalts could have been (counter-intuitively) originated from a high-Ti basalt source. The mid-range olivine compositions have capability of flotation in a dense ilmenite magma. Thus, the olivine-rich, VLT basalts could also have been differentiated and float in the Fe-rich, high-Ti magma before eruption (Boesenberg and Delaney 2006).

The low incompatible element material suggests that the heat source that produced basalts possibly derived from Fecunditatis and Crisium, are not related to large amounts of radiogenic elements derived from mantle regions rich in KREEP (Swindle et al. 1991; Gillis and Spudis 2000; Jolliff et al. 2000). Also, Fecunditatis and Crisium are outside from the geometric pattern of the PKT border structures that may represent the magma plumbing system to the PKT high KREEP basalts (Andrews-Hanna et al. 2014). They could, however, have been formed as consequence of a mantle plume that have reached the thinner crust of the impact basin and extruded flooding the circular topography.

5.5.2.2. Oceanus Procellarum

The enhanced KREEP signature in the LAP group and NWA 032, suggest a PKT origin (Figure 5.3-5.4). I suggest that the most probably source of these meteorites is Oceanus Procellarum, since they exhibit some similarities to low-Ti A12 samples and young ages <3.0 Ga (Anand et al. 2006) agreeing with young ages obtained for lava flows in the western part of Oceanus Procellarum (Hiesinger et al. 2011). LAP and NWA 032 basalts were crystallized from a parent liquid with similar composition to olivine A12 and A15 basalts or lunar low-Ti pyroclastic clasts that underwent extreme fractionation (Day et al. 2006; Anand et al. 2006). Andrews-Hanna et al. (2014) has identified linear depressions surrounding the PKT. These rift-like depressions could have been formed by crustal thinning that combined with passive upwelling and the elevated heat flux in the PKT associated to radioactive elements from the urKREEP drags, could have led to the widespread partial melting of the underlying mantle in this area.

5.5.3. The Imbrium basin-formating event

The bulk-rock compositions enriched in KREEP and possible launch locations of NWA 4472 and SaU 169 suggest that they contain impact melt breccia from a basin-forming event within PKT that took place between 3.91-3.94 Ga, probably either from the Imbrium basin formation that took place at the final stages of the basin formation on the Moon (Gnos et al. 2004; Joy et al. 2011).

Among the clasts within NWA 4471, phosphates ages for KREEP basalt clast and zircon reset ages indicate a re-setting impact event that happened between 3.93-3.94 Ga (Arai et al. 2010; Joy et al. 2011). Previously, it was not possible to link these clasts to the formation of Imbrium or Serenitatis basins because they have been created within a short interval (Joy et al. 2011). However, a launch location in the northeastern area of Sinus Roris (Figure 5.14) agrees with these clasts being the ejecta of the Imbrium formation event.

The SaU 169 impact melt breccia portion have shown an age of 3.909 ± 0.013 Ga (Gnos et al. 2004). These ages are similar to those obtained for Apollo 12 high-Th impact melts (3.916 ±

0.015 Ga; Liu et al. 2012) and consistent to Imbrium basin ejecta (Liu et al. 2012). A possible launch location close to the southern rim of Imbrium (Gnos et al. 2004), therefore, agrees with the impact melt being derived from the Imbrium basin excavation event (Figure 5.15).

5.5.4. Mare-highlands mixtures, or the South Pole-Aitken basin?

The SPA basin is a large terrane distinct from the FHT, and moderately mafic with a moderate concentrations of Th (Jolliff et al. 2000). The mafic signature and the Th abundances could be caused by a mixture of anorthosite, KREEP and mare basalt within brecciated meteorites. However, some geochemical characteristics could indicate an origin within SPA rather than from the PKT nor the Apollo sites. Low bulk-rock Eu abundances in comparison to Apollo samples of similar Sm concentrations is not consistent with KREEP or Mg-suite from the PKT and it could be an indicative of an origin within SPA (Korotev et al. 2006; 2009).

Among the meteorites studied during this work, Calcalong Creek appears to be the most likely candidate for a SPA origin. FeO, TiO_2 and Th bulk-rock compositions are similar to those observed in SPA, but also Sm-Eu systematics for this meteorite are consistent with my results (Korotev et al. 2009). Sm/Eu ratio does not plot along or parallel to the mixing trend (Figure 5.17), indicating that Calcalong Creek is possibly not derived from the missing between PKT, anorthositic and basaltic material. Instead, it can represent the composition of the lower crust as excavated during the SPA impact event (Korotev et al. 2009).

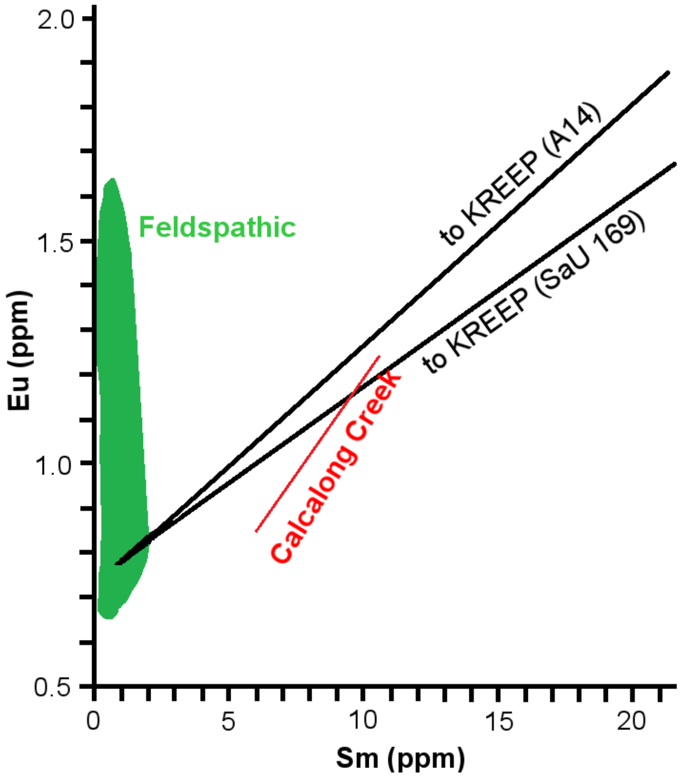

Figure 5.17 Variation of Eu (ppm) with Sm (ppm). The red line is the regression line through the measurements of 11 subsamples for the lunar meteorite Calcalong Creek. The solid lines are mixing lines between typical feldspathic lunar meteorites and two types of KREEP representing PKT (N=1344), with different Eu/Sm ratios, high K KREEP of Apollo 14 and SaU 169. (Modified from Korotev et al. 2009).

5.6. Conclusions

During early lunar magmatism (>4.0 Ga) several mechanisms including extensional tectonic processes, heat flux caused by radioactive elements and mantle plumes could have been working at the same time in different areas to produce these ancient basalts. High-Al basalts appear to have been extruded in Mare Frigoris early in the lunar history, however, other types of basalts, such as low-Fe basalts were extruded in other areas of the lunar surface such as Mendel-Rydberg in the same lunar period.

This work shows that VLT and low-Ti basaltic meteorites were launched from different mare areas, indicating that these compositions are widespread across the lunar maria. This was already suggested based on the number of basaltic meteorites with low-Ti compositions in contrast to samples from the Apollo collection where moderate to high-Ti content is present (e.g. Apollo 12, Apollo 17; Joy and Arai 2013).

Mare volcanism shows a wide compositional range reflecting differences in their parental melt sources. A heterogeneous, depleted to very depleted mantle melt appears to be the source of basalts localized within Mare Fecunditatis.

The basaltic meteorites possibly launched from Mare Crisium indicates a primitive, VLT, slightly enriched mantle source that underwent fractional crystallization in a closed-system. Alternatively, these VLT basalts could be the result of the differentiation and flotation of the VLT basalt in a Fe-rich, high-Ti magma.

Basalts crystallized from a parent liquid with compositions similar to olivine basalts that underwent extreme fractionation, and are the most likely source for meteorites launched from the Oceanus Procellarum. The volcanism in this region of the Moon lasted longer because of the high abundances of heat-producing radioactive materials below this area (see also Snyder et al. 1995). The differences in KREEP components between PKT and other areas of the Moon is the principal indication of a heterogeneous lunar mantle.

The SaU 169 impact melt breccia portion has shown an age similar to those obtained for Apollo 12 high-Th impact melts (~3.9 Ga) and consistent with being ejecta from the Imbrium basin excavation event.

Chapter 6. Investigating the Source Regions of Feldspathic Meteorites[4]

6.1. Introduction

The composition of the lunar feldspathic highland crust is essential to understand the early differentiation and magmatic evolution of the Moon (NRC 2007). Outlined below are several key questions that feldspathic lunar meteorites can help to address to understand the processes that led to the diversity of lunar crustal rocks as well as shed light into the formation of the major impact basins and the bombardment history of the Moon.

Investigations of feldspathic lunar meteorites and remote sensing observations have shown a larger chemical diversity among the lunar highlands than previously thought based only on samples from the Apollo collection (Palme et al. 1991; Korotev et al. 2003; Warren et al. 2005; Joy and Arai 2013; Gross et al. 2014). For example, granulites from the farside appear to have been derived from a magnesian anorthositic protolith based on their higher Mg# compared to the nearside highlands (Russell et al. 2014; Gross et al. 2014; Crites et al. 2015). The nearside seems to be dominated by ferroan anorthosites similar to those observed in the Apollo 16 samples (Korotev 2012; Zeigler et al. 2012). These differences between the nearside and the farside indicates that the lunar crust is compositionally heterogeneous. Together with the higher abundances of magnesian anorthosite-derived lithologies, it suggests that the lunar crust was probably formed by more complex geological processes than a simple magma ocean flotation event (e.g. Joy and Arai 2013; Russell et al. 2014; Gross et al. 2014; Crites et al. 2015; Pernet-Fisher and Joy 2016). Feldspathic meteorites ejected from the farside of the Moon should exhibit low REE abundances (e.g. Th) compared to the samples from the Apollo 16 landing site and closer to the PKT (Laul and Schmitt 1973; Wänke et al. 1973; Wieczorek and Phillips 2000; Jolliff et al. 2000). The KREEP layer resulting from the fractionation of the lunar magma

---

[4] Aspects of the work presented in this chapter have been published in "**Constraining the source regions of lunar meteorites using orbital geochemical data,"** Calzada-Diaz A, Joy K. H., Crawford I.A, and Nordheim T. A. (*Meteoritics and Planetary Sciences* 50, 214-229. 2015)

ocean does not appear to be global and it should be necessary to revisit the processes under which the formation of the lunar crust took place.

Some lunar feldspathic meteorites contain mare basaltic clasts, the presence and the Ti-content of these basalts offers insights into the nature and distribution of mare volcanism in the Moon (Robinson et al. 2012).

It is also possible to determine the ages of major basin forming events using isotopic studies of impact-melts in feldspathic meteorites (Cohen et al. 2000; Liu et al. 2012). This potentially will be useful in determining the unknown ages of the lunar impact basins such as South Pole-Aitken and Orientale. Also, it could help to prove or disprove the existence and the age of ancient, hidden basins such as the North Australe basin observed by GRAIL (Neumann et al. 2015).

The primary aim of this chapter is to identify the possible source localities of feldspathic meteorites and therefore, to investigate the processes that led to the lunar crustal formation and evolution through the analysis of the possible launch location of lunar feldspathic meteorites.

I have investigated the possible launch sites of 22 lunar feldspathic meteorites (46 individual stones) with bulk rock contents of <10 wt.% FeO, >20 wt.% Al_2O_3 and low Th abundances (<3 ppm). They are different type of breccias (granulitic, fragmental, impact melt and regolith breccias, see sections 1.4 and 1.9). Sometimes they may contain basaltic fragments (<10 % vol.). Bulk rock FeO, TiO_2 and Th abundances were used to assess their possible launch locations using 2-degree Lunar Prospector Gamma Ray Spectrometer datasets (Prettyman et al. 2006), bulk rock FeO, TiO_2 and Th compositions ± 2 standard deviation compiled from the literature (Table 6.1) and implementing the software described in Chapter 2.When the use of 2σ does not report any results, I have increased the compositional range using the following standard deviation (i.e. 3σ and so on) until obtaining the first results. This procedure was described in Chapter 2 (see Figure 2.5).

Meteorite	Breccia type	No. of literature bulk rock analyses used	Std. Dev	Literature references	FeO (wt.%)	% error	TiO_2 (wt.%)	% error	Th (ppm)	% error
ALHA 81005	Regolith breccia	5	± 2σ	Palme et al. 1983, Laul et al. 1983, Korotev et al. 1983, Warren et al. 1983, Boynton et al. 1983	5.49 ± 0.17	3	0.29 ± 0.08	28	0.298 ± 0.12	40
DaG 262 Group	Fragmental to regolith breccia	8	± 2σ	Bischoff et al. 1998, Korotev et al. 2003, 2008, Warren et al. 2005)	4.42 ± 0.22	5	0.21 ± 0.06	29	0.41 ± 0.08	19
DaG 400	Regolith to impact melt breccia	3	± 3σ	Korotev et al. 2003, Joy et al. 2010	3.67 ± 0.29	8	0.18 ± 0.018	10	0.23 ± 0.24	104
Dho 025/301/304	Regolith breccia	7	±2σ	Korotev et al. 2003, Cahill et al. 2004, Warren et al. 2005, Demidova et al. 2007	4.98 ± 0.47	9	0.32 ± 0.03	9	0.77 ± 0.47	61
Dho 026 Group	Granulitic to impact melt breccia	13	±2σ	Cohen et al. 2004, Warren et al. 2005, Demidova et al. 2007	4.12 ± 0.24	6	0.21 ± 0.03	14	0.37 ± 0.05	13
Dho 081/280	Fragmental breccia	2	±2σ	Warren et al. 2005, Demidova et al. 2007	3.22 ± 0.25	8	0.17 ± 0.028	16	0.265 ± 0.09	34
Dho 302	Impact melt breccia	2	±2σ	Demidova et al. 2007, Korotev 2012	3.59 ± 0.61	17	0.22 ± 0.06	27	0.38 ± 0.07	18
Dho 489 Group	Impact melt breccia	14	±2σ	Takeda et al. 2006, Korotev et al. 2006, Demidova et al. 2007	2.94 ± 1.02	35	0.13 ± 0.03	23	0.28 ± 0.28	100
Dho 490/1084	Fragmental breccia	4	±4σ	Korotev 2012	3.93 ± 0.60	15	0.20 ± 0.02	10	0.44 ± 0.02	4
Dho 733	Granulitic breccia	2	±2σ	Foreman et al. 2008, Demidova et al. 2007	3.175 ± 0.13	4	0.3 ± 0.04	13	0.35 ± 0.35	100
Dho 1436/1443	Impact melt breccia	3	±3σ	Korotev et al. 2012	5.21 ± 1.89	36	0.29 ± 0.10	34	0.36 ± 0.024	7
MAC 88105	Regolith breccia	6	±2σ	Lindstrom et al. 1991, Neal et al. 1991, Palme et al. 1991, Warren et al. 1991	4.09 ± 0.5	12	0.24 ± 0.024	10	0.38 ± 0.12	32

Meteorite	Breccia type	No. of literature bulk rock analyses used	Std. Dev	Literature references	FeO (wt.%)	%	TiO_2 (wt.%)	%	Th (ppm)	%
NWA 482	Impact melt breccia	4	±2σ	Daubar et al. 2002, Korotev et al. 2003, Warren et al. 2005	3.57 ± 1.01	28	0.16 ± 0.05	31	0.23 ± 0.014	6
NWA 4936	Granulitic breccia	2	±2σ	Korotev et al. 2009	5.94 ± 1.1	18	0.75 ± 0.3	40	1.95 ± 0.9	46
PCA 02007	Regolith breccia	9	±3σ	Taylor et al. 2004, Zeigler et al. 2004, 2005, Joy et al. 2006, Korotev et al. 2006	6.39 ± 0.72	11	0.28 ± 0.012	4	0.42 ± 0.15	36
QUE 93069	Regolith breccia	2	±2σ	Korotev et al. 1996, Grossman et al. 1996	4.44 ± 0.81	18	0.24 ± 0.014	6	0.52 ± 0.24	46
Yamato 791197	Regolith breccia	4	±2σ	Ostertag et al. 1986, Warren and Kallemeyn 1986, Fukukoa et al. 1986	6.42 ± 1.0	16	0.32 ± 0.07	22	0.35 ± 0.15	43
Yamato 82192/82193/86032	Fragmental breccia	17	±2σ	Fukukoa et al. 1986, Warren and Kallemeyn 1987, Bischoff et al. 1987, Koeberl et al. 1988, 1989, Lindstrom et al. 1991, Karouji et al. 2004, Nyquist et al. 2006	4.8 ± 0.75	16	0.21 ± 0.11	52	0.2 ± 0.02	10
Dho 925/961	Regolith breccia	3	±2σ	Demidova et al. 2007, Korotev et al. 2009	9.11 ± 3.79	42	0.42 ± 0.38	90	1.58 ± 1.11	70
SaU 300	Impact melt breccia	2	±2σ	Korotev et al. 2009	7.3 ± 1.5	20	0.295 ± 0.014	5	0.5 ± 0.08	16
NWA 4932	Impact melt breccia	2	±2σ	Korotev et al. 2009	8.55 ± 1.56	18	0.34 ± 0.14	41	0.5 ± 0.23	46
NWA 2996	Impact melt breccia	2	±3σ	Korotev et al. 2009, Mercer et al. 2013	9.75 ± 2.7	28	0.68 ± 0.42	62	1.55 ± 1.17	75
					Average % error	***16***		***26***		***39***

Table 6.1 Average bulk composition of feldspathic meteorites (± the corresponding standard deviation) for each element, averaged from measurements reported in the literature.

6.2. Feldspathic Lunar Meteorites

This section will study the possible launch origin of feldspathic meteorites and anorthositic norite and troctolite breccias with compositional abundances of >20 wt. % Al_2O_3 and <10 wt.% FeO (Figure 6.1).

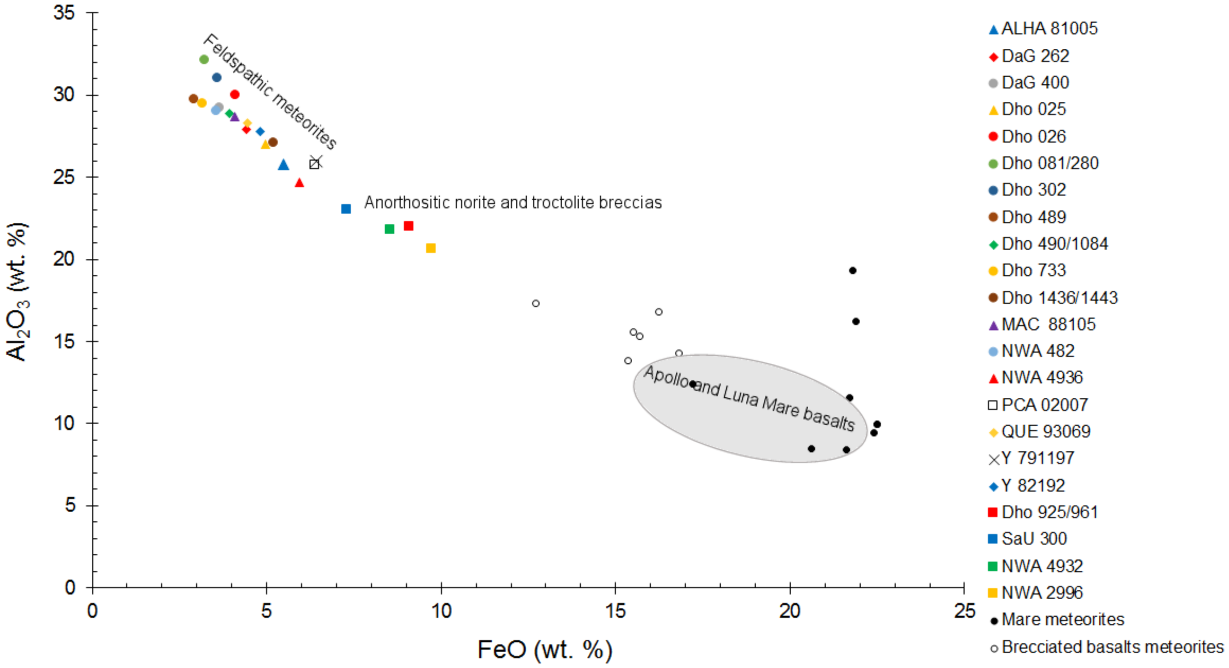

Figure 6.1 Compositional range of lunar meteorites addressed in this chapter (feldspathic and anorthositic norite and troctolite breccias) compared to brecciated basalts and mare meteorites studied in the Chapter 5, and Apollo and Luna Mare basalts. Data from the sources in Table 5.1, Table 6.1, Korotev 1999, Korotev et al. 2003. Error bars are too small to be shown.

6.2.1. Allan Hills 81005

Allan Hills (ALHA) 81005 is a regolith breccia. It contains larger polymineralic clasts with sizes up to 4 mm and smaller individual mineral grains <0.3 mm in size (Simon et al. 1983; Boynton and Hill 1983). Larger clasts are mostly formed by Ca-rich plagioclase grains, pyroxenes (Wo_{1-41}, En_{44-79}, Fs_{7-47}) and occasional olivine (Fa_{11-40}), although individual clasts of VLT basalts, magnesian granulites and hyperferroan anorthosites that only has been reported in this meteorite. Pure anorthosites have also been reported (Goodrich et al. 1984; Gross and Treiman 2011; Gross et al. 2014).

U-Th-Pb isotopic analysis have shown a stage model age of <4 Ga and an impact metamorphism event dated ~3.9 Ga (Chen and Wasserburg 1985). Cosmogenic radionuclides have found that the meteorite was ejected from near the surface of the Moon (~1.5 m) and had a transition time <0.1 Ma from the Moon to the Earth (Nishiizumi et al. 1991).

The first launch location results appear with the averaged measurements ± 2σ standard deviation (Table 6.1). Three matches were located in the surroundings of Mare Australe, and another in Mare Orientale. A fifth match appeared in the nearside FHT-O (Figure 6.2). These results agree with previous studies that suggests that its launch location should be in the farside because the meteorites have low Th abundances. The meteorites must have been sourced close to a mare basalt or cryptomare lava field to account for the VLT basalt clasts found in the meteorite since lateral transport of regolith material is inefficient for distances greater than 100 km (Pieters et al. 1983; Delano 1991). A nearside southern limb source area appears to be a probable source (Figure 6.2).

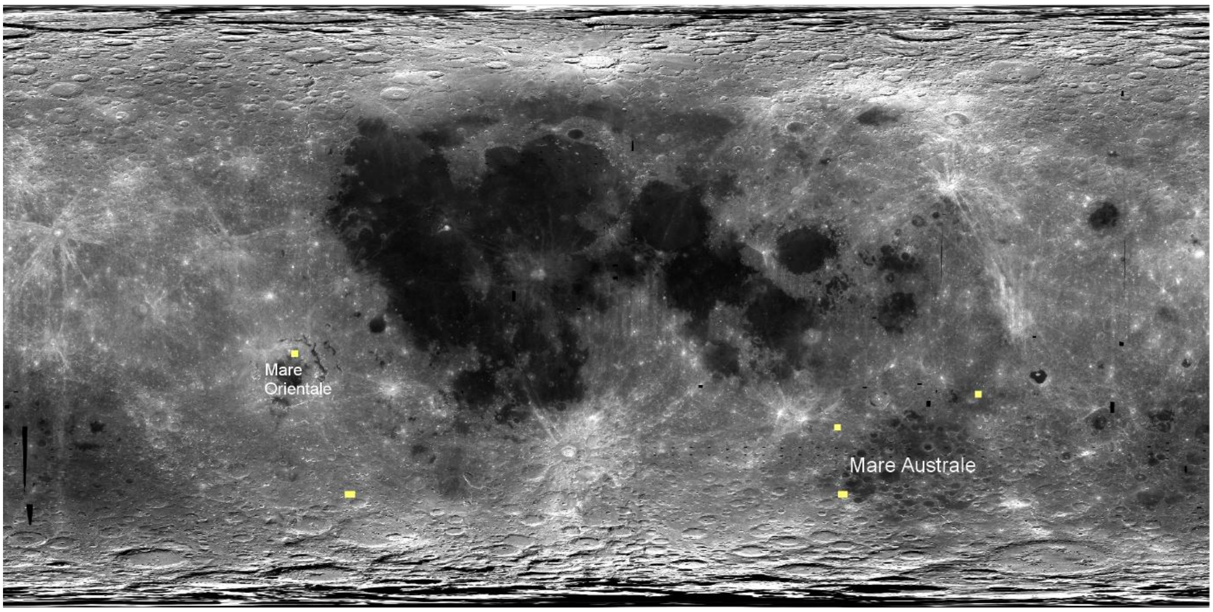

Figure 6.2 Identification of lunar regolith with similarities in composition to the regolith breccia ALHA 81005 ± 2σ standard deviation for each FeO, TiO_2 and Th bulk rock compositions in yellow.

6.2.2. Dar al Gani 262

Dar al Gani (DaG) 262 is an anorthositic regolith breccia consisting of anorthositic clasts that are compositionally both FAN and MAN, fine-grained and crystalline impact melt breccias, glass fragments and spherules in a fine-grained, well-consolidated matrix (Bischoff et al. 1998; Warren et al. 2005). DaG 262 is grouped with DaG 996, 1042 and 1048 based on compositional similarities as well as the proximity of the places where they were found on Earth (Korotev 2008).

^{40}Ar-^{39}Ar isotope studies of impact melt clasts from DaG 262 have shown three groups of ages. An oldest clast of 4.1 ± 0.5 Ga, and two younger clasts of 3.5 and 2.4 Ga (Cohen et al. 2005). Cosmogenic isotopes indicated that the meteorite was ejected from a depth of ~20 cm and had a transition time from the Moon to the Earth of ~0.5 Ma (Nishiizumi and Caffee 1998).

It has been suggested that DaG 262 and paired stones represent a type of highland terrane derived from the KREEP-signature impact melt breccias from the central highlands in the nearside of the Moon (Cahill et al. 2004). It could have been ejected from the farside based on the geochemical signatures and lithologies, although the nearside should not be dismissed as a possibility (Cahill et al. 2004). Their possible launch location was investigated (Table 6.1) obtaining results in the central area of the farside as well as some regions in the nearside limbs (Figure 6.3).

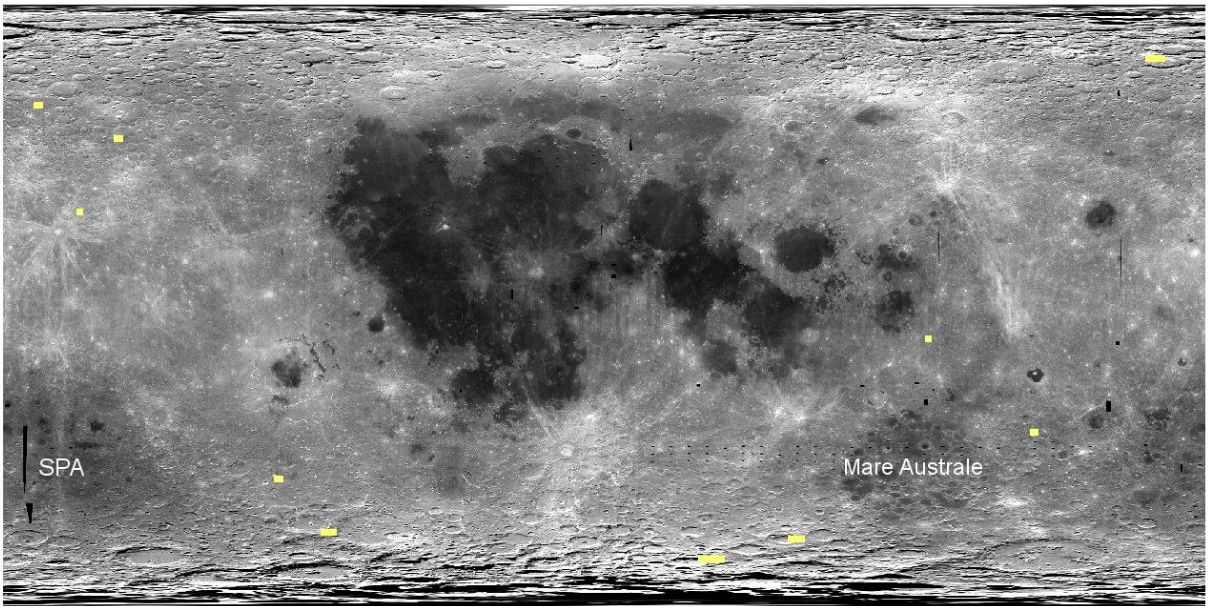

Figure 6.3 Regions where surface regolith composition measurements match the analytical compositions (yellow) of the averaged bulk-rock FeO, TiO_2 and Th regolith breccias DaG 262, 996, 1042 and 1048 ± 2σ standard deviation.

6.2.3. Dar al Gani 400

Dar al Gani (DaG) 400 is a feldspathic polymict regolith breccia containing impact melt breccias (~50 % total volume), MAN, gabbroic and noritic anorthosites, granulitic clasts and mineral fragments in a pale glassy matrix. Accessory minerals are spinel, ilmenite, FeNi metal, troilite, and silica (Zipfel et al. 1998; Cahill et al. 2004; Joy et al. 2010).

^{40}Ar-^{39}Ar age indicate at least 6 or 7 resetting events, including one at ~3.8 Ga, during the impact cataclysm, with the last one at ~2.4 Ga (Bogard et al. 2000; Cohen et al. 2005). Cosmogenic nuclides indicates a short exposure to cosmic rays, between 1 and 3 Ma (Scherer et al. 1998).

DaG 400 has shown similarities in bulk rock composition and mineralogy to DaG 1058, and both meteorites were found in close locations, indicating that both rocks are probably paired (Korotev and Irving 2013).

The source location for DaG 400/1058 was investigated using bulk rock FeO, TiO_2 and Th compositions ± 3σ standard deviation (Table 6.1). The results indicate that the probable source origin of this sample is located in the central farside, although some matches were found in the western and eastern limbs of the FHT-O (Figure 6.4). These possible areas are similar to those proposed in previous studies, Joy et al. (2010) suggested the central farside or the western and eastern parts of the FHT-O terrane as possible launch locations.

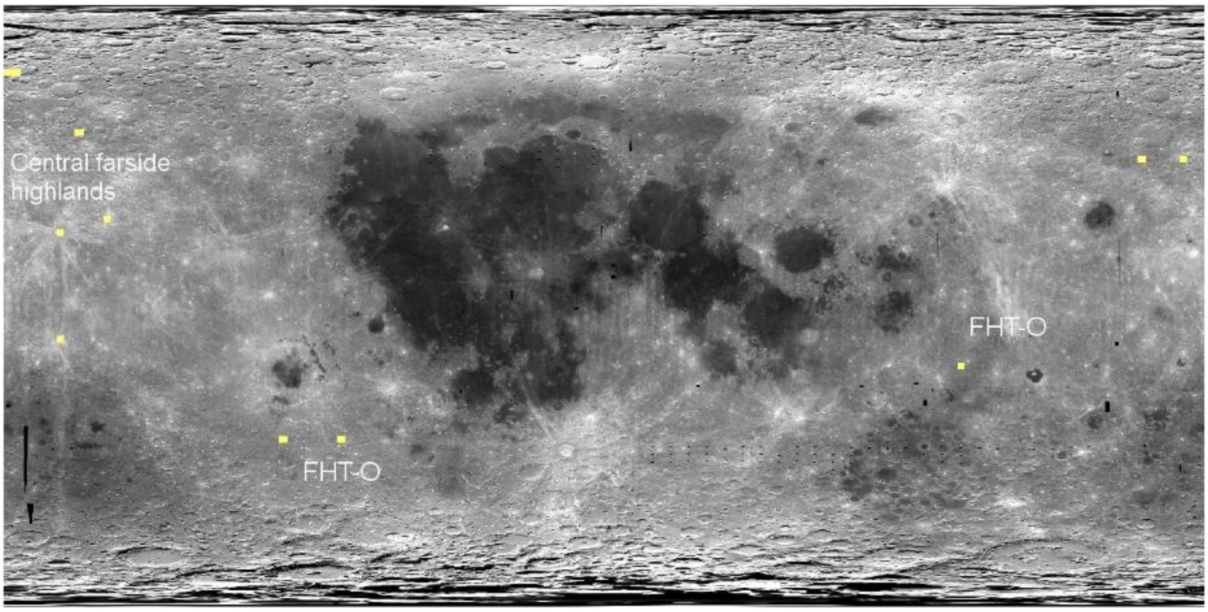

Figure 6.4 Identification of lunar regolith with similarities in composition to the averaged bulk rock DaG 400 ± 3σ standard deviation.

6.2.4. Dhofar 025/301/304

Dhofar (Dho) 025 is a regolith breccia formed from lithic clasts of anorthositic to troctolitic-anorthositic compositions. Monomict rocks are crystals of plagioclase (An_{96-98}) with olivine inclusions (Fo_{69-80}). Polymict rocks are recrystallized anorthosites (MAN) and crystalline melt rocks formed mainly by plagioclase (An_{94-98}) with minor amounts of mafic minerals (Mg# 64-83). Accessory minerals include spinel, ilmenite, FeNi metal, troilite, and silica (Cahill et al. 2004; Warren et al. 2005). Dho 301 and 304 are two clast-rich impact melt breccias containing clasts of impact-melt breccia, igneous rocks and granulites, and mineral fragments, in a fine-grained impact melt matrix (Nazarov et al. 2002; Demidova et al. 2003).

^{40}Ar-^{39}Ar analysis on DaG 025 indicates three distinct resetting events at ~4.0, ~3.1 and ~0.5 Ga (Cohen et al. 2002). The exposure age was estimated to be 5 Ma with a total transition time of 13-20 Ma. This meteorite also exhibited a long terrestrial age between 0.5-0.6 Ma (Nishiizumi and Caffee 2001).

Grouping relationships among these meteorites were established on the basis of similarities in mineral chemistry, matrix composition and the proximity where they were found (Russell et al. 2003; Demidova et al. 2007; Korotev 2012).

Investigation of the possible launch source of this group (Table 6.1) have shown many possible locations within the near and the farside of the Moon (Figure 6.5). Other authors have suggested a farside origin for Dho 025 (Taylor et al. 2001; Leont’eva et al. 2005), in any case far from the KREEP-enhanced Apollo 16 highland samples. This is consistent with my results where all the matches are far from the Apollo 16 landing site.

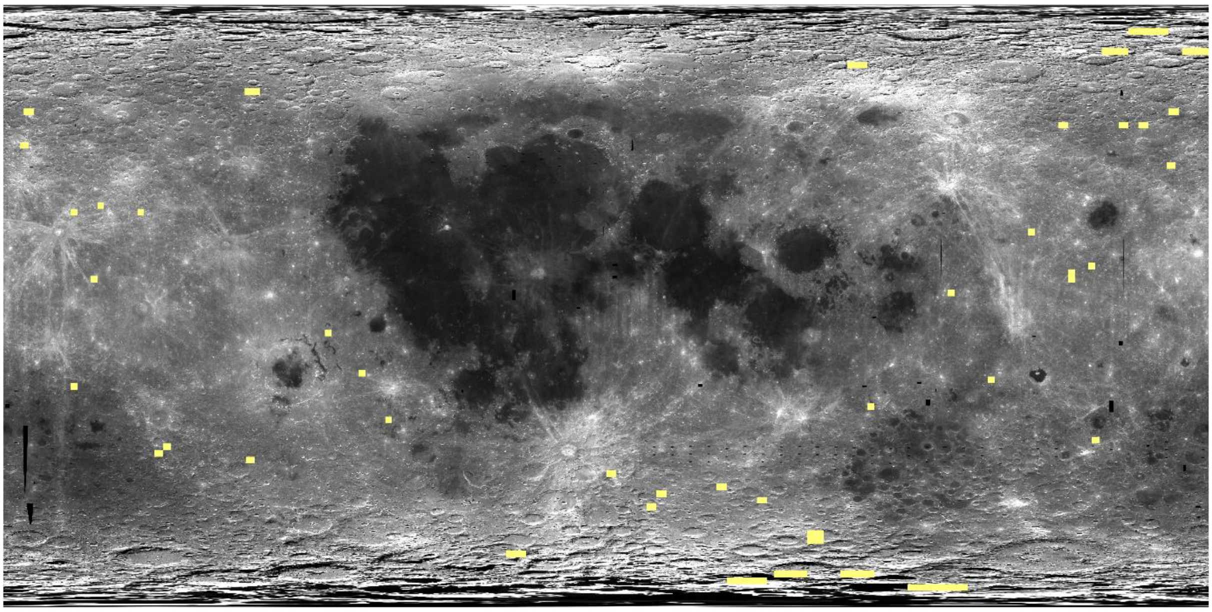

Figure 6.5 Image showing the area where surface regolith composition measurements match the analytical composition of averaged Dho 025/301/304 ± 2σ standard deviation.

6.2.5. Dhofar 026

Dhofar (Dho) 026 is a clast-poor, shocked, partially melted, granulitic breccia with compositions close to FAN (James et al. 2003; Cohen et al. 2004). Other authors identified this meteorite as an impact melt breccia (e.g. Warren et al. 2005). Dho 026 is grouped with other 11 smaller stones (Dho 457-468) discovered in its proximity on the basis of their compositions and petrography (Korotev 2012).

^{40}Ar-^{39}Ar systems have recorded a resetting event in the meteorite at 0.5 Ga (Cohen et al. 2002). However, the impact melt nature of the sample has made difficult the age determination of this meteorite as reported by Cohen et al. (2002) and Fernandes et al. (2004). Dho 026 has very low concentrations of cosmogenic radionuclides and noble gases, limiting the transfer time between the Moon and the Earth to ~ 10^4 years (Shukolyukov et al. 2001), an ejection from a depth of ~4-5 m , and a regolith exposure time of ~10 Ma (Nishiizumi and Caffee 2001).

FeO, TiO_2 and Th bulk rock compositions of Dho 026 and grouped stones were averaged and the 2σ standard deviation calculated to investigate their possible source region (Table 6.1). The most probable launch location is in the western limb of the Moon: a cluster of results appeared to the north of Mare Orientale (Figure 6.6), although a farside central highlands origin should not be completely dismissed. A similar origin location was previously suggested by Taylor et al. (2001) based in the FAN nature of this meteorite and the lack of KREEP components.

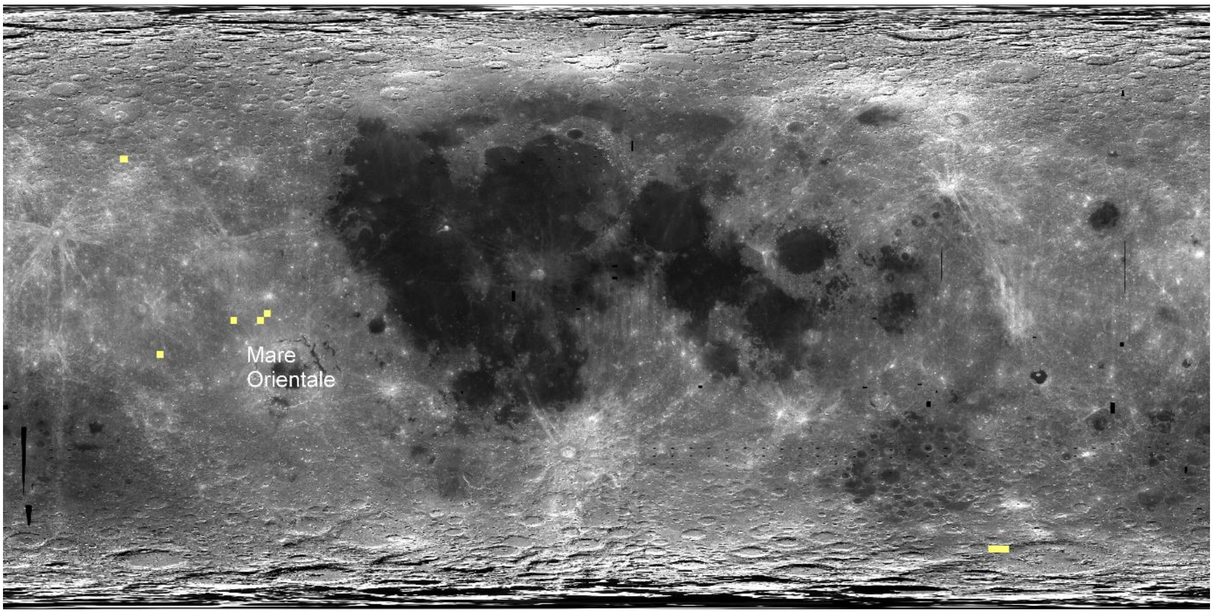

Figure 6.6 Identification of lunar regolith with similar compositions to averaged Dho 026 group ± 2σ standard deviation.

6.2.6. Dhofar 081/280

Dhofar (Dho) 081 is a fragmental breccia formed by clasts of anorthosites (both FAN and MAN), impact melt breccias, bimineralic clasts, granulites and mineral fragments in a glass and melt-rich matrix with no regolith component observed (Greshake et al. 2001; Cahill et al. 2002; 2004).

Dho 280 is a regolith breccia formed by lithic clasts (up to 2 cm) and mineral fragments (0.5-5 mm) in a matrix composed by impact melt glass and fine-grained mineral fragments (Anand et al. 2002). Lithic clasts comprise mainly feldspathic fragments, impact melt and regolith breccias. This meteorite is considered paired to Dho 081 based on their similarities in mineralogy, chemistry and cosmogenic nuclide (Cahill et al. 2002; Nishiizumi et al. 2004).

^{40}Ar-^{39}Ar analysis performed in plagioclases from Dho 280 included in the matrix, have indicated ages of 2.33 ± 0.41 and 2.77 ± 0.61 Ga (Fernandes et al. 2004), and recorded resetting events <1 Ga (Korochantseva et al. 2016). Exposure studies indicate that Dho 081/280 were ejected from a depth between ~80 cm and 1 m on the Moon at 40 ± 20 kyr ago, and they experienced a transition time from the Moon to the Earth shorter than 10000 years (Nishiizumi et al. 2004).

Bulk rock FeO, TiO_2 and Th compositions from Dho 081 and 280 were averaged and the 2σ standard deviation used to study possible launch regions (Table 6.1). The results indicate that the probable origin locations for these meteorites are located on the farside of the Moon (Figure 6.7). This is consistent with the lack of basaltic and KREEP-rich lithologies within both samples.

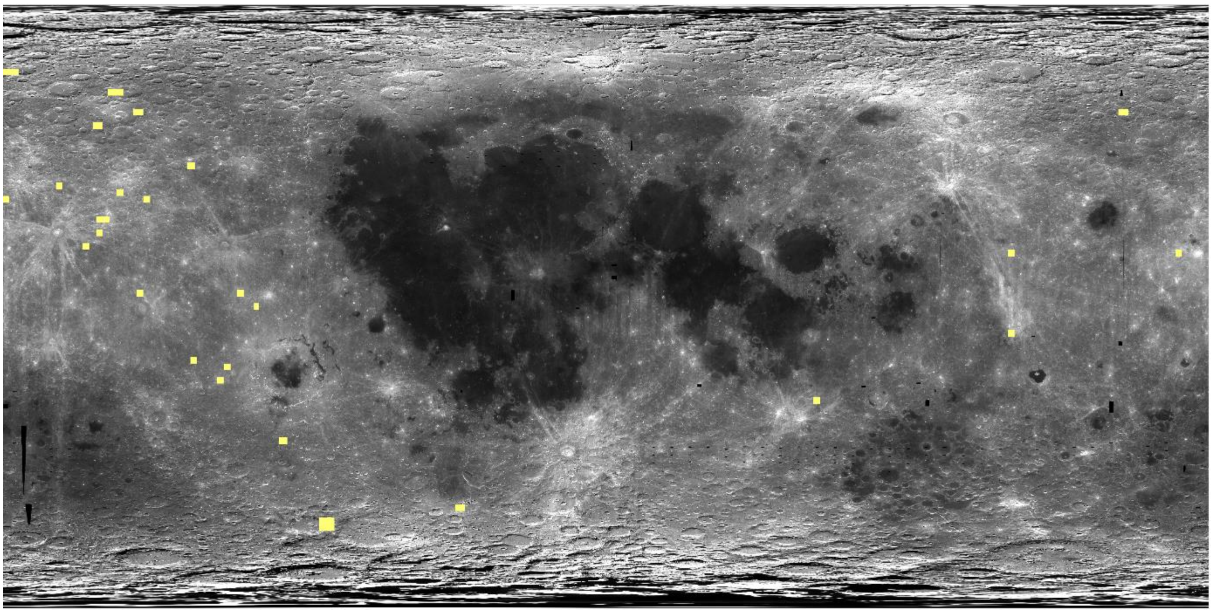

Figure 6.7 Identification of lunar regolith with similarities in composition to the averaged FeO, TiO2 and Th abundances of Dho 081 and 280 ± 2σ standard deviation.

6.2.7. Dhofar 302

Dhofar (Dho) 302 is a clast-rich impact melt breccia formed by lithic clasts and mineral fragments in a poorly crystallized impact melt glassy matrix. Clasts include impact melt breccias, anorthosites (FAN and MAN) and granulites of anorthositic, gabbro-noritic and troctolitic compositions. In addition, some KREEP-rich glass fragments were found (Nazarov et al. 2002; Korotev 2012). Radiogenic ages or exposures have not been reported for this sample.

Bulk rock FeO, TiO_2 and Th compositions reported for this sample were averaged and together with the 2σ standard deviation used to investigate its possible launch region (Table 6.1). It was found that large areas of the farside lunar highlands match the compositions of this meteorite (Figure 6.8). However, the presence of KREEP-bearing clasts suggests that its possible source should not be far from the PKT in the nearside of the Moon. The inconsistency between my results and the petrography observed within the sample, could be because the KREEP-bearing clasts are not larger enough in size nor abundant enough to account in the bulk-rock composition of the sample. More bulk-rock compositional data would be needed in order to constrain further the Dho 302 provenance

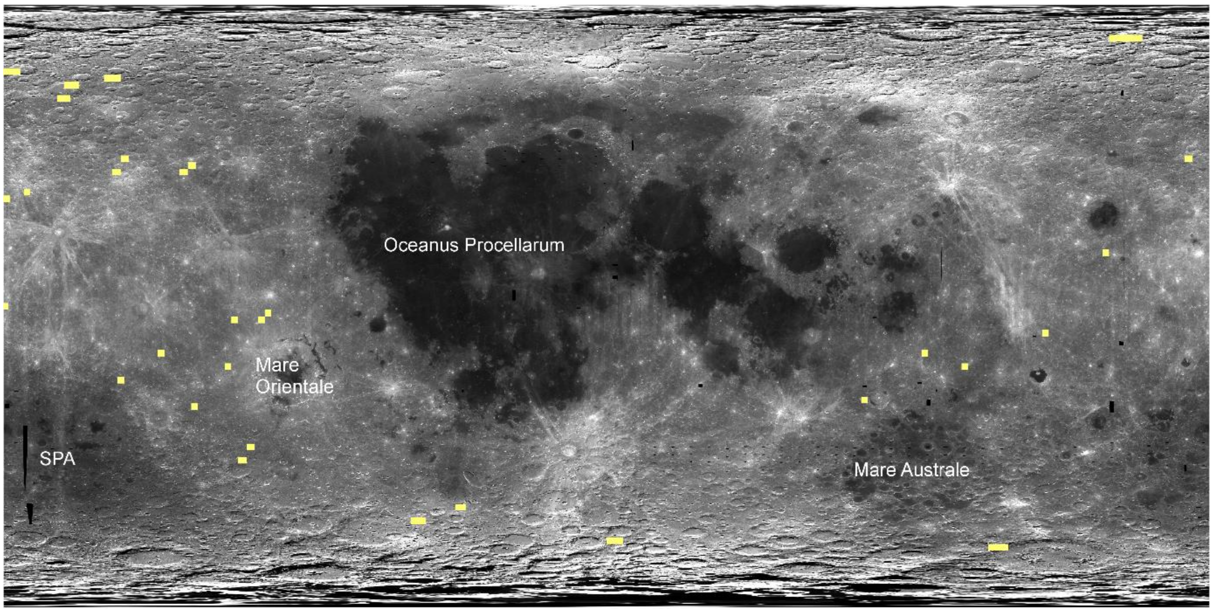

Figure 6.8 Regolith compositions that match the composition of regolith breccia Dho 302 ± 2σ standard deviation.

6.2.8. Dhofar 489 group

The Dhofar (Dho) 489 group is a collective of 16 individual impact melt breccia stones (Dho 489/303/305-307/309-311/730/731/908/909/911/950/1085/2047) formed of lithic clasts and mineral fragments of magnesian nature in a fine-grained crystalline impact melt or glassy matrix. The lithic clasts comprise cataclastic magnesian anorthosites, troctolites, gabbros, impact melt breccias and granulites of anorthositic and troctolitic composition (Takeda et al. 2003; 2006; Nazarov et al. 2003; Korotev et al. 2006).

^{40}Ar-^{39}Ar analysis have given three ages for Dho 303: one between 4.0 to 4.4 Ga, a second one ~3.6 Ga and a younger one at ~2.44 Ga (Fernandes et al. 2004). Dho 489 and 908 have yielded ages of ~4.2 Ga. These ages are likely to be resetting events due to major impact events (Nyquist et al. 2011). Exposure ages were obtained in Dho 489 showing a transition time of 6 ± 2 kyr and an ejection depth over 4 m (Nishiizumi et al. 2004).

The likely launch origin for this group is within the farside highlands of the Moon (Table 6.1; Figure 6.9). These results are consistent with remote sensing observations carried out by other authors that also place the source of this group in the northern farside crust (Korotev et al. 2006; Arai et al. 2008; Takeda et al. 2008; 2010; 2012; Nagaoka et al. 2011). However, my results also show that few other areas within the FHT-O should be considered as possible provenances.

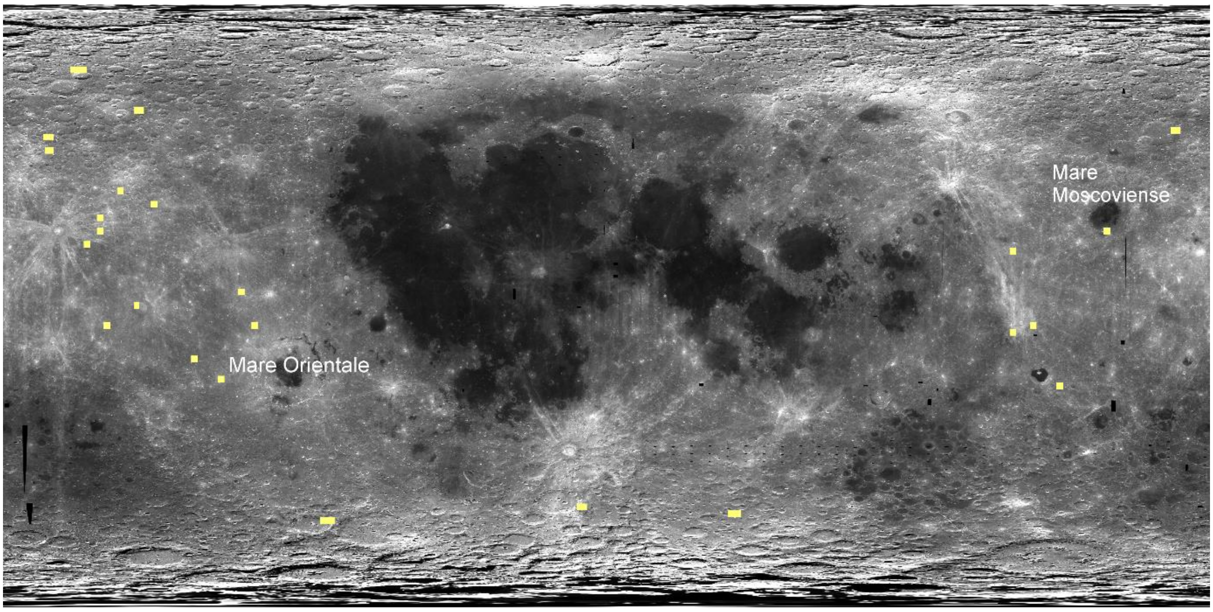

Figure 6.9 Areas where surface regolith composition measurements match the analytical composition of the averaged stones Dho 303/305-307/310/311/489/730 ± 2σ standard deviation.

6.2.9. Dhofar 490

Dhofar (Dho) 490 is an anorthositic fragmental breccia with clasts (<3 mm) of impact melt breccias, impact melts, gabbroic anorthosites and large feldspar crystals in a glassy, fine-grained matrix (Russell et al. 2003). No ages have been reported for this meteorite.

My results have shown that areas within the farside highlands region are the most likely launch origin for this meteorite (Table 6.1; Figure 6.10). A farside launch provenance is consistent with the lithologies, the mineral compositions, and the lack of any basaltic or KREEP components.

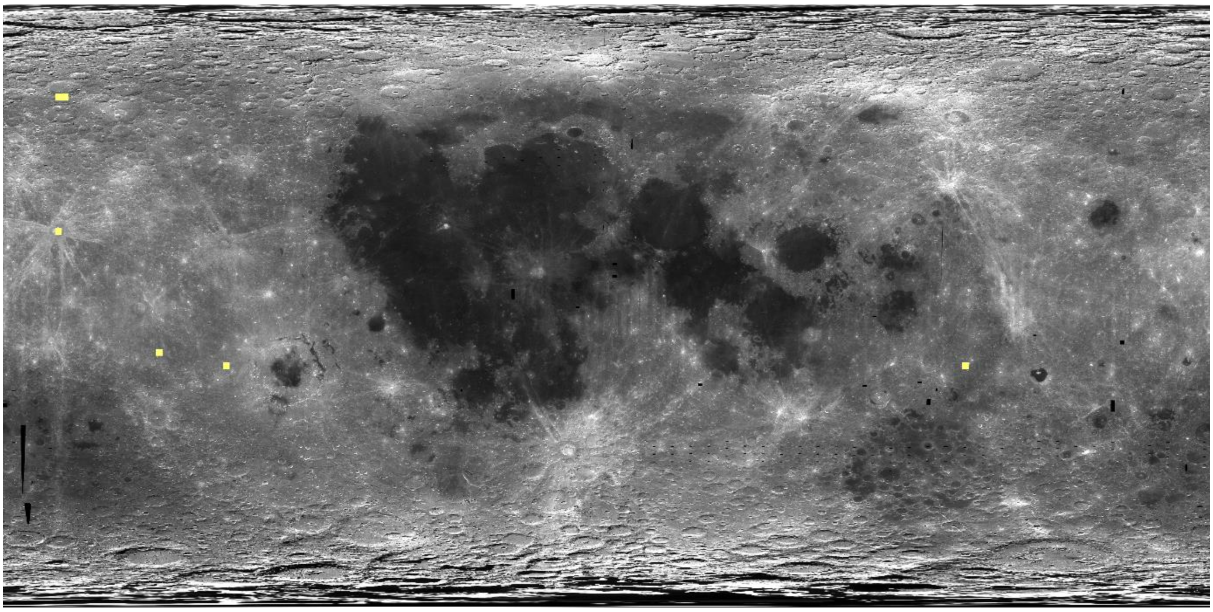

Figure 6.10 Identification of lunar regolith with similarities in composition to Dho 490 ± 4σ standard deviation.

6.2.10. Dhofar 733

Dhofar (Dho) 733 is a granulitic breccia with granoblastic or poikiloblastic texture (Greshake and Kurz in Russell et al. 2003; Demidova et al. 2007; Foreman et al. 2008). Bulk-clast compositions in granulites indicates that they probably derive from a MAN protolith. This meteorite differs from the other feldspathic meteorites in having higher bulk rock Na and Eu concentrations, about twice compared to other meteorites. This could be because the plagioclase is more sodic than the typical plagioclase observed on lunar samples (Foreman et al. 2008; Korotev et al. 2009).

^{40}Ar-^{39}Ar dating indicates that the meteorite was affected by impact events younger than 1 Ga, a short transition time (~0.5 Ma) and a low exposure age (~1.8 Ma; Shukolyukov et al. 2004; Korotev 2012; Korochantseva et al. 2016).

The results obtained from this study show the farside of the Moon and both the eastern and western limbs as possible launch sources (Table 6.1; Figure 6.11). Foreman et al. (2008) suggested that this meteorite does not derive from alkali anorthosites that are the product of the PKT, but rather derives from the feldspathic highlands; this agrees with the results obtained during this work, where all results are localized in areas far from the PKT.

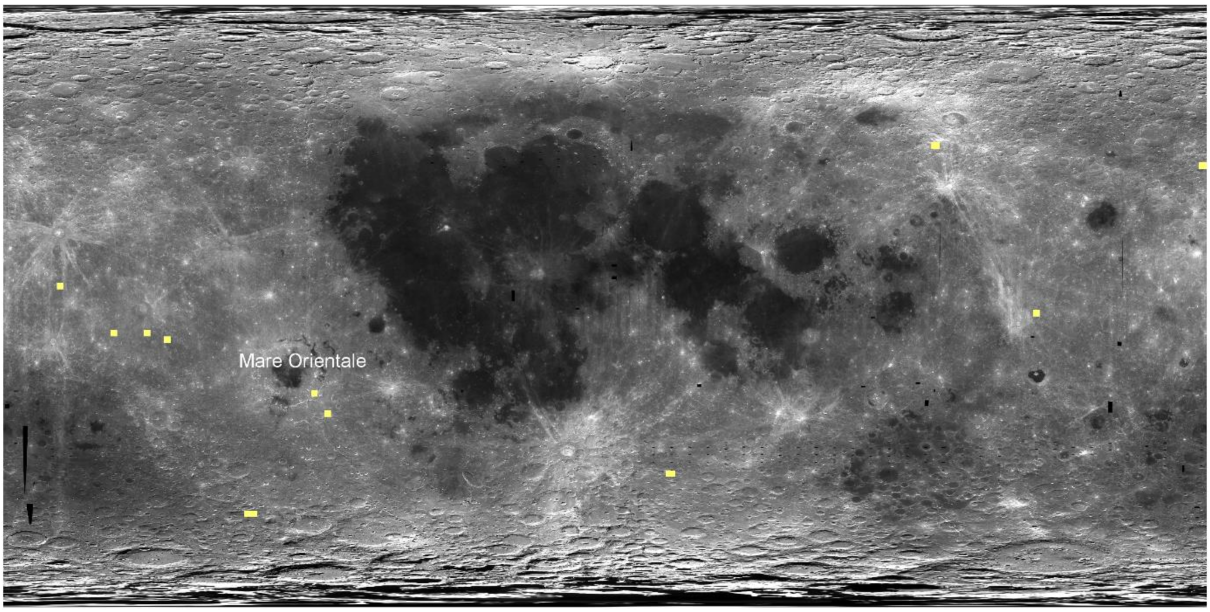

Figure 6.11 Image showing the area where surface regolith composition measurements match the analytical composition of Dho 733 ± 2σ standard deviation.

6.2.11. Dhofar 1436/1443

Dhofar (Dho) 1436 is an impact melt breccia formed by lithic clasts and mineral fragments in a glassy matrix. Lithic clasts of sizes between 0.1-7 mm, comprise impact melt breccias, granular breccias and rocks of ferroan anorthositic, gabbro-anorthositic and gabbro-noritic compositions (Connolly et al. 2007; Korotev 2012). Dho 1443 is an anorthositic fragmental breccia with anorthosites of FAN compositions and impact melt clasts in a partially molten matrix (Weisberg et al. 2009).

Both rocks are considered paired based in their identical composition and similar petrography (Korotev 2008). ^{40}Ar-^{39}Ar analysis for Dho 1436 have shown ages between 3 and 4.2 Ga (Korotev et al. 2009; Korochantseva et al. 2016).

Investigations of the launch origin (Table 6.1) suggest two possible origins for this sample: Mare Orientale and north of Mare Australe (Figure 6.12). The meteorite is at the mafic end of the range for feldspathic meteorites, which could indicate a portion of basalts from Orientale or Australe, however no mare basalt has been reported for these rocks until date (Korotev 2012). I increased the σ value for this meteorite in order to see other areas that possibly have similar compositions to these meteorites. Figure 6.13 shows that most of the lunar crust with the exception of the Apollo 16 landing site area (nearside central highlands) match the given bulk-rock composition. These results within the highlands and the lack of basaltic clasts could indicate that the mafic signature of the meteorite is not the result of basaltic clasts in the sample but of material from deeper zones of the lunar crust.

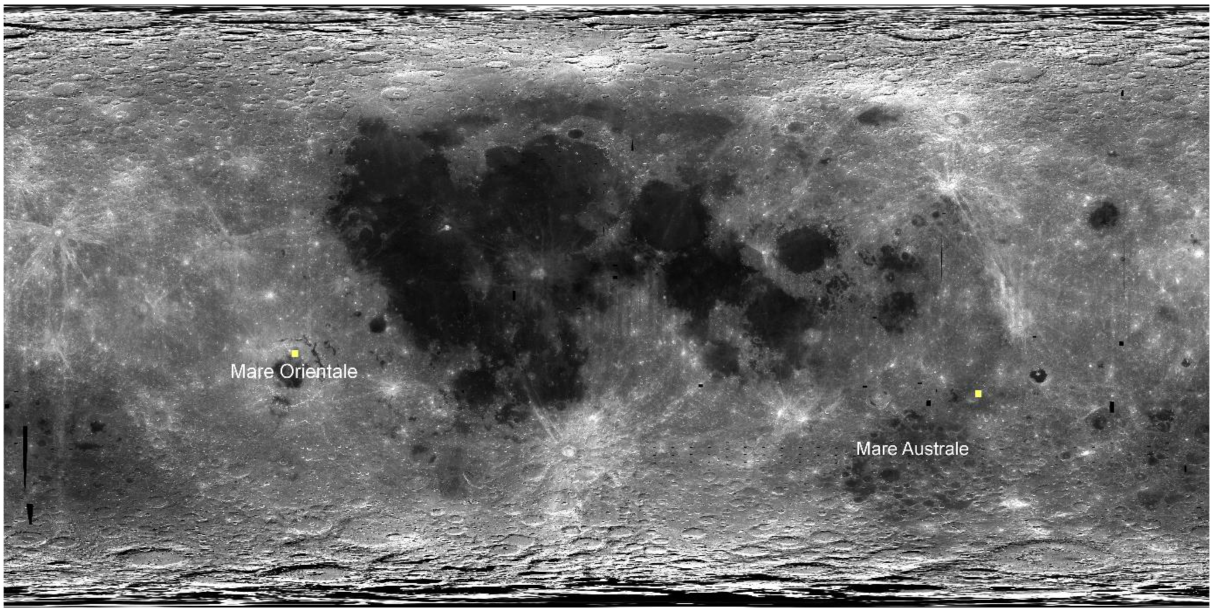

Figure 6.12 Identification of lunar regolith with similar compositions to fragmental breccia Dho 1436/1443 ± 3σ standard deviation.

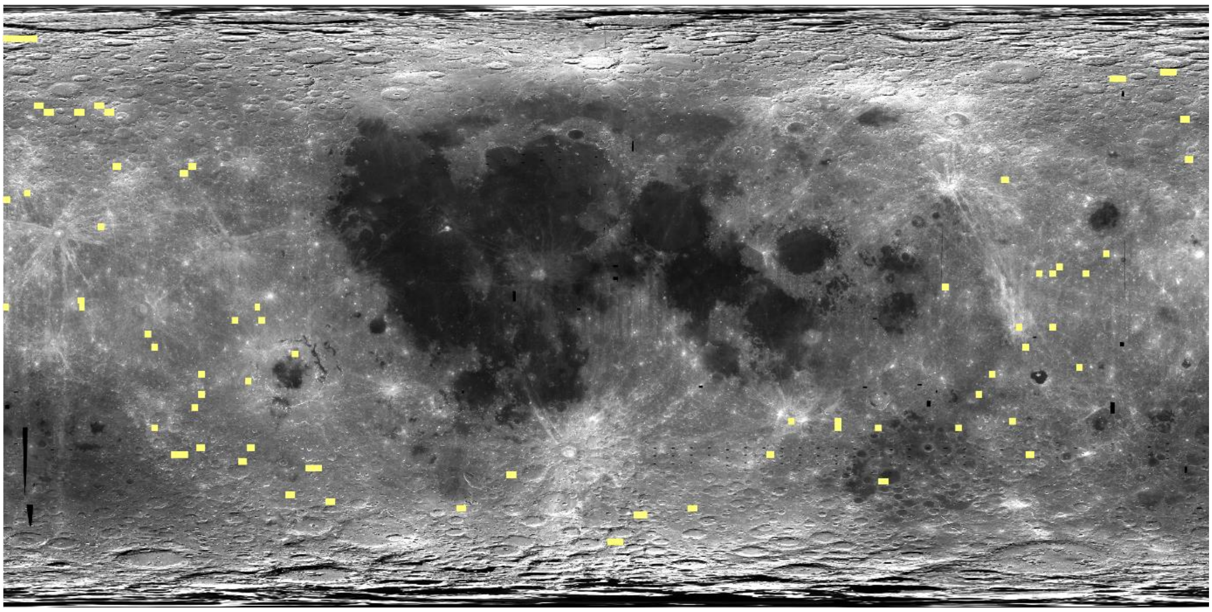

Figure 6.13 Image showing lunar regolith that matches bulk-rock Dho 1436/1443 FeO, TiO_2 and Th compositions ± 4σ standard deviation.

6.2.12. MacAlpine Hills 88105

MacAlpine Hills (MAC) 88105 (and its paired stone MAC 88104) is a polymict fragmental breccia with lithic clasts and mineral grains in a fine-grained, fragmental and partly glassy matrix. The clasts are ferroan anorthosites, granulites, highland impact melt glasses, impact melt breccias, and VLT and low-Ti basaltic fragments (Lindstrom et al. 1991a; Lindstrom et al. 1991b; Delano 1991; Neal et al. 1991; Koeberl et al. 1991b; Joy et al. 2010). One high-Ti basalt clast was also reported (Robinson et al. 2012)

^{40}Ar-^{39}Ar analysis indicates that 6 to 9 impact events are recorded in MAC 88105, from ~4 Ga to ~2.5 Ga, including an impact event ~3.9 Ga consistent with the cluster of ages observed in the Apollo and other meteoritic samples (Bogard et al. 2000; Cohen et al. 2005). Cosmogenic nuclides indicate that the meteorite lay within a few meters below the lunar surface for ~150 Ma and it was ejected <1.6 Ma (Eugster 1990; Vogt et al. 1991).

Bulk rock composition of this meteorite (Table 6.1) shows similarities to the regolith from the northern farside highlands and the southern limbs of the nearside, such as the surroundings of Tsiolkovskiy and Lacus Excellentiae (Figure 6.14). As previously noted, the presence of basaltic clasts in the sample indicates that the launch region of this meteorite should not be far from the source of these basaltic clasts (e.g. Robinson et al. 2012). The VLT and low-Ti basaltic clasts suggest a likely source within the eastern and western limbs of the lunar nearside, however a high-Ti basaltic clasts source should exist in the vicinity of the launch region of this meteorite. The farside should not been completely dismissed since there are patches of mare (e.g. Tsiolkovsky), some of them could contain small areas of high-Ti basalts not observed by the remote sensing instruments.

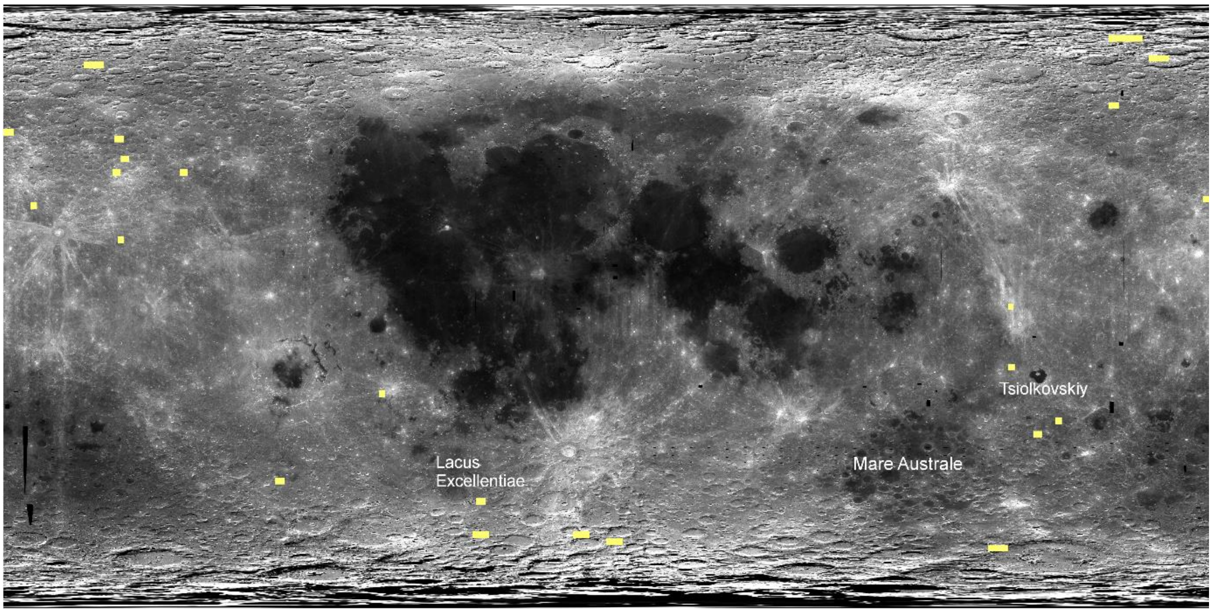

Figure 6.14 Identification of lunar regolith with similarities in composition to the fragmental breccia MAC 88105 ± 2σ standard deviation for each FeO, TiO_2 and Th bulk rock compositions.

6.2.13. Northwest Africa 482

Northwest Africa (NWA) 482 is a crystalline impact melt breccia which mineralogical and bulk-rock composition indicates a FAN-like to FAN-MAN-like anorthositic parent lithologies. No KREEP or basaltic fragment has been observed (Warren and Kallemeyn 2001; Daubar et al. 2002).

Isotopic analysis indicates resetting events from ~3.6 to ~3.1 Ga (Daubar et al. 2002; Joy et al. 2014), and the meteorite experienced an exposure time of ~2.07 Ga according to Lorenzetti et al. (2005), although other authors obtained shorter exposure times of ~199 Ma (Joy et al. 2014).

This investigation indicates a possible launch origin within the farside highland crust of the Moon (Table 6.1; Figure 6.15). Other authors, based on petrographic and chemical observations, as well as fact that this meteorite does not have any ages that precede the Imbrium impact, have also suggested a farside highland launch location (Daubar et al. 2002; Takeda et al. 2010).

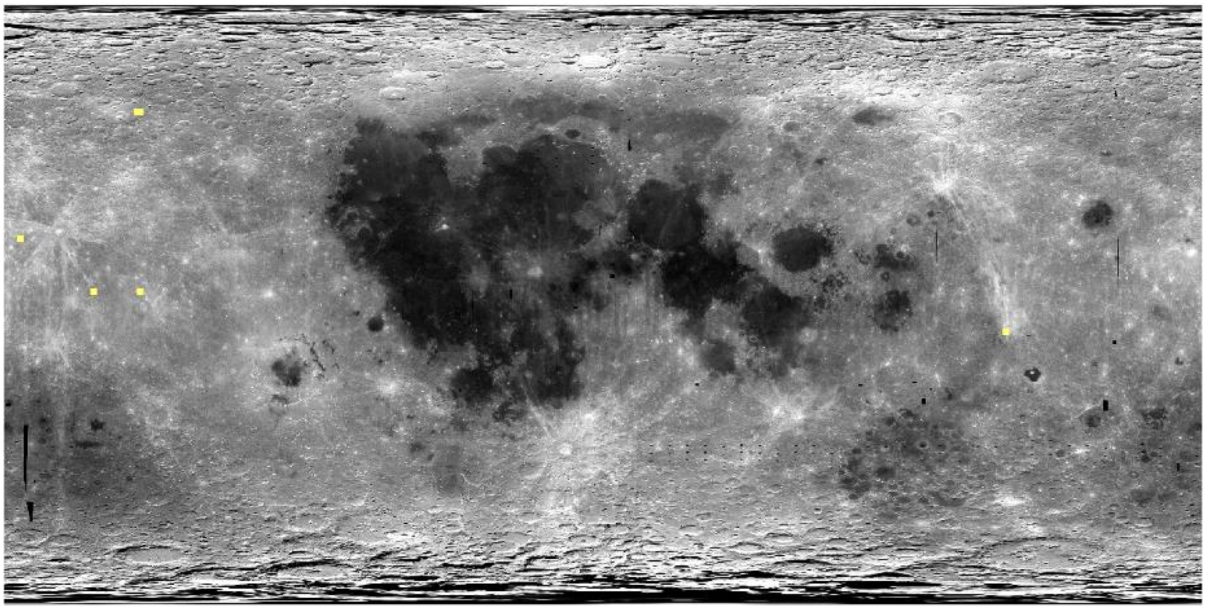

Figure 6.15 Image showing the area where surface regolith composition measurements match the analytical compositions (yellow) of the averaged bulk-rock FeO, TiO_2 and Th crystalline impact melt breccia NWA 482 ± 2σ standard deviation.

6.2.14. Northwest Africa 4936

Northwest Africa (NWA) 4936 is a glassy impact melt breccia containing small mineral fragments and lithic clasts in a very fine-grained matrix. The mineral fragments include anorthitic plagioclase, pigeonite, augite, olivine Mg-bearing ilmenite, troilite, and FeNi metal grains. Lithic clasts comprise troctolitic clasts and some mare basalts. This meteorite has signatures indicating components from FAN and MAN lithologies (Korotev et al. 2009).

Using bulk rock FeO, TiO_2 and Th abundances ± 2 standard deviation (Table 6.1) compositional similarities with lunar regolith was investigated. The results show matches in the surroundings of the mare regions on the nearside (including the Apollo 16 landing site), as well as the surroundings of the SPA basin (Figure 6.16). Korotev et al. (2009) reported compositional similarities to the Apollo 16 regolith samples, indicating that the possible launch site could be close to the Apollo 16 landing site. More bulk-rock analytical and petrographic data will be needed in order to constrain further the provenance of this meteorite.

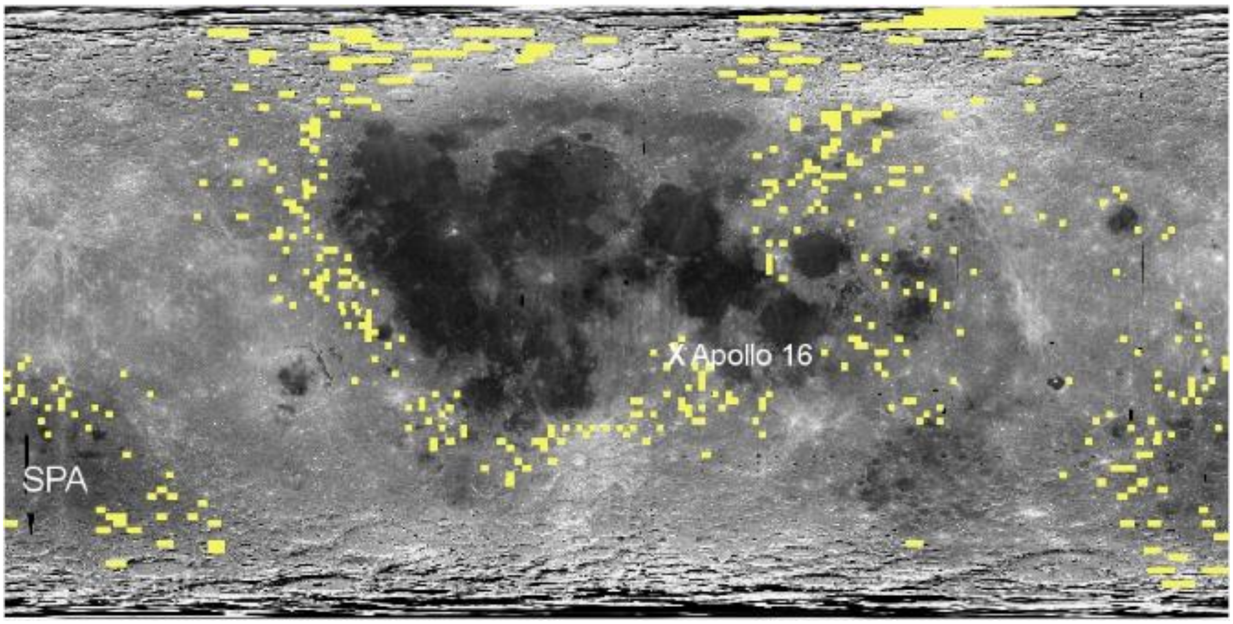

Figure 6.16 Identification of lunar regolith with similarities in composition to the averaged bulk rock NWA 4936 ± 2σ standard deviation.

6.2.15. Pecora Escarpment 02007

Pecora Escarpent (PCA) 02007 is a polymict regolith breccia formed of lithic clasts in an extremely fine-grained matrix. Lithic clasts include FAN, MAN, noritic and troctolitic clasts, granulites, agglutinates, impact melt glasses and occasionally basaltic fragments of mare and non-mare affinitites (Taylor et al. 2004; Day et al. 2006; Korotev et al. 2006; Joy et al. 2006; 2010). Cosmogenic radionuclide concentrations indicate exposure time on the lunar surface (<1 cm) of ~3 Ma for PCA 02007 and a terrestrial age <30 Kyr (Nishiizumi et al. 2006).

All the results suggests an origin within the FHT-O terrane, some of them are very close to cryptomare regions (Table 6.1; Figure 6.17). These matches agree with previous results based on bulk rock compositions and petrography where it was suggested that the basaltic clasts could be samples from cryptomare origin (Joy et al. 2010).

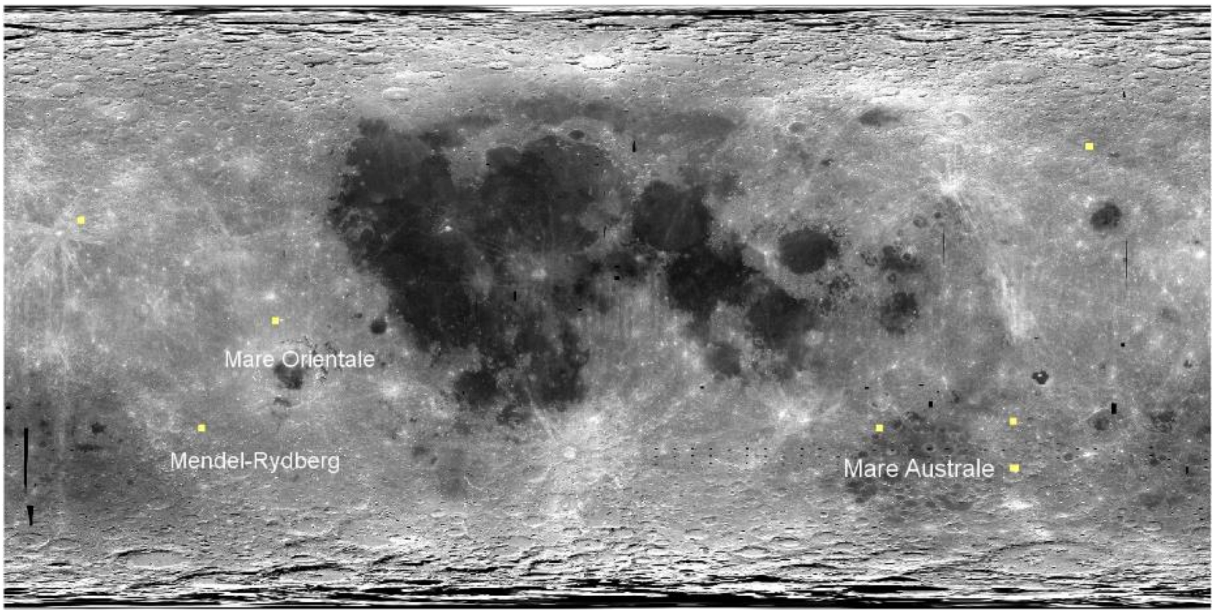

Figure 6.17 Locations of regolith composition measurements match the analytical compositions (yellow) of the averaged bulk-rock FeO, TiO_2 and Th regolith breccia PCA 02007 ± 3σ standard deviation.

6.2.16. Queen Alexandra Range 93069/94269

Queen Alexandra Range (QUE) 93069 (and paired stone 94269) is a clast-rich regolith breccia with melt rock clasts (<1.5 mm) and mineral grains that include plagioclase and glass fragments (Warren and Kallemeyn 1995; Warren et al. 2005; Spettel et al. 1995; Lindstrom et al. 1995; Grier et al. 1995; Korotev 1996; Koeberl et al. 1996; Bischoff 1996). All the clasts and mineral fragments have compositions similar to FAN, with the exception of one mineral fragment with a Mg# of 64 that appear to have been derived from HMS (Koeberl et al. 1996).

Cosmogenic radionuclides indicate a long exposure age for this meteorite (~400 Ma) at a depth <10 cm. It was ejected ~0.25-0.3 Ma, experienced a Moon-Earth transfer of ~0.16 Ma and had a terrestrial age between 0.05 to 0.1 Ma (Thalmann et al. 1996; Nishiizumi et al. 1996).

Bulk rock FeO, TiO_2 and Th abundances ± 2 standard deviation (Table 6.1) matches regolith compositions from several highland regions both from the farside and the nearside of the Moon (Figure 6.18). Robinson et al. (2012) suggested that it is possible to discriminate possible launch areas based in the VLT to low-Ti nature of two basalt clasts found in the meteorite. Using this approach we could dismiss a possible origin within the farside FHT due to the lack of mare regions, suggesting that the eastern and western limbs of the nearside are the most probable source for this meteorite. The existence of clasts that maybe derive from HMS rocks could indicate either that the rock was launched from areas relatively close to PKT, although the meteorite does not appear to have an enhance KREEP signature, or that the presence of HMS lithologies are not necessary related with the presence of KREEP.

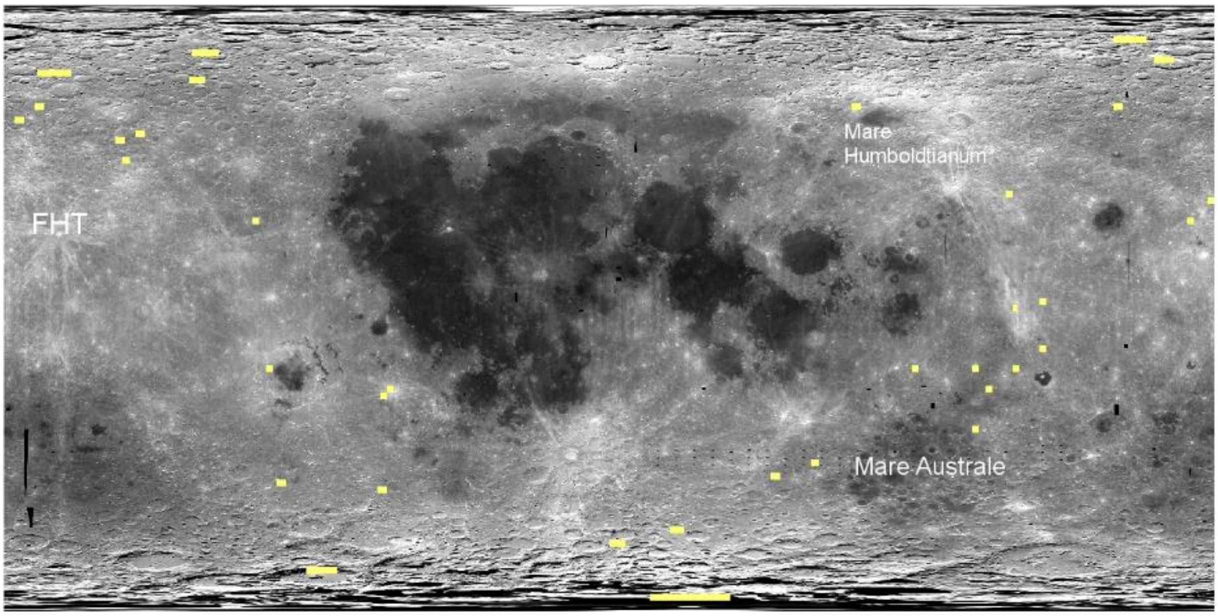

Figure 6.18 Identification of lunar regolith with similarities in composition to the regolith breccia QUE 93069 ± 2σ standard deviation for each FeO, TiO_2 and Th bulk rock compositions in yellow.

6.2.17. Yamato 791197

Yamato 791197 is a polymict regolith breccia with lithic clasts and mineral fragments in a fine-grained to glassy matrix. The lithic clasts are magnesian granulites, granulitic breccias, polymict fragmental breccias and impact melt breccias (Ostertag et al. 1985; Lindstrom et al. 1986). A VLT basalt clast has also been reported (Goodrich and Keil 1987). Mineral fragments are mostly plagioclases (An_{95-97}), although occasional clinopyroxene and olivine (Fa_{36-49}) have been reported (Ostertag et al. 1985; Lindstrom et al. 1986).

Isotopic studies indicated a formation age of >4.0 Ga for Yamato 791197, and it was brecciated ≤4.0 Ga (Nakamura et al. 1986; Kaneoka and Takaoka 1986). The meteorite was ejected ~0.06 Ma from the near surface of the Moon (<10 cm; Takahashi and Masuda 1987; Nishiizumi et al. 1991).

Bulk rock FeO, TiO_2 and Th compositions ± 2σ standard deviation (Table 6.1) match regolith compositions from areas within the western and eastern areas of the FHT-O. Any matches were found in the Apollo 16 landing site (Figure 6.19).

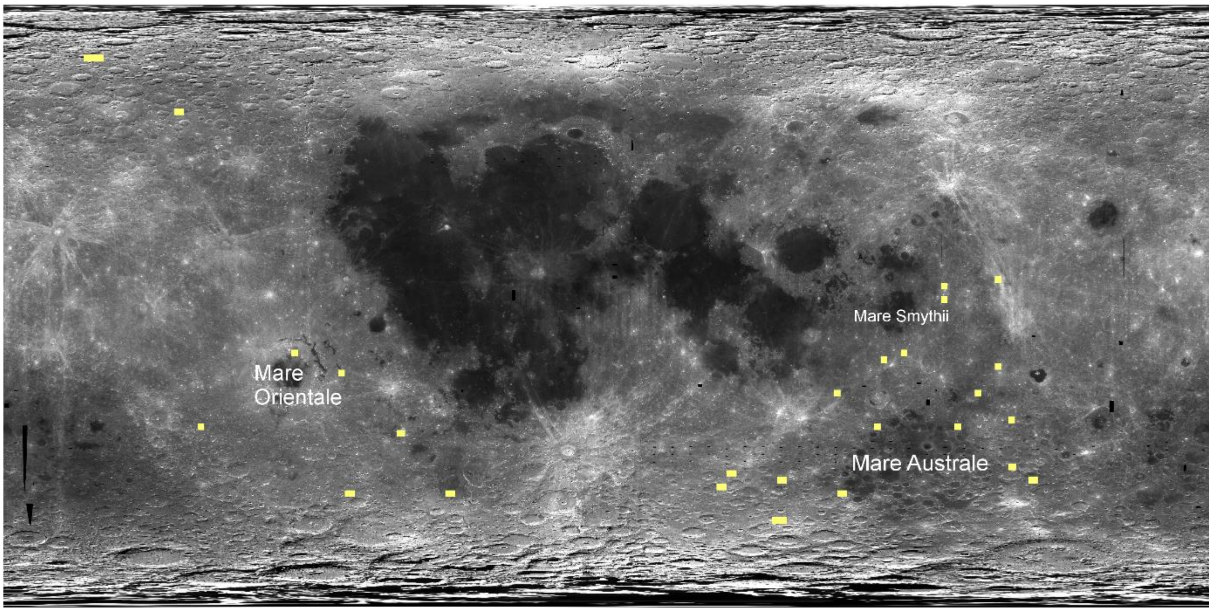

Figure 6.19 Identification of lunar regolith with similarities in composition to the regolith breccia Yamato 791197 ± 2σ standard deviation for each FeO, TiO_2 and Th bulk rock compositions in yellow.

6.2.18. Yamato 82192/82193/86032

Yamato 82192, 82193 and 86032 are polymict fragmental breccias formed by lithic and mineral fragments in a fine-grained, compacted clastic matrix. The lithic clasts are FAN, magnesian granulitic breccias probably derived from a MAN photolith, crystalline impact melt breccias and some low-Ti basalts. Some regolith component has been observed as well as very minor troilite and Ca-phosphate. No KREEP carrying lithic component has been described in these meteorites (Takeda et al. 1987; 1989; Bischoff et al. 1987; Goodrich and Keil 1987; Koeberl et al. 1990; Yamaguchi et al. 2004; 2010; Nyquist et al. 2006).

^{40}Ar-^{39}Ar and U-Pb analyses indicate a formation age for the protolith of the Yamato stones of ~4.4 Ga (Tatsumoto and Premo 1991; Kaneoka and Nagao 1993; Bogard et al. 2000; Nyquist et al. 2006), and resetting events at 4.1 Ga, indicating the initial brecciation of the material, and a final melt and assembly at 3.8 Ga (Kaneoka and Takaoka 1986; Eugster et al. 1989; Tatsumoto and Premo 1991) The rock experienced shallow shielding from cosmic rays at ~15 cm depth and it had an exposure in free space of ~10 Ma. Finally, the meteorite has a terrestrial age between 70000 and 80000 years (Eugster 1988; Eugster et al. 1989).

During this work, it was found that 4 matches within the surroundings of the Mendel, a couple of matches in the FHT and a single match in Mare Australe (Figure 6.20) match the bulk-rock compositions of this meteorite (Table 6.1). All these matches agree with previous authors who have suggested the farside highlands as possible launch origin based on bulk-rock compositions and lack of KREEP (Takeda et al. 2007; Yamaguchi et al. 2010). The observation of low-Ti to VLT basalt clasts within the meteorite, suggest that Mendel surroundings or Mare Australe could be the source region for these meteorites since cryptomare and mare patches have been reported in that area (Whitten and Head 2015).

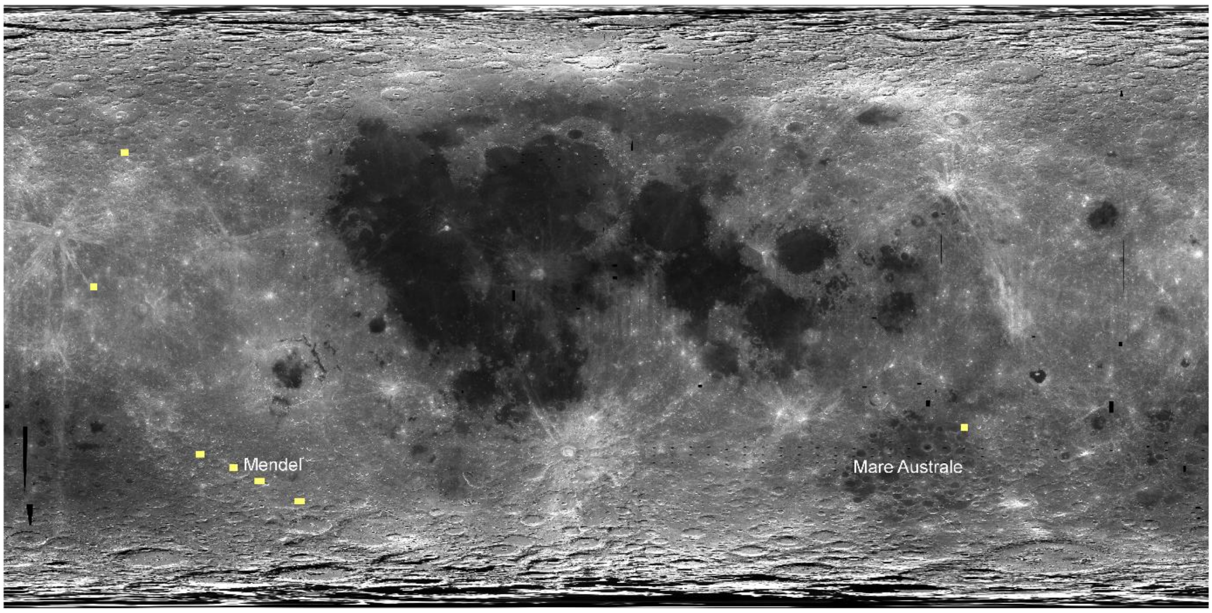

Figure 6.20 Identification of lunar regolith with similarities in composition to the averaged bulk rock Yamato 82192/82193/86032 ± 2σ standard deviation.

6.2.19. Dhofar 925/961

Dhofar (Dho) 925 and 961 are polymict impact melt breccias containing abundant lithic clasts and mineral fragments in a glassy impact melt matrix. The lithic clasts are crystalline and clast-bearing glassy impact melt breccias, magnesian granulites, VLT crystalline basalts and KREEPy rocks with plagioclase (An_{92-96}) and Fe-rich olivine (Fo_{49-59}). Mineral clasts are mainly plagioclases (An_{88-98}) and pyroxenes and olivines with a wide range of compositions (Demidova et al. 2005; Zeigler et al. 2010; Joy et al. 2014). Dho 925 and 961 have been considered paired based in find locations and petrographic descriptions (Demidova et al. 2005; Zeigler et al. 2010).

U-Pb analyses in phosphates indicate an age of ~4.0 Ga of crystallization for impact melt within Dho 961 and a ~3.8 Ga upper limit for the lithification age of the meteorite (Joy et al. 2014). However, ^{40}Ar-^{39}Ar studies in impact melt breccias indicates ages of ~3.5 and ~3.4 Ga that could represent the youngest age for the meteorite (Cohen et al. 2016).

Many matches were obtained for these meteorites including the SPA basin, Mare Australe, the maria in the eastern nearside, even Mare Moscoviense appears as a possible launch region (Table 6.1; Figure 6.21). Previous works have suggested a launch origin within the SPA basin based in compositional differences with Apollo samples collected from the PKT but high REE abundances (Jolliff et al. 2009; Zeigler et al. 2013; Joy et al. 2014; Cohen et al. 2016). My results indicate that a SPA origin is possible but other locations cannot be excluded yet. The study of crystallization ages of impact-melts contained in the meteorite will help to dismiss or not a SPA origin.

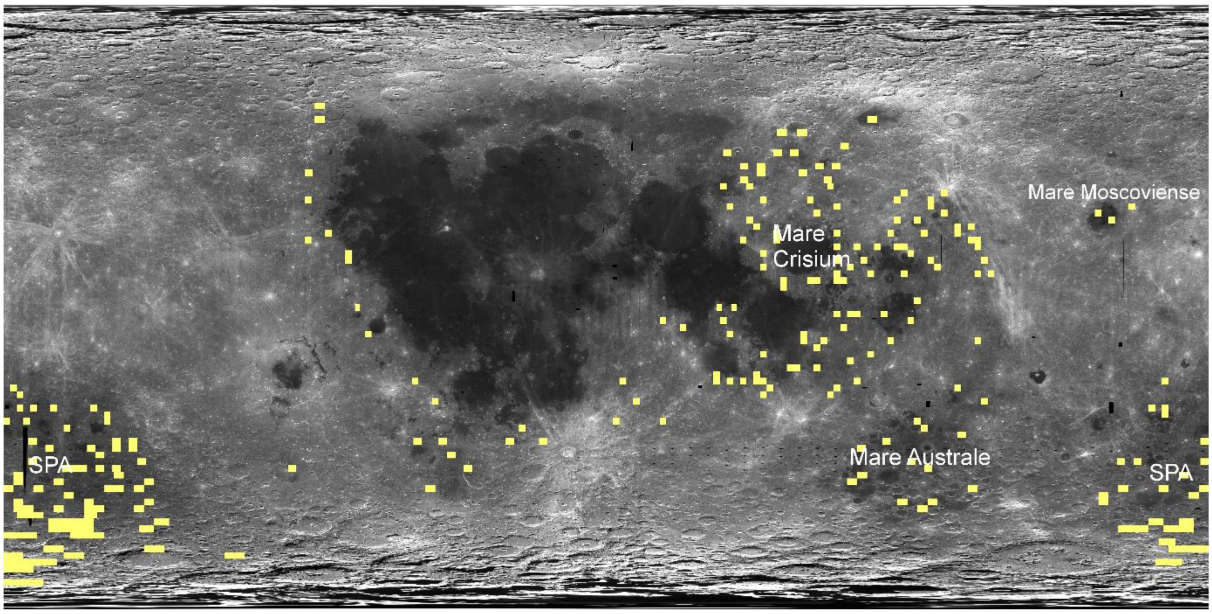

Figure 6.21 Surface regolith composition measurements match the analytical compositions (yellow) of the averaged bulk rock FeO, TiO_2 and Th of Dho 925 and 961 ± 2σ standard deviation.

6.2.20. Sayh al Uhaymir 300

Sayh al Uhaymir (SaU) 300 is a polymict crystalline impact melt breccia formed by lithic clasts and mineral fragments in a microcrystalline (<10 μm) matrix of anorthositic olivine-gabbro composition. Lithic clasts include glassy impact melts, impact melt breccias, ferroan anorthosites, troctolitic anorthosites, noritic gabbros, and anorthositic gabbros. No KREEP or basaltic component was found in this meteorite (Bartoschewitz et al. 2005a; Hudgins et al. 2007; Hsu et al. 2008).

The meteorite has experienced at least two episodes of shock metamorphism, first the impact melt matrix was formed and the lithic and mineral clasts brecciated. A second impact ejected the rock from depth (as indicated by low concentrations of solar-wind gases) to the lunar surface, shocking and altering the mineral and lithic clasts (Hudgins et al. 2007). K-Ar analysis indicates a minimum crystallization age of ~2.9 Ga, although because ^{40}Ar could have been lost during thermal metamorphism, it is probable that the real crystallization age for this meteorite is older (Bartoschewitz et al. 2005b).

Four possible launch locations were obtained within the southern FHT-O from both the nearside and the farside (Table 6.1; Figure 6.22). SaU 300 consists in mafic but ferroan lithologies of the feldspathic highlands. It could be material of the lower crust excavated by basin forming impacts (Korotev et al. 2009) according to the presence of troctolitic and noritic material that could be derived from deeper layers of the lunar crust. Any of the matches are in the SPA basin, however, many of them are close to Mare Australe and areas that could have old impact basin that possibly excavated the lower crust.

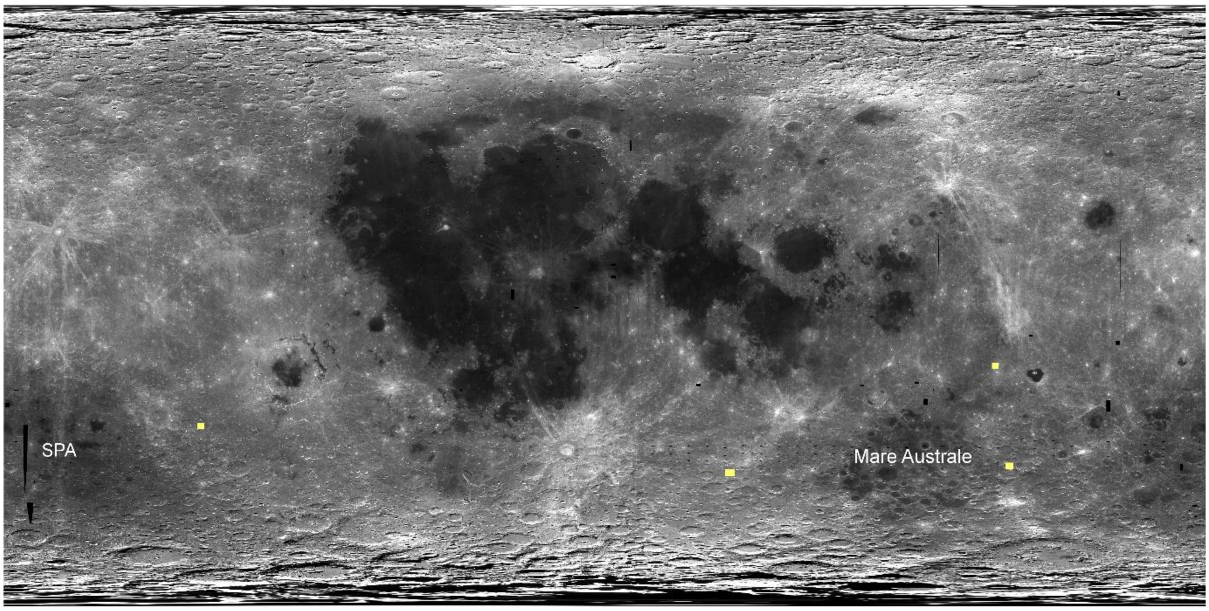

Figure 6.22 Image showing the areas where surface regolith composition measurements match the analytical composition of the impact melt breccia SaU 300 ± 2σ standard deviation.

6.2.21. Northwest Africa 4932

Northwest Africa (NWA) 4932 is a crystalline impact melt breccia very similar compositionally to SaU 300. It has been proposed by Korotev (2008) that the two stones may have been ejected from the Moon by a common impact. NWA 4932 is formed by gabbroic to troctolitic clasts, grains of kamacite and large grains of silica in a very fine-grained matrix (Korotev et al. 2009). It has not been reported any ages for this meteorite yet.

Most of the possible launch locations are located within the Mare Australe with some matches in the FHT-O in the farside, sparse matches in other FHT-O areas and even one match in SPA (Table 6.1; Figure 6.23).

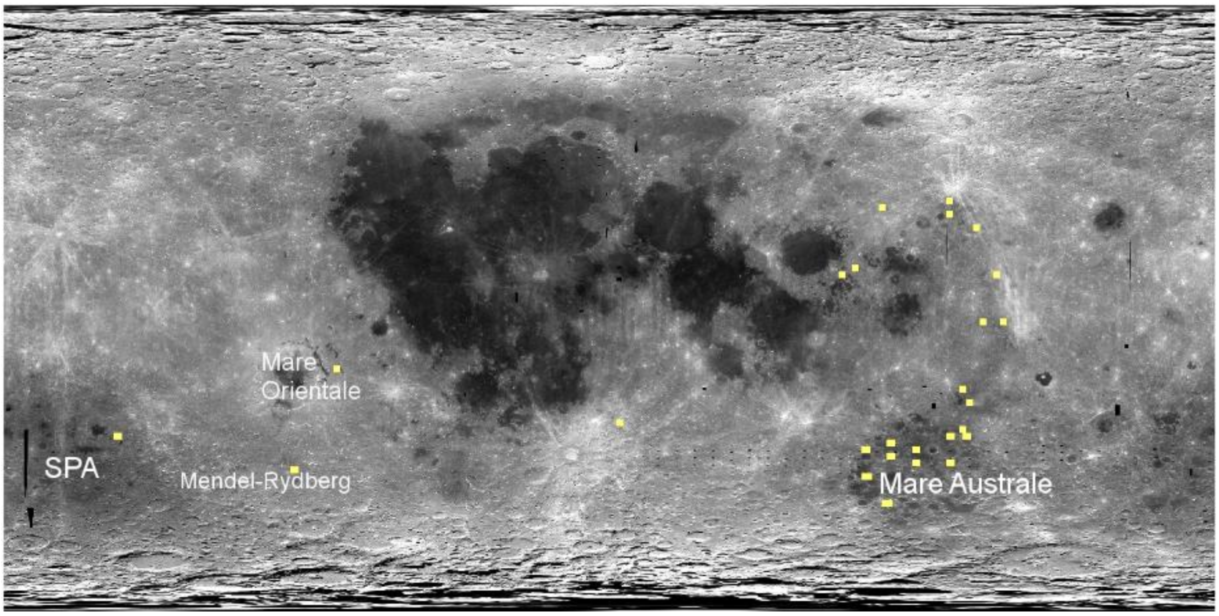

Figure 6.23 Image showing regolith composition that matches the composition of the impact melt breccia NWA 4932 ± 2σ standard deviation.

6.2.22. Northwest Africa 2996

Northwest Africa (NWA) 2996 is an impact melt breccia containing lithic clasts and mineral fragments. Lithic clasts include MAN, noritic and troctolitic anorthosites ($An_{\sim98}$), gabbros and impact melt clasts. Mineral fragments are anorthite, olivine ($Fo_{3\text{-}91}$) and low-Ca pyroxene. Lithic clasts and mineral fragments are included in a glassy matrix with abundant maskelynite and anorthitic melt and spheres of FeNi metal (Korotev et al. 2009; Mercer et al. 2013). Isotopic studies indicate an exposure duration to cosmic rays of 700-1000 Ma in the lunar surface (Hidaka and Yoneda 2013).

The results obtained for this meteorite (Table 6.1) indicate that the most likely sources are the surroundings of the eastern Mare Smythii and Margini, eastern peripheral regions of Mare Fecunditatis, Tranquillitatis and Serenitatis, and the interior of the SPA basin (Figure 6.24).

Previous studies have suggested similar areas as a possible origin for NWA 2996 (Mercer et al. 2013).

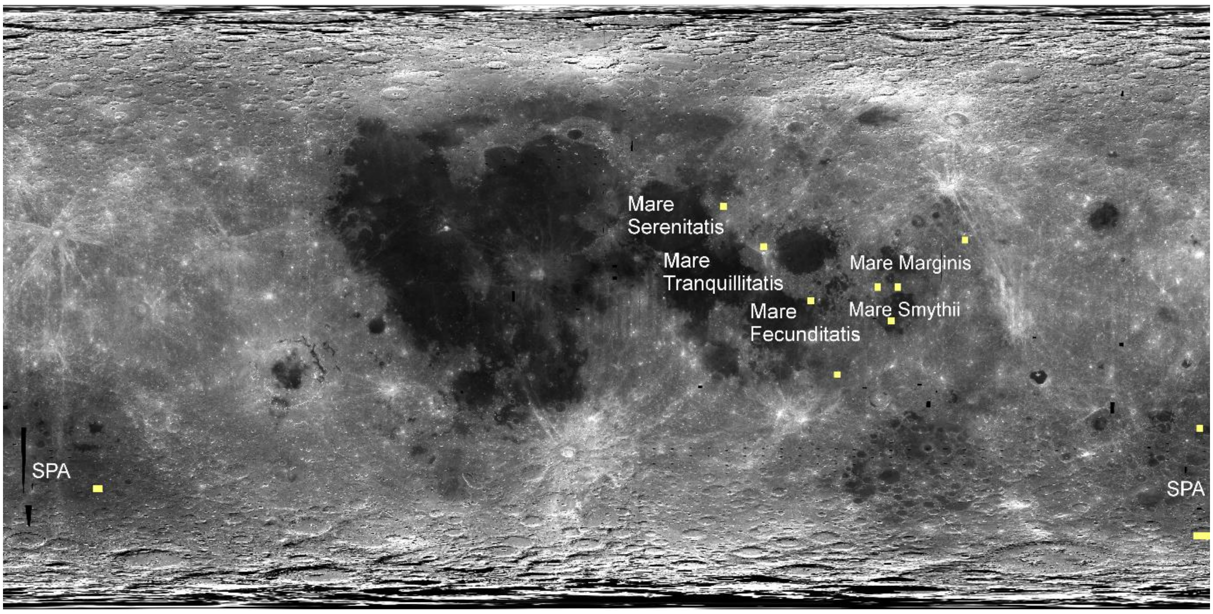

Figure 6.24 Areas where surface regolith composition measurements match the analytical compositions (yellow) of the averaged bulk rock FeO, TiO_2 and Th of NWA 2996 ± 3σ standard deviation.

6.3. Discussion

6.3.1. Distribution of ferroan and magnesian anorthosite

Remote sensing observations have shown differences between the farside and the nearside indicating that the former is more magnesian and less ferroan than the nearside (Arai et al. 2008; Ohtake et al. 2012; Crites and Lucey 2015). Also within the farside rocks, the main mafic phase appears to be olivine in contrast to the nearside whose main mafic phase is orthopyroxene (Arai et al. 2008). Although my results suggest the existence of FAN patches within the central farside highlands, it appears that this presence is minor compared to the nearside (Figure 6.25), supporting remote sensing observations.

Is the feldspathic lunar meteorite suite dominated by ferroan (i.e., Apollo-like) anorthosites or more magnesian anorthosites? From the feldspathic meteorites studied during this work, it was found that 7 contain clasts dominantly derived from magnesian anorthosite (MAN) lithologies (e.g., with mafic minerals Mg# >75). Eight meteorites contain a clast component of both ferroan and magnesian anorthosites and, 3 meteorites contain only FAN sourced clasts (e.g., with mafic minerals Mg# <75).

This diversity supports the idea that the magnesian anorthositic rocks may be more representative of the crustal composition of the lunar highlands than just ferroan anorthosites which were dominantly collected at the Apollo 16 landing site (e.g. Gross et al. 2014). However, although fewer meteorites contain FAN only sourced crustal rocks, my results suggest that these were sourced from a wide range of possible sites around the Moon. Meteorites with only FAN compositions (MAC 88105, Dho 026 and QUE 93069/94269) suggest that FAN lithologies are more abundant in the nearside and in some areas of the outer parts of the lunar farside, and less abundant within the central FHT. However, FAN material may also be present to a small extent within the central FHT, some FAN-MAN bearing meteorites were possible derived from the central farside highlands (e.g. Dho 081, Dho 302, NWA 482; Figure 6.25).

The outer feldspathic highlands (FHT-O) traditionally includes the highlands in the nearside close to the Apollo 16 landing site, as well as the eastern and western limbs of the Moon. However, based in the results obtained during this work it is possible to differentiate if the crust is more or less dominated by FAN or MAN between the Apollo 16 landing site terrane and the FHT-O situated in the Moon's limbs. Some of the meteorites studied (e.g. DaG 400, NWA 733) have shown matches with regolith both in the FHT and FHT-O, however, any of the meteorites have returned similarities with regolith from the surroundings of the Apollo 16 landing site and the limbs of the FHT-O at the same time. This suggests that although it was considered one terrane previously based on remote sensing observations (e.g. Jolliff et al. 2000), it is possible to differentiate between at least two distinct areas within the FHT-O (Figure 6.25). This difference is likely to be because these regions are dominated by different basin ejecta blankets (all sampling slightly different depths of the lunar crust). For example, samples from the Apollo 16 landing site are dominated by Imbrium ejecta (Norman et al. 1971; Stöffler et al. 1985; McKay et al. 1986). The compositional differences between these types of samples and those lunar meteorites launched from the FHT-O in the eastern and western limbs of the Moon probably is related to differences in pre-basin components of the Imbrium area and the Crisium regions.

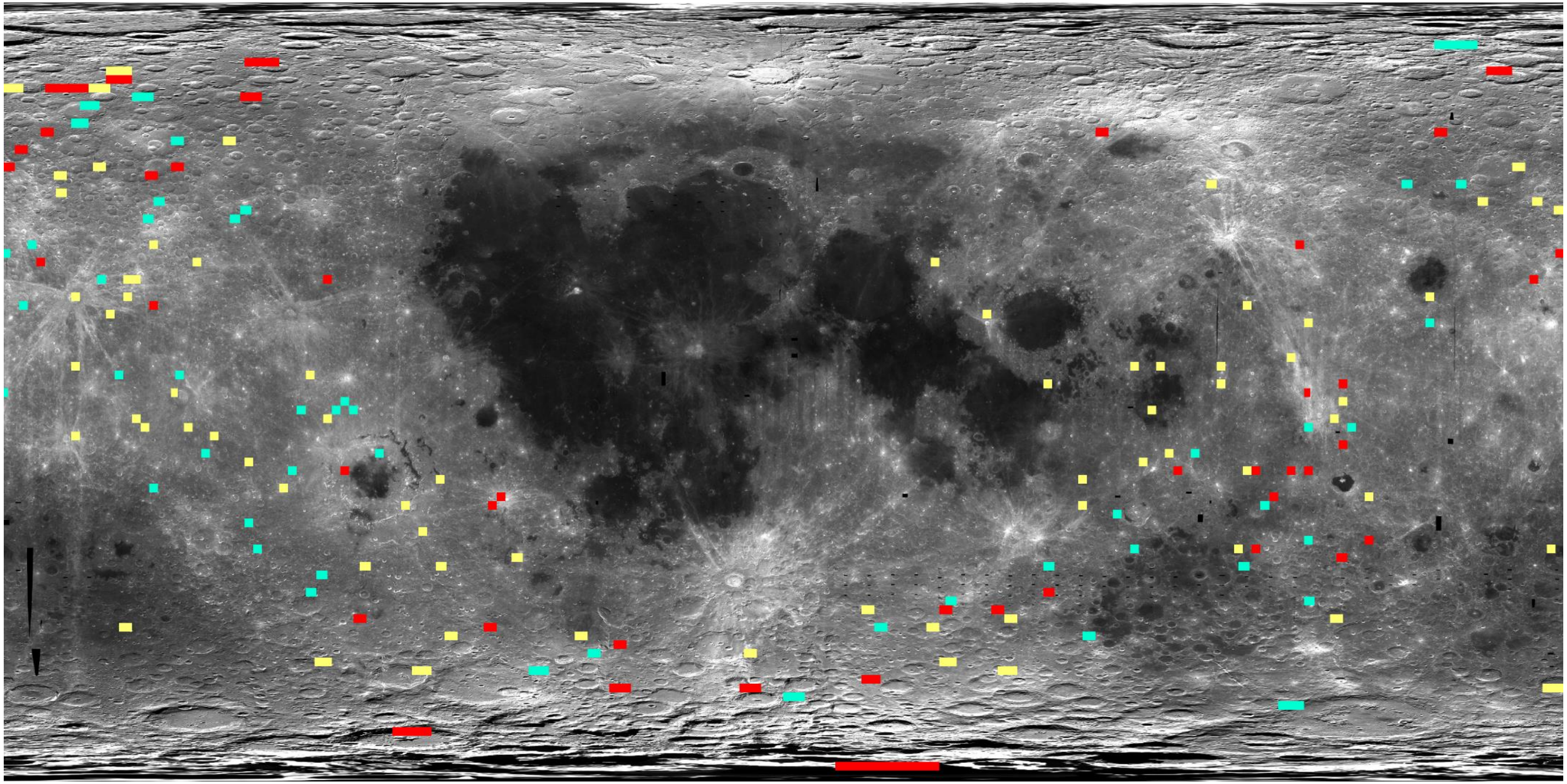

Figure 6.25 Image showing the distribution of possible launch regions for meteorites that only contains FAN lithologies in red (MAC 88105, Dho 026, SaU 300 and QUE 93069 and 94269), meteorites only containing MAN granulites in yellow (Dho 026, NWA 2996, Y 791197, DaG 400, Dho 489 and Dho 733), and meteorites that contain both FAN and MAN components in green (ALHA 81005, Dho 081, Dho 302, NWA 482, PCA 02007, Y 82192, NWA 4936 and DaG 262).

There is a key petrological difference between the types of magnesian lithologies found in lunar meteorites and those in the Apollo collection. Magnesian granulites have also been observed in the Apollo collection, however, these are enriched in a KREEP chemical component compared to MAN found in from meteorites derived from the FHT. Furthermore, MAN granulites possible derived from the FHT-O (e.g. ALHA 81005) contains more augite and almost twice the amount of titanium than MAN granulites from the farside (e.g. Dho 489 group; Treiman et al. 2010).

The wide range of meteorite compositions, ages, and distributions together with remote sensing observations suggest that the formation of the lunar crust is a process more complex than simply plagioclase flotation within the LMO (e.g. Gross et al. 2014; Russell et al. 2014). Lunar feldspathic lithologies exhibit some similarities to terrestrial massif anorthosites such as the high variation in Mg# within the mafic phases and the low variability in the An# in plagioclases (Gross et al. 2014). This suggests that the lunar crust could have been formed by serial magmatism (Longhi and Ashwal 1985; Longhi 2003) consisting of many bodies similar to massif anorthosites (Gross et al. 2014).

In this model, anorthosites are formed as plagioclase cumulates in layered mafic intrusions close to the crust-mantle boundary. Because of their lower density compared to the surrounding crust, they rise as diapirs, leaving their cogenetic mafic cumulates at depth (Longhi 2003; Borg et al. 2011; Gross et al. 2014). In this scenario, FAN lithologies would not be globally distributed but restricted to a small portion of the lunar crust (Gross et al. 2014). However, it is possible that the existence of FAN clasts in meteorites possibly derived from the central FHT could be the result of the large Mg# range on anorthosites formed by serial magmatism and not to be the direct product of the lunar magma ocean crystallization. This agrees with the mixture FAN-MAN components in meteorites possibly derived from the central highlands and the lack of meteorites with only FAN clasts from the same area.

6.3.2. Cryptomare regions

Yamato 82192/82193/86032 contains low-Ti basaltic clasts not represented by the Apollo samples and that probably represent ancient volcanism prior to the Imbrium basin event 3.8-4.1 Ga (Goodrich and Keil 1987; Yamaguchi et al. 2010). The absence of KREEP components within these rocks also suggest an origin far from the PKT (Yamaguchi et al. 2004). My results have indicate the Mendel cryptomare region as a possible source for this meteorite group. When these basaltic clasts are compared to the basaltic meteorite Kalahari 009 that have shown also results within the Mendel cryptomare region, some similarities are observed. Both the Yamato basaltic clasts and Kalahari 009 have low REE abundances, low Th content and a low-Ti nature (Karouji et al. 2004; Terada et al. 2007). It has been suggested that the Lomonosov-Fleming region is a possible source region for the Yamato group (Yamaguchi et al. 2010), however, no matches were obtained in that area using FeO, TiO_2 and Th abundances. Other regions as Mare Moscoviens and the Balmer-Kepteyn region can be dismissed based in the post-Nectarian age in the first case and the higher Th abundances in the second case (Giguere et al. 2003; Yamaguchi et al. 2010).

The feldspathic clasts of the Yamato group comprises FAN and magnesian materials that suggest that the sources and processes that create these magnesian rocks are not dependent on the presence of KREEP and therefore, not unique to the PKT.

6.3.3. Mare Australe

Mare Australe was originally thought to be a circular basin of ~ 900 km of diameter (Whitford-Stark 1979). More recent observations by NASA’s Gravity Recovery and Interior Laboratory (GRAIL) have shown that Mare Australe as originally described, does not have neither a Bouguer contrast nor relief indicative of a basin (Neumann et al. 2015). However, its northern part does have an open depression with a circular positive Bouguer anomaly suggesting the presence of a 600-km-diameter basin named Australe North (Figure 6.26; Neumann et al. 2015).

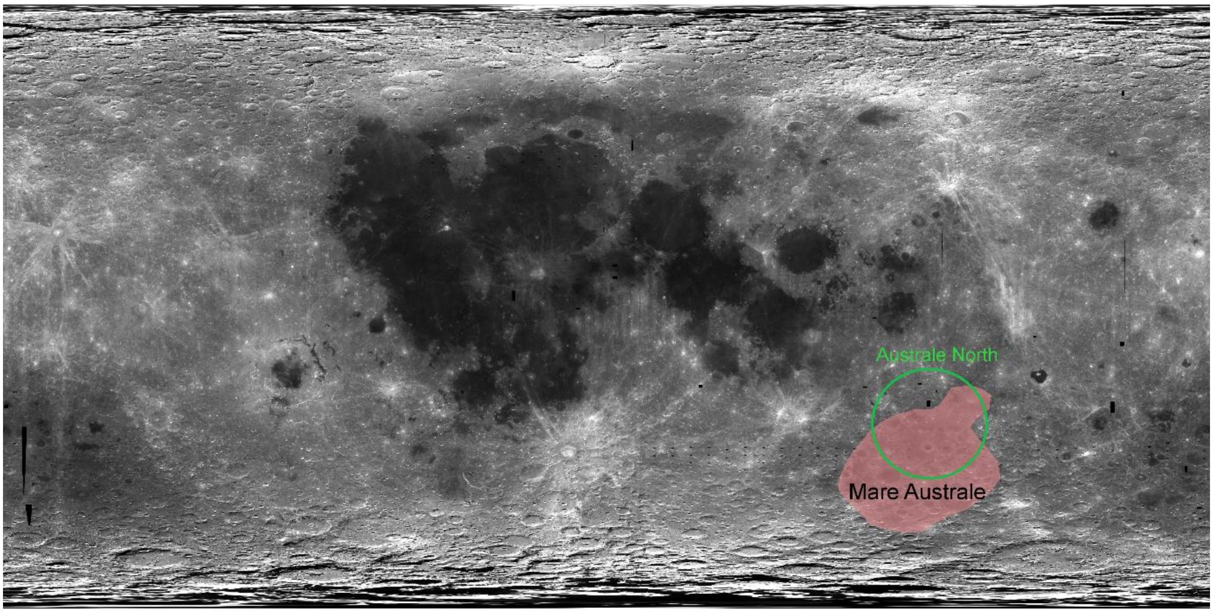

Figure 6.26 Mare Australe as traditionally delineated in red and Australe North proposed basin based on GRAIL data (Neumann et al. 2015) in green.

Three lunar meteorites have shown possible launch origin close or within Mare Australe: Dho 1436/1443, PCA 02007 and NWA 4932. These three rocks have in common the lack of KREEP components and the presence of clasts of gabbroic, noritic and troctolitic clasts. PCA 02007 also contains basaltic fragments of low-Ti to VLT that could be of cryptomare origin (Joy et al. 2010) but no basaltic clasts were reported in the other two meteorites. The more mafic compositions of these meteorites compared to the more feldspathic meteorites could be the consequence of a mixture between feldspathic and basaltic lithologies. However, those compositions are also similar to the compositions that should be expected from the lower crust of the Moon (Korotev et al. 2009). The meteorites possibly originating from Australe contain plutonic lithologies such as gabbros, troctolites and norites that could have been excavated from the deeper lunar crust (Taylor et al. 2004; Day et al. 2006; Korotev et al. 2006; Joy et al. 2006; 2010; Vaughan et al. 2013). ^{40}Ar-^{39}Ar analysis have shown disturbances, probably due to resetting events, between 4.2 and 3.0 Ga (Korotev et al. 2009; Korochantseva et al. 2016). If these meteorites were in fact launched from the Australe region, analysis of isotopic systems less susceptible to resetting events on clasts of impact melts and impact melt breccias could provide with an approximate age for the Australe North basin-forming impact event.

6.3.4. Basaltic contamination of feldspathic meteorites

Most of the basaltic clasts observed in the feldspathic meteorites described in this chapter are Low-Ti to VLT basalts, with the exception of a high-Ti basaltic clast reported in MAC 88105 (Robinson et al. 2012). This distribution agrees with the remote sensing observations that states that the high-Ti basalts in Mare Tranquillitatis are overrepresented in the Apollo collection (Robinson et al. 2012).

During this study, it has been observed than the meteorites with results only localized in the farside central highlands usually does not exhibit basaltic (mare or gabbroic) clasts (e.g. DaG 400, Dho 081/280, Dho 490, NWA 482). Although it has been observed that mare areas within the farside highlands, for example Mare Moscoviense, these occurrences are far less abundant than in the nearside. The absence of basalts in these samples suggest that if mare volcanism occurred on the farside of the Moon (after the period of basin formation), then any lavas must never have made it to the lunar surface and may only occur as dikes (Wilson and Head 2016; Head and Wilson 2016), confined deeper in the farside crust: thus, the impacts that sampled these meteorites were not able to reach them.

6.4. Conclusions

Results obtained from the study of possible launch origin of lunar feldspathic meteorites suggest that the lunar crust is highly heterogeneous. It has been observed that magnesian anorthosites appear to be more representative of the lunar crust that the ferroan anorthosites from the Apollo 16. The results of this study support this statement but it also suggests that ferroan anorthosites are widely distributed although less abundant within the central farside highlands. The large number of feldspathic meteorites that contains both magnesian and ferroan anorthosites could indicate that they are genetically related and produced by serial magmatism and therefore, the FAN (or at least some of it) would not be the direct product of the magma ocean crystallization.

Compositional differences between the FHT-O and the Apollo 16 landing site area appears to be a consequence of the deposit of ejecta from the Imbrium basin forming event. The composition of the Apollo 16 samples is similar to that on feldspathic meteorites when the Imbrium ejecta component is eliminated.

Feldspathic clasts of the Yamato group comprises ferroan anorthosites and Mg-rich lithologies suggesting that the sources and processes that create these magnesian rocks are not dependent on the presence of KREEP and therefore, not necessarily restricted to the PKT.

Some meteorites with impact melt clasts appear to be derived from the Australe region (Dho 1436/1443, PCA 02007 and NWA 4932). Determination of formation ages on impact melt clasts from these meteorites could be useful to determine the time of the event that created the Australe North basin observed by GRAIL. This is also relevant when studying the possible SPA origin of some of the samples (e.g. Dho 925), where the study of the crystallization ages of impact melts could be used to discriminate their origin.

The basaltic clasts contained in the feldspathic meteorites are mostly low-Ti to VLT basalts with only one high-Ti basaltic clast observed in MAC 88105. This is consistent with remote sensing observations that indicates that low-Ti mare basalts are widespread among the lunar maria. Also, the lack of clasts of basaltic nature on lunar meteorites that show possible launch origin in the farside central highlands indicates that if dykes of basaltic magma intruded in the farside crust, they were trapped in deeper layers not being reached by impact processes.

Chapter 7. Conclusions and Future Work

7.1. Introduction

This chapter summarises the discussions and conclusions from the previous chapters. Some recommendations for future research opportunities are also addressed.

7.2. Lunar Meteorite Miller Range 090036

Miller Range (MIL) 090036 is a feldspathic immature regolith breccia that exhibits a Th-enrichment. This enrichment could be related to a high alkali component that has been observed within an impact melt breccia clast and possibly could be included in other clasts and the matrix. Alternatively, it also could be related to a KREEP component that, although not observed in this sample, cannot be precluded. The clasts of the sample have suffered shock metamorphism as indicated by the presence of granulite clasts and plagioclase transformed into glass.

Petrography and bulk-rock major element composition show some similarities with regolith and soils from the Apollo 16 site and other lunar feldspathic meteorites (e.g. NWA 4936). Differences in major elements among Apollo 16 soils, NWA 4936 and MIL 090036, mainly MgO and Na_2O, as well as in REE, suggest that they derive from different source regions. FeO, TiO_2 and Th bulk-rock compositions have been used to investigate possible launch locations of the MIL 090036 meteorite. The results show that the regolith from the surroundings of the PKT on the nearside are the most similar in composition to the meteorite and therefore the likely source location for MIL 090036. However, because of the differences already mentioned, it also could be possible that this sample was launched from an area with similarities to the Apollo 16 samples but not affected by the Imbrium ejecta blanket.

7.3. Lunar Meteorite Miller Range 090070

MIL 090070 is a feldspathic immature regolith breccia with a low Th abundance. It contains impact melt-breccias and heavily fractured monomict plagioclase clasts, all embedded in a glassy feldspathic matrix with fragments of plagioclase, pyroxene, olivine and meteoritic components of small size. This meteorite is considered to be paired with MIL 090075 and possibly with MIL 090034.

Petrography, bulk-rock and trace element compositions show similarities with feldspathic meteorites NWA 2200, Dho 081, DaG 400 and DaG 262. The geochemistry of all these meteorites and MIL 090070 may be formed by a mixture of FAN and MAN rocks. Another possible explanation could be that they were all essentially FAN-derived and that this rock type is related to HMS.

MIL 090070 was probably launched from the farside of the Moon as suggested by its bulk-rock FeO, TiO_2 and Th compositions and the lack of KREEP components. If this is correct, it would mean that FAN and MAN lithologies are globally distributed.

7.4. Launch Origin of Lunar Meteorites

The present work has studied the possible launch locations of 37 lunar meteorites (67 individual stones) using bulk-rock FeO, TiO_2 and Th compositions and the 2-degree LP-GRS dataset from (Prettyman et al. 2006). The implications of this study are summarized below.

7.4.1. Lunar magmatism

Several mechanisms could have been working at the same time in different areas during the early history of the Moon (>4.0 Ga) to produce basalts. These mechanisms include extensional tectonic processes that allows the magma to rise, heat flux because of radioactive elements, and mantle plumes.

High-Al basalts appear to have been extruded in Mare Frigoris early in the lunar history. However, other types of basalts, such as low-Fe basalts were extruded in other areas of the lunar surface (e.g. Mendel-Rydberg) during the same lunar period (<4.0 Ga). This indicates several magmatic reservoirs with different compositional characteristics existed early in the lunar history.

VLT and low-Ti basaltic meteorites appear to have been launched from different mare areas. Also, most of the basaltic clasts found in feldspathic meteorites are low-Ti and VLT. It seems that these compositions are widespread across the lunar maria, and that high-Ti mare basalts appear to be overrepresented in the Apollo sample collection.

Differences in KREEP components between the PKT and other areas of the Moon is not the only indicator of a heterogeneous mantle. This heterogeneity is also suggested by the possible provenances obtained from mare basaltic meteorites and basaltic clasts found in feldspathic meteorites:

- A heterogeneous depleted mantle melt appears to be the source of basalts from Mare Fecunditatis.
- The basaltic meteorites possibly launched from Mare Crisium indicates a primitive, VLT, slightly enriched mantle source that underwent fractional crystallization in a closed-system. Alternatively, these VLT basalts could be the result of the differentiation and flotation of the VLT basalt in a Fe-rich, high-Ti magma.
- Parent liquid with compositions, similar to olivine basalts that underwent extreme fractionation, are the probable source for meteorites originating from Oceanus Procellarum.

7.4.2. Mare Imbrium impact event

Northwest Africa (NWA) 4472 and Sayh al Uhaymir (SaU) 169 have bulk-rock compositions enriched in KREEP, suggesting that they contain impact melt breccia components derived from a basin-forming event within the PKT. Isotopic ages measured in those meteorites indicates that this event took place between 3.91-3.94 Ga, probably the Imbrium basin formation that took place at the final stages of the basin formation on the Moon.

7.4.3. South Pole-Aitken basin

The lunar meteorite Calcalong Creek appears to be the most likely candidate for an origin within the South Pole-Aitken basin. Bulk-rock FeO, TiO_2 and Th compositions are similar to those observed by remote sensing instruments in SPA. The Sm/Eu ratio does not agree with the PKT, anorthositic and basaltic mixing triangle, but this meteorite could represent the composition of the lower crust as excavated during the SPA impact event

7.4.4. Mare Australe

Three lunar meteorites have shown possible launch locations close to, or within, Mare Australe: Dhofar (Dho) 1436/1443, Pecora Escarpment (PCA) 02007 and Northwest Africa (NWA) 4932. The more mafic compositions of these meteorites compared to the highly feldspathic meteorites could be the consequence of a mixture between feldspathic and basaltic lithologies. Alternatively, they could derive from the lower crust, since those compositions are also similar to the compositions that are expected in the lower crust of the Moon. Isotopic argon analyses have shown resetting events between 4.2 and 3.0 Ga. However, less susceptible isotopic systems in impact melt clasts and impact melt breccias could determine whether these samples are in fact from Mare Australe and in that case, the formation age of the Australe North basin discovered by GRAIL (Neumann et al. 2015) could be determined.

7.4.5. Lunar highlands: FAN-MAN

Granulites derived from magnesian anorthosites (MAN) appear to be more representative of the lunar crust that the ferroan anorthosites (FAN) collected from the Apollo 16 (Gross et al. 2014). However, this study also suggests that FAN are widely distributed with patches within the central farside highlands. The large number of feldspathic meteorites that contains both magnesian and ferroan anorthosites compared to those that contain either one type or another, could indicate that they are genetically related and the wide Mg# distribution in FAN and MAN would be produced by serial magmatism. If this is correct, the FAN lithologies (or at least some of them) would not be the direct product of the magma ocean crystallization.

Compositional differences between the FHT-O and the Apollo 16 landing site area could be a consequence of the deposit of ejecta from the Imbrium basin forming event that covers the older feldspathic material, which is similar to the feldspathic components within the FHT-O. Based on the distribution of meteorites possibly launched for the FHT-O, I suggest this terrane could be differentiated in 2 terranes: The FHT-O and the Apollo 16 area (Figure 7.1).

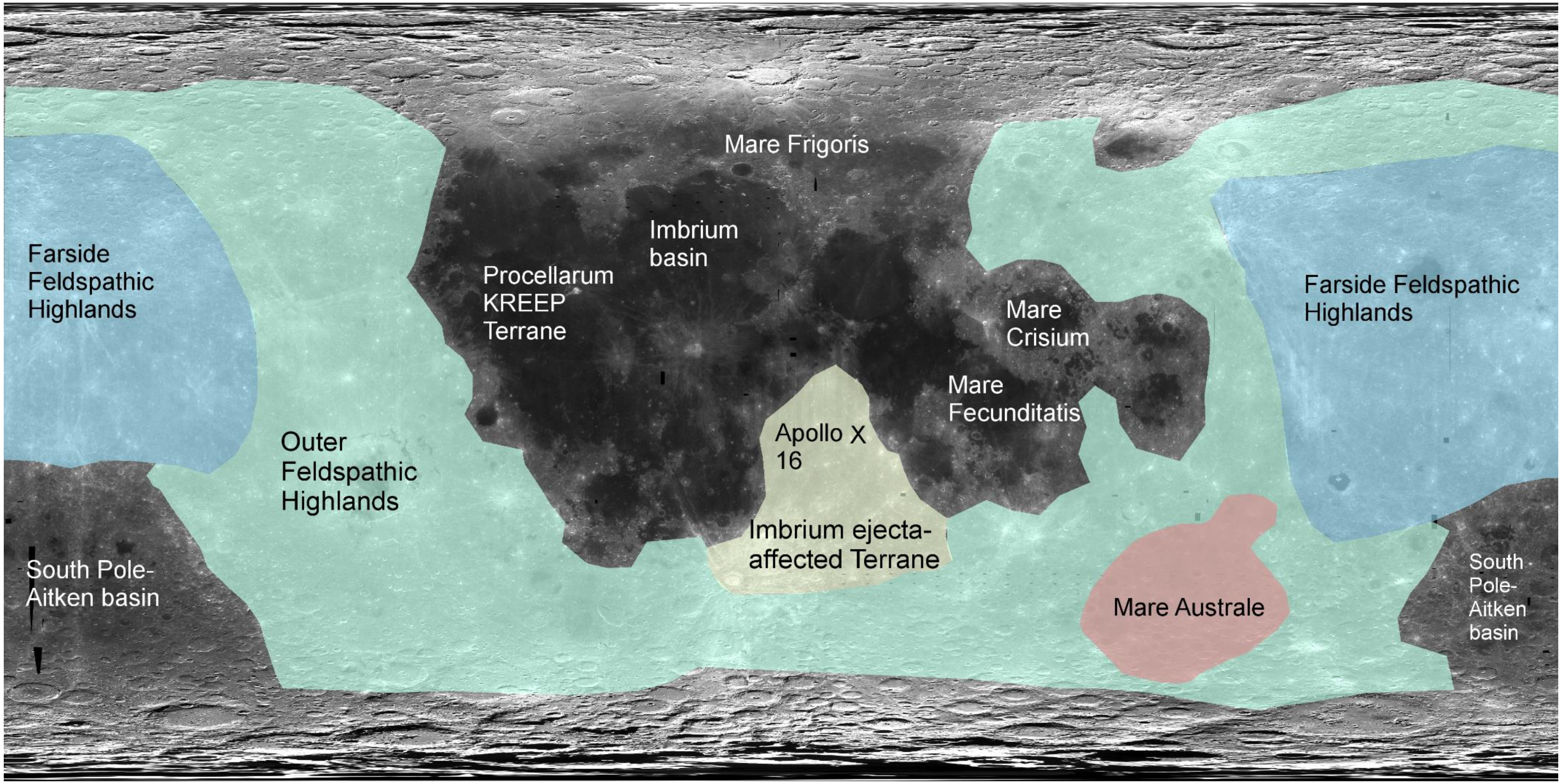

Figure 7.1 Approximate lunar highland areas proposed in this work based on feldspathic meteoritic compositions, surface expressions of major crustal terranes from Jolliff et al. (2000), and Mg maps from Crites et al. (2015).

7.5. Ongoing and Future Work

The most significant ongoing work in the localization of possible launch sites of lunar meteorites involves the integration of multiple datasets. MgO measurements from Prettyman et al. 2006, were not used because of their poor analytical resolution and high error values. However, MgO abundances allow for a better discrimination among feldspathic meteorites, therefore it will help us to understand the true nature of the feldspathic highlands and the heterogeneity of the LMO crystallization. Currently, I am working on an implementation of the method using the improved LP-GRS Mg-dataset from Peplowski and Lawrence (2013) and Crites et al. (2015) that will include MgO as a new component into the algorithm. The first step of this work is to translate this new dataset into a format readable for the program.

Also, in the near future I am considering developing a more user-friendly interface for the software in order to make it available to the scientific community worldwide. This will allow to an easier and quicker way for researchers to investigate the possible launch locations of lunar meteorites.

Chandrayaan-1’s Moon Mineralogy Mapper (M^3) is a high resolution imaging spectrometer that operates from the visible into the near infrared where highly diagnostic mineral absorption bands occur (Pieters et al. 2009). This instrument identifies minerals and rock composition across the lunar surface. Mineralogical measurements will also provide additional information to compare with the mineralogy observed in the lunar meteorites. During this work, the possibility of including these datasets into the study was considered. However, currently there is an absence of global maps derived from M^3 data, and information available today is restricted to locations of special interest (e.g. Kramer et al. 2013). Future work should include the creation of global maps from M^3 data and the implementation of my technique to use this data together with LP-GRS datasets.

The comparison between the lunar meteorites and the LP-GRS dataset have been difficult because of the large differences between the scale of the lunar meteorites (cm) and the 2-degree spatial resolution of the remote sensing dataset (60 km). Improvements in the spatial, spectral and radiometric resolutions of the multispectral and GRS remote sensing instruments would allow more accurate pinpointing of possible launch sites. Currently, there are not future lunar missions planned or proposed by any space agency in the oncoming years that includes a high resolution multispectral and GRS remote sensing instruments.

Additional petrographic, geochemical and isotopic analyses on both already known lunar meteorites, and those yet to be discovered, are necessary to improve the analytical averages, bringing the meteorites' compositions closer to the regolith averages measured by the remote sensing instruments. Ar-Ar and U-Pb isotopic analyses of impact melts from Dho 1436/1443, PCA 02007 and NWA 4932 could be very useful to determine their age and therefore to shed light into the possible launch location of these samples. If these samples are from Australe North basin as suggested by this work, these ages could provide us with a confirmation of the existence of this basin basin discovered by NASA's GRAIL mission (Neumann et al. 2015) as well as with an approximate age for its formation.

Finally, this technique could be revised in the future to be used for meteorites from other planetary bodies, especially meteorites from Mars. This future work should take into account the different surface processes (for example those related to the existence of an atmosphere), that take place into the different planetary bodies and that could cause the movement and reworking of the materials.

Apollo samples and lunar meteorites are currently the only material we have from the Moon. Their usefulness to understand lunar composition and evolution is beyond doubt. However, the limited area that the Apollo program sampled, and the limitations in knowing precisely the launch sites of the meteorites, argues for future lunar sample return missions to recover material from key locations. The South Pole-Aitken basin is one of these locations as it is thought to have excavated the lower lunar crust, and therefore it is one of the first locations to be considered for future lunar exploration missions (Duke 2003; Hurwitz and Kring 2014). Mare Australe could have been excavated the lower lunar crust as suggested during this work, if this is correct, it could be an interesting place for a future lunar sample return mission. Also, robotic or human fieldwork in the lunar farside will provide with important information to investigate the differences between the nearside and farside compositions.

Appendix 2A

Table with the compositions of the certified reference materials (CRM) used for sample calibration.

	USGS													
CRM Type	**AGV-2 Andesite**		**BCR-2 Basalt**		**BHVO-2 USGS Basalt**		**DNC-1 ISGS Dolerite**		**DTS-1 USGS Dunite**		**GSP-2 USGS Granodiorite**		**STM-1 USGS Syenite**	
	wt.%	±	wt.%	±	wt.%	±	wt.%	±	wt.%	±	wt.%	±	wt.%	±
SiO_2	59.3	0.7	54.1	0.8	49.9	0.6	47.15	0.21	40.41	0.47	66.6	0.8	59.6	0.49
TiO_2	1.05	0.22	2.26	0.05	2.73	0.04	0.48	0.007	0.005		0.66	0.02	0.14	0.01
Al_2O_3	16.91	0.21	13.5	0.2	13.5	0.2	18.34	0.17	0.19		14.9	0.2	18.4	0.23
Fe_2O_3	6.69	0.13	13.8	0.2	12.3	0.2	9.97	0.15	1.03	0.36	4.9	0.16	2.87	0.02
MnO							0.15	0.003	0.12	0.01				
MgO	1.79	0.03	3.59	0.05	7.23	0.12	10.13	0.11	49.59	0.33	0.96	0.03	0.1	0.02
CaO	5.2	0.13	7.12	0.11	11.4	0.2	11.49	0.07	0.17	0.03	2.1	0.06	1.09	0.06
Na_2O	4.19	0.13	3.16	0.11	2.22	0.08	1.89	0.057	0.01		2.78	0.09	8.94	0.2
K_2O	2.88	0.11	1.79	0.05	0.52	0.01	0.234	0.009	0.001		5.38	0.14	4.28	0.07
P_2O_5	0.48	0.02	0.35	0.02	0.27	0.02	0.07	0.005	0.002		0.29	0.02	0.16	0.01
Cr_2O_3														
CO_2														
	ppm	±	Ppm	±	ppm	±	ppm	±	ppm	±	ppm	±	ppm	±
Li	11		9	2	5		5.2	0.29	2.1	0.12	36	1	32	
Be	2.3	0.4									1.5	0.2	9.6	0.6
Sc	13	1	33	2	32	1	31	1			6.3	0.7	0.61	0.07
V	120	5	416	14	317	11	148	8.3	11		52	4	8.7	
Co	16	1	37	3	45	3	57	2.2	140	15	7.3	0.8	0.9	
Cr	17	2	18	2	280	19	270	8.5	3990	300	20	6	4.3	
Ni	19	3			119	7	247	12	2360	170	17	2	3	
Cu	53	4	19	2	127	7	100	2.6	7.1		43	4	4.6	
Zn	86	8	127	9	103	6	70	2.4	46		120	10	235	22
Ga	20	1	23	2	21.7	0.9	15				22	2	35	5
Rb	68.6	2.3	48	2	9.8	1	4.5				245	7	118	6
Sr	658	17	346	14	389	23	144	1.8	0.32		240	10	700	30

USGS														
CRM	**AGV-2**		**BCR-2**		**BHVO-2 USGS**		**DNC-1 ISGS**		**DTS-1 USGS**		**GSP-2 USGS**		**STM-1 USGS**	
Type	**Andesite**		**Basalt**		**Basalt**		**Dolerite**		**Dunite**		**Granodiorite**		**Syenite**	
	ppm	±	Ppm	±	ppm	±	ppm	±	ppm	±	ppm	±	ppm	±
Y	20	1	37	2	26	2	18	0.8			28	2	46	5
Zr	230	4	188	16	172	11	39	1			550	30	1210	120
Nb	15	1	28	2	18	2	3				27	2	270	12
Mo			248	17							2.1	0.6	5.2	
Sb	0.6						0.96	0.03	0.5				1.7	0.2
Cs	1.16	0.08	1.1	0.1							1.2	0.1	1.5	0.1
Ba	1140	32	683	28	130	13	118	11	1.7		1340	44	560	60
La	38	1	25	1	15	1	3.6	0.3			180	12	150	6
Ce	68	3	53	2	38	2			0.07	0.02	410	30	260	18
Pr	8.3	0.6	6.8	0.3							51	5		
Nd	15	1	28	2	25	1.8	5.2	0.56			200	12	79	7
Sm	5.7	0.3	6.7	0.3	6.2	0.4					27	1	13	1
Eu	1.54	0.1	2	0.1			0.59	0.03			2.3	0.1	3.6	0.3
Gd	4.69	0.26	6.8	0.3	6.3	0.2	2				12	2	9.5	0.8
Tb	0.64	0.04	1.07	0.04	0.9								1.6	0.2
Dy	3.6	0.2					3				6.1		8.1	0.5
Ho	0.71	0.08	1.33	0.06	1.04	0.04	0.62				1	0.1		
Er	1.79	0.11									2.2		4.2	0.4
Tm	0.26	0.02	0.54								0.29	0.02	0.7	
Yb	1.6	0.2	3.5	0.2	2	0.2	2	0.1			1.6	0.2	4.4	0.4
Lu	0.25	0.01	0.51	0.02	0.28	0.01					0.23	0.03		
Hf	5.08	0.2	4.8	0.2	4.1	0.3					14	1	28	2
Ta	0.89	0.08			1.4								19	1.2
W														
Tl	0.27										1.1			
Pb	13	1	11	2			6.3		12				18	1.8
Th	6.1	0.6	6.2	0.7	1.2	0.3			0.01	0	105	8	31	3
U	1.88	0.16	1.69	0.19					0.0036	0	2.4	0.19	9.1	0.1

	GSJ				**NIMTEK**			**CCRMP**	**GIT-IWG**
CRM **Type**	**JDo-1** **Dolomite** wt.%	**JG-1** **Granodiorite** wt.%	**JLk-1** **Lake Sediment** wt.%	**JLs-1** **Limestone** wt.%	**NIM-G** **Granite** wt.%	**NIM-P** **Pyroxenite** wt.%	**NIM-S** **Syenite** wt.%	**MRG-1** **Gabbro** wt.%	**AC-E** **Granite** wt.%
SiO2	0.2	72.3	57.16	0.12	75.7	51.1	63.63	39.12	70.35
TiO2	<0.002	0.26	0.668	0.002	0.09	0.2		3.77	0.11
Al2O3	0.013	14.24	16.73	0.0207	12.08	4.18	17.34	8.47	14.7
Fe2O3	0.02	0.38	4.251	0.0178	2	0.87	1.11	17.94	1.34
MnO	0.006	0.063	0.266	0.00209		0.22		0.17	0.058
MgO	18.4	0.74	1.736	0.606		25.33	0.46	13.55	0.03
CaO	34.12	2.2	0.686	55.09	0.78	2.66	0.68	14.7	0.34
Na2O	0.009	3.38	1.051	0.00194	3.36	0.37	0.43	0.74	6.54
K2O	0.002	3.98	2.805	0.00297	4.99	0.09	15.35	0.18	4.49
P2O5	0.034	0.099	0.208	0.0295			0.12	0.08	0.014
Cr2O3						3.5			
CO2	46.87						0.09		
	ppm	Ppm	ppm	ppm	ppm	ppm	ppm	ppm	ppm
Li	0.4	86.6	51.5	0.2					93
Be	<0.1	3.15	3.31						12
Sc		6.53	15.9	0.0307					0.11
V	<5	25.2	117	3.59		230	10		3
Co	<0.3	4.06	18	0.0825		110	3		0.2
Cr		53.2	69	3.37	12	24000	12		3.4
Ni	2.9	7.47	35	0.362		555	7		1.5
Cu		2.52	62.9	0.268	12	18	19		4
Zn	34.4	41.1	152	3.19	50	100	10		224
Ga		17.8	21.4		27	8	11		39
Rb	<0.2	182	147	0.18	325		530		152
Sr		184	67.5	295	10	32	62		3
Y		30.6	40	0.223	143	5			184
Zr		111	137	4.19	300		33		780
Nb		12.4	15.8	1	53				110
Mo		1.75	2.19						2.5

	GSJ				**NIMTEK**			**CCRMP**	**GIT-IWG**
CRM Type	**JDo-1 Dolomite** ppm	**JG-1 Granodiorite** Ppm	**JLk-1 Lake Sediment** ppm	**JLs-1 Limestone** ppm	**NIM-G Granite** ppm	**NIM-P Pyroxenite** ppm	**NIM-S Syenite** ppm	**MRG-1 Gabbro** ppm	**AC-E Granite** ppm
Mo		0.13	1.68	0.0166					0.4
Sb	<0.2	10.1	10.9	0.0201					3
Cs		466	574	476		46	2400		55
Ba		22.4	40.6	0.153	109	2	5		59
La		45.8	87.9	0.521	195		11.9		154
Ce		4.83	8.53	0.032					22.2
Pr		19.3	35.7	0.136	72		6		92
Nd		4.62	7.87	0.135	15.8		1		24.2
Sm		0.73	1.27	0.0072	0.35	0.2			2
Eu		4.28	6.02	0.03			14		26
Gd		0.78	1.23	0.0041	3				4.8
Tb		4.14	6.57	0.0283			0.4		29
Dy		0.81	1.06						
Ho		2.16	3.59						17.7
Er		0.41	0.531						2.6
Tm		2.47	3.99	0.0164	14.2	0.6	0.07		17.4
Yb		0.39	0.571	0.022					2.45
Lu		3.56	3.78	0.126					27.9
Hf		1.79	1.57	0.014					8.4
Ta		1.58	3.99						1.5
W			1.17	0.003					0.9
Tl	1	1.03	43.7	0.7	40		5		39
Pb		13.2	19.5	0.0287	51		1		18.5
Th		3.47	3.83	1.75					4.6

USGS: United States Geological Survey; **GSJ**: Geological Survey Japan; **NIMTEK**: Council for Mineral Technology; **CCRMP**: Canadian Certified Reference Material Project; **GIT-IWG**: Groupe International de Travail- International Working Group.

Appendix 2B

Python code used to match elemental analytical compositions to measurements from remote sensing datasets.

```
#Title: Code_3element.py
#Description: This is the code for 2 variable of composition. It creates a
text file with the coordinates and create a polygon shapefile compatible
with ArcGIS 10.1.
#Developed by Abigail Calzada-Diaz
#Last update 29/10/2013

#Import all the modules required
import shapely
import fiona
import csv
from shapely.geometry import box,mapping
from fiona import collection
#Open to read the dataset in .txt. The dataset has to have the following
schema: #long_min, long_max, lat_min, lat_max, SiO2(*), TiO2, Al2O3(*), FeO,
MgO(*), #CaO(*), Th, K(*)
#(*) --> depending of the composition data that will be used.
f=open('<remote_sensing_file.txt>','r') #If necessary, change dataset
data=[]
for line in f:
    columns=line.split() #split the line into columns
    source={} # creates a dictionary
    source['long_min']=float(columns[0])
    source['long_max']=float(columns[1])
    source['lat_min']=float(columns[2])
    source['lat_max']=float(columns[3])
    source['SiO2']=float(columns[4])
    source['TiO2']=float(columns[5])
    source['Al2O3']=float(columns[6])
    source['FeO']=float(columns[7])
    source['MgO']=float(columns[8])
    source['CaO']=float(columns[9])
    source['Th']=float(columns[10])
    source['K']=float(columns[11])
    source['SiO2_error']=float(columns[12])
    source['TiO2_error']=float(columns[13])
    source['Al2O3_error']=float(columns[14])
    source['FeO_error']=float(columns[15])
    source['MgO_error']=float(columns[16])
    source['CaO_error']=float(columns[17])
    source['Th_error']=float(columns[18])
    source['K_error']=float(columns[19])
    data.append(source)
f.close #finally there is a list of dictionaries

#The next function creates a text file where the coordinates that matches a
```

certain criteria are written.

```
Def
abi_file(data,element1,low1,up1,elem_err1,element2,low2,up2,elem_err2,elem
ent3,low3,up3,elem_err3):
    i=0
    outputfile=csv.writer(open("<destination_file>","wb"))
    selectedpoints=[]
    while i<len(data):
        if low1<data[i][element1]<up1 and low2<data[i][element2]<up2 and
       low3<data[i][element3]<up3:
            outputfile.writerow([data[i]['long_min'],data[i]['long_max'],
data[i]['lat_min'],data[i]['lat_max']])
            selectedpoints.append(data[i])
        elif      low1<(data[i][element1]-data[i][elem_err1])<up1      and
low2<(data[i][element2]-data[i][elem_err2])<up2                         and
low3<(data[i][element3]-data[i][elem_err3])<up3:
            outputfile.writerow([data[i]['long_min'],data[i]['long_max'],
data[i]['lat_min'],data[i]['lat_max']])
            selectedpoints.append(data[i])
        elif      low1<(data[i][element1]+data[i][elem_err1])<up1      and
low2<(data[i][element2]+data[i][elem_err2])<up2                         and
low3<(data[i][element3]+data[i][elem_err3])<up3:
            outputfile.writerow([data[i]['long_min'],data[i]['long_max'],
data[i]['lat_min'],data[i]['lat_max']])
            selectedpoints.append(data[i])
        elif      low1<(data[i][element1]-data[i][elem_err1])<up1      and
low2<(data[i][element2]+data[i][elem_err2])<up2                         and
low3<(data[i][element3]-data[i][elem_err3])<up3:
           outputfile.writerow([data[i]['long_min'],data[i]['long_max'],
data[i]['lat_min'],data[i]['lat_max']])
            selectedpoints.append(data[i])
        elif      low1<(data[i][element1]+data[i][elem_err1])<up1      and
low2<(data[i][element2]-data[i][elem_err2])<up2                         and
low3<(data[i][element3]-data[i][elem_err3])<up3:
            outputfile.writerow([data[i]['long_min'],data[i]['long_max'],
data[i]['lat_min'],data[i]['lat_max']])
            selectedpoints.append(data[i])
        elif      low1<(data[i][element1]-data[i][elem_err1])<up1      and
low2<(data[i][element2]-data[i][elem_err2])<up2                         and
low3<(data[i][element3]+data[i][elem_err3])<up3:
            outputfile.writerow([data[i]['long_min'],data[i]['long_max'],
data[i]['lat_min'],data[i]['lat_max']])
            selectedpoints.append(data[i])
        elif      low1<(data[i][element1]-data[i][elem_err1])<up1      and
low2<(data[i][element2]+data[i][elem_err2])<up2                         and
low3<(data[i][element3]+data[i][elem_err3])<up3:
            outputfile.writerow([data[i]['long_min'],data[i]['long_max'],
data[i]['lat_min'],data[i]['lat_max']])
            selectedpoints.append(data[i])
        elif      low1<(data[i][element1]+data[i][elem_err1])<up1      and
low2<(data[i][element2]-data[i][elem_err2])<up2                         and
low3<(data[i][element3]+data[i][elem_err3])<up3:
            outputfile.writerow([data[i]['long_min'],data[i]['long_max'],
```

```
data[i]['lat_min'],data[i]['lat_max']])
            selectedpoints.append(data[i])
        elif      low1<(data[i][element1]+data[i][elem_err1])<up1      and
low2<(data[i][element2]+data[i][elem_err2])<up2                       and
low3<(data[i][element3]-data[i][elem_err3])<up3:
            outputfile.writerow([data[i]['long_min'],data[i]['long_max'],
data[i]['lat_min'],data[i]['lat_max']])
            selectedpoints.append(data[i])
            #writing the new file
        i=i+1
    return selectedpoints

#The next function create the shapefile compatible with ArcGIS 10.1 using
the fiona module.

def create_shapefile(newlist):
    j=0
    schema = { 'geometry': 'Polygon', 'properties': { 'name': 'str' } }
    #step through things
    #with collection etc.(indent while loop)
    print '       ',' long_min',' long_max',' lat_min',' lat_max'
    with   collection("<destination_file.shp>",   "w",   "ESRI   Shapefile",
schema) as output:
        while j<len(newlist): #loop
            long_min=newlist[j]['long_min']
            long_max=newlist[j]['long_max']
            lat_min=newlist[j]['lat_min']
            lat_max=newlist[j]['lat_max']

            #make a string to hold the pixel name
            featurename='pixel_'
            featurename=featurename+str(j)  #convers  j(current  index  in
list) to a string and adds to end of name

            print featurename,':    ',long_min,' ', long_max,' ',lat_min,'
', lat_max
            #create polygon object in shapely using points
            temp_polygon=box(long_min,lat_min,long_max,lat_max)
            #print temp_polygon
            #add polygon object to (new line?) of shape file

            output.write({'properties':  {'name':  featurename},'geometry':
mapping(temp_polygon)})
            j=j+1


newlist=abi_file(data,'FeO',<min_value>,<max_value>,'FeO_error','TiO2',<mi
n_value>,<max_value>,'TiO2_error','Th',<min_value>,<max_value>,'Th_error')
#Input the three compositional variables
create_shapefile(newlist) #create the shapefile

#END
```

References

l-Kathiri A., Gnos E., and Hofmann B. A. 2007. The regolith portion of the lunar meteorite Sayh al Uhaymir 169. *Meteoritics & Planetary Science* 42: 2137–2152.

Alexander E. C., Bates A., Coscio M. R., Dragon J. C., Murthy V. R., Pepin R. O., and Venkatesan T. R. 1976. K/Ar dating of lunar soils II. *Proceedings Lunar Planetary Science 7th* 625–648.

Anand M., Taylor L. A., Floss C., Neal C. R., Terada K., and Tanikawa S. 2006. Petrology and geochemistry of LaPaz Icefield 02205: A new unique low-Ti mare-basalt meteorite. *Geochimica et Cosmochimica Acta* 70: 246–264.

Anand M., Taylor L. A., Misra K. C., Demidova S. I., and Nazarov M. A. 2003. KREEPy lunar meteorite Dhofar 287A: A new lunar mare basalt. *Meteoritics & Planetary Science* 38: 485–499.

Anand M., Taylor L., Patchen A., and Cahill J. 2002. New minerals from a new lunar meteorite, Dhofar 280. *Lunar and Planetary Science XXXIII.*

Anders E., and Grevesse N. 1989. Abundances of the elements: Meteoritic and solar. *Geochimica et Cosmochimica Acta* 53: 197–214.

Andrews-Hanna J. C. et al. 2014. Structure and evolution of the lunar Procellarum region as revealed by GRAIL gravity data. *Nature* 514: 68–71.

Antonenko I. 1999. Volumes of cryptomafic deposits on the Western Limb of the Moon: Implications for lunar Volcanism. Brown University, Providence, RI.

Antonenko I., Head J. W., Mustard J. F., and Hawke B. R. 1995. Criteria for the detection of lunar cryptomaria. *Earth, Moon and Planets* 69: 141–172.

Arai T., Misawa K., and Kojima H. 2005. A new lunar meteorite MET 01210: Mare breccia with a low-Ti ferrobasalt. *Lunar and Planetary Science XXXVI* Abstract #2361.

Arai T., Misawa K., and Kojima H. 2007. Lunar meteorite MIL 05035: Mare basalt paired with Asuka-881757. *Lunar and Planetary Science XXXVIII.*

Arai T., Ray Hawke B., Giguere T. A., Misawa K., Miyamoto M., and Kojima H. 2010. Antarctic lunar meteorites Yamato-793169, Asuka-881757, MIL 05035, and MET 01210 (YAMM): Launch pairing and possible cryptomare origin. *Geochimica et Cosmochimica Acta* 74: 2231–2248.

Arai T., Takeda H., and Warren P. H. 1996. Four Lunar Mare Meteorites: Crystallization Trends of Pyroxenes and Spinels. *Meteoritics & Planetary Science* 31: 877–892.

Arai T., Takeda H., Yamaguchi A., and Ohtake M. 2008. A new model of lunar crust : asymmetry in crustal composition and evolution. *Earth Planets Space* 60: 433–444.

Arai T., and Warren P. H. 1999. Lunar meteorite Queen Alexandra Range 94281: Glass compositions and other evidence for launch pairing with Yamato 793274. *Meteoritics & Planetary Science* 34: 209–234.

Arai T., Yoshitake M., Tomiyama T., Niihara T., Yokoyama T., Kaiden H., Misawa K., and Irving A. J. 2010. Support for a prolonged KREEP magmatism: U-Pb age dating of zircon and baddeleyite in lunar meteorite NWA4485. In *41st Lunar and Planetary Science Conference*. p. Abstract #2379.

Bartoschewitz R., Niedergesaess R., Pepelnik R., Reus U., Kraehenbueh U., and Kurtz T. 2005. Chemical classification of “SaU 300.” *68th Annual Meteoritical Society Meeting*.

Bartoschewitz R., Park J., Nagao K., Okazaki R., Niedergesaess R., Pepelnik R., Reus U., and Kurtz T. 2005. Lunar meteorite SaU 300- Noble gas isotopes. *68th Annual Meteoritical Society Meeting*.

Basilevsky A. T., Neukum G., and Nyquist L. 2010. The spatial and temporal distribution of lunar mare basalts as deduced from analysis of data for lunar meteorites. *Planetary and Space Science* 58: 1900–1905.

Beauchemin D. 2010. Inductively Coupled Plasma Mass Spectrometry. *Analytical Chemistry* 82: 4786–4810.

Beauchemin D., Kyser K., and Chipley D. 2002. Inductively Coupled Plasma MAss Spectrometry with On-line Leaching: A Method to Assess the Mobility and Fractionation of Elements. *Analytical Chemistry* 74.

Bell J. F., and Hawke B. R. 1984. Lunar dark-haloed impact craters - Origin and implications for early mare volcanism. *Journal of Geophysical Research* 89: 6899–6910.

Besserer J., Nimmo F., Wieczorek M. A., Weber R. C., Kiefer W. S., Mcgovern P. J., Andrews-Hanna J. C., Smith D. E., and Zuber M. T. 2014. GRAIL gravity constraints on the vertical and lateral density structure of the lunar crust. *Geophysical Research Letters* 41: 1–7.

Bischoff A. 1996. Lunar meteorite Queen Alexandra Range 93069: A lunar highland regolith breccia with very low abundances of mafic components. *Meteoritics & Planetary Science* 31: 849–855.

Bischoff A. et al. 1998. Petrology, chemistry, and isotopic compositions of the lunar highland regolith breccia Dar al Gani 262. *Meteoritics & Planetary Science* 33: 1243–1257.

Bischoff A., Palme H., Weber H. W., Stöffler D., Braun O., Spettel B., Begemann F., Wänke H., and Ostertag R. 1987. Petrography, shock history, chemical composition and noble gas content of the lunar meteorites Yamato-82192 and -82193. *National Institute of Polar Research NII-Electronic Library Service* 46: 21–42.

Boesenberg J. S., and Delaney J. S. 2006. Elephant Moraine 87521 : two pyroxenes , two chromites , and two ilmenites , but only one fractionation series. *Lunar and Planetary Science XXXVII*.

Bogard D. D., Garrison D. H., and McCoy T. J. 2000. Chronology and petrology of silicates from IIE iron meteorites: Evidence of a complex parent body evolution. *Geochimica et Cosmochimica Acta* 64: 2133–2154.

Bogard D. D., Garrison D. H., and Nyquist L. E. 2000. Argon-39-Argon-40 ages of lunar highlands rocks and meteorites. *Lunar and Planetary Science XXXI*.

Bogard D. D., Garrison D. H., Shih C. Y., and Nyquist L. E. 1994. 39Ar-40Ar dating of two lunar granites: The age of Copernicus. *Geochimica et Cosmochimica Acta* 58: 3093–3100.

Borg L. E., Connelly J. N., Boyet M., and Carlson R. W. 2011. Chronological evidence that the Moon is either young or did not have a global magma ocean. *Nature* 477: 70–72.

Borg L. E., Gaffney A. M., and Shearer C. K. 2015. A review of lunar chronology revealing a preponderance of 4.34-4.37 Ga ages. *Meteoritics and Planetary Science* 50: 715–732.

Borg L. E., Gaffney A. M., Shearer C. K., DePaolo D. J., Hutcheon I. D., Owens T. L., Ramon E., and Brennecka G. 2009. Mechanisms for incompatible-element enrichment on the Moon deduced from the lunar basaltic meteorite Northwest Africa 032. *Geochimica et Cosmochimica Acta* 73: 3963–3980.

Borg L. E., Shearer C. K., Asmerom Y., and Papike J. J. 2004. Prolonged KREEP magmatism on the Moon indicated by the youngest dated lunar igneous rock. *Nature* 432: 209–211.

Bouvier A., Romaniello S. J., Wadhwa M., Korotev R. L., and Hartmann W. K. 2013. Pb-Pb dating of Apollo 67016 and MIL 090034 lunar impact breccias. *76th Annual Meteoritical Society Meeting* Abstract#5312.

Boyet M., Carlson R. W., Borg L. E., and Horan M. 2015. Sm–Nd systematics of lunar ferroan anorthositic suite rocks: Constraints on lunar crust formation. *Geochimica et Cosmochimica Acta* 148: 203–218.

Boynton W. V, and Hill D. H. 1983. Composition of bulk samples and a possible pristine clast from Allan Hills A81005. *Geophysical Research Letters* 10: 837–840.

Cahill J. T., Floss C., Anand M., Taylor L. A., Nazarov M. A., and Cohen B. A. 2004. Petrogenesis of lunar highlands meteorites: Dhofar 025, Dhofar 081, Dar al Gani 262, and Dar al Gani 400. *Meteoritics & Planetary Science* 39: 503–529.

Cahill J. T., Taylor L. A., Anand M., Patchen A., and Nazarov M. A. 2002. Mineralogy, Petrography, and Geochemistry of Lunar Meteorite Dhofar 081: New Developments. *Lunar and Planetary Science XXXIII*.

Calzada-Diaz A., Joy K. H., Crawford I. A., and Nordheim T. A. 2015. Constraining the source regions of lunar meteorites using orbital geochemical data. *Meteoritics & Planetary Science* 15: 214–228.

Cameron A. G. W., and Ward W. R. 1976. The Origin of the Moon. *Abstracts of the Lunar and Planetary Science Conference* 7: 120–122.

Canup R. M. 2012. Forming a Moon with an Earth-like composition via Giant Impact. *Science* 419: 1052–1056.

Canup R. M., and Asphaug E. 2001. Origin of the Moon in a giant impact near the end of the Earth's formation. *Nature* 412: 708–712.

Chapman C. R., Cohen B. A., and Grinspoon D. H. 2007. What are the real constraints on the existence and magnitude of the late heavy bombardment? *Icarus* 189: 233–245.

Chen J. H., and Wasserburg G. J. 1985. U-Th-Pb Isotopic studies on meteorite ALHA 81005 and Ibitira. *Lunar and Planetary Science XVI* 119–120.

Cohen B. A., Frasl B., Jolliff B. L., Korotev R. L., and Zeigler R. A. 2016. 40Ar-39Ar of an impact-melt lithology in Dhofar 961. *47th Lunar and Planetary Science Conference*.

Cohen B. A., James O. B., Taylor L. A., Nazarov M. A., and Barsukova L. D. 2004. Lunar highland meteorite Dhofar 026 and Apollo sample 15418: Two strongly shocked, partially melted, granulitic breccias. *Meteoritics & Planetary Science* 39: 1419–1447.

Cohen B. A., Swindle T. D., and Kring D. A. 2005. Geochemistry and 40 Ar-39 Ar geochronology of impact-melt clasts in feldspathic lunar meteorites: Implications for lunar bombardment history. *Meteoritics & Planetary Science* 40: 755–777.

Cohen B. A., Swindle T. D., and Kring D. A. 2000. Support for the lunar cataclysm hypothesis from lunar meteorite impact melt ages. *Science* 290: 1754–1756.

Cohen B. A., Swindle T. D., Taylor L. A., and Nazarov M. A. 2002. 40Ar-39Ar ages from impact melt clasts in lunar meteorites Dhofar 025 and Dhofar 026. *Lunar and Planetary Science XXXIII* 0.

Committee on the Scientific Context for Exploration of the Moon. 2007. *The Scientific Context for the Exploration of the Moon*,.

Connolly H. C. et al. 2007. The Meteoritical Bulletin, No. 91, 2007 March. *Meteoritics & Planetary Science* 42: 413–466.

Corrigan C. M., Dombard A. J., Spudis P. D., Bussey D. B. J., and McCoy T. J. 2009. Candidate source regions for the lunar meteorites. In *72nd Annual Meteoritical Society Meeting*. p. Abstract #5375.

Crites S. T., and Lucey P. G. 2015. Revised mineral and Mg # maps of the Moon from integrating results from the Lunar Prospector neutron and gamma-ray spectrometers with Clementine spectroscopy †. *American Mineralogist* 100: 973–982.

Crites S. T., Lucey P. G., and Taylor G. J. 2015. The mafic component of the lunar crust : Constraints on the crustal abundance of mantle and intrusive rock , and the mineralogy of lunar anorthosites †. *American Mineralogist* 100: 1708–1716.

Cuk M., and Stewart S. T. 2012. Making the Moon from a Fast-Spinning Earth: A Giant Impact Followed by Resonant Despinning. *Science* 1047: 1047–1053.

Çushing J. A., Taylor G. J., Norman M. D., and Keil K. 1999. The granulitic impactite suite: Impact melts and metamorphic breccias of the early lunar crust. *Meteoritics & Planetary Science* 34: 185–195.

Darwin G. H. 1879. On the precession of a viscous spheroid , and on the remote history of the Earth. *Philosophical Transactions of the Royal Society of London* 170: 447–538.

Dasch E. ., Shih C.-Y., Bansal B. ., Wiesmann H., and Nyquist L. E. 1987. Isotopic analysis of basaltic fragments from lunar breccia 14321 : Chronology and petrogenesis of pre-Imbrium mare volcanism. *Geochimica et Cosmochimica Acta* 51: 3241–3254.

Daubar I. J., Kring D. A., Swindle T. D., and Jull A. J. T. 2002. Northwest Africa 482: A crystalline impact-melt breccia from the lunar highlands. *Meteoritics & Planetary Science* 37: 1797–1813.

Day J. M. D., and Taylor L. A. 2007a. On the structure of mare basalt lava flow from textural analysis of the LaPaz Icefield and Northwest Africa 032 lunar meteorites. *Meteoritics & Planetary Science* 42: 3–17.

Day J. M. D., and Taylor L. A. 2007b. On the structure of mare basalt lava flows from textural analysis of the LaPaz Icefield and Northwest Africa 032 lunar meteorites. *Meteoritics & Planetary Science* 42: 3–17. http://doi.wiley.com/10.1111/j.1945-5100.2007.tb00213.x.

Day J. M. D., Taylor L. A., Floss C., Patchen A. D., Schnare D. W., and Pearson D. G. 2006. Comparative petrology, geochemistry, and petrogenesis of evolved, low-Ti lunar mare basalt meteorites from the LaPaz Icefield, Antarctica. *Geochimica et Cosmochimica Acta* 70: 1581–1600.

Delaney J. S. 1989. Lunar basalt breccia identified among Antarctic meteorites. *Nature* 342: 889–890.

Delaney J. S., Hervig R. L., Leitch C. A., Steele I. M., and Smith J. V. 1979. Mn/Fe/Mg distribution between silicate minerals from upper-mantle peridotites: complexities in garnet/clinopyroxene Mn/Mg thermometer: signicance of Fe/Mn ratio in meteorites and Moon. *Lunar and Planetary Science X* 277–279.

Delano J. W. 1991. Geochemical comparison of impact glasses from lunar meteorites ALHA81005 and MAC88105 and Apollo 16 regolith 64001. *Geochimica et Cosmochimica Acta* 55: 3019–3029.

Demidova S. I., Nazarov M. A., Anand M., and Taylor L. A. 2003. Lunar regolith breccia Dhofar 287B: A record of lunar volcanism. *Meteoritics & Planetary Science* 38: 501–514.

Demidova S. I., Nazarov M. A., Kurat G., Brandstätter F., and Ntaflos T. 2005. New lunar meteorites from Oman: Dhofar 925, 960 and 961. In *Lunar and Planetary Science XXXVI*. p. Abstract #1607.

Demidova S. I., Nazarov M. A., Lorenz C. A., Kurat G., Brandstätter F., and Ntaflos T. 2007. Chemical composition of lunar meteorites and the lunar crust. *Petrology* 15: 386–407.

Drozd R. J., Hohenberg C. M., Morgan C. J., Podosek F. A., and Wroge M. L. 1977. Cosmic-ray exposure history at Taurus-Littrow. *Proceedings Lunar Planetary Science 8th* 3027–3043.

Duke M. B. 2003. Sample return from the lunar South Pole-Aitken Basin. *Advances in Space Research* 31: 2347–2352.

Eberhardt P., Geiss J., Grögñer N., and Stettler A. 1973. How old is the crater Copernicus? *Earth, Moon and Planets* 8: 104–114.

Elardo S. M., Shearer C. K., Fagan A. L., Borg L. E., Gaffney A. M., Burger P. V., Neal C. R., Fernandes V. A., and Mccubbin F. M. 2014. The origin of young mare basalts inferred from lunar meteorites Northwest Africa 4734, 032, and LaPaz Icefield 02205. *Meteoritics and Planetary Science* 49: 261–291.

Elkins-Tanton L. T., Burgess S., and Yin Q. Z. 2011. The lunar magma ocean: Reconciling the solidification process with lunar petrology and geochronology. *Earth and Planetary Science Letters* 304: 326–336.

Elphic R. C., Lawrence D. J., Feldman W. C., Barraclough B. L., Maurice S., Binder A. B., and Lucey P. G. 1998. Lunar Fe and Ti Abundances: Comparison of Lunar Prospector and Clementine Data. *Science* 281: 1493–1496.

Eugster O. 1999. Chronology of dimict breccias and the age of South Ray crater at the Apollo 16 site. *Meteoritics & Planetary Science* 34: 385–391.

Eugster O. 1988. Cosmic-ray production rates for 3He, 21Ne, 38Ar, 83Kr, and 126Xe in chondrites based on 81Kr-Kr exposure ages. *Geochimica et Cosmochimica Acta* 52: 1649–1662.

Eugster O. 1990. Lunar meteorite MAC88105: History derived from cosmic-ray produced and solar wind trapped noble gases. *Lunar and Planetary Science XXI* 337.

Eugster O., Michel T., and Niedermann S. 1992. Solar wind and cosmic ray exposure history of lunar meteorite Yamato-793274. *Proceedings of the NIPR Symp. Antarct. Meteorites* 5: 23–35.

Eugster O., Niedermann S., Burger M., Krahenbuhl U., Weber H., Clayton R. N., and Mayeda T. K. 1989. Preliminary report on the Yamato-86032 lunar meteorite: III. Ages, noble gas isotopes, oxygen isotopes and chemical abundances. *Proc. NIPR Symp. Antarct. Meteorites* 2: 25–35.

Eugster O., Terribilini D., Polnau E., and Kramers J. 2001. The antiquity indicator argon-40/argon-36 for lunar surface samples calibrated by uranium-235-xenon-136 dating. *Meteoritics & Planetary Science* 36: 1097–1115.

Eugster O., Thalmann C., Albrecht A., Herzog G. F., Delaney J. S., Klein J., and Middleton R. 1996. Exposure history of glass and breccia phases of lunar meteorite EET87521. *Meteoritics & Planetary Science* 31: 299–304.

Fagan A. L., Joy K. H., Bogard D. D., and Kring D. A. 2014. Ages of Globally Distributed Lunar Paleoregoliths and Soils from 3.9 Ga to the Present. *Earth, Moon, and Planets* 112: 59–71.

Fagan T. J. et al. 2000. Northwest Africa 032, a new lunar mare basalt. *Meteoritics & Planetary Science* 35: Supplement.

Fagan T. J. et al. 2002. Northwest Africa 032: Product of lunar volcanism. *Meteoritics and Planetary Science* 37: 371–394.

Fagan T. J. et al. 2003. Northwest Africa 773: Lunar origin and iron-enrichment trend. *Meteoritics & Planetary Science* 38: 529–554.

Feldman W. C., Barraclough B. L., Fuller K. R., Lawrence D. J., Maurice S., Miller M. C., Prettyman T. H., and Binder A. B. 1999. The Lunar Prospector gamma-ray and neutron spectrometers. *Nuclear Instruments and Methods in Physics Research A.* 422: 562–566.

Fernandes V. A., Anand M., Burgess R., and Taylor L. A. 2004. Ar-Ar studies of Dhofar clast-rich feldspathic highland meteorites: 025, 026, 280, 303. *Lunar and Planetary Science XXXV* 11.

Fernandes V. A., and Burgess R. 2005. Volcanism in Mare Fecunditatis and Mare Crisium: Ar-Ar age studies. *Geochimica et Cosmochimica Acta* 69: 4919–4934.

Fernandes V. A., Burgess R., Bischoff A., Sokol A. K., and Haloda J. 2007. Kalahari 009 and North East Africa 003: Young (<2.5 Ga) Lunar Mare Basalts. *Lunar and Planetary Science XXXVIII.*

Fernandes V. A., Burgess R., and Morris A. 2009. 40Ar- 39Ar age determinations of lunar basalt meteorites Asuka 881757, Yamato 793169, Miller Range 05035, La Paz Icefield 02205, Northwest Africa 479, and basaltic breccia Elephant Moraine 96008. *Meteoritics & Planetary Science* 44: 805–821.

Fernandes V. A., Burgess R., and Turner G. 2003. 40Ar-30Ar chronology of lunar meteorites Northwest Africa 032 and 773. *Meteoritics & Planetary Science* 38: 555–564.

Fernandes V. A., Fritz J., Weiss B. P., Garrick-Bethell I., and Shuster D. L. 2013. The bombardment history of the Moon as recorded by 40 Ar-39 Ar chronology. *Meteoritics and Planetary Science* 48: 241–269.

Fink D., Klein J., Middleton R., Vogt S., Herzog G. F., and Reedy R. C. 1998. 41Ca, 26Al and 10Be in lunar basalt 74275 and 10Be in the double drive tube 74002/74001. *Geochimica et Cosmochimica Acta* 62: 2389–2402.

Foreman A. B., Korotev R. L., Jolliff B. L., and Zeigler R. A. 2008. Petrography and geochemistry of Dhofar 733- An unusual sodic, feldspathic lunar meteorite. *39th Lunar and Planetary Science Conference*.

Fukuoka T. 1990. Chemistry of Yamato-793274 lunar meteorite. *Antartic Meteorites XV. Papers presented to the 15th Symposium on Antarctic Meteorites* 122–123.

Fukuoka T. 1992. Geochemistry of lunar meteorites, Asuka-31 and Yamato-793169. *17th Symposium on Antartic Meteorites* 251–253.

Gaffney A. M., Borg L. E., Depaolo D. J., Irving A. J., and Livermore L. 2008. Age and isotope systematics of Northwest Africa 4898, a new type of highly-depleted mare basalt. *Lunar and Planetary Science XXXIX*.

Garrick-Bethell I., and Zuber M. T. 2009. Elliptical structure of the lunar South Pole-Aitken basin. *Icarus* 204: 399–408. http://dx.doi.org/10.1016/j.icarus.2009.05.032.

Gerstenkorn H. 1955. Über Gezeitenreibung beim Zweikörperproblem. *Zeitschrift für Astrophysik* 36: 345–374.

Giguere T. A., Ray Hawke B., Blewett D. T., Bussey D. B. J., Lucey P. G., Smith G. A., Spudis P. D., and Taylor G. J. 2003. Remote sensing studies of the Lomonosov-Fleming region of the Moon. *Journal of Geophysical Research* 108: 5118.

Giguere T. A., Taylor G. J., Hawke B. R., and Lucey P. G. 2000. The titanium contents of lunar mare basalts. *Meteoritics & Planetary Science* 35: 193–200.

Gillis J. J., and Jolliff B. L. 1999. Lateral and vertical heterogeneity of Thorium in the Procellarum KREEP Terrane: As reflected in the ejecta deposits of Post-Imbrium craters. *Workshop on New Views of the Moon 2: Understanding the Moon through the integration of diverse datasets*.

Gillis J. J., Jolliff B. L., and Korotev R. L. 2004. Lunar surface geochemistry: Global concentrations of Th, K, and FeO as derived from Lunar Prospector and Clementine data. *Geochimica et Cosmochimica Acta* 68: 3791–3805.

Gillis J. J., and Spudis P. D. 2000. Geology of the Smythii and Marginis Region of the Moon: Using Integrated Remotely Sensed Data. *Journal of Geophysical Research* 105: 4217–4233.

Glotch T. D. et al. 2010. Highly silicic compositions on the Moon. *Science* 329: 1510–1513.

Gnos E. et al. 2003. Lunar meteorite SaU 169: an extremely KREEP-rich Conference Item. *66th Annual Meteoritical Society Meeting*.

Gnos E. et al. 2004. Pinpointing the source of a lunar meteorite: implications for the evolution of the Moon. *Science* 305: 657–659.

Gnos E., Hofmann B. A., Al-Kathiri A., and Whitehouse M. J. 2006. The KREEP-rich Imbrium Impact Melt Breccia of the Lunar Meteorite Sayh al Uhaymir 169. *Meteoritics & Planetary Science* 41: 5111.

Gong S., Wieczorek M. A., Nimmo F., Kiefer W. S., Head J. W., Huang C., Smith D. E., and Zuber M. T. 2016. Thicknesses of mare basalts on the Moon from gravity and topography. *Journal of Geophysical Research: Planets* 121: 854–870.

Goodrich C. A., Jeffrey G., and Keil K. 1984. Petrology and Chemistry of Hyperferroan Anorthosites and Other Clasts from. *Journal of Geophysical Research* 89: C87–C94.

Goodrich C. A., and Keil K. 1987. Mare basalt and other clasts in Yamato lunar meteorites Y-791197, -82192 and -82193. *Memoirs of the National Institute of Polar Research* 46: 56–70.

El Goresy A., Prinz M., and Ramdohr P. 1976. Zoning in spinels as an indicator of the crystallization histories of mare basalts. *Proc. Lunar Planet. Sci. Conf 7th* 1261–1279.

Green D. H., Ringwood A. E., Hibberson W. O., and Ware N. G. 1975. Experimental petrology of Apollo 17 mare basalts. *Proceedings Lunar Planetary Science 6th* 871–893.

Greenhagen B. T. et al. 2010. Global silicate mineralogy of the Moon from the Diviner lunar radiometer. *Science* 329: 1507–1509.

Greshake A., Irving A. J., Kuehner S. M., Korotev R. L., Gellisen M., and Palme H. 2008. Northwest Africa 4898: A new high-alumina mare basalt from the Moon. *Lunar and Planetary Science XXXIX*.

Greshake A., Schmitt R. T., Stöffler D., Pätsch M., and Schultz L. 2001. Dhofar 081: A new lunar highland meteorite. *Meteoritics & Planetary Science* 36: 459–470.

Grier J. A., Kring D. A., and Swindle T. D. 1995. Impact melt and anorthositic clasts in lunar meteorites QUE93069 and MAC88105. *Lunar and Planetart Science XXVI* 513–514.

Gross J., and Treiman A. H. 2011. Unique spinel-rich lithology in lunar meteorite ALHA 81005: Origin and possible connection to M 3 observations of the farside highlands. *Journal of Geophysical Research* 116: E10009.

Gross J., Treiman A. H., and Mercer C. N. 2014. Lunar feldspathic meteorites: Constraints on the geology of the lunar highlands, and the origin of the lunar crust. *Earth and Planetary Science Letters* 388: 318–328.

Hagerty J. J., Lawrence D. J., Hawke B. R., Vaniman D. T., Elphic R. C., and Feldman W. C. 2006. Refined thorium abundances for lunar red spots: Implications for evolved, nonmare volcanism on the Moon. *Journal of Geophysical Research* 111: E06002.

Haloda J. et al. 2009. Petrology, geochemistry, and age of low-Ti mare-basalt meteorite Northeast Africa 003-A: A possible member of the Apollo 15 mare basaltic suite. *Geochimica et Cosmochimica Acta* 73: 3450–3470.

Haloda J., Korotev R. L., Tycova P., Jakes P., and Gabzdyl P. 2006. Lunar meteorite Northeast Africa 003-A: A new lunar mare basalt. *37th Annual Lunar and Planetary Science Conference*.

Haloda J., Tycova P., Jakes P., Gabzdyl P., and Kosler J. 2006. Lunar meteorite Northeast Africa 003-B: A new lunar mare basaltic breccia. *37th Annual Lunar and Planetary Science Conference*.

Hartmann W. K. et al. 1981. Chronology of planetary volcanism by comparative studies of planetary craters. In *Basaltic volcanism on the terrestrial planets*. Pergamon Press. pp. 1049–1128.

Hartmann W. K. 2003. Megaregolith evolution and cratering cataclysm models—Lunar cataclysm as a misconception (28 years later). *Meteoritics & Planetary Science* 38: 579–593.

Hartmann W. K., and Davis D. R. 1975. Satellite-sized planetesimals and lunar origin. *Icarus* 24: 504–515.

Hartmann W. K., Phillips R. J., and Taylor G. . J. 1984. *Origin of the Moon*, Houston, Texas: The Lunar and Planetary Institute.

Haskin L. a, Gillis J., Korotev R. L., and Jolliff L. 2000. The materials of the Procellarum KREEP Terrane: A synthesis of data from geomorphological mapping, remote sensing, and sample analyses. *Journal of Geophysical Research* 105: 403–415.

Head J. W., Adams J. B., McCord T. B., Pieters C., and Zisk S. 1978. Regional stratigraphy and geologic history of Mare Crisium. In *Mare Crisium: The View from Luna 24*, edited by Merrill R. B., and Papike J. J. New York: Pergamon Press. pp. 43–74.

Head J. W., and Wilson L. 2016. Generation, ascent and eruption of magma on the Moon: New insights into source depths, magma supply, intrusions and effusive/explosive eruptions (Part 1: Theory). *Icarus*.

Head J. W., and Wilson L. 1992. Lunar mare volcanism: Stratigraphy , eruption conditions , and the evolution of secondary crusts. *Geochimica et Cosmochimica Acta* 56: 2155–2175.

Heiken G. H., Vaniman D. T., and French B. M., eds. 1991. *Lunar Sourcebook*, Cambridge, New York, Melbourne: Cambridge University Press.

Hess P. C., and Parmentier E. M. 1995. A model for the thermal and chemical evolution of the Moon's interior: implications for the onset of mare volcanism. *Earth and Planetary Science Letters* 134: 501–514.

Hidaka H., Ebihara M., and Yoneda S. 2000. Neutron capture effects on samarium, europium, and gadolinium in Apollo 15 deep drill-core samples. *Meteoritics & Planetary Science* 589: 581–589.

Hidaka H., and Yoneda S. 2013. Isotopic studies of radiogenic and neutron-captured REE of lunar meteorites. *76th Annual Meteoritical Society Meeting*.

Hiesinger H., and Head III J. W. 2006. New Views of Lunar Geoscience. *Reviews in Mineralogy & Geochemistry* 60: 1–81.

Hiesinger H., Head III J. W., Wolf U., Jaumann R., and Neukum G. 2011. Ages and stratigraphy of lunar mare basalts: A synthesis. *GSA Special Papers* 477: 1–51.

Hiesinger H., Head III J. W., Wolf U., Jaumann R., and Neukum G. 2003. Ages and stratigraphy of mare basalts in Oceanus Procellarum, Mare Nubium, Mare Cognitum, and Mare Insularum. *Journal of Geophysical Research* 108: 5065–5092.

Hiesinger H., Head III J. W., Wolf U., Jaumann R., and Neukum G. 2006. New ages for basalts in Mare Fecunditatis based on crater size-frequency measurements. In *Lunar and Planetary Science XXXVII.* p. Abstract #1151.

Hiesinger H., Jaumann R., Neukum G., and Head J. W. 2000. Ages of mare basalts on the lunar nearside. *Journal of Geophysical Research* 105: 29,239-29,275.

Hill D. H., and Boynton W. V. 2003. Chemistry of the Calcalong Creek lunar meteorite and its relationship to lunar terranes. *Meteoritics & Planetary Science* 38: 595–626.

Holliday A. E., and Beauchemin D. 2004. Spatial profiling of analyte signal intensities in inductively coupled plasma mass spectrometry. *Spectrochimica Acta - Part B Atomic Spectroscopy* 59: 291–311.

Hopkins M. D., and Mojzsis S. J. 2015. A protracted timeline for lunar bombardment from mineral chemistry, Ti thermometry and U-Pb geochronology of Apollo 14 melt breccia zircons. *Contributions to Mineralogy and Petrology* 169.

Hsu W. et al. 2008. Petrography , mineralogy , and geochemistry of lunar meteorite Sayh al Uhaymir 300. *Meteoritics & Planetary Science* 1381: 1363–1381.

Hudgins J. A., Kelley S. P., Korotev R. L., and Spray J. G. 2011. Mineralogy, geochemistry, and 40Ar–39Ar geochronology of lunar granulitic breccia Northwest Africa 3163 and paired stones: Comparisons with Apollo samples. *Geochimica et Cosmochimica Acta* 75: 2865–2881.

Hudgins J. A., Spray J. G., Kelley S. P., Korotev R. L., and Sherlock S. C. 2008. A laser probe 40Ar/39Ar and INAA investigation of four Apollo granulitic breccias. *Geochimica et Cosmochimica Acta* 72: 5781–5798.

Hudgins J. A., Walton E. L., and Spray J. G. 2007. Mineralogy, petrology, and shock history of lunar meteorite Sayh al Uhaymir 300: A crystalline impact-melt breccia. *Meteoritics & Planetary Science* 42: 1763–1779.

Hurwitz D. M., and Kring D. A. 2014. Differentiation of the South Pole-Aitken basin impact melt sheet: implications for lunar exploration. *Journal of Geophysical Research: Planets* 1–24.

James O. B., Cohen B. A., and Taylor L. A. 2003. Lunar meteorite Dhofar 026: A shocked granulitic breccia, not an impact melt. *Lunar and Planetary Science XXXIV*.

James O. B., and Jackson E. D. 1970. Petrology of the Apollo 11 ilmerite basalts. *Journal of Geophysical Research* 75: 5793–5824.

Jaumann R. et al. 2012. Geology, geochemistry, and geophysics of the Moon: Status of current understanding. *Planetary and Space Science* 74: 15–41.

Jerde E. A., Morris R. V., and Warren P. H. 1990. In quest of lunar regolith breccias of exotic provenance: a uniquely anorthositic sample from the Fra Mauro (Apollo 14) highlands. *Earth and Planetary Science Letters* 98: 90–108.

Jerde E. A., Warren P. H., Morris R. V, Heiken G. H., and Vaniman D. T. 1987. A Potpourri of Regolith Breccias :“ New ” Samples from the Apollo 14 , 16 , and 17 Landing Sites. *Proceedings of the 17th Lunar and Planetary Science Conference, Part 2. Journal of Geophysical Research* 92: E526–E536.

Jilly C. E., Sharma P., Shouchon A. L., Blanchette-Guertin J. F., Flahaut J., and Kring D. A. 2011. Lunar landing sites to explore the extent of KREEP and its significance to key planetary processes. *42nd Lunar and Planetary Science Conference*.

Jolliff B. L. 1991. Fragments of quarts monzodiorite and felsite in Apollo 14 soil particles. *Proceedings Lunar Planetary Science* 21: 101–118.

Jolliff B. L. et al. 2011. Non-mare silicic volcanism on the lunar farside at Compton–Belkovich. *Nature Geoscience* 4: 566–571.

Jolliff B. L., Carpenter P. . ., Korotev R. L., Wittmann A., and Zeigler R. A. 2014. Connecting Lunar Meteorites to Source Terrains on the Moon. *The International Union of Microbeam Analysis Societies Quadrennial Meeting (IUMAS 6)* 9–10.

Jolliff B. L., Gillis J. J., Haskin L. A., Korotev R. L., and Wieczorek M. A. 2000. Major lunar crustal terranes : Surface expressions and crust-mantle origins. *Journal of Geophysical Research* 105: 4197–4216.

Jolliff B. L., Korotev R. L., and Rockow K. M. 1998. Geochemistry and petrology of lunar meteorite Queen Alexandra Range 94281, a mixed mare and highland regolith breccia, with special emphasis on very-low-titanium mafic components. *Meteoritics & Planetary Science* 33: 581–601.

Jolliff B. L., Korotev R. L., Zeigler R. A., and Floss C. 2003. Northwest Africa 773: lunar mare breccia with a shallow-formed olivine-cumulate component, inferred very-low-Ti (VLT) heritage, and a KREEP connection. *Geochimica et Cosmochimica Acta* 67: 4857–4879.

Jolliff B. L., Korotev R. L., Zeigler R. A., and Prettyman T. H. 2009. Connecting lunar meteorite Dhofar 961 to the South Pole-Aitken Basin through Lunar Prospector Gamma-Ray data. In *40th Lunar and Planetary Science Conference*. p. Abstract #2555.

Joy K. H., and Arai T. 2013a. Lunar meteorites: new insights into the geological history of the Moon. *Astronomy & Geophysics* 54: 4–28.

Joy K. H., and Arai T. 2013b. Lunar meteorites: new insights into the geological history of the Moon. *Astronomy & Geophysics* 54: 4.28-4.32.

Joy K. H., Burgess R., Hinton R., Fernandes V. A., Crawford I. A., Kearsley A. T., and Irving A. J. 2011. Petrogenesis and chronology of lunar meteorite Northwest Africa 4472: A KREEPy regolith breccia from the Moon. *Geochimica et Cosmochimica Acta* 75: 2420–2452.

Joy K. H., Burgess R., Ruzié L., and Clay P. L. 2014. Composition, age and regolith history of feldspathic lunar meteorites. *77th Annual Meeting of the Meteoritical Society*.

Joy K. H., Crawford I. A., Anand M., Greenwood R. C., Franchi I. A., and Russell S. S. 2008. The petrology and geochemistry of Miller Range 05035: A new lunar gabbroic meteorite. *Geochimica et Cosmochimica Acta* 72: 3822–3844.

Joy K. H., Crawford I. A., Downes H., Russell S. S., and Kearsley A. T. 2006. A petrological, mineralogical and chemical analysis of the lunar mare basalt meteorites LaPaz Icefield 02205, 02224 and 02226. *Meteoritics & Planetary Science* 41 (7): 1003–1025.

Joy K. H., Crawford I. A., Kearsley A. T., Fernandes V. A., Burgess R., and Irving A. J. 2008. The petrography and composition of lunar meteorite Northwest Africa 4472. In *Lunar and Planetary Science XXXIX*. p. Abstract #1132.

Joy K. H., Crawford I. A., Russell S. S., and Kearsley A. T. 2010. Lunar meteorite regolith breccias: An in situ study of impact melt composition using LA-ICP-MS with implications for the composition of the lunar crust. *Meteoritics & Planetary Science* 45: 917–946.

Joy K. H., Kring D. A., Bogard D. D., McKay D. S., and Zolensky M. E. 2011. Re-examination of the formation ages of the Apollo 16 regolith breccias. *Geochimica et Cosmochimica Acta* 75: 7208–7225.

Joy K. H., Nemchin A., Grange M., Lapen T. J., Peslier A. H., Ross D. K., Zolensky M. E., and Kring D. A. 2014. Petrography, geochronology and source terrain characteristics of lunar meteorites Dhofar 925, 961 and Sayh al Uhaymir 449. *Geochimica et Cosmochimica Acta* 144: 299–325.

Kallemeyn G. W., and Warren P. H. 1983. Compositional implications regarding the lunar origin of the ALHA81005 meteorite. *Geophysical Research Letters* 10: 833–836.

Kaneoka I., and Nagao K. 1993. 40Ar-39Ar analyses of a lunar meteorite (Yamato-86032) and a few LL2 and LL4 chondrites from Antarctica. *Proc. NIPR Symp. Antarct. Meteorites* 6: 88–99.

Kaneoka I., and Takaoka N. 1986. 40Ar-39Ar analyses of an antartic meteorite Yamato-791197 of probable lunar origin. *Proceedings of the Tenth Symposium on Antarctic Meteorites, 1985. Memoirs of National Institute of Polar Research* 105–112.

Karouji Y., Ebihara M., and Yamaguchi A. 2004. Chemical characterization of lunar meteorites, Yamato 86032 and Dhofar 489 (abstract). *Antarctic Meteorites XXVIII.* 29–30.

Klima R. L. et al. 2011. New insights into lunar petrology: Distribution and composition of prominent low-Ca pyroxene exposures as observed by the Moon Mineralogy Mapper (M 3). *Journal of Geophysical Research* 116.

Koeberl C., Kurat G., and Brandstatter F. 1990. Lunar Meteorite Yamato-86032: mineralocal, petrological, and geochemical studies. *Proc. NIPR Symp. Antarct. Meteorites* 3: 3–18.

Koeberl C., Kurat G., and Brandstätter F. 1993. Gabbroic lunar mare meteorites Asuka-881757 (Asuka 31) and Yamato-793169: Geochemical and mineralogical study. *Proceedings of the NIPR Symp. Antarct. Meteorites* 6: 14–34.

Koeberl C., Kurat G., and Brandstätter F. 1991a. Lunar Meteorite Yamato-793274: Mixture of Mare and Highland Components, and Barringerite from the Moon. *Proc. NIPR Symp. Antarct. Meteorites* 4: 33–55.

Koeberl C., Kurat G., and Brandstätter F. 1991b. MAC88105-A regolith breccia from the lunar highlands : petrological , and geochemical studies. *Geochimica et Cosmochimica Acta* 55: 3073–3087.

Koeberl C., Kurat G., and Brandstätter F. 1996. Mineralogy and geochemistry of lunar meteorite Queen Alexandra Range 93069. *Meteoritics & Planetary Science* 31: 897–908.

Korochantseva E. V, Buikin A. I., Hopp J., Korochantsev A. V, and Trieloff M. 2016. 40Ar-39Ar results of lunar meteorites Dhofar 025, 280, 309, 730, 733, 1436, 1442, SaU 449, NWA 6888. *79th Annual Meeting of the Meteoritical Society*.

Korotev R. L. 1999. A new estimate of the composition of the feldspathic upper crust of the Moon. *Lunar and Planetary Science XXX*.

Korotev R. L. 2005. Lunar geochemistry as told by lunar meteorites. *Chemie der Erde - Geochemistry* 65: 297–346.

Korotev R. L. 2012. Lunar meteorites from Oman. *Meteoritics & Planetary Science* 47: 1365–1402.

Korotev R. L. 1996. On the relationship between the Apollo 16 ancient regolith breccias and feldspathic fragmental breccias, and the composition of the prebasin crust in the Central Highlands of the Moon. *Meteoritics & Planetary Science* 31: 403–412.

Korotev R. L. 1997. Some things we can infer about the Moon from the composition of the Apollo 16 regolith. *Meteoritics & Planetary Science* 32: 447–478.

Korotev R. L. 2000. The great lunar hot spot and the composition and origin of the Apollo mafic ("LKFM") impact-melt breccias. *Journal of Geophysical Research* 105: 4317–4345.

Korotev R. L. 2008. Using composition to assess pairing relationships among lunaites. *Geochimica et Cosmochimica Acta* 72: A492.

Korotev R. L., and Irving A. J. 2005. Compositions of three lunar meteorites: Meteorite Hills 01210, Northeast Africa 001, and Northwest Africa 3136. *Lunar and Planetary Science XXXVI*.

Korotev R. L., and Irving A. J. 2013. Keeping up with the lunar meteorites-2013. In *44th Lunar and Planetary Science Conference*.

Korotev R. L., Jolliff B. L., and Carpenter P. K. 2011. Miller Range Feldspathic Lunar Meteorites. *42nd Lunar and Planetary Science Conference* Abstract #1999.

Korotev R. L., Jolliff B. L., Zeigler R. A., Gillis J. J., and Haskin L. A. 2003. Feldspathic lunar meteorites and their implications for compositional remote sensing of the lunar surface and the composition of the lunar crust. *Geochimica et Cosmochimica Acta* 67: 4895–4923.

Korotev R. L., and Zeigler R. A. 2015. ANSMET Meteorites from the Moon. In *35 Seasons of U.S. Antarctic Meteorites*, edited by Righter K., Corrigan C. M., McCoy T. J., and Harvey R. . Washington D.C.: American Geophysical Union. pp. 101–130.

Korotev R. L., Zeigler R. a., and Jolliff B. L. 2006. Feldspathic lunar meteorites Pecora Escarpment 02007 and Dhofar 489: Contamination of the surface of the lunar highlands by post-basin impacts. *Geochimica et Cosmochimica Acta* 70: 5935–5956.

Korotev R. L., Zeigler R. A., Jolliff B. L., Irving A. J., and Bunch T. E. 2009. Compositional and lithological diversity among brecciated lunar meteorites of intermediate iron concentration. *Meteoritics & Planetary Science* 44: 1287–1322.

Kramer G. Y., Jaiswal B., Hawke B. R., Öhman T., Giguere T. A., and Johnson K. 2015. The basalts of Mare Frigoris. *Journal of Geophysical Research* 120: 1646–1670.

Kramer G. Y., Kring D. A., Nahm A. L., and Pieters C. M. 2013. Spectral and photogeologic mapping of Schrödinger Basin and implications for post-South Pole-Aitken impact deep subsurface stratigraphy. *Icarus* 223: 131–148. http://linkinghub.elsevier.com/retrieve/pii/S001910351200454X (Accessed June 23, 2014).

Kring D. A., and Cohen B. A. 2002. Cataclysmic bombardment throughout the inner solar system 3 . 9 – 4 . 0 Ga. *Journal of Geophysical Research* 107.

Kuehner S. M., Irving A. J., and Gregory D. A. 2005. Lunar feldspathic meteorite NWA 2200; A polymict glassy impact-melt breccia with ferroan anorthosite (FAN) affinities. *68th Annual Meteoritical Society Meeting*.

Kuehner S. M., Irving A. J., Korotev R. L., Hupé G. M., and Ralew S. 2007. Zircon-Baddeleyte-Bearing Silica+K-Feldspar Granophyric Clasts in KREEP-rich Lunar Breccias Northwest Africa 4472 and 4485. *Lunar and Planetary Science XXXVIII*.

Lanfang X., Hongyi C., Bingkui M., Zhipeng X., and Jie Y. 2014. Petrography and mineralogy of new lunar meteorite MIL 090036. *Advances in Polar Science* 25: 17–25.

Laul L. C., and Schmitt R. A. 1973. Chemical composition of Apollo 15, 16 and 17 samples. *Proceedings of the Fourth Lunar Science Conference* 4: 1349.

Lawrence D. J., Elphic R. C., Feldman W. C., Prettyman T. H., Gasnault O., and Maurice S. 2003. Small-area thorium features on the lunar surface. *Journal of Geophysical Research* 108: 5102–5127.

Lawrence D. J., Feldman W. C., Barraclough B. L., Binder A. B., Elphic R. C., Maurice S., Miller M. C., and Prettyman T. H. 2000. Thorium abundances on the lunar surface. *Journal of Geophysical Research* 105: 20,307-20,331.

Lawrence D. J., Feldman W. C., Barraclough B. L., Binder A. B., Elphic R. C., Maurice S., and Thomsen D. R. 1998. Global Elemental Maps of the Moon: The Lunar Prospector Gamma-Ray Spectrometer. *Science* 281: 1484–1489.

Lawrence D. J., Maurice S., and Feldman W. C. 2004. Gamma-ray measurements from Lunar Prospector: Time series data reduction for the Gamma-Ray Spectrometer. *Journal of Geophysical Research* 109. http://doi.wiley.com/10.1029/2003JE002206 (Accessed July 19, 2013).

Lawrence D. J., Puetter R. C., Elphic R. C., Feldman W. C., Hagerty J. J., Prettyman T. H., and Spudis P. D. 2007. Global spatial deconvolution of Lunar Prospector Th abundances. *Geophysical Research Letters* 34: L03201.

Leont’eva E. M., Matukov D. I., Nazarov M. A., Sergeev S. A., Shukolyukov Y. A., and Brandstaetter F. 2005. First determination of the isotopic age of a lunar meteorite by the uranium-lead zircon method. *Petrology* 13: 193–196.

Lichte F. E., Meier A. L., and Crock J. G. 1987. Determination of the Rare-Earth Elements in Geological Materials by Inductively Coupled Plasma Mass Spectrometry. *Analytical Chemistry* 59: 1150–1157.

Lindstrom M. M., Lindstrom D. J., Korotev R. L., and Haskin L. A. 1986. Lunar meteorite Yamato-791197: A polymict anorthositic norite breccia. *Memoirs of the National Institute of Polar Research* 58–75.

Lindstrom M. M., Mittlefehldt D. W., Martinez R. R., Lipschutz M. E., and Wang M.-S. 1991. Geochemistry of Yamato-82192, -86032 and -793274. In *Proceedings of the NIPR Symp. Antarct. Meteorites*. pp. 12–32.

Lindstrom M. M., Mittlefehldt D. W., Morris R. V, Martinez R. R., and Wentworth S. J. 1995. QUE93069, a more mature regolith breccia for the Apollo 25th anniversary. *Lunar and Planetart Science XXVI* 849–850.

Lindstrom M. M., Schwarz C., Score R., and Masons B. 1991. MacAlpine Hills 88104 and 88105 lunar highland meteorites: General description and consortium overview. *Geochimica et Cosmochimica Acta* 55: 2999–3007.

Lindstrom M. M., Wentworth S. J., Martinez R. R., Mittlefehldt D. W., McKay D. S., Ming-Sheng W., and Lipschutz M. E. 1991. Geochemistry and petrography of the MacAlpine Hills lunar meteorites. *Geochimica et Cosmochimica Acta* 55: 3089–3103.

Liu D., Jolliff B. L., Zeigler R. A., Korotev R. L., Wan Y., Xie H., Zhang Y., Dong C., and Wang W. 2012. Comparative zircon U–Pb geochronology of impact melt breccias from Apollo 12 and lunar meteorite SaU 169, and implications for the age of the Imbrium impact. *Earth and Planetary Science Letters* 319–320: 277–286.

Liu Y., Patchen A., and Taylor L. A. 2011. Lunar Highland Breccias MIL 090034/36/70/75: a significant KREEP Component. *42nd Lunar and Planetary Science Conference* Abstract #1261.

Lloyd G. E. 1987. Atomic Number and Crystallographic Contrast Images with the SEM: A Review of Backscattered Electron Techniques. *Mineralogical Magazine* 51: 3–19.

Longhi J. 2003. A new view of lunar ferroan anorthosites: Postmagma ocean petrogenesis. *Journal of Geophysical Research* 108: 5083.

Longhi J. 1992. Experimental petrology and petrogenesis of mare volcanics. *Geochimica et Cosmochimica Acta* 56: 2235–2251.

Longhi J., and Ashwal L. D. 1985. Two-Stage Models for Lunar and Terrestrial Anorthosites Petrogenesis without a Magma Ocean. *Proceedings Lunar Planetary Science* 90: C571–C584.

Loper D. E., and Werner C. L. 2002. On lunar asymmetries 1. Tilted convection and crustal asymmetry. *Journal of Geophysical Research* 107.

Lorenzetti S., Busemann H., and Eugster O. 2005. Regolith history of lunar meteorites. *Meteoritics & Planetary Science* 40: 315–327.

Lucey P. G. et al. 2006. Understanding the Lunar Surface and Space-Moon Interactions. In *New Views of the Moon*, edited by Jolliff B. L., Wieczorek M. A., Shearer C. K., and Neal C. R. Mineralogical Society of America. pp. 83–219.

Lucey P. G., David T. B., and Hawke B. R. 1998. Mapping the FeO and TiO2 content of the lunar surface with multispectral imagery. 103: 3679–3699.

Lyman C. E., Goldstein J. I., Williams D. B., Ackland D. W., Von Harrach S., Nicholls A. W., and Statham P. J. 1994. High-performance X-ray detection in a new analytical electron microscope. *Journal of Microscopy* 176: 85–98.

Ma M.-S., Schmitt R. A., Taylor G. J., Warner R. D., Lange D. E., and Keil K. 1978. Chemistry and petrology of Luna 24 lithic fragments and <250 m soils: Constraints on the origin of VLT mare basalts. *In: Mare Crisium: The view from Luna 24; Proceedings of the Conference* 569–592.

Manning T. J., and Grow W. R. 1997. *Introduction to Inductively Coupled Plasma Atomic Emission Spectrometry,.*

Martin D. J. P., Joy K. H., Wogelius R., Morlok A., and Hiesinger H. 2016. Using quantitative micro-FTIR spectroscopy to characterise the shock history of feldspathic lunar meteorites Miller Range 090034, 090070 and 090075. *47th Lunar and Planetary Science Conference* Abstract #1547.

Marvin U. B., and Holmberg B. B. 1992. Highland and mare components in the Calcalong Creek lunar meteorite. *Lunar and Planetary Science Conference XXIII* 849–850.

McKay D. S., Bogard D. D., Morris R. V., Korotev R. L., Johnson P., and Wentworth S. J. 1986. Apollo 16 Regolith Breccias: Characterization and Evidence for Early Formation in the Mega-Regolith. *Journal of Geophysical Research: Proceedings of the sixteenth lunar and planetay science conference* 91: D277–D303.

McKay D. S., Heiken G. H., Basu A., Blandford G., Simon S., Reedy R., French B. M., and Papike J. J. 1991. The Lunar Regolith. In *The Lunar Sourcebook,* edited by Heiken G. H., Vaniman D. T., and French B. M. Cambridge University Press. pp. 285–356.

McLeod C. L., Brandon A. D., and Armytage R. M. G. 2014. Constraints on the formation age and evolution of the Moon from 142Nd-143Nd systematics of Apollo 12 basalts. *Earth and Planetary Science Letters* 396: 179–189.

Mercer C. N., Treiman A. H., and Joy K. H. 2013. New lunar meteorite Northwest Africa 2996: A window into farside lithologies and petrogenesis. *Meteoritics & Planetary Science* 48: 289–315.

Miljkovic K., Wieczorek M. A., Collins G. S., Solomon S. C., Smith D. E., and Zuber M. T. 2015. Excavation of the lunar mantle by basin-forming events on the Moon. *Earth and Planetary Science Letters* 409: 243–251.

Moore H. J., Boyce J. M., and Hahn D. A. 1980. Small impact craters in the lunar regolith- Their morphologies, relative ages, and rates of formation. *Earth, Moon and Planets* 23: 231–252.

Morbidelli A., Marchi S., Bottke W. F., and Kring D. A. 2012. A sawtooth-like timeline for the first billion years of lunar bombardment. *Earth and Planetary Science Letters* 355–356: 144–151. http://dx.doi.org/10.1016/j.epsl.2012.07.037.

Morris R. V, Score R., Dardano C., and Heiken G. 1983. *Handbook of lunar soils*, Houston, Texas: Planetary Materials Branch, NASA.

Nagaoka H., Karouji Y., Arai T., Ebihara M., and Hasebe N. 2013. Geochemistry and mineralogy of a feldspathic lunar meteorite (regolith breccia), Northwest Africa 2200. *Polar Science* 7: 241–259.

Nagaoka H., Takeda H., Karouji Y., Ohtake M., Yamaguchi A., Yoneda S., and Hasebe N. 2011. Mineral chemistry and reflectance spectra for the anorthosite clast in lunar meteorite Dhofar 489 with reference to the lunar farside crust. *The 34th Symposium on Antarctic Meteorites* 56–57.

Nakamura N., Unruh D. M., and Tatsumoto M. 1986. REE, Rb-Sr and Pb isotopic characteristics of the Yamato-791197 meteorite: Evidence for a lunar highland origin. *Proceedings of the Tenth Symposium on Antarctic Meteorites, 1985. Memoirs of the National Institute of Polar Research* 106–115.

Nazarov M. A., Demidova S. I., Patchen A., and Taylor L. A. 2002. Dhofar 301, 302, and 303: Three new lunar highland meteorites from Oman. *Lunar and Planetary Science Conference XXXIII*.

Nazarov M. A., Demidova S. I., and Taylor L. A. 2003. Trace element chemistry of lunar highland meteorites from Oman. *Lunar and Planetary Science XXXIV*.

Neal C. R., and Taylor L. A. 1992. Petrogenesis of mare basalts: A record of lunar volcanism. *Geochimica et Cosmochimica Acta* 56: 2177–2211.

Neal C. R., Taylor L. A., Lui Y.-G., and Schmitt R. A. 1991. Paired lunar meteorites MAC88104 and MAC88105: A new “ FAN ” of lunar petrology. *Geochimica et Cosmochimica Acta* 55: 3037–3049.

Neal C. R., Wu Y. Z., Cui X. Z., Peng W. X., and Ping J. S. 2015. Regolith at the Chang’e-3 landing site: a new type of mare basalt composition. *46th Lunar and Planetary Science Conference*.

Nemchin A. A., Pidgeon R. T., Whitehouse M. J., Vaughan J. P., and Meyer C. 2008. SIMS U-Pb study of zircon from Apollo 14 and 17 breccias: Implications for the evolution of lunar KREEP. *Geochimica et Cosmochimica Acta* 72: 668–689.

Neukum G., and Ivanov B. A. 1994. Crater size distribution and impact probabilities on Earth from lunar terrestrial-planet and asteroid cratering data. In *Hazards due to Comets and Asteroids*, edited by Gehrels T. University of Arizona Press. pp. 359–416.

Neumann G. A. et al. 2015. Lunar impact basins revealed by Gravity Recovery and Interior Laboratory measurements. *Science Advances* 1: 1–11.

Niihara T., Beardm S. P., Swindle T. D., and Kring D. A. 2013. Petrography and mineral compositions: *44th Lunar and Planetary Science Conference*.

Nishiizumi K. 1995. Final results of cosmogenic nuclides in lunar rock 64455. *LPS XXVI* 1055–1056.

Nishiizumi K., Arnold J. R., Klein J., Fink D., Middleton R., Kubik P. W., Sharma P., Elmore D., and Reedy R. C. 1991. Exposure histories of lunar meteorites: ALHA81005, MAC88104, MAC88105, and Y791197. *Evolution of Solar System Materials: A New Perspective from Antarctic meteorites* 55: 3149–3155.

Nishiizumi K., Arnold R. J., Caffee M. W., Finkel C. R., and Reedy C. R. 1992. Cosmic ray exposure histories of lunar meteorites Asuka-881757, Yamato-793169, and Calcalong Creek. *17th Symposium on Antartic Meteorites* 129–132.

Nishiizumi K., and Caffee M. W. 2001. Exposure Histories of Lunar Meteorites Northwest Africa 032 and Dhofar 081. *32nd Lunar and Planeary Conference*.

Nishiizumi K., and Caffee M. W. 1998. Measurements of cosmogenic calcium-41 and calcium-41/chlorine-36 terrestrial ages. *Meteoritics & Planetary Science* 33: A117.

Nishiizumi K., and Caffee M. W. 2013. Relationships among six lunar meteorites from Miller Range, Antarctica based on cosmogenic radionuclides. *44th Lunar and Planetary Science Conference* Abstract #2715.

Nishiizumi K., Caffee M. W., Jull A. J. T., and Reedy R. C. 1996. Exposure history of lunar meteorites Queen Alexandra range 93069 and 94269. *Meteoritics & Planetary Science* 31: 893–896.

Nishiizumi K., Fink D., Klein J., Middleton R., Masarik J., Reedy R. C., and Arnold J. R. 1997. Depth profile of41Ca in an Apollo 15 drill core and the low-energy neutron flux in the Moon. *Earth and Planetary Science Letters* 148: 545–552.

Nishiizumi K., Hillegonds D. J., McHargue L. R., and Jull A. J. T. 2004. Exposure and terrestrial histories of new lunar and martian meteorites. *Lunar and Planetary Science XXXV*.

Nishiizumi K., Hillegonds D. J., and Welten K. C. 2006. Exposure and terrestrial histories of lunar meteorites.

Norman M. D., Hui S., and Adena K. 2011. The Lunar Impact Record: Greatest Hits and One Hit Wonders. In *Proceedings from the 11th Australian Space Science Conference*. pp. 93–104.

Nyquist L. et al. 2006. Feldspathic clasts in Yamato-86032: Remnants of the lunar crust with implications for its formation and impact history. *Geochimica et Cosmochimica Acta* 70: 5990–6015.

Nyquist L. ., and Shih C.-Y. 1992. The isotopic record of lunar volcanism. *Geochimica et Cosmochimica Acta* 56: 2213–2234.

Nyquist L. E., Shih C.-Y., and Reese Y. D. 2007. Sm-Nd and Rb-Sr ages for MIL 05035: Implications for surface and mantle sources. *38th Lunar and Planetary Science Conference*.

Nyquist L. E., Shih C.-Y., Reese Y. D., and Bogard D. . 2005. Age of lunar meteorite LAP 02205 and implications for impact sampling of planetary surfaces. *36th Lunar and Planetary Science Conference*.

Nyquist L. E., Shih C.-Y., Reese Y. D., Park J., Bogard D. D., Garrison D. H., and Yamaguchi A. 2011. Sm-Nd and Ar-Ar studies of Dho 908 and 489: Implications for lunar crustal history. *42nd Lunar and Planetary Science Conference*.

O'Donnell S. P., Jolliff B. L., Zeigler R. A., and Korotev R. L. 2008. Identifying the Mafic Components in Lunar Regolith Breccia NWA 3136. *Lunar and Planetary Science XXXIX*.

Ohtake M. et al. 2012. Asymmetric crustal growth on the Moon indicated by primitive farside highland materials. *Nature Geoscience* 5: 384–388.

Ohtake M. et al. 2013. One Moon, Many Measurements 3: Spectral reflectance. *Icarus* 226: 364–374.

Ohtake M. et al. 2009. The global distribution of pure anorthosite on the Moon. *Nature* 461: 236–240.

Ostertag R., Stöffler D., Bischoff A., Palme H., Schultz L., Spettel B., Weber H., Weckwerth G., and Wänke H. 1985. Lunar meteorite Yamato-791197: Petrography, shock history and chemical composition. *Memoirs of the National Institute of Polar Research* 17–44.

Oxford Instruments. 2006. INCA Energy Operator Manual. INCA Energy Operator Manual.

Palme H., Spettel B., Jochum K. P., Dreibus G., Weber H., Weckwerth G., Wanke H., Bischoff A., and Stöffler D. 1991. Lunar highland meteorites and the composition of the lunar crust. *Geochimica et Cosmochimica Acta* 55: 3105–3122.

Papike J. J. 1998. *Planetary materials*, Reviews in Mineralogy.

Park J. et al. 2013. Late bombardment of the lunar highlands recorded in MIL 090034, MIL 090036 and MIL 090070 lunar meteorites. *44th Lunar and Planetary Science Conference* Abstract #2576.

Parmentier E. M., and Hess P. C. 1998. On the possible role of chemical stratification in the evolution of the Moon. *Lunar and Planetary Science XXIX*.

Parmentier E. M., Zhong S., and Zuber M. T. 2002. Gravitational differentiation due to initial chemical stratification: Origin of lunar asymmetry by the creep of dense KREEP? *Earth and Planetary Science Letters* 201: 473–480.

Peplowski P. N., and Lawrence D. J. 2013. New insights into the global composition of the lunar surface from high-energy gamma rays measured by Lunar Prospector. *Journal of Geophysical Research: Planets* 118: 671–688.

Pernet-Fisher J., and Joy K. H. 2016. The lunar highlands : old crust , new ideas. *Astronomy & Geophysics* 57: 26–30.

Petro N. E., and Pieters C. M. 2004. Surviving the heavy bombardment: Ancient material at the surface of South Pole-Aitken basin. *Journal of Geophysical Research E: Planets* 109: 1–13.

Pieters C. M. et al. 2011. Mg-spinel lithology: A new rock type on the lunar farside. *Journal of Geophysical Research* 116: E00G08.

Pieters C. M., Hawke B. R., Gaffey M., and Mcfadden L. A. 1983. Possible lunar source areas of meteorite ALHA81005: Geochemical remote sensing information. *Geophysical Research Letters* 10: 813–816.

Pieters C. M., Head J. W., Gaddis L., Jolliff B., and Duke M. 2001. Rock types of South Pole-Aitken basin and extent of basaltic volcanism. *Journal of Geophysical Research* 106: 28001–28022.

Polnau E., and Eugster O. 1998. Cosmic-ray produced, radiogenic, and solar noble gases in lunar meteorites Queen Alexandra Range 94269 and 94281. *Meteorit. Planet. Sci.* 33: 313–319.

Potter R. W. K., Kring D. A., and Collins G. S. 2015. Scaling of basin-sized impacts and the influence of target temperature. In *Large Meteorite Impacts and Planetary Evolution V*, edited by Osinski G. ., and Kring D. A.

Potter R. W. K., Kring D. A., Collins G. S., Kiefer W. S., and McGovern P. J. 2012. Estimating transient crater size using the crustal annular bulge: Insights from numerical modeling of lunar basin-scale impacts. *Geophysical Research Letters* 39.

Prettyman T. H., Hagerty J. J., Elphic R. C., Feldman W. C., Lawrence D. J., McKinney G. W., and Vaniman D. T. 2006. Elemental composition of the lunar surface: Analysis of gamma ray spectroscopy data from Lunar Prospector. *Journal of Geophysical Research* 111: E12007.

Rhodes J. M., and Blanchard D. P. 1981. Apollo 11 breccias and soils: Aluminous mare basalts or multi-component mixtures? *Proceedings Lunar Planetary Science* 12B: 607–620.

Righter K. 2010. Antarctic Meteorite Newsletter. 33.

Righter K., and Bussey B. 2006. Mineralogy and petrology of the mare basalt-rich breccia MET 01210. *69th Annual Meteoritical Society Meeting*.

Righter K., and Canup R. M. 2016. Testing and resilience of the impact origin of the Moon. *47th Lunar and Planetary Science Conference*.

Righter K., Collins S. J., and Brandon A. D. 2005. Mineralogy and petrology of the LaPaz Icefield lunar mare basaltic meteorites. *Meteoritics & Planetary Science* 40: 1703–1722.

Robinson K. L., Treiman A. H., and Joy K. H. 2012. Basaltic fragments in lunar feldspathic meteorites: Connecting sample analyses to orbital remote sensing. *Meteoritics & Planetary Science* 47: 387–399.

Rollison H. 1993. *Using geochemical data,*.

Rubin A. E. 2015. Maskelynite in asteroidal, lunar and planetary basaltic meteorites: An indicator of shock pressure during impact ejection from their parent bodies. *Icarus* 257: 221–229.

Russell S. S., Joy K. H., Jeffries T. E., Consolmagno G. J., and Kearsley A. 2014. Heterogeneity in lunar anorthosite meteorites: implications for the lunar magma ocean model. *Philosophical transactions. Series A, Mathematical, physical, and engineering sciences* 372: 20130241.

Russell S. S., Zipfel J., Folco L., Jones R. H., Grady M. M., McCoy T., and Grossman J. N. 2003. The Meteoritical Bulletin, No. 87, 2003 July. *Meteoritics & Planetary Science* 38: A189–A248.

Ryder G. 1982. Lunar anorthosite 60025, the petrogenesis of lunar anorthosites, and the composition of the Moon. *Geochimica et Cosmochimica Acta* 46: 1591–1601.

Ryder G. 1990. Lunar samples, lunar accretion and the early bombardment of the moon. *Eos* 71: 313, 322–323.

Ryder G. 2002. Mass flux in the ancient Earth-Moon system and benign implications for the origin of life on Earth. *Journal of Geophysical Research* 107: 794–795.

Sands D. G., De Laeter J. R., and Rosman K. J. R. 2001. Measurements of neutron capture effects on Cd, Sm and Gd in lunar samples with implications for the neutron energy spectrum. *Earth and Planetary Science Letters* 186: 335–346.

Schaeffer G. A., and Shaeffer O. A. 1977. 39Ar-40Ar ages of lunar rocks. *Proceedings Lunar Planetary Science 8th* 2253–2300.

Scherer P., Pätsch M., and Schultz L. 1998. Noble-gas study of the new lunar highland meteorite Dar al Gani 400. *Meteoritics & Planetary Science* 33: A135–A136.

Schmidt O., Hanna G. H., and Lebedinsky A. 1959. *A theory of the Origin og the Earth: 4 Lectures,* Lawrence & Wishart.

Schultz P. H., and Spudis P. D. 1983. Beginning and end of lunar mare volcanism. *Nature* 302: 233–236.

Scott Hubbard G., Feldman W., Cox S. A., Smith M. A., and Chu-Thielbar L. 2002. Lunar Prospector: First results and lessons learned. *Acta Astronautica* 50: 39–47.

Semenova A. S., Nazarov M. A., Kononkova N. N., Patchen A., and Taylor L. A. 2000. Mineral chemistry of lunar meteorite Dar al Gani 4000. *Lunar and Planetary Science XXXI*.

Shaulis, B.J., Righter, M., Lapen, T.J., and Irving A. J. 2013. 3.1 Ga crystallization age of magnesian and ferroan gabbro lithologies in lunar meteorites Northwest Africa 773, 6950 and 7007, and evidence 3.95 Ga components in NWA 773 polymict breccia. *44th Lunar and Planetary Science Conference*.

Shearer C. K. et al. 2006. Thermal and Magmatic Evolution of the Moon. In *New Views of the Moon*, edited by Jolliff B. L., Wieczorek M. A., Shearer C. K., and Neal C. R. Chantilly, Virginia: Mineralogical Society of America. pp. 365–518.

Shearer C. K., and Papike J. J. 1993. Basaltic magmatism on the Moon: A perspective from volcanic picritic glass beads. *Geochimica et Cosmochimica Acta* 57: 4785–4812.

Shearer C. K., and Papike J. J. 1999. Magmatic evolution of the Moon. *American Mineralogist* 84: 1469–1494.

Shervais J. W., and McGee J. J. 1998. Ion and electron microprobe study of troctolites, norite, and anorthosites from Apollo 14: Evidence for urKREEP assimilation during petrogenesis of Apollo 14 Mg-suite rocks. *Geochimica et Cosmochimica Acta* 62: 3009–3023.

Shih C.-Y., Nyquist L. E., Reese Y., Wiesmann H., Nazarov M. A., and Taylor L. A. 2002. The chronology and petrogenesis of the mare basalt clast from lunar meteorite Dhofar 287: Rb-Sr and Sm-Nd isotopic studies. In *Lunar and Planetary Science XXXIII*. p. Abstract #1344.

Shirai N., Ebihara M., Sekimoto S., Yamaguchi A., Nyquist L. ., Shih C.-Y., Park J., and Nagao K. 2012. Chemical characteris tics of MIL 090034, 090036 and 090070. *43rd Lunar and Planetary Science Conference* Abstract #1659.

Shukolyukov Y. A., Nazarov M. A., and Ott U. 2004. Noble gases in new lunar meteorites from Oman: Irradiation history, trpped gases, and cosmic-ray exposure and K-Ar ages. *Geochemistry International 42* 1001–1017.

Shukolyukov Y. A., Nazarov M. A., Pätsch M., and Schultz L. 2001. Noble gases in three lunar meterites from Oman. *Lunar and Planetary Science XXXII*.

Simon S. B., Papike J. J., Gosselin D. C., and Laul J. C. 1985. Petrology and Chemistry of Apollo 12 Regolith Breccias. *Journal of Geophysical Research* 90: D75–D86.

Simon S. B., Papike J. J., and Shearer C. K. 1983. Petrology of ALHA 81005, the first lunar meteorite. *Geophysical Research Letters* 10: 787–790.

Snape J. F., Joy K. H., and Crawford I. A. 2011. Characterization of multiple lithologies within the lunar feldspathic regolith breccia meteorite Northeast Africa 001. *Meteoritics & Planetary Science* 46: 1288–1312.

Snape J. F., Nemchin A. A., Thiessen F., Bellucci J. J., and Whitehouse M. J. 2015. The impact history of the Moon : implications of new high-resolution U-Pb analyses of Apollo impact breccias. *Geophysical Research Abstracts* 17: 11373.

Snyder A., Neal C. R., Taylor A., and Halliday A. N. 1997. Anatexis of lunar cumulate mantle in time and space : Clues from trace-element , strontium , and neodymium isotopic chemistry of parental Apollo 12 hasalts. *Geochimica et Cosmochimica Acta* 61: 2731–2737.

Snyder G. A., Lawrence T. A., and Hallyday A. N. 1995. Chronology and petrogenesis of the lunar highlands alkali suite : Cumulates from KREEP basalt crystallization. *Geochimica et Cosmochimica Acta* 59: 1185–1203.

Sokol A. K. et al. 2008. Geochemistry, petrology and ages of the lunar meteorites Kalahari 008 and 009: New constraints on early lunar evolution. *Geochimica et Cosmochimica Acta* 72: 4845–4873.

Sokol A. K., and Bischoff A. 2005. Meteorites from Botswana. *Meteoritics & Planetary Science* 40: A177–A184.

Spettel B., Dreibus G., Burghele A., Jochum K. P., Schultz L., Weber H. W., Wlotzka F., and Wanke H. 1995. Chemistry, petrology, and noble gases of lunar highland meteorite Queen Alexandra Range 93069. *Meteoritics* 30: 581–582.

Spray J. G. 2016. Lithification Mechanisms for Planetary Regoliths: The Glue that Binds. *Annual Review of Earth and Planetary Sciences* 44: 139–174. http://www.annualreviews.org/doi/10.1146/annurev-earth-060115-012203.

Spudis P. D., and Davis P. A. 1987. A chemical and petrological model of the lunar crust. *Journal of Geophysical Research* 91: E84–E90.

Spudis P. D., Gillis J. J., and Reisse R. a. 1994. Ancient multiring basins on the moon revealed by clementine laser altimetry. *Science (New York, N.Y.)* 266: 1848–1851.

Spudis P. D., and Hawke B. R. 1986. The Apennine bench formation revisited. *Worshop on the Geology and Petrology of the Apollo 15 Landing Site* 105.

Stöffler D., and Grieve R. A. F. 2007. Impactites. In *Metamorphic rocks: a classification and glossary of terms, recommendations of the International Union of Geological Sciences*, edited by Fettes, D. and Desmons J. Cambridge University Press. pp. 111–125.

Stöffler D., Keil K., and Scott E. R. D. 1991. Shock metamorphism of ordinary chondrites. *Geochimica et Cosmochimica Acta* 55: 3845–3867.

Stöffler D., Knöll H. D., and Maerz U. 1979. Terrestrial and lunar impact breccias and the classification of lunar highland rocks. *Proceedings of 10th Lunar Planetary Science Conference* 639–675.

Stöffler D., Knöll H. D., Marvin U. B., Simonds C. H., and Warren P. H. 1980. Recommended classification and nomenclature of lunar highland rocks- a committee report. *Proceedings Conference on Lunar Highlands Crust* 51–70.

Stöffler D., and Ryder G. 2001. STRATIGRAPHY AND ISOTOPE AGES OF LUNAR GEOLOGIC UNITS : Chronological standard for the inner solar system. *Space Science Reviews* 96: 9–54.

Stöffler D., Ryder G., Ivanov B. A., Artemieva N. A., Cintala M. J., and Grieve R. A. . 2006. Cratering history and lunar chronology. In *New Views of the Moon*, edited by Jolliff B. L., Wieczorek M. A., Shearer C. K., and Neal C. R. Mineralogical Society of America. pp. 519–596.

Swindle T. D., Spudis P. D., Taylor G. J., Korotev R. L., Nichols Jr R. G., and Olinger C. . 1991. Searching for Crisium basin ejecta: chemistry and ages of Luna 20 impact melts. *Proceedings Lunar Planetary Science* 21: 167–181.

Swinyard B. M. et al. 2009. X-ray fluorescence observations of the moon by SMART-1/D-CIXS and the first detection of Ti Kα from the lunar surface. *Planetary and Space Science* 57: 744–750.

Takahashi K., and Masuda A. 1987. Two lunar meteorites, Yamato-791197 and -82192: REE abundances and geochronological dating. *Memoirs of the National Institute of Polar Research* 71–88.

Takeda H. et al. 2012. Comparisons of Mineralogy of Lunar Meteorites Possibly From the Farside and the Kaguya Remote Sensing Data to Reconstruct the Eariest Anortositic Crust of the Moon. *43rd Lunar and Planetary Science Conference*.

Takeda H., Arai T., Yamaguchi A., Otsuki M., and Ohtake M. 2008. Granulitic lithologies in Dhofar 307 lunar meteorite and magnesian, Th-poor terrane of the northern farside crust. *Lunar and Planetary Science XXXIX*.

Takeda H., Arai T., Yamaguchi A., Otuki M., and Ishii T. 2007. Mineralogy of Dhofar 309, 489, and Yamato-86032 and varieties of lithologies of the lunar farside crust. *Lunar and Planetary Science Conference XXXVIII* 38: 1607.

Takeda H., Kazuto S., Ishii T., and Otsuki M. 2003. Mineralogy of the Dhofar 489 Lunar Meteorite, Cyrstalline, Matrix Breccia With Magnesian Anorthositic Clasts. *Lunar and Planetary Science XXXIV*.

Takeda H., Kojima H., Nishio F., Yanai K., and Lindstrom M. M. 1989. Preliminary report on the Yamato-86032 lunar meteorite: I Recovery, sample descriptions, mineralogy and petrography. *Proceedings of the NIPR Symposium on Antarctic Meteorites* 2: 3–14.

Takeda H., Miyamoto M., Mori H., Wentworth S. J., and McKay D. S. 1990. Mineralogical Comparison of the Y86032-type Lunar Meteorites to Feldspathic Fragmental Breccia 67016. *Proceedings of the 20th Lunar and Planetary Science Conference* 91–100.

Takeda H., Mori H., and Tagai T. 1987. Mineralogy of lunar meteorites, Yamato-82192 and -82193 with reference to breccias in a breccia. *Memoirs of the National Institute of Polar Research* 43–55.

Takeda H., Yamaguchi A., Bogard D., Karouji Y., Ebihara M., Ohtake M., Saiki K., and Arai T. 2006. Magnesian anorthosites and a deep crustal rock from the farside crust of the moon. *Earth and Planetary Science Letters* 247: 171–184.

Takeda H., Yamaguchi A., Otsuki M., Hiroi T., Ohtake M., and Katou M. 2010. Mineralogical interpretation on the feldspathic highlands of the Moon on the basis of some feldspathic lunar meteorites. *73th Annual Meteoritical Society Meeting*.

Tatsumoto M., and Premo W. R. 1991. U-Pb isotopic characteristics of lunar meteorites Yamato-793274 and Yamato-86032. *Proc. NIPR Symp. Antarct. Meteorites* 4: 56–69.

Taylor G. . J., Warren P. H., Ryder G., Delano J., Pieters C. M., and Lofgren G. 1991. Lunar rocks. In *Lunar sourcebook: A user's guide to the Moon*. pp. 183–284.

Taylor L. A., Anand M., Neal C. R., Patchen A., and Kramer G. Y. 2004. Lunar meteorite PCA 02 007: A feldspathic regolith breccia with mixed mare/highland components. *Lunar and Planetary Science XXXV*.

Taylor L. A., Nazarov M. A., Cohen B. A., Warren P. H., and Barsukova L. D. 2001. Bulk chemistry and oxygen isotopic compositions of lunar meteorites Dhofar 025 and Dhofar 026. *Lunar and Planetary Science XXXII*.

Taylor L. A., Shervais J. W., Hunter R. H., Shih C.-Y., Bansal B. M., Wooden J., Nyquist L. E., and Laul L. C. 1983. Pre-4.2 AE mare-basalt volcanism in the lunar highlands. *Earth and Planetary Science Letters* 66: 33–47.

Taylor S. R. 1988. Growth of planetary crusts. *Tectonophysics* 161: 147–156.

Taylor S. R. 1982. Lunar and terrestrial crusts: a constrast in origin and evolution. *Physics of the Earth and Planetary Interiors* 29: 233–241.

Taylor S. R. 1975. *Lunar Science: A Post-Apollo view*, Pergamon Press.

Taylor S. R., and McLennan S. M. 2009. *Planetary Crusts: Their composition, Origin and Evolution*, Cambridge Planetary Science.

Tera F., Papanastassiou D. A., and Wasserburg G. J. 1973. A lunar cataclysm at ~3.95 AE and the structure of the lunar crust. *Abstract of the Lunar and Planetary Science Conference* 4: 723.

Tera F., Papanastassiou D. A., and Wasserburg G. J. 1974. Isotopic evidence for a terminal lunar cataclysm. *Earth and Planetary Science Letters* 22.

Terada K., Anand M., Sokol A. K., Bischoff A., and Sano Y. 2007. Cryptomare magmatism 4.35 Gyr ago recorded in lunar meteorite Kalahari 009. *Nature* 450: 849–852.

Terada K., Saiki T., Oka Y., Hayasaka Y., and Sano Y. 2005. Ion microprobe U-Pb dating of phosphates in lunar basaltic breccia, Elephant Moraine 87521. *Geophysical Research Letters* 32.

Terada K., Sasaki Y., Anand M., Sano Y., Taylor L. A., and Horie K. 2008. Uranium–lead systematics of low-Ti basaltic meteorite Dhofar 287A: Affinity to Apollo 15 green glasses. *Earth and Planetary Science Letters* 270: 119–124.

Thalmann C., Eugster O., Herzog G. F., Klein J., Krähenbühl U., Vogt S., and Xue S. 1996. History of lunar metorites Queen Alexandra Range 93069, Asuka 881757, and Yamato 793169 based on noble gas isotopic abundances, radionuclide concentrations, and chemical composition. *Meteorit. Planet. Sci.* 31: 857–868.

The Lunar Sample Preliminay Examination Team. 1971. Preliminary Examination of Lunar Samples from Apollo 14. *Science* 173: 681–693.

Treiman A. H., Maloy A. K., Shearer C. K., and Gross J. 2010. Magnesian anorthositic granulites in lunar meteorites Allan Hills A81005 and Dhofar 309: Geochemistry and global significance. *Meteoritics & Planetary Science* 45: 163–180.

Vaniman D., Dietrich J., Taylor G. . J., and Heiken G. 1991. Exploration, samples, and recent concepts of the Moon. In *Lunar sourcebook: A user's guide to the Moon*, edited by Heiken G. H., Vaniman D. T., and French B. M. Cambridge University Press. pp. 5–26.

Vaughan W. M., Head J. W., Wilson L., and Hess P. C. 2013. Geology and petrology of enormous volumes of impact melt on the Moon: A case study of the Orientale basin impact melt sea. *Icarus* 223: 749–765.

Vogt S., Fink D., Klein J., Middleton R., Dockhorn B., Korschinek G., Nolte E., and Herzog G. F. 1991. Exposure histories of the lunar meteorites : MAC88104 ,. *Geochimica et Cosmochimica Acta* 55: 3157–3165.

Walker D., Longhi J., Stolper E. M., Grove T. L., and Hays J. F. 1975. Origin of titaniferous lunar basalts. *Geochimica et Cosmochimica Acta* 39: 1219–1235.

Wang K., and Jacobsen S. B. 2016. Potassium Isotopic Evidence for the Origin of the Moon. *Nature* 1–10. http://dx.doi.org/10.1038/nature19341.

Wänke H., Baddenhausen H., Dreibus G., Jagoutz E., Kruse H., Palme H., Spettel B., and Teschke F. 1973. Multielement anlyses of Apollo 15, 16 and 17 samples and the bulk composition of the Moon. *Proceedings Lunar Planetary Science* 2: 1461–1481.

Warner J. L., Simonds C. H., and Phinney W. C. 1976. Genetic distinction between anorthosites and Mg-rich plutonic rocks: new data from 76255. *Lunar and Planetary Science Conference* 915–917.

Warren P. H. 1994. Lunar and Martian Meteorite Delivery Services. *Icarus* 111: 338–363.

Warren P. H. 1990. Lunar anorthosites and the magma-ocean plagioclase-flotation hypothesis: Importance of FeO enrichment in the parent magma. *American Mineralogist* 75: 46–58.

Warren P. H. 2001. Porosities of lunar meteorites: Strength, porosity, and petrologic screening during the meteorite delivery process. *Journal of Geophysical Research* 106: 10101.

Warren P. H., and Kallemeyn G. W. 1989. Elephant Moraine 87521: The first lunar meteorite composed of predominantly mare material. *Geochimica et Cosmochimica Acta* 53: 3323–3330.

Warren P. H., and Kallemeyn G. W. 1991. Geochemical investigation of five lunar meteorites: implications for the composition, origin and evolution of the lunar crust. *Proc. NIPR Symp. Antarct. Meteorites* 4: 91–117.

Warren P. H., and Kallemeyn G. W. 1993. Geochemical investigation of two lunar mare meteorites: Yamato-793169 and Asuka-881757. *Proc. NIPR Symp. Antarct. Meteorites* 6: 35–57.

Warren P. H., and Kallemeyn G. W. 2001. New lunar meteorite Northwest Africa 482: An anorthositic impact melt breccia with low-KREEP content. *64th Annual Meteoritical Society Meeting*.

Warren P. H., and Kallemeyn G. W. 1995. QUE93069: A lunar meteorite rich in HASP glasses. *Lunar and Planetary Science XXVI* 1465–1466.

Warren P. H., Taylor G. . J., and Keil K. 1983. Regolith breccia Allan Hills A81005: Evidence of lunar origin, and petrography of pristine and nonpristine clasts. *Geophysical Research Letters* 10: 779–782.

Warren P. H., and Ulff-Møller F. 1999. Lunar Meteorite EET96008: Paired with EET87521, but Rich in Diverse Clasts. *Lunar and Planetary Science XXX*.

Warren P. H., Ulff-Møller F., and Kallemeyn G. W. 2005. “New” lunar meteorites: Impact melt and regolith breccias and large-scale heterogeneities of the upper lunar crust. *Meteoritics & Planetary Science* 40: 989–1014.

Warren P. H., and Wasson J. T. 1977. Pristine nonmare rocks and the nature of the lunar crust. *Proc. Lunar Sci. Conf.* 2215–2235.

Warren P. H., and Wasson J. T. 1979. The compositional-petrographic search for pristine nonmare rocks: third foray. *Proceedings Lunar Planetary Science Conference 10th* 583–610.

Weisberg M. K., Smith C., Benedix G., Folco L., Righter K., Zipfel J., Yamaguchi A., and Aoudjehane H. C. 2009. The Meteoritical Bulletin, No. 95. *Meteoritics & Planetary Science* 44: 429–462.

White R., and McKenzie D. 1989. Magmatism at rift zones: The generation of volcanic continental margins and flood basalts. *Journal of Geophysical Research: Solid Earth* 94: 7685–7729.

Whitford-Stark J. L. 1979. Charting the Southern Seas: The evolution of the lunar Mare Australe. *Lunar and Planetary Science Conference 10th* 2975–2994.

Whitten J., and Head J. W. 2015. Lunar cryptomaria: Mineralogy and composition of ancient volcanic deposits. *Planetary and Space Science* 106: 67–81.

Whitten J. L., and Head J. W. 2015. Lunar cryptomaria: Physical characteristics, distribution, and implications for ancient volcanism. *Icarus* 247: 150–171.

Wiechert U., Hallyday A. N., Lee D.-C., Snyder G. A., Taylor L. A., and Rumble D. 2010. Oxygen Isotopes and the Moon-Forming Giant Impact. *Science* 294: 345–348.

Wieczorek M. A. et al. 2006. The constitution and structure of the lunar interior edited by Jolliff B. L., Wieczorek M. A., Shearer C. K., and Neal C. R. *Reviews* 60: 221–364.

Wieczorek M. A. et al. 2013. The Crust of the Moon as seen by GRAIL. *Science* 339: 671–675.

Wieczorek M. A., and Phillips J. 2000. The “Procellarum KREEP Terrane”: Implications for mare volcanism and lunar evolution. *Journal of Geophysical Research* 105: 20,417-20,430.

Wieczorek M. A., and Phillips R. J. 2000. The “Procellarum KREEP Terrane”: Implications for mare volcanism and lunar evolution. *Journal of Geophysical Research* 105: 20417–20430.

Wieczorek M. a., and Zuber M. T. 2001. The composition and origin of the lunar crust: Constraints from central peaks and crustal thickness modeling. *Geophysical Research Letters* 28: 4023–4026.

Wieler R. 2016. Do lunar and meteoritic archives record temporal variations in the composition of solar wind noble gases and nitrogen? A reassessment in the light of Genesis data. *Chemie der Erde - Geochemistry* 1–18. http://linkinghub.elsevier.com/retrieve/pii/S0009281916300137.

Wilhelms D. E., and John F. 1987. *The geologic history of the Moon*,.

Wilson L., and Head J. W. 2016. Generation, ascent and eruption of magma on the Moon: New insights into source depths, magma supply, intrusions and effusive/explosive eruptions (Part 1: Theory). *Icarus*.

Wise D. U. 1963. An origin of the Moon by rotational fission during formation of the Earth’s core. *Journal of Geophysical Research* 68: 1547.

Wolfe E. W., Lucchitta B. K., Reed G. E., Ulrich G. E., and Sanchez A. G. 1975. Geology of the Taurus-Littrow valley floor. *Proceedings of Lunar and Planetary Science Conference 6th* 2463–2482.

Yamaguchi A. et al. 2010. The variety of lithologies in the Yamato-86032 lunar meteorite: Implications for formation processes of the lunar crust. *Geochimica et Cosmochimica Acta* 74: 4507–4530.

Yamaguchi A., Takeda H., Nyquist L. E., Bogard D. D., Ebihara M., and Karouji Y. 2004. The origin and impact history of lunar meteorite Yamato 86032. *35th Lunar and Planetary Science Conference*.

Yanai K., and Kojima H. 1991. Varieties of lunar meteorites recovered from Antarctica. *Proceedings of the NIPR Symp. Antarct. Meteorites* 4: 70–90.

Yingst R. A., and Head III J. W. 1999. Geology of mare deposits in South Pole-Aitken basin as seen by Clementine UV/VIS data. *Journal of Geophysical Research-Planets* 104: 18957–18979.

Zeigler R. A., Jolliff B. L., and Korotev R. L. 2013. Lunar Meteorites Sayh al Uhaymir 449 and Dhofar 925, 960, and 961: Windows into South Pole Aitken Basin? *44th Lunar and Planetary Science Conference* 2437.

Zeigler R. A., Korotev R. L., and Jolliff B. L. 2007. Miller Range 05035 and Meteorite Hills 01210: Two basaltic lunar meteorites, both likely source-crater paired with Asuka 881757 and Yamato 793169. In *Lunar and Planetary Science XXXVIII*.

Zeigler R. A., Korotev R. L., and Jolliff B. L. 2012. Pairing Relationships among Feldspathic Lunar Meteorites from Miller Range, Antarctica. *43rd Lunar and Planetary Science Conference* Abstract #2377.

Zeigler R. A., Korotev R. L., and Jolliff B. L. 2011. Petrography and geochemistry of lunar meteorite Dhofar 1442. *42nd Lunar and Planetary Science Conference*.

Zeigler R. A., Korotev R. L., and Jolliff B. L. 2010. The Dhofar 961 meteorite group: A view into the interior of South Pole Aitken basin? *The 33rd Symposium on Antarctic Meteorites*.

Zeigler R. A., Korotev R. L., Jolliff B. L., and Haskin L. A. 2005. Petrography and geochemistry of the LaPaz Icefield basaltic lunar meteorite and source crater pairing with Northwest Africa 032. *Meteoritics & Planetary Science* 40: 1073–1101.

Zeigler R. A., Korotev R. L., Jolliff B. L., Haskin L. A., and Floss C. 2006. The geochemistry and provenance of Apollo 16 mafic glasses. *Geochimica et Cosmochimica Acta* 70: 6050–6067.

Zipfel J., Spettel B., Palme H., Wolf D., Franchi I., Sexton A. S., Pillinger C. T., and Bischoff A. 1998. Dar al Gani 400: Chemistry and petrology of the largest lunar meteorite. *Meteoritics & Planetary Science* 33: A171.

Zuber M. T., Smith D. E., Lemoine F. G., and Neumann G. a. 1994. The shape and internal structure of the moon from the clementine mission. *Science (New York, N.Y.)* 266: 1839–1843.

Appendix 3A

Plagioclases

MIL 090036 **Monomict plagioclase**

SiO2	44,47	44,08	43,17	42,58	42,88	43,09	42,86	43,81
TiO2	0,05	b.d.	b.d.	b.d.	b.d.	b.d.	b.d.	b.d.
Al2O3	34,57	34,54	36,04	35,72	35,82	35,64	35,71	34,67
Cr2O3	b.d.	b.d.	b.d.	b.d.	b.d.	b.d.	b.d.	b.d.
FeO	0,83	0,45	0,07	0,08	b.d.	0,10	0,12	0,09
MnO	b.d.	b.d.	b.d.	b.d.	b.d.	b.d.	b.d.	b.d.
MgO	0,42	0,35	0,11	0,14	0,11	0,09	0,07	0,19
CaO	18,30	18,50	18,88	18,95	18,91	19,06	19,23	19,44
Na2O	0,75	0,67	0,40	0,41	0,43	0,45	0,41	0,49
K2O	0,15	0,00	0,00	0,00	0,00	0,00	0,00	0,06
Total	*99,53*	*98,60*	*98,67*	*97,87*	*98,14*	*98,44*	*98,40*	*98,75*
An	92,30	93,89	96,28	96,28	96,09	95,88	96,25	95,28
Ab	6,80	6,11	3,72	3,72	3,91	4,12	3,75	4,36
Or	0,89	0,00	0,00	0,00	0,00	0,00	0,00	0,35
Cations per 8 Oxygens								
Si	2,070	2,067	2,021	2,012	2,019	2,025	2,016	2,054
Ti	0,002	0,000	0,000	0,000	0,000	0,000	0,000	0,000
Al (IV)	1,896	1,909	1,988	1,990	1,988	1,974	1,980	1,916
Cr	0,000	0,000	0,000	0,000	0,000	0,000	0,000	0,000
Fe	0,032	0,018	0,003	0,003	0,000	0,004	0,005	0,004
Mn	0,000	0,000	0,000	0,000	0,000	0,000	0,000	0,000
Mg	0,029	0,025	0,008	0,010	0,008	0,006	0,005	0,013
Ca	0,913	0,930	0,947	0,960	0,954	0,959	0,969	0,976
Na	0,067	0,061	0,037	0,037	0,039	0,041	0,038	0,045
K	0,009	0,000	0,000	0,000	0,000	0,000	0,000	0,004
Total Cations	5,018	5,009	5,003	5,011	5,007	5,009	5,013	5,012
Tet site	*3,966*	*3,976*	*4,009*	*4,002*	*4,006*	*3,998*	*3,996*	*3,970*

Granulitic breccias

SiO2	45,25	44,32	43,67	43,58	43,30	43,97	44,01	43,85
TiO2	0,05	0,13	0,00	0,12	0,16	b.d.	0,10	0,13
Al2O3	35,09	34,56	34,39	34,53	34,18	34,72	34,71	34,12
Cr2O3	0,05	0,06	0,22	b.d.	0,19	b.d.	b.d.	0,24
FeO	0,09	0,43	0,37	0,16	0,22	0,32	0,23	0,22
MnO	b.d.	b.d.	b.d.	0,14	b.d.	0,05	b.d.	b.d.
MgO	0,34	0,21	0,40	0,29	0,47	0,30	0,30	0,24
CaO	19,18	19,45	19,22	19,06	18,99	19,45	19,31	19,38
Na2O	0,59	0,57	0,65	0,56	0,66	0,49	0,46	0,51
K2O	0,14	0,11	0,10	0,16	0,15	0,18	0,05	0,11
Total	*100,78*	*99,85*	*99,03*	*98,60*	*98,32*	*99,48*	*99,17*	*98,78*
An	93,98	94,34	93,65	94,02	93,27	94,62	95,57	94,86

Ab	5,20	5,03	5,76	5,04	5,85	4,35	4,15	4,50
Or	0,82	0,63	0,58	0,94	0,88	1,03	0,27	0,64
Cations per 8 Oxygens								
Si	2,075	2,060	2,048	2,049	2,044	2,051	2,055	2,059
Ti	0,002	0,005	0,000	0,004	0,006	0,000	0,003	0,004
Al (IV)	1,896	1,893	1,901	1,914	1,902	1,909	1,910	1,888
Cr	0,002	0,002	0,008	0,000	0,007	0,000	0,000	0,009
Fe	0,003	0,017	0,015	0,006	0,009	0,012	0,009	0,009
Mn	0,000	0,000	0,000	0,006	0,000	0,000	0,000	0,000
Mg	0,023	0,015	0,028	0,020	0,033	0,021	0,021	0,016
Ca	0,942	0,968	0,966	0,960	0,961	0,972	0,966	0,975
Na	0,052	0,052	0,059	0,051	0,060	0,045	0,042	0,046
K	0,008	0,006	0,006	0,010	0,009	0,011	0,003	0,007
Total Cations	5,004	5,017	5,030	5,020	5,030	5,022	5,009	5,014
Tet site	*3,971*	*3,952*	*3,949*	*3,963*	*3,946*	*3,961*	*3,965*	*3,948*

Impact melt breccias								
SiO_2	43,45	43,24	43,70	44,02	44,19	44,36	43,78	44,10
TiO_2	0,10	0,07	0,17	0,20	0,00	0,00	0,10	0,08
Al_2O_3	34,72	34,51	34,18	34,10	34,26	34,68	34,32	34,29
Cr_2O_3	0,13	b.d.	b.d.	b.d.	b.d.	0,08	0,00	0,06
FeO	0,14	0,27	0,33	0,22	0,51	0,22	0,37	0,45
MnO	b.d.	b.d.	b.d.	b.d.	b.d.	b.d.	b.d.	b.d.
MgO	0,46	0,31	0,27	0,15	0,36	0,33	0,22	0,12
CaO	19,22	19,30	18,96	18,90	19,02	18,90	18,55	18,95
Na_2O	0,64	0,51	0,66	0,73	0,87	0,66	0,68	0,56
K_2O	0,10	0,15	0,11	0,18	0,11	0,10	0,16	0,16
Total	*98,95*	*98,35*	*98,37*	*98,51*	*99,33*	*99,34*	*98,17*	*98,77*
An	93,80	94,65	93,42	92,44	91,77	93,44	92,94	94,00
Ab	5,64	4,48	5,92	6,49	7,62	5,95	6,12	5,05
Or	0,56	0,86	0,66	1,07	0,61	0,61	0,93	0,95
Cations per 8 Oxygens								
Si	2,037	2,041	2,059	2,070	2,065	2,066	2,065	2,069
Ti	0,004	0,002	0,006	0,007	0,000	0,000	0,003	0,003
Al (IV)	1,918	1,919	1,898	1,890	1,887	1,904	1,907	1,896
Cr	0,005	0,000	0,000	0,000	0,000	0,003	0,000	0,002
Fe	0,006	0,011	0,013	0,009	0,020	0,008	0,015	0,018
Mn	0,000	0,000	0,000	0,000	0,000	0,000	0,000	0,000
Mg	0,032	0,022	0,019	0,011	0,025	0,023	0,015	0,008
Ca	0,965	0,976	0,957	0,952	0,952	0,943	0,937	0,953
Na	0,058	0,046	0,061	0,067	0,079	0,060	0,062	0,051
K	0,006	0,009	0,007	0,011	0,006	0,006	0,009	0,010
Total Cations	5,030	5,025	5,019	5,017	5,034	5,014	5,014	5,009
Tet site	*3,955*	*3,959*	*3,957*	*3,960*	*3,952*	*3,970*	*3,972*	*3,965*

Poikiloblastic impact melt clast								
SiO_2	44,24	46,67	44,85	44,84	44,67	46,39	44,91	43,61
TiO_2	b.d.	0,13	b.d.	0,04	b.d.	0,02	0,12	0,10
Al_2O_3	34,43	32,66	34,19	33,89	33,65	32,85	34,22	34,16
Cr_2O_3	0,16	b.d.	b.d.	b.d.	0,04	0,10	b.d.	0,06
FeO	0,56	0,30	0,19	0,49	0,29	0,33	0,28	0,26
MnO	b.d.	0,17	0,06	b.d.	b.d.	b.d.	b.d.	0,05
MgO	0,42	0,53	0,45	0,35	0,17	0,41	0,44	0,30
CaO	18,51	17,00	18,45	18,60	18,54	17,22	17,98	19,47
Na_2O	0,78	1,66	0,97	0,82	0,91	1,53	0,93	0,62
K_2O	0,17	0,29	0,16	0,15	0,16	0,16	0,21	0,23
Total	*99,26*	*99,40*	*99,31*	*99,18*	*98,42*	*99,00*	*99,08*	*98,86*
An	91,99	83,58	90,49	91,75	91,03	85,32	90,34	93,35
Ab	6,99	14,75	8,57	7,34	8,05	13,71	8,43	5,35
Or	1,03	1,67	0,94	0,90	0,91	0,97	1,23	1,30
Cations per 8 Oxygens								
Si	2,07	2,17	2,09	2,09	2,10	2,16	2,09	2,05
Ti	0,00	0,00	0,00	0,00	0,00	0,00	0,00	0,00
Al (IV)	1,89	1,79	1,88	1,86	1,86	1,80	1,88	1,89
Cr	0,01	0,00	0,00	0,00	0,00	0,00	0,00	0,00
Fe	0,02	0,01	0,01	0,02	0,01	0,01	0,01	0,01
Mn	0,00	0,00	0,00	0,00	0,00	0,00	0,00	0,00
Mg	0,03	0,04	0,03	0,02	0,01	0,03	0,03	0,02
Ca	0,93	0,85	0,92	0,93	0,93	0,86	0,90	0,98
Na	0,07	0,15	0,09	0,07	0,08	0,14	0,08	0,06
K	0,01	0,02	0,01	0,01	0,01	0,01	0,01	0,01
Total Cations	5,02	5,02	5,02	5,02	5,01	5,01	5,01	5,03
Tet site	*3,96*	*3,95*	*3,97*	*3,96*	*3,96*	*3,96*	*3,97*	*3,94*

43,98	43,22	43,44	44,58	44,16	43,41	43,44	43,48	43,77
b.d.	0,18	0,13	0,18	b.d.	0,10	0,07	0,09	0,09
34,42	34,41	34,55	34,13	34,88	34,54	34,58	34,69	34,58
0,04	b.d.	b.d.	b.d.	0,09	0,16	0,20	0,11	b.d.
b.d.	0,09	b.d.	0,19	0,06	0,12	b.d.	0,07	0,16
0,09	b.d.	b.d.	0,06	0,09	b.d.	0,04	b.d.	0,08
0,20	0,25	0,32	0,38	0,29	0,20	0,37	0,34	0,26
19,17	19,42	19,25	18,87	19,59	19,28	19,36	19,51	19,77
0,48	0,51	0,46	0,82	0,43	0,44	0,60	0,52	0,38
0,08	0,16	0,00	0,15	0,12	0,10	0,18	0,08	0,07
98,46	*98,24*	*98,16*	*99,37*	*99,71*	*98,34*	*98,84*	*98,90*	*99,17*
95,24	94,60	95,84	91,84	95,54	95,51	93,65	94,92	96,27
4,30	4,50	4,16	7,27	3,76	3,91	5,29	4,60	3,31
0,47	0,90	0,00	0,89	0,70	0,59	1,06	0,48	0,42
2,067	2,041	2,048	2,078	2,053	2,046	2,040	2,039	2,048
0,000	0,007	0,004	0,006	0,000	0,003	0,002	0,003	0,003
1,907	1,915	1,919	1,875	1,912	1,918	1,914	1,917	1,907
0,001	0,000	0,000	0,000	0,003	0,006	0,007	0,004	0,000
0,000	0,004	0,000	0,008	0,002	0,005	0,000	0,003	0,006
0,000	0,000	0,000	0,000	0,000	0,000	0,000	0,000	0,003
0,014	0,018	0,023	0,026	0,020	0,014	0,026	0,024	0,018
0,966	0,983	0,972	0,942	0,976	0,973	0,974	0,980	0,991
0,044	0,047	0,042	0,075	0,038	0,040	0,055	0,048	0,034
0,005	0,009	0,000	0,009	0,007	0,006	0,011	0,005	0,004
5,003	5,023	5,009	5,020	5,012	5,012	5,030	5,023	5,015
3,974	*3,956*	*3,967*	*3,953*	*3,965*	*3,964*	*3,954*	*3,957*	*3,954*

43,97	44,03	44,08	43,93	43,93	44,16	43,91	44,29	43,59
0,08	b.d.	b.d.	0,16	0,02	0,19	b.d.	0,03	b.d.
33,88	34,22	34,61	34,38	34,13	33,91	34,13	33,90	34,29
b.d.	0,09	0,05	0,04	0,11	b.d.	b.d.	b.d.	b.d.
0,34	0,32	0,44	0,14	0,36	0,25	0,27	0,14	0,11
0,08	0,03	b.d.	0,04	b.d.	b.d.	b.d.	b.d.	b.d.
0,17	0,35	0,31	0,32	0,32	0,41	0,28	0,51	0,15
18,78	19,15	19,22	19,42	18,85	18,45	18,77	18,29	19,14
0,74	0,71	0,62	0,61	0,75	0,94	0,75	0,86	0,42
0,06	0,15	0,24	0,13	0,13	0,18	0,08	0,27	0,15
98,09	*99,05*	*99,57*	*99,18*	*98,60*	*98,50*	*98,18*	*98,29*	*97,86*
93,07	92,96	93,15	93,92	92,54	90,54	92,84	90,65	95,26

6,60	6,21	5,47	5,35	6,68	8,39	6,71	7,75	3,82
0,33	0,84	1,38	0,73	0,77	1,08	0,45	1,59	0,92

2,077	2,063	2,055	2,055	2,066	2,076	2,070	2,084	2,062
0,003	0,000	0,000	0,006	0,001	0,007	0,000	0,001	0,000
1,886	1,889	1,902	1,896	1,891	1,879	1,896	1,880	1,912
0,000	0,003	0,002	0,002	0,004	0,000	0,000	0,000	0,000
0,013	0,013	0,017	0,005	0,014	0,010	0,011	0,006	0,004
0,000	0,001	0,000	0,000	0,000	0,000	0,000	0,000	0,000
0,012	0,025	0,021	0,023	0,022	0,029	0,020	0,036	0,010
0,950	0,961	0,960	0,973	0,950	0,929	0,948	0,922	0,970
0,067	0,064	0,056	0,055	0,069	0,086	0,069	0,079	0,039
0,003	0,009	0,014	0,008	0,008	0,011	0,005	0,016	0,009
5,013	5,028	5,028	5,022	5,024	5,027	5,018	5,023	5,006
3,963	*3,952*	*3,957*	*3,951*	*3,957*	*3,955*	*3,967*	*3,964*	*3,974*

53,04	52,26	51,87	51,63	52,79	52,50	52,80	52,28	52,07
0,14	b.d.	0,08	0,07	0,05	b.d.	0,08	b.d.	b.d.
28,47	28,42	28,71	28,43	28,85	28,07	28,64	28,31	28,55
0,11	0,08	0,05	b.d.	0,07	0,12	b.d.	b.d.	0,04
0,50	0,52	0,43	0,43	0,52	0,50	0,37	0,47	0,40
b.d.	b.d.	b.d.	b.d.	b.d.	b.d.	0,07	b.d.	0,10
0,41	0,34	0,24	0,22	0,32	0,14	0,42	0,24	0,19
12,27	12,31	12,67	12,80	12,34	12,36	12,08	12,26	12,90
4,31	4,37	4,05	4,13	4,38	4,10	4,48	4,33	4,06
0,25	0,17	0,37	0,25	0,31	0,21	0,27	0,28	0,23

99,49	*98,46*	*98,48*	*97,95*	*99,64*	*98,00*	*99,20*	*98,18*	*98,54*

60,26	60,31	61,97	62,20	59,78	61,67	58,89	60,02	62,87
38,31	38,72	35,86	36,35	38,43	37,07	39,56	38,37	35,80
1,43	0,97	2,17	1,45	1,79	1,26	1,55	1,61	1,33

2,421	2,412	2,397	2,399	2,409	2,431	2,416	2,419	2,405
0,005	0,000	0,003	0,002	0,002	0,000	0,003	0,000	0,000
1,532	1,546	1,564	1,557	1,552	1,532	1,545	1,544	1,554
0,004	0,003	0,002	0,000	0,002	0,004	0,000	0,000	0,001
0,019	0,020	0,017	0,017	0,020	0,019	0,014	0,018	0,015
0,000	0,000	0,000	0,000	0,000	0,000	0,003	0,000	0,000
0,028	0,023	0,017	0,015	0,022	0,009	0,028	0,017	0,013
0,600	0,609	0,627	0,637	0,603	0,613	0,592	0,608	0,639
0,382	0,391	0,363	0,372	0,388	0,368	0,398	0,389	0,364
0,014	0,010	0,022	0,015	0,018	0,013	0,016	0,016	0,014
5,004	5,014	5,010	5,014	5,016	4,991	5,015	5,011	5,005
3,953	*3,958*	*3,960*	*3,956*	*3,960*	*3,964*	*3,962*	*3,963*	*3,960*

43,77	43,77	44,71	44,36	44,25	43,87	45,03	44,06	44,15
0,17	0,11	0,09	b.d.	0,09	0,07	0,09	0,15	b.d.
34,19	34,14	34,07	34,36	34,58	34,61	34,44	34,12	34,22
b.d.	b.d.	0,08	0,07	0,05	0,16	0,15	b.d.	0,10
0,37	0,22	0,25	0,21	0,29	0,01	0,14	0,24	0,34
b.d.	0,13	b.d.	b.d.	b.d.	0,04	0,10	0,07	b.d.
0,16	0,21	0,12	0,19	0,26	0,37	0,21	0,34	0,22
19,04	18,99	18,68	19,05	19,04	19,07	19,01	19,03	19,10
0,53	0,55	0,69	0,61	0,65	0,69	0,63	0,65	0,60
0,15	0,12	0,13	0,08	0,13	0,08	0,10	0,05	0,16
98,36	*98,24*	*98,82*	*98,91*	*99,34*	*98,96*	*99,92*	*98,72*	*98,90*
94,39	94,31	93,03	94,09	93,45	93,44	93,78	93,85	93,73
4,75	4,98	6,22	5,46	5,80	6,08	5,62	5,83	5,33
0,86	0,71	0,75	0,45	0,75	0,48	0,61	0,32	0,95
2,06	2,07	2,09	2,07	2,06	2,05	2,09	2,07	2,07
0,01	0,00	0,00	0,00	0,00	0,00	0,00	0,01	0,00
1,90	1,90	1,88	1,89	1,90	1,91	1,88	1,89	1,89
0,00	0,00	0,00	0,00	0,00	0,01	0,01	0,00	0,00
0,01	0,01	0,01	0,01	0,01	0,00	0,01	0,01	0,01
0,00	0,00	0,00	0,00	0,00	0,00	0,00	0,00	0,00
0,01	0,01	0,01	0,01	0,02	0,03	0,01	0,02	0,02
0,96	0,96	0,94	0,95	0,95	0,96	0,94	0,96	0,96
0,05	0,05	0,06	0,06	0,06	0,06	0,06	0,06	0,05
0,01	0,01	0,01	0,00	0,01	0,00	0,01	0,00	0,01
5,01	5,01	5,00	5,01	5,02	5,02	5,00	5,01	5,02
3,96	*3,96*	*3,97*	*3,97*	*3,96*	*3,96*	*3,97*	*3,96*	*3,96*

44,02	43,77	43,36	43,50	44,64	45,90	43,37	43,64	43,14
b.d.	b.d.	0,08	0,12	b.d.	b.d.	0,02	b.d.	b.d.
34,77	34,53	34,44	34,47	34,16	33,42	34,47	34,69	34,53
b.d.	b.d.	b.d.	0,09	0,06	0,13	0,11	0,07	0,10
b.d.	0,08	0,10	0,14	0,24	0,23	0,04	b.d.	0,19
0,08	b.d.	0,04	0,07	b.d.	b.d.	b.d.	0,14	b.d.
0,40	0,39	0,21	0,27	0,31	0,34	0,34	0,20	0,33
19,29	19,29	19,29	19,14	18,42	18,30	19,39	19,55	19,40
0,60	0,59	0,48	0,51	0,86	1,17	0,50	0,29	0,35
0,04	0,16	0,10	0,05	0,09	0,06	0,12	0,12	0,09
99,18	*98,81*	*98,10*	*98,36*	*98,78*	*99,55*	*98,37*	*98,69*	*98,12*
94,51	93,88	95,15	95,08	91,72	89,34	94,86	96,74	96,36
5,28	5,21	4,25	4,60	7,76	10,30	4,47	2,57	3,12
0,21	0,91	0,60	0,32	0,52	0,37	0,68	0,70	0,52
2,055	2,053	2,048	2,050	2,088	2,128	2,044	2,050	2,039
0,000	0,000	0,003	0,004	0,000	0,000	0,001	0,000	0,000
1,913	1,908	1,917	1,914	1,883	1,827	1,915	1,921	1,923
0,000	0,000	0,000	0,003	0,002	0,005	0,004	0,003	0,004
0,000	0,003	0,004	0,005	0,009	0,009	0,002	0,000	0,008
0,000	0,000	0,002	0,000	0,000	0,000	0,000	0,000	0,000
0,028	0,028	0,015	0,019	0,022	0,024	0,024	0,014	0,023
0,965	0,969	0,976	0,966	0,923	0,909	0,979	0,984	0,982
0,054	0,054	0,044	0,047	0,078	0,105	0,046	0,026	0,032
0,002	0,009	0,006	0,003	0,005	0,004	0,007	0,007	0,005
5,017	5,024	5,015	5,012	5,011	5,010	5,022	5,005	5,016
3,968	*3,961*	*3,966*	*3,964*	*3,971*	*3,955*	*3,959*	*3,971*	*3,962*

43,11	43,43	43,21	43,74	45,92	44,32	44,26	44,49	43,78
b.d.	b.d.	b.d.	0,13	0,05	b.d.	b.d.	0,05	b.d.
34,22	34,77	34,31	34,42	32,53	33,75	34,27	33,68	34,04
b.d.	b.d.	0,08	b.d.	0,07	b.d.	0,04	b.d.	0,15
0,15	0,32	0,32	0,24	0,25	0,23	0,04	0,32	0,12
b.d.	0,03	0,10	b.d.	b.d.	b.d.	0,05	b.d.	b.d.
0,40	0,42	0,13	0,24	0,06	0,30	0,11	0,32	0,18
19,38	19,21	19,37	19,03	17,39	18,61	19,01	18,70	19,36
0,61	0,47	0,41	0,54	1,34	0,84	0,66	0,85	0,55
0,11	0,12	0,11	0,13	0,20	0,26	0,11	0,11	0,13
97,97	*98,78*	*98,04*	*98,48*	*97,83*	*98,32*	*98,55*	*98,52*	*98,32*
94,00	95,04	95,71	94,37	86,70	91,06	93,47	91,79	94,34

5,39	4,22	3,64	4,87	12,10	7,43	5,89	7,55	4,89
0,61	0,74	0,65	0,76	1,20	1,51	0,64	0,66	0,77

2,042	2,040	2,046	2,057	2,162	2,087	2,078	2,090	2,064
0,000	0,000	0,000	0,005	0,002	0,000	0,000	0,002	0,000
1,911	1,925	1,915	1,908	1,805	1,873	1,896	1,865	1,892
0,000	0,000	0,003	0,000	0,003	0,000	0,001	0,000	0,006
0,006	0,012	0,013	0,009	0,010	0,009	0,001	0,013	0,005
0,000	0,000	0,004	0,000	0,000	0,000	0,000	0,000	0,000
0,028	0,029	0,009	0,017	0,004	0,021	0,008	0,023	0,013
0,984	0,967	0,983	0,959	0,878	0,939	0,956	0,941	0,978
0,056	0,043	0,037	0,049	0,122	0,077	0,060	0,077	0,051
0,006	0,007	0,007	0,008	0,012	0,016	0,007	0,007	0,008
5,034	5,023	5,017	5,013	4,999	5,022	5,007	5,018	5,016
3,953	*3,964*	*3,961*	*3,966*	*3,968*	*3,961*	*3,974*	*3,955*	*3,956*

43,84	43,72	43,10	44,12	43,73	44,20	43,90	44,32	44,19
0,12	b.d.	0,13	b.d.	b.d.	0,07	b.d.	b.d.	b.d.
34,09	34,55	34,32	34,77	35,02	35,09	34,37	33,69	34,07
0,03	b.d.	0,13	b.d.	b.d.	0,10	0,06	0,04	0,07
0,11	0,15	0,49	0,35	0,00	0,28	0,29	0,18	0,42
b.d.	b.d.	b.d.	b.d.	0,07	b.d.	0,15	b.d.	b.d.
0,36	0,25	0,34	0,51	0,38	0,41	0,37	0,23	0,36
19,12	19,30	19,45	19,30	19,48	19,71	19,33	18,64	19,02
0,50	0,41	0,40	0,59	0,40	0,38	0,47	0,70	0,57
0,14	0,04	0,08	0,16	0,10	0,16	0,04	0,21	0,17
98,30	*98,42*	*98,44*	*99,81*	*99,19*	*100,40*	*98,98*	*98,00*	*98,87*
94,68	96,09	95,98	93,87	95,81	95,75	95,53	92,50	93,89
4,51	3,69	3,54	5,18	3,60	3,30	4,22	6,26	5,11
0,81	0,22	0,48	0,95	0,59	0,95	0,24	1,24	0,99

2,065	2,056	2,035	2,051	2,043	2,043	2,057	2,091	2,072
0,004	0,000	0,005	0,000	0,000	0,003	0,000	0,000	0,000
1,892	1,915	1,910	1,905	1,928	1,911	1,898	1,874	1,883
0,001	0,000	0,005	0,000	0,000	0,003	0,002	0,001	0,003
0,004	0,006	0,019	0,014	0,000	0,011	0,011	0,007	0,016
0,000	0,000	0,000	0,000	0,000	0,000	0,006	0,000	0,000
0,025	0,018	0,024	0,036	0,027	0,028	0,026	0,016	0,025
0,965	0,973	0,984	0,961	0,975	0,976	0,970	0,943	0,955
0,046	0,037	0,036	0,053	0,037	0,034	0,043	0,064	0,052
0,008	0,002	0,005	0,010	0,006	0,010	0,002	0,013	0,010
5,011	5,006	5,023	5,028	5,015	5,019	5,016	5,009	5,016
3,957	*3,971*	*3,946*	*3,955*	*3,971*	*3,954*	*3,955*	*3,965*	*3,955*

44,36	43,83	43,84	44,26	44,17	44,61	44,06	43,87	45,15
0,15	0,12	b.d.	b.d.	0,10	b.d.	0,24	b.d.	b.d.
34,08	34,33	34,22	34,19	32,52	34,60	34,52	33,82	34,39
0,08	0,03	0,05	0,00	0,09	b.d.	b.d.	0,03	b.d.
0,23	0,18	0,16	0,26	0,64	0,21	0,24	0,42	0,24
b.d.	b.d.	0,03	b.d.	0,11	0,06	0,00	0,14	b.d.
0,18	0,19	0,29	0,29	0,93	0,24	0,31	0,06	0,39
18,45	19,41	18,62	19,02	18,65	19,25	19,04	19,19	18,86
0,72	0,48	0,66	0,70	0,63	0,70	0,60	0,56	0,76
0,15	0,11	0,21	0,18	0,21	0,13	0,22	0,20	0,22
98,39	*98,69*	*98,09*	*98,90*	*98,05*	*99,80*	*99,24*	*98,31*	*100,01*
92,60	95,10	92,83	92,83	93,07	93,14	93,36	93,88	92,05
6,51	4,27	5,93	6,16	5,66	6,10	5,36	4,95	6,67
0,89	0,63	1,24	1,02	1,27	0,76	1,28	1,17	1,28
2,08	2,06	2,07	2,07	2,09	2,07	2,06	2,07	2,09
0,01	0,00	0,00	0,00	0,00	0,00	0,01	0,00	0,00
1,89	1,90	1,90	1,89	1,82	1,89	1,90	1,88	1,87
0,00	0,00	0,00	0,00	0,00	0,00	0,00	0,00	0,00
0,01	0,01	0,01	0,01	0,03	0,01	0,01	0,02	0,01
0,00	0,00	0,00	0,00	0,00	0,00	0,00	0,00	0,00
0,01	0,01	0,02	0,02	0,07	0,02	0,02	0,00	0,03
0,93	0,98	0,94	0,95	0,95	0,96	0,95	0,97	0,93
0,07	0,04	0,06	0,06	0,06	0,06	0,05	0,05	0,07
0,01	0,01	0,01	0,01	0,01	0,01	0,01	0,01	0,01
5,00	5,01	5,02	5,02	5,03	5,02	5,02	5,02	5,01
3,97	*3,96*	*3,97*	*3,96*	*3,91*	*3,96*	*3,96*	*3,96*	*3,96*

43,49	43,27	43,79	43,44	43,85	43,13	43,46	43,97	44,21
0,05	b.d.	b.d.	0,12	b.d.	0,03	0,14	b.d.	b.d.
34,61	34,24	34,38	34,54	34,65	34,77	34,56	34,40	34,44
0,06	0,06	b.d.	b.d.	b.d.	b.d.	0,14	0,06	0,07
0,21	0,21	0,27	0,16	0,15	0,18	0,05	0,18	0,14
0,12	b.d.	0,04	0,17	0,11	b.d.	0,06	b.d.	b.d.
0,33	0,34	0,21	0,24	0,26	0,50	0,28	0,23	0,32
19,52	19,47	19,30	19,25	19,47	19,24	19,55	19,26	19,42
0,55	0,42	0,52	0,38	0,55	0,40	0,41	0,42	0,47
0,16	0,05	0,16	0,00	0,09	0,06	0,12	0,10	0,16
99,09	*98,06*	*98,67*	*98,31*	*99,14*	*98,29*	*98,78*	*98,62*	*99,23*
94,28	95,94	94,43	96,54	94,62	96,09	95,64	95,65	94,93
4,80	3,74	4,64	3,46	4,86	3,58	3,66	3,74	4,13
0,92	0,31	0,93	0,00	0,52	0,33	0,70	0,60	0,94
2,039	2,047	2,058	2,047	2,052	2,033	2,041	2,064	2,064
0,002	0,000	0,000	0,004	0,000	0,001	0,005	0,000	0,000
1,912	1,909	1,905	1,918	1,911	1,932	1,913	1,903	1,895
0,002	0,002	0,000	0,000	0,000	0,000	0,005	0,002	0,003
0,008	0,008	0,010	0,006	0,006	0,007	0,002	0,007	0,005
0,005	0,000	0,000	0,007	0,000	0,000	0,003	0,000	0,000
0,023	0,024	0,015	0,017	0,018	0,035	0,020	0,016	0,022
0,981	0,987	0,972	0,972	0,976	0,972	0,984	0,968	0,972
0,050	0,038	0,048	0,035	0,050	0,036	0,038	0,038	0,042
0,010	0,003	0,010	0,000	0,005	0,003	0,007	0,006	0,010
5,032	5,018	5,018	5,007	5,020	5,020	5,017	5,005	5,013
3,952	*3,956*	*3,963*	*3,966*	*3,964*	*3,965*	*3,954*	*3,967*	*3,959*

43,40	44,59	47,02	44,31	43,61	43,06	43,89
b.d.	b.d.	0,07	b.d.	b.d.	b.d.	0,16
34,15	33,62	32,46	33,43	34,26	34,41	34,85
0,17	b.d.	0,12	b.d.	0,04	0,15	0,05
0,07	0,08	0,06	0,31	0,35	0,16	0,31
0,07	0,16	0,08	b.d.	0,03	b.d.	b.d.
0,28	0,32	0,29	0,24	0,11	0,26	0,22
18,97	18,18	17,03	18,91	19,58	19,37	19,27
0,65	1,08	1,78	0,67	0,50	0,43	0,48
0,15	0,12	0,29	0,17	0,07	0,12	0,14
97,91	*98,14*	*99,19*	*98,04*	*98,54*	*97,97*	*99,37*
93,30	89,70	82,70	93,08	95,25	95,47	94,87

5,81	9,62	15,64	5,95	4,36	3,83	4,30
0,89	0,68	1,66	0,97	0,39	0,70	0,83

2,056	2,101	2,182	2,093	2,055	2,039	2,047
0,000	0,000	0,002	0,000	0,000	0,000	0,006
1,906	1,867	1,776	1,861	1,902	1,921	1,916
0,006	0,000	0,004	0,000	0,001	0,006	0,002
0,003	0,003	0,002	0,012	0,014	0,006	0,012
0,000	0,000	0,003	0,000	0,000	0,000	0,000
0,020	0,022	0,020	0,017	0,008	0,019	0,015
0,963	0,918	0,847	0,957	0,988	0,983	0,963
0,060	0,098	0,160	0,061	0,045	0,039	0,044
0,009	0,007	0,017	0,010	0,004	0,007	0,008
5,023	5,018	5,014	5,012	5,018	5,021	5,014
3,962	*3,969*	*3,958*	*3,954*	*3,957*	*3,960*	*3,964*

44,34	43,76	44,16	46,46	50,61	42,95	43,28	43,47	43,79
b.d.	0,08	0,08	b.d.	0,10	0,10	b.d.	0,08	0,06
33,55	34,37	34,31	32,82	31,21	34,47	34,24	34,09	34,56
0,06	b.d.	0,04	0,05	0,04	0,17	0,10	0,13	0,10
0,32	0,56	0,30	0,39	0,45	0,39	0,58	0,13	0,40
b.d.	0,03	0,12	0,06	0,11	b.d.	b.d.	b.d.	b.d.
0,27	0,68	0,44	0,42	0,48	0,22	0,43	0,43	0,20
18,78	19,10	19,02	17,61	14,87	19,44	19,33	19,10	19,34
0,99	0,36	0,69	1,45	2,91	0,37	0,33	0,52	0,37
0,17	0,15	0,10	0,22	0,31	0,06	0,08	0,06	0,12
98,48	*99,09*	*99,24*	*99,47*	*101,09*	*98,18*	*98,38*	*98,01*	*98,93*

90,38	95,84	93,29	85,95	72,54	96,27	96,53	94,94	96,01
8,65	3,28	6,12	12,77	25,66	3,35	2,99	4,71	3,28
0,96	0,88	0,59	1,28	1,80	0,38	0,48	0,35	0,71

2,088	2,049	2,064	2,156	2,291	2,032	2,044	2,055	2,053
0,000	0,003	0,003	0,000	0,004	0,003	0,000	0,003	0,002
1,862	1,897	1,890	1,795	1,665	1,922	1,906	1,899	1,910
0,002	0,000	0,001	0,002	0,001	0,006	0,004	0,005	0,004
0,013	0,022	0,012	0,015	0,017	0,016	0,023	0,005	0,016
0,000	0,001	0,000	0,000	0,004	0,000	0,000	0,000	0,000
0,019	0,047	0,031	0,029	0,033	0,015	0,030	0,030	0,014
0,947	0,959	0,952	0,876	0,721	0,986	0,978	0,967	0,971
0,091	0,033	0,062	0,130	0,255	0,034	0,030	0,048	0,033
0,010	0,009	0,006	0,013	0,018	0,004	0,005	0,004	0,007
5,031	5,020	5,022	5,017	5,009	5,019	5,019	5,016	5,009
3,949	*3,946*	*3,954*	*3,952*	*3,956*	*3,955*	*3,949*	*3,954*	*3,962*

44,07
0,07
33,79
0,05
0,35
0,09
0,16
18,94
0,63
0,15
98,31
93,50
5,60
0,91
2,08
0,00
1,88
0,00
0,01
0,00
0,01
0,96
0,06
0,01
5,01
3,96

44,13	43,63	43,29	43,62	43,46	46,12	46,09	46,41	46,32
0,06	b.d.	0,08	b.d.	0,05	b.d.	0,03	0,07	0,06
34,40	34,53	34,85	34,72	34,02	32,36	33,02	32,44	32,45
0,15	0,03	0,01	0,13	0,13	0,08	0,14	b.d.	b.d.
0,04	0,24	0,17	0,18	0,14	0,21	0,27	0,16	0,07
0,04	b.d.	b.d.	b.d.	0,12	0,06	b.d.	0,09	b.d.
0,37	0,32	0,44	0,42	0,25	0,27	0,36	0,34	0,23
19,22	19,28	19,70	19,32	19,22	17,46	17,62	17,50	17,43
0,43	0,43	0,50	0,48	0,57	1,54	1,38	1,60	1,55
0,11	0,08	0,04	0,05	0,08	0,08	0,19	0,15	0,08
98,94	*98,55*	*99,08*	*98,93*	*98,05*	*98,19*	*99,11*	*98,74*	*98,19*
95,49	95,72	95,35	95,42	94,42	85,80	86,63	85,07	85,78
3,87	3,83	4,40	4,28	5,10	13,71	12,28	14,07	13,76
0,64	0,45	0,25	0,30	0,48	0,49	1,09	0,86	0,46
2,064	2,051	2,029	2,044	2,057	2,165	2,145	2,167	2,171
0,002	0,000	0,003	0,000	0,002	0,000	0,001	0,002	0,002
1,896	1,914	1,924	1,917	1,898	1,790	1,812	1,786	1,792
0,005	0,001	0,000	0,005	0,005	0,003	0,005	0,000	0,000
0,001	0,010	0,007	0,007	0,006	0,008	0,011	0,006	0,003
0,002	0,000	0,000	0,000	0,000	0,002	0,000	0,000	0,000
0,026	0,023	0,031	0,029	0,018	0,019	0,025	0,024	0,016
0,963	0,971	0,989	0,970	0,975	0,878	0,879	0,876	0,875
0,039	0,039	0,046	0,044	0,053	0,140	0,125	0,145	0,140
0,006	0,005	0,003	0,003	0,005	0,005	0,011	0,009	0,005
5,006	5,013	5,031	5,019	5,018	5,011	5,013	5,014	5,004
3,960	*3,965*	*3,953*	*3,961*	*3,955*	*3,955*	*3,957*	*3,953*	*3,963*

44,10	43,36	43,56
0,15	b.d.	b.d.
33,81	34,54	34,43
0,06	b.d.	b.d.
0,13	0,41	0,30
b.d.	0,08	0,00
0,33	0,40	0,29
18,85	19,67	19,42
0,67	0,43	0,51
0,20	0,07	0,15
98,31	*98,95*	*98,66*
92,85	95,79	94,62
6,00	3,81	4,53
1,15	0,40	0,86
2,077	2,037	2,049
0,005	0,000	0,000
1,877	1,912	1,909
0,002	0,000	0,000
0,005	0,016	0,012
0,000	0,003	0,000
0,023	0,028	0,020
0,951	0,990	0,979
0,062	0,039	0,047
0,012	0,004	0,009
5,015	5,029	5,024
3,954	*3,949*	*3,958*

45,87	46,38	45,90	46,42	46,47	46,60	46,21	45,95	46,14
0,12	0,10	0,08	0,05	b.d.	0,04	b.d.	0,12	0,16
33,10	32,99	32,53	32,97	32,57	32,49	32,32	32,40	32,73
0,14	0,25	0,13	0,18	0,03	0,08	b.d.	b.d.	b.d.
0,05	0,22	0,15	0,09	0,48	0,13	0,08	0,10	0,03
b.d.	b.d.	0,05	b.d.	b.d.	b.d.	0,10	b.d.	0,08
0,27	0,23	0,42	0,33	0,50	0,46	0,26	0,27	0,23
17,45	17,46	17,45	17,76	17,02	17,17	17,69	17,60	17,28
1,38	1,28	1,54	1,49	1,61	1,77	1,48	1,38	1,46
0,24	0,19	0,18	0,11	0,07	0,15	0,00	0,10	0,07
98,61	*99,12*	*98,44*	*99,40*	*98,76*	*98,87*	*98,13*	*97,91*	*98,17*
86,26	87,26	85,31	86,23	85,05	83,60	86,87	87,09	86,36
12,32	11,61	13,65	13,12	14,51	15,55	13,13	12,34	13,20
1,41	1,13	1,03	0,66	0,44	0,85	0,00	0,58	0,43
2,143	2,155	2,151	2,152	2,167	2,170	2,170	2,161	2,162
0,004	0,003	0,003	0,002	0,000	0,001	0,000	0,004	0,006
1,822	1,807	1,797	1,802	1,790	1,784	1,788	1,796	1,807
0,005	0,009	0,005	0,007	0,001	0,003	0,000	0,000	0,000
0,002	0,009	0,006	0,003	0,019	0,005	0,003	0,004	0,001
0,000	0,000	0,002	0,000	0,000	0,000	0,000	0,000	0,003
0,019	0,016	0,029	0,023	0,035	0,032	0,018	0,019	0,016
0,874	0,869	0,876	0,882	0,851	0,857	0,890	0,887	0,867
0,125	0,116	0,140	0,134	0,145	0,159	0,135	0,126	0,133
0,014	0,011	0,011	0,007	0,004	0,009	0,000	0,006	0,004
5,008	4,997	5,020	5,012	5,012	5,019	5,003	5,002	4,998
3,966	*3,962*	*3,948*	*3,954*	*3,957*	*3,954*	*3,958*	*3,957*	*3,968*

46,60	46,13	46,03	46,45
0,11	0,10	0,04	0,10
32,59	32,59	32,36	33,88
b.d.	0,15	b.d.	0,24
0,04	0,24	0,27	b.d.
b.d.	b.d.	0,06	b.d.
0,34	0,39	0,44	0,68
17,13	17,66	17,40	17,80
1,57	1,48	1,49	1,80
0,06	0,10	0,21	0,13
98,45	*98,85*	*98,32*	*101,08*
85,44	86,27	85,49	83,88
14,18	13,12	13,25	15,38
0,38	0,60	1,26	0,74
2,174	2,153	2,160	2,122
0,004	0,003	0,001	0,003
1,792	1,793	1,790	1,824
0,000	0,006	0,000	0,009
0,002	0,009	0,011	0,000
0,000	0,000	0,002	0,000
0,024	0,027	0,031	0,046
0,856	0,883	0,875	0,871
0,142	0,134	0,136	0,160
0,004	0,006	0,013	0,008
4,998	5,015	5,018	5,042
3,967	*3,946*	*3,950*	*3,946*

Appendix 3B

Pyroxenes

MIL 090036 **Granulitic breccias**

Oxide Weight Percent							
SiO_2	52,78	51,76	52,74	52,55	50,55	52,34	50,93
TiO_2	0,66	1,22	0,58	0,47	1,56	0,68	1,23
Al_2O_3	1,37	2,43	1,31	1,22	3,17	1,43	2,47
Cr_2O_3	0,48	0,63	0,25	0,35	0,82	0,28	0,47
FeO	17,65	9,53	18,88	16,80	8,89	17,05	8,78
MnO	0,28	0,26	0,37	0,32	0,11	0,45	0,33
MgO	23,54	17,51	24,22	22,75	16,31	23,04	17,05
CaO	4,28	18,11	2,68	5,66	18,60	4,84	18,70
Na_2O	0,07	0,42	0,20	0,21	0,25	0,35	0,26
K_2O	0,01	0,11	b.d.	b.d.	0,11	b.d.	0,06
Total	*101,12*	*101,98*	*101,23*	*100,33*	*100,36*	*100,47*	*100,28*
Mg#	70,38	76,60	69,58	70,71	76,58	70,65	77,59
En	64,45	48,80	65,92	62,77	47,04	63,83	48,14
Fs	27,12	14,91	28,83	26,00	14,39	26,52	13,90
Wo	8,43	36,29	5,25	11,23	38,57	9,65	37,96
Cations per 6 Oxygens							
Si	1,928	1,887	1,927	1,936	1,871	1,926	1,886
Ti	0,018	0,033	0,016	0,013	0,043	0,019	0,034
Al (IV)	0,072	0,113	0,073	0,064	0,129	0,074	0,114
Al	0,059	0,105	0,057	0,053	0,138	0,062	0,108
Al (VI)	0,000	0,000	0,000	0,000	0,009	0,000	0,000
Cr	0,014	0,018	0,007	0,010	0,024	0,008	0,014
Fe	0,539	0,291	0,577	0,518	0,275	0,525	0,272
Mn	0,009	0,008	0,012	0,010	0,003	0,014	0,010
Mg	1,281	0,951	1,319	1,249	0,900	1,263	0,941
Ca	0,168	0,707	0,105	0,223	0,738	0,191	0,742
Na	0,005	0,030	0,014	0,015	0,018	0,025	0,019
K	0,000	0,005	0,000	0,000	0,005	0,000	0,003
Total Cations	4,034	4,044	4,049	4,039	4,016	4,045	4,035
Tet. Site	*2,000*	*2,000*	*2,000*	*2,000*	*2,000*	*2,000*	*2,000*

Impact melt breccias

SiO_2	51,59	52,87	49,68	50,73	52,24	51,67	52,74
TiO_2	1,01	0,57	0,40	1,14	0,70	1,07	0,43
Al_2O_3	2,11	1,45	7,93	2,42	1,65	1,83	2,08
Cr_2O_3	0,59	0,31	0,31	0,62	0,24	0,65	0,26
FeO	11,11	20,00	16,42	9,48	19,88	10,38	19,47
MnO	0,26	0,30	0,26	0,06	0,41	0,00	0,25
MgO	16,56	23,92	19,01	15,14	23,74	15,89	23,83
CaO	17,27	1,90	5,58	19,10	1,97	19,51	1,81
Na_2O	0,17	0,11	0,19	0,18	0,26	0,24	0,26
K_2O	b.d.	b.d.	b.d.	0,03	0,03	0,06	b.d.

Total	*100,67*	*101,43*	*99,78*	*98,90*	*101,13*	*101,29*	*101,14*
Mg#	72,67	68,06	67,35	74,00	68,04	73,17	68,58
En	47,04	65,52	58,97	44,28	65,38	44,46	66,10
Fs	17,70	30,74	28,58	15,56	30,72	16,30	30,29
Wo	35,26	3,75	12,44	40,16	3,90	39,24	3,61
Cations per 6 Oxygens							
Si	1,911	1,931	1,831	1,910	1,917	1,908	1,926
Ti	0,028	0,016	0,011	0,032	0,019	0,030	0,012
Al (IV)	0,089	0,069	0,169	0,090	0,083	0,092	0,074
Al	0,092	0,062	0,345	0,108	0,071	0,080	0,089
Al (VI)	0,003	0,000	0,176	0,017	0,000	0,000	0,015
Cr	0,017	0,009	0,009	0,018	0,007	0,019	0,008
Fe	0,344	0,611	0,506	0,299	0,610	0,321	0,594
Mn	0,008	0,009	0,008	0,002	0,013	0,000	0,008
Mg	0,914	1,302	1,044	0,850	1,299	0,874	1,297
Ca	0,685	0,074	0,220	0,770	0,078	0,772	0,071
Na	0,012	0,008	0,014	0,013	0,019	0,017	0,019
K	0,000	0,000	0,000	0,001	0,001	0,003	0,000
Total Cations	4,013	4,029	3,988	4,003	4,045	4,035	4,023
Total tet	*2,000*	*2,000*	*2,000*	*2,000*	*2,000*	*2,000*	*2,000*

Poikiloblastic impact melt clasts						
SiO_2	52,42	51,84	52,38	45,13	52,65	43,31
TiO_2	0,60	0,86	0,75	2,23	0,37	b.d.
Al_2O_3	2,63	2,33	2,28	12,62	2,16	22,41
Cr_2O_3	0,40	0,36	0,47	0,30	0,55	0,23
FeO	17,53	19,49	18,68	15,81	16,16	4,22
MnO	0,44	0,39	0,04	0,16	0,28	b.d.
MgO	21,86	22,04	22,71	12,47	26,24	18,88
CaO	4,46	4,22	2,99	11,51	1,92	11,87
Na_2O	0,24	0,39	0,27	0,42	0,42	0,68
K_2O	b.d.	b.d.	b.d.	0,14	b.d.	0,03
Total	*100,58*	*101,92*	*100,57*	*100,79*	*100,74*	*101,63*
Mg#	68,97	66,83	68,41	58,43	74,31	88,85
En	62,64	61,19	64,26	42,10	71,52	63,39
Fs	28,18	30,37	29,67	29,95	24,72	7,95
Wo	9,18	8,43	6,08	27,95	3,76	28,65
Cations per 6 Oxygens						
Si	1,924	1,898	1,923	1,681	1,907	1,515
Ti	0,016	0,024	0,021	0,063	0,010	0,000
Al (IV)	0,076	0,102	0,077	0,319	0,093	0,485
Al	0,114	0,100	0,099	0,554	0,092	0,924

Al (VI)	0,038	0,000	0,021	0,235	0,000	0,438
Cr	0,012	0,010	0,014	0,009	0,016	0,006
Fe	0,538	0,597	0,574	0,493	0,490	0,123
Mn	0,014	0,012	0,001	0,005	0,009	0,000
Mg	1,196	1,202	1,242	0,692	1,416	0,984
Ca	0,175	0,166	0,118	0,460	0,074	0,445
Na	0,017	0,028	0,020	0,030	0,029	0,046
K	0,000	0,000	0,000	0,007	0,000	0,001
Total Cations	4,005	4,039	4,010	3,993	4,044	4,044
Tet. Site	*2,000*	*2,000*	*2,000*	*2,000*	*2,000*	*2,000*

50,08	51,46	52,09	51,85	52,74	51,78	52,00	50,56	51,97
1,65	1,19	0,62	0,51	0,33	0,57	0,55	0,48	0,89
3,45	2,26	1,32	1,36	1,53	1,57	1,30	8,06	2,05
0,69	0,68	0,33	0,27	0,26	0,48	0,22	0,22	0,72
7,97	9,54	21,50	21,66	20,37	20,77	22,00	18,62	9,52
0,07	0,18	0,39	0,45	0,37	0,20	0,15	0,07	0,15
15,71	17,23	21,27	21,44	23,46	20,94	21,81	17,34	15,30
19,39	18,03	3,40	2,96	1,98	3,92	2,68	4,67	19,92
0,32	0,24	0,21	0,35	0,43	0,23	0,19	0,33	0,22
0,03	0,03	b.d.	b.d.	b.d.	b.d.	b.d.	b.d.	0,12
99,37	*100,84*	*100,89*	*100,34*	*100,89*	*100,34*	*100,34*	*100,34*	*100,89*
77,84	76,30	58,58	58,88	58,58	58,88	58,88	58,88	58,58
46,04	48,48	35,10	56,24	35,10	56,24	56,24	56,24	35,10
13,11	15,06	24,82	39,27	24,82	39,27	39,27	39,27	24,82
40,85	36,46	40,08	4,49	40,08	4,49	4,49	4,49	40,08
1,869	1,895	1,928	1,942	1,928	1,942	1,942	1,942	1,928
0,046	0,033	0,020	0,011	0,020	0,011	0,011	0,011	0,020
0,131	0,105	0,072	0,058	0,072	0,058	0,058	0,058	0,072
0,152	0,098	0,062	0,062	0,062	0,062	0,062	0,062	0,062
0,020	0,000	0,000	0,004	0,000	0,004	0,004	0,004	0,000
0,020	0,020	0,009	0,005	0,009	0,005	0,005	0,005	0,009
0,249	0,294	0,491	0,775	0,491	0,775	0,775	0,775	0,491
0,002	0,005	0,016	0,013	0,016	0,013	0,013	0,013	0,016
0,874	0,946	0,695	1,110	0,695	1,110	1,110	1,110	0,695
0,775	0,712	0,794	0,089	0,794	0,089	0,089	0,089	0,794
0,023	0,017	0,005	0,012	0,005	0,012	0,012	0,012	0,005
0,001	0,002	0,000	0,000	0,000	0,000	0,000	0,000	0,000
4,012	4,029	4,029	4,019	4,029	4,019	4,019	4,019	4,029
2,000	*2,000*	*2,000*	*2,000*	*2,000*	*2,000*	*2,000*	*2,000*	*2,000*

53,29	53,07	51,61	51,88	51,78	51,26	52,23	50,73	52,03
0,51	0,46	0,99	0,79	0,77	0,51	0,59	1,22	1,16
1,40	1,44	1,87	1,84	1,50	1,66	1,44	2,93	2,03
0,25	0,22	0,66	0,22	0,22	0,17	0,44	0,52	0,39
20,17	20,00	10,44	19,88	19,70	19,70	20,17	15,90	17,98
0,11	0,43	0,19	0,28	0,41	0,20	0,31	0,28	0,32
24,06	23,63	15,83	23,48	22,29	20,93	22,74	18,83	20,70
1,76	1,74	19,62	1,90	3,48	4,05	2,88	10,05	6,66
0,27	0,27	0,29	0,27	0,26	0,34	0,20	0,27	0,27
b.d.	b.d.	0,14	0,12	b.d.	0,05	b.d.	b.d.	b.d.

101,83	*101,26*	*101,65*	*100,64*	*100,42*	*98,87*	*101,01*	*100,72*	*101,55*
68,01	67,80	72,99	67,79	66,86	65,44	66,76	67,85	67,23
65,66	65,45	44,23	65,22	62,19	59,99	62,94	53,84	58,19
30,89	31,09	16,37	30,99	30,83	31,68	31,33	25,51	28,36
3,45	3,46	39,40	3,80	6,99	8,34	5,73	20,65	13,45
1,937	1,941	1,903	1,913	1,922	1,935	1,926	1,882	1,910
0,014	0,013	0,028	0,022	0,021	0,014	0,016	0,034	0,032
0,063	0,059	0,097	0,087	0,078	0,065	0,074	0,118	0,090
0,060	0,062	0,081	0,080	0,066	0,074	0,063	0,128	0,088
0,000	0,003	0,000	0,000	0,000	0,009	0,000	0,010	0,000
0,007	0,006	0,019	0,006	0,007	0,005	0,013	0,015	0,011
0,613	0,612	0,322	0,613	0,611	0,622	0,622	0,493	0,552
0,003	0,013	0,006	0,009	0,013	0,006	0,010	0,009	0,010
1,303	1,288	0,870	1,291	1,233	1,177	1,250	1,041	1,133
0,069	0,068	0,775	0,075	0,139	0,164	0,114	0,400	0,262
0,019	0,019	0,021	0,019	0,019	0,025	0,015	0,019	0,019
0,000	0,000	0,007	0,006	0,000	0,003	0,000	0,000	0,000
4,029	4,022	4,048	4,041	4,043	4,025	4,039	4,022	4,020
2,000	*2,000*	*2,000*	*2,000*	*2,000*	*2,000*	*2,000*	*2,000*	*2,000*

51,58	51,67	53,06	52,31	52,65	50,54	51,33	52,64	51,66
0,49	0,39	0,58	0,50	0,66	1,46	1,00	0,55	1,03
1,29	1,38	1,30	4,51	1,60	2,61	1,58	1,25	1,82
0,56	0,35	0,09	0,06	0,09	0,74	0,55	0,07	0,48
21,63	22,03	18,36	16,89	17,82	9,28	9,42	17,96	9,26
0,37	0,23	0,42	0,60	0,29	0,27	0,22	0,31	0,36
21,14	21,40	25,25	22,94	24,62	15,50	16,34	24,36	16,27
3,46	2,98	1,78	3,09	2,00	19,44	19,21	2,36	18,64
0,15	0,27	0,26	0,35	0,22	0,35	0,32	0,14	0,31
b.d.	b.d.	b.d.	b.d.	0,07	0,04	b.d.	b.d.	0,07
100,68	*100,71*	*101,11*	*101,25*	*100,02*	*100,22*	*99,96*	*99,66*	*99,90*
63,53	63,39	71,03	70,77	71,11	74,86	75,56	70,74	75,79
59,11	59,61	66,23	68,27	44,69	46,11	67,42	46,67	66,94
33,94	34,43	27,35	27,74	15,01	14,92	27,89	14,90	28,95
6,95	5,96	6,42	3,99	40,30	38,97	4,70	38,43	4,11
1,927	1,928	1,931	1,892	1,933	1,883	1,914	1,942	1,922
0,014	0,011	0,016	0,014	0,018	0,041	0,028	0,015	0,029
0,073	0,072	0,069	0,108	0,067	0,117	0,086	0,058	0,078
0,057	0,061	0,056	0,192	0,069	0,115	0,069	0,055	0,080
0,000	0,000	0,000	0,084	0,002	0,000	0,000	0,000	0,002
0,016	0,010	0,003	0,002	0,003	0,022	0,016	0,002	0,014
0,676	0,688	0,559	0,511	0,547	0,289	0,294	0,554	0,288
0,012	0,007	0,013	0,019	0,009	0,008	0,007	0,010	0,011
1,177	1,191	1,369	1,237	1,347	0,861	0,908	1,339	0,902
0,138	0,119	0,069	0,120	0,079	0,776	0,767	0,093	0,743
0,011	0,019	0,018	0,025	0,016	0,025	0,023	0,010	0,022
0,000	0,000	0,000	0,000	0,003	0,002	0,000	0,000	0,003
4,045	4,045	4,047	4,010	4,023	4,024	4,043	4,024	4,015
2,000	*2,000*	*2,000*	*2,000*	*2,000*	*2,000*	*2,000*	*2,000*	*2,000*
50,80	51,04	50,32	51,51	50,01	51,09	51,53	49,94	51,29
0,87	1,14	1,08	1,13	1,24	1,04	0,65	0,47	1,24
1,75	2,32	2,15	2,87	3,04	2,30	1,99	1,97	2,29
0,41	0,45	0,52	0,61	0,55	0,48	0,37	0,57	0,43
11,00	10,18	12,02	9,60	9,28	9,59	20,39	21,83	10,07
0,16	0,24	0,21	0,17	0,18	0,20	0,35	0,41	0,24
15,82	15,56	15,96	15,09	15,20	15,34	21,53	15,20	15,05
17,89	19,37	15,76	19,99	19,27	20,23	3,18	9,84	19,78
0,00	0,19	0,14	0,23	0,40	0,18	0,46	0,10	0,07
b.d.	0,05	0,07	0,05	0,15	0,05	0,06	0,04	0,06

98,69	*100,55*	*98,22*	*101,25*	*99,32*	*100,51*	*100,49*	*100,38*	*100,51*
71,94	73,15	70,29	73,69	74,49	74,03	65,30	55,38	72,71
45,39	44,21	46,89	43,30	44,36	43,50	61,07	44,03	43,10
17,71	16,23	19,82	15,46	15,19	15,26	32,45	35,48	16,17
36,90	39,56	33,29	41,23	40,44	41,24	6,48	20,49	40,72
1,922	1,898	1,914	1,898	1,880	1,900	1,917	1,912	1,907
0,025	0,032	0,031	0,031	0,035	0,029	0,018	0,014	0,035
0,078	0,102	0,086	0,102	0,120	0,100	0,083	0,088	0,093
0,078	0,102	0,097	0,125	0,135	0,101	0,087	0,089	0,100
0,000	0,000	0,010	0,022	0,015	0,001	0,004	0,001	0,008
0,012	0,013	0,016	0,018	0,016	0,014	0,011	0,017	0,013
0,348	0,317	0,382	0,296	0,292	0,298	0,634	0,699	0,313
0,005	0,008	0,007	0,005	0,006	0,006	0,011	0,013	0,007
0,892	0,863	0,905	0,829	0,851	0,850	1,194	0,868	0,834
0,725	0,772	0,642	0,789	0,776	0,806	0,127	0,404	0,788
0,000	0,014	0,010	0,017	0,029	0,013	0,033	0,008	0,005
0,000	0,003	0,003	0,002	0,007	0,002	0,003	0,002	0,003
4,008	4,020	4,006	4,009	4,028	4,021	4,034	4,026	4,006
2,000	*2,000*	*2,000*	*2,000*	*2,000*	*2,000*	*2,000*	*2,000*	*2,000*

52,85	51,08	51,47	52,36	51,66	50,68
0,67	1,32	0,80	1,09	0,68	0,76
1,70	2,47	0,93	1,72	1,82	1,39
0,17	0,74	0,54	0,32	0,61	0,29
18,87	11,37	18,77	19,78	17,10	18,80
0,30	0,15	0,45	0,12	0,32	0,27
24,48	17,01	21,41	21,64	21,07	21,26
2,09	16,25	4,98	4,48	6,16	4,26
0,12	0,44	0,13	0,40	0,40	0,21
b.d.	b.d.	b.d.	b.d.	0,05	0,06
101,26	*100,82*	*99,47*	*101,90*	*99,87*	*97,97*
69,81	72,73	67,03	66,10	68,71	66,83
48,50	60,28	60,18	60,04	60,97	46,96
18,19	29,65	30,87	27,34	30,26	17,11
33,31	10,07	8,95	12,62	8,78	35,94
1,924	1,890	1,932	1,917	1,922	1,928
0,018	0,037	0,023	0,030	0,019	0,022
0,076	0,110	0,068	0,083	0,078	0,072
0,073	0,108	0,041	0,074	0,080	0,062
0,000	0,000	0,000	0,000	0,002	0,000
0,005	0,022	0,016	0,009	0,018	0,009
0,575	0,352	0,589	0,606	0,532	0,598
0,009	0,005	0,014	0,004	0,010	0,009
1,328	0,938	1,198	1,181	1,168	1,205
0,082	0,644	0,200	0,176	0,246	0,174
0,008	0,032	0,010	0,028	0,029	0,015
0,000	0,000	0,000	0,000	0,002	0,003
4,025	4,028	4,049	4,033	4,026	4,034
2,000	*2,000*	*2,000*	*2,000*	*2,000*	*2,000*

51,10	51,16
1,08	1,15
2,61	2,68
0,54	0,73
10,25	10,20
0,24	0,08
15,79	15,27
19,15	19,38
0,43	0,29
b.d.	0,08

101,18	*101,01*
73,30	72,74
44,72	43,72
16,29	16,38
38,99	39,90
1,889	1,894
0,030	0,032
0,111	0,106
0,114	0,117
0,003	0,011
0,016	0,021
0,317	0,316
0,007	0,002
0,870	0,842
0,758	0,769
0,031	0,021
0,000	0,004
4,032	4,017
2,000	*2,000*

Appendix 3C

Olivines

MIL 090036	**Gabbroic granulitic breccias**					
Oxide Weight Percent						
SiO_2	36,68	36,59	36,67	36,37	36,66	36,35
TiO_2	b.d.	b.d.	0,25	0,09	0,22	0,17
Al_2O_3	0,48	0,63	0,63	0,78	0,59	0,93
Cr_2O_3	0,05	0,01	0,07	0,10	0,06	0,18
FeO	29,97	29,37	29,49	28,78	29,37	29,49
MnO	0,28	0,45	0,22	0,34	0,13	0,26
MgO	33,74	33,61	33,97	33,39	33,45	33,71
CaO	0,22	0,15	0,31	0,28	0,39	0,43
Na_2O	0,37	0,47	0,38	0,41	0,47	0,49
K_2O	b.d.	b.d.	b.d.	b.d.	b.d.	b.d.
Total	*101,79*	*101,28*	*101,98*	*100,53*	*101,34*	*102,01*
Mg#	66,736	67,104	67,245	67,398	66,999	67,078
Fe#	33,264	32,896	32,755	32,602	33,001	32,922
Cations per 4 Oxygens						
Si	0,975	0,976	0,971	0,975	0,977	0,964
Ti	0,000	0,000	0,005	0,002	0,004	0,003
Al	0,015	0,020	0,020	0,025	0,018	0,029
Cr	0,001	0,000	0,001	0,002	0,001	0,004
Fe	0,666	0,655	0,653	0,645	0,654	0,654
Mn	0,006	0,010	0,005	0,008	0,003	0,006
Mg	1,337	1,336	1,340	1,334	1,328	1,332
Ca	0,006	0,004	0,009	0,008	0,011	0,012
Total Cations	3,026	3,026	3,024	3,020	3,021	3,029

	Impact melt breccias				
Oxide Weight Percent					
SiO_2	37,04	35,87	35,90	35,18	35,97
TiO_2	0,07	0,08	b.d.	0,27	0,06
Al_2O_3	1,46	0,51	0,61	0,96	0,80
Cr_2O_3	b.d.	b.d.	b.d.	b.d.	0,09
FeO	26,66	33,44	33,27	31,44	32,20
MnO	0,13	0,26	0,50	0,42	0,40
MgO	33,71	31,39	30,97	30,37	31,35
CaO	0,84	b.d.	0,12	0,31	0,36
Na_2O	0,45	0,25	0,26	0,43	0,43
K_2O	0,03	b.d.	0,07	b.d.	0,09
Total	100,38	101,81	101,68	99,40	101,76
Mg#	30,73	37,41	37,61	36,74	36,56
Fe#	68,42	62,59	62,29	62,96	63,10

Cations per 4 Oxygens					
Si	0,983	0,970	0,972	0,970	0,969
Ti	0,001	0,002	0,000	0,006	0,001
Al	0,046	0,016	0,019	0,031	0,025
Cr	0,000	0,000	0,000	0,000	0,002
Fe	0,591	0,756	0,753	0,725	0,726
Mn	0,003	0,006	0,011	0,010	0,009
Mg	1,333	1,265	1,250	1,247	1,259
Ca	0,024	0,000	0,003	0,009	0,010
Na	0,023	0,013	0,014	0,023	0,022
K	0,001	0,000	0,002	0,000	0,003
Total Cations	3,005	3,027	3,026	3,021	3,028

🟩
🟦
36,74
b.d.
0,53
b.d.
28,78
0,27
33,72
0,34
0,23
b.d.
100,62
67,617
32,383
0,983
0,000
0,017
0,000
0,644
0,006
1,344
0,010
3,015

Appendix 3D

Ilmenite

MIL 090036	**Granulitic breccias**				
Oxide Weight Percent					
SiO_2	0,06	0,89	0,10	0,04	2,02
TiO_2	52,03	51,31	52,78	54,48	44,93
Al_2O_3	0,09	0,22	0,09	b.d.	2,18
Cr_2O_3	0,08	0,15	0,12	0,36	7,29
FeO	41,81	40,95	41,74	38,68	35,66
MnO	0,32	0,25	0,32	0,38	0,31
MgO	3,42	3,86	3,53	5,43	4,72
CaO	0,34	0,20	0,26	0,18	1,36
Na_2O	b.d.	b.d.	b.d.	b.d.	b.d.
K_2O	b.d.	b.d.	b.d.	b.d.	b.d.
V_2O_3	0,04	0,06	0,03	0,04	0,12
Total	*98,20*	*97,90*	*98,97*	*99,59*	*98,59*
Cations per 3 Oxygens					
Si	0,001608	0,022295	0,002536	0,001021	0,049311
Ti	0,983172	0,964418	0,987044	0,995679	0,825147
Al	0,002784	0,00651	0,002638	0	0,062838
Cr	0,001609	0,002905	0,00234	0,006859	0,140829
Fe	0,87863	0,856055	0,868096	0,785984	0,728445
Mn	0,006768	0,005356	0,006698	0,007842	0,006434
Mg	0,128232	0,143953	0,130765	0,196572	0,171644
Ca	0,009072	0,005222	0,007007	0,004687	0,035536
Na	0	0	0	0	0
K	0	0	0	0	0
V	0,000766	0,001242	0,000538	0,000818	0,00235
Total Cations	*2,01264*	*2,007958*	*2,007662*	*1,999462*	*2,022533*

Appendix 4A

Plagioclases

MIL 090070	**Impact melts**					
SiO_2	43,63	43,12	43,65	43,24	43,51	43,26
TiO_2	0,07	b.d.	b.d.	b.d.	b.d.	b.d.
Al_2O_3	34,79	34,50	34,36	34,76	34,62	34,81
Cr_2O_3	b.d.	b.d.	b.d.	b.d.	0,09	0,09
FeO	0,07	0,27	0,32	0,22	0,05	0,21
MnO	0,00	0,00	0,00	0,13	0,00	0,00
MgO	0,38	0,28	0,29	0,19	0,32	0,24
CaO	20,03	20,33	19,96	19,81	20,02	20,42
Na_2O	0,45	0,37	0,44	0,38	0,33	0,31
K_2O	0,12	0,14	0,08	0,15	0,14	0,05
Total	*99,52*	*99,01*	*99,10*	*98,87*	*99,08*	*99,38*
An	95,50	96,04	95,75	95,85	96,35	97,03
Ab	3,84	3,19	3,78	3,30	2,84	2,70
Or	0,65	0,77	0,47	0,85	0,80	0,28
Cations per 8 Oxygens						
Si	2,036	2,028	2,047	2,032	2,039	2,025
Ti	0,002	0,000	0,000	0,000	0,000	0,000
Al (IV)	1,913	1,912	1,899	1,926	1,912	1,921
Cr	0,000	0,000	0,000	0,000	0,003	0,003
Fe	0,003	0,011	0,012	0,009	0,002	0,008
Mn	0,000	0,000	0,000	0,005	0,000	0,000
Mg	0,026	0,020	0,021	0,013	0,022	0,017
Ca	1,001	1,024	1,003	0,998	1,005	1,024
Na	0,040	0,034	0,040	0,034	0,030	0,028
K	0,007	0,008	0,005	0,009	0,008	0,003
Total Cations	5,029	5,037	5,026	5,026	5,022	5,029
Tet site	*3,949*	*3,940*	*3,946*	*3,958*	*3,951*	*3,946*

Monomict plagioclase						
SiO_2	44,19	43,29	44,45	43,76	42,69	43,44
TiO_2	b.d.	0,14	b.d.	b.d.	b.d.	0,11
Al_2O_3	35,21	34,86	33,37	34,06	35,14	34,42
Cr_2O_3	0,04	0,04	0,10	b.d.	0,21	0,04
FeO	0,23	0,19	0,64	0,40	0,48	0,32
MnO	0,09	b.d.	0,04	b.d.	0,03	0,08
MgO	0,03	0,32	0,66	0,67	0,14	0,21
CaO	20,33	19,82	19,09	19,82	20,50	20,15
Na_2O	0,27	0,33	0,52	0,46	0,11	0,30
K_2O	0,03	0,13	0,17	0,12	0,05	0,09
Total	*100,41*	*99,13*	*99,05*	*99,29*	*99,35*	*99,16*
An	97,53	96,34	94,34	95,27	98,81	96,90

Ab	2,30	2,90	4,67	4,03	0,93	2,57
Or	0,16	0,77	0,99	0,70	0,26	0,52
Cations per 8 Oxygens						
Si	2,043	2,028	2,084	2,049	2,004	2,039
Ti	0,000	0,005	0,000	0,000	0,000	0,004
Al (IV)	1,919	1,925	1,844	1,880	1,943	1,904
Cr	0,001	0,001	0,004	0,000	0,008	0,001
Fe	0,009	0,007	0,025	0,016	0,019	0,013
Mn	0,004	0,000	0,000	0,000	0,000	0,000
Mg	0,002	0,022	0,046	0,046	0,010	0,014
Ca	1,007	0,995	0,959	0,994	1,031	1,013
Na	0,024	0,030	0,047	0,042	0,010	0,027
K	0,002	0,008	0,010	0,007	0,003	0,005
Total Cations	5,010	5,022	5,020	5,035	5,027	5,021
Tet site	*3,962*	*3,953*	*3,929*	*3,929*	*3,947*	*3,943*

43,73	43,52	44,13	44,00	43,48	45,24	44,14	43,45
0,04	0,15	0,18	b.d.	b.d.	0,10	0,08	b.d.
33,95	35,07	34,17	34,69	34,41	34,21	34,94	34,49
b.d.	0,24	b.d.	0,11	b.d.	0,09	0,06	b.d.
0,52	0,12	0,13	0,13	0,35	0,18	0,43	0,30
0,03	b.d.	b.d.	b.d.	0,03	0,11	b.d.	b.d.
0,31	0,35	0,25	0,35	0,04	0,36	0,16	0,08
19,90	20,00	19,92	19,69	20,28	19,37	19,69	20,05
0,51	0,48	0,46	0,59	0,27	0,76	0,34	0,41
0,07	0,12	0,15	0,09	0,08	0,15	0,15	0,13
99,07	*100,04*	*99,38*	*99,66*	*98,94*	*100,57*	*100,00*	*98,92*
95,15	95,14	95,19	94,37	97,19	92,61	96,09	95,71
4,44	4,17	3,98	5,11	2,35	6,54	3,01	3,55
0,41	0,69	0,83	0,53	0,46	0,85	0,90	0,74
2,054	2,023	2,061	2,049	2,044	2,085	2,049	2,042
0,002	0,005	0,006	0,000	0,000	0,003	0,003	0,000
1,879	1,921	1,881	1,904	1,906	1,858	1,911	1,910
0,000	0,009	0,000	0,004	0,000	0,003	0,002	0,000
0,021	0,005	0,005	0,005	0,014	0,007	0,017	0,012
0,001	0,000	0,000	0,000	0,000	0,004	0,000	0,000
0,022	0,024	0,017	0,024	0,003	0,025	0,011	0,006
1,002	0,996	0,997	0,982	1,021	0,957	0,979	1,010
0,047	0,044	0,042	0,053	0,025	0,068	0,031	0,037
0,004	0,007	0,009	0,005	0,005	0,009	0,009	0,008
5,031	5,033	5,017	5,027	5,018	5,019	5,012	5,025
3,933	*3,944*	*3,942*	*3,952*	*3,950*	*3,943*	*3,960*	*3,953*

42,63	43,79	43,30	43,84	44,13	44,07	44,20	43,74
b.d.	b.d.	b.d.	0,11	0,12	b.d.	0,29	b.d.
34,82	33,56	34,99	35,41	34,66	34,41	32,33	34,61
0,07	0,03	0,05	0,07	0,16	0,09	0,05	0,05
0,16	0,15	0,24	0,30	0,35	0,30	2,09	0,25
b.d.	b.d.	b.d.	0,05	b.d.	0,05	0,00	0,06
0,30	0,18	0,19	0,22	0,24	0,20	2,09	0,42
19,85	19,82	19,99	20,42	19,70	19,90	18,95	19,78
0,25	0,46	0,40	0,31	0,45	0,39	0,53	0,47
b.d.	0,05	0,03	0,10	0,06	0,24	0,15	0,15
98,08	*98,04*	*99,20*	*100,82*	*99,87*	*99,65*	*100,69*	*99,52*
97,81	95,72	96,34	96,76	95,71	95,26	94,30	95,09

2,19	4,01	3,50	2,68	3,92	3,37	4,81	4,07
0,00	0,27	0,17	0,56	0,37	1,36	0,89	0,83

2,018	2,072	2,028	2,023	2,051	2,056	2,058	2,043
0,000	0,000	0,000	0,004	0,004	0,000	0,010	0,000
1,943	1,872	1,931	1,926	1,898	1,892	1,774	1,905
0,003	0,001	0,002	0,002	0,006	0,003	0,002	0,002
0,007	0,006	0,009	0,011	0,014	0,012	0,082	0,010
0,000	0,000	0,000	0,002	0,000	0,000	0,000	0,000
0,021	0,013	0,014	0,015	0,017	0,014	0,145	0,029
1,007	1,005	1,003	1,010	0,981	0,995	0,945	0,990
0,023	0,042	0,036	0,028	0,040	0,035	0,048	0,042
0,000	0,003	0,002	0,006	0,004	0,014	0,009	0,009
5,020	5,014	5,025	5,026	5,015	5,021	5,073	5,029
3,961	*3,944*	*3,959*	*3,948*	*3,949*	*3,948*	*3,832*	*3,948*

43,89	43,68	43,59	44,29	43,86	43,44	43,76	43,37
b.d.	b.d.	0,19	b.d.	b.d.	b.d.	0,07	b.d.
34,77	34,93	34,75	34,62	34,21	34,59	34,31	33,99
b.d.	b.d.	0,11	0,06	b.d.	0,03	0,07	b.d.
0,11	0,17	0,19	0,16	0,22	0,34	0,19	0,41
b.d.	0,09	b.d.	b.d.	0,10	0,04	0,04	0,11
0,15	0,32	0,16	0,31	0,45	0,29	0,25	0,04
20,08	20,55	19,93	19,99	19,31	20,02	19,61	19,61
0,27	0,37	0,39	0,53	0,57	0,44	0,43	0,43
0,11	0,07	0,06	0,03	0,17	0,13	0,08	0,11
99,38	*100,17*	*99,38*	*99,98*	*98,89*	*99,34*	*98,81*	*98,09*
96,97	96,49	96,21	95,25	94,01	95,46	95,68	95,50
2,37	3,10	3,42	4,58	4,99	3,77	3,83	3,83
0,65	0,40	0,37	0,17	1,01	0,77	0,49	0,67
2,048	2,030	2,037	2,055	2,059	2,035	2,054	2,056
0,000	0,000	0,007	0,000	0,000	0,000	0,002	0,000
1,912	1,913	1,914	1,894	1,893	1,910	1,899	1,899
0,000	0,000	0,004	0,002	0,000	0,001	0,003	0,000
0,004	0,006	0,007	0,006	0,009	0,013	0,007	0,016
0,000	0,000	0,000	0,000	0,000	0,000	0,001	0,000
0,010	0,022	0,011	0,021	0,031	0,021	0,017	0,003
1,004	1,023	0,998	0,994	0,971	1,005	0,986	0,996
0,025	0,033	0,035	0,048	0,052	0,040	0,039	0,040
0,007	0,004	0,004	0,002	0,010	0,008	0,005	0,007
5,011	5,032	5,017	5,022	5,025	5,033	5,015	5,018
3,961	*3,943*	*3,951*	*3,949*	*3,952*	*3,945*	*3,953*	*3,955*

44,41	44,97	43,65	43,18	43,54	43,45	43,27	44,06
0,14	0,15	b.d.	b.d.	b.d.	b.d.	0,11	0,11
34,02	34,40	34,23	34,91	34,77	33,83	34,44	34,24
0,12	b.d.	0,04	b.d.	b.d.	b.d.	0,11	b.d.
0,19	0,51	0,35	0,48	0,19	0,28	0,05	0,32
0,07	b.d.	b.d.	b.d.	b.d.	0,06	b.d.	0,13
0,14	0,38	0,55	0,38	0,37	0,24	0,34	0,40
19,22	19,05	19,60	20,34	19,72	19,89	20,01	19,80
0,67	0,71	0,62	0,41	0,54	0,55	0,53	0,65
0,20	0,13	0,08	0,05	0,07	0,06	0,07	0,05
99,17	*100,29*	*99,11*	*99,74*	*99,19*	*98,36*	*98,92*	*99,77*
93,02	92,99	94,15	96,22	94,89	94,94	95,07	94,12

5,84	6,26	5,37	3,50	4,72	4,71	4,52	5,62
1,14	0,75	0,48	0,27	0,38	0,35	0,41	0,26

2,077	2,078	2,047	2,017	2,037	2,055	2,033	2,055
0,005	0,005	0,000	0,000	0,000	0,000	0,004	0,004
1,875	1,873	1,891	1,922	1,918	1,885	1,907	1,882
0,004	0,000	0,001	0,000	0,000	0,000	0,004	0,000
0,008	0,020	0,014	0,019	0,007	0,011	0,002	0,013
0,000	0,000	0,000	0,000	0,000	0,000	0,000	0,000
0,010	0,026	0,038	0,027	0,026	0,017	0,024	0,028
0,963	0,943	0,985	1,018	0,989	1,008	1,007	0,989
0,060	0,063	0,056	0,037	0,049	0,050	0,048	0,059
0,012	0,008	0,005	0,003	0,004	0,004	0,004	0,003
5,014	5,016	5,037	5,042	5,030	5,029	5,034	5,032
3,952	*3,951*	*3,938*	*3,939*	*3,955*	*3,940*	*3,940*	*3,937*

45,45	44,13	43,61	43,62	43,44	43,55	44,25	44,62
b.d.	0,05	b.d.	b.d.	0,17	0,06	0,07	0,04
33,32	34,36	34,65	34,32	34,06	35,40	33,78	34,18
0,04	b.d.	0,03	0,10	b.d.	b.d.	b.d.	0,10
0,73	0,26	0,26	0,25	0,55	0,60	0,29	0,32
b.d.	b.d.	b.d.	b.d.	0,11	b.d.	b.d.	b.d.
0,55	0,31	0,16	0,33	0,51	0,42	0,55	0,40
18,98	19,81	20,06	20,07	19,78	20,27	18,98	19,38
0,88	0,46	0,43	0,49	0,46	0,36	0,85	0,57
0,17	0,10	0,18	0,08	0,06	0,08	0,24	0,16
100,12	*99,47*	*99,39*	*99,26*	*99,13*	*100,76*	*98,99*	*99,78*
91,38	95,45	95,23	95,36	95,63	96,42	91,28	94,02
7,63	3,98	3,73	4,18	4,01	3,14	7,36	5,04
0,99	0,57	1,04	0,46	0,36	0,44	1,35	0,94
2,107	2,059	2,040	2,044	2,040	2,014	2,074	2,074
0,000	0,002	0,000	0,000	0,006	0,002	0,002	0,002
1,820	1,889	1,911	1,895	1,885	1,929	1,866	1,872
0,002	0,000	0,001	0,004	0,000	0,000	0,000	0,004
0,028	0,010	0,010	0,010	0,021	0,023	0,011	0,012
0,000	0,000	0,000	0,000	0,004	0,000	0,000	0,000
0,038	0,022	0,011	0,023	0,036	0,029	0,039	0,028
0,942	0,990	1,006	1,008	0,995	1,004	0,953	0,965
0,079	0,041	0,039	0,044	0,042	0,033	0,077	0,052
0,010	0,006	0,011	0,005	0,004	0,005	0,014	0,010
5,027	5,019	5,029	5,032	5,034	5,038	5,036	5,018
3,927	*3,948*	*3,951*	*3,938*	*3,926*	*3,943*	*3,940*	*3,946*

44,02	43,89	43,32	43,60	43,68	43,40	43,99	43,58
b.d.	0,17	0,11	0,05	b.d.	b.d.	0,08	b.d.
34,40	34,48	34,97	34,66	34,96	34,61	34,86	35,04
b.d.	b.d.	b.d.	b.d.	0,03	b.d.	b.d.	b.d.
0,25	0,19	0,27	0,22	0,24	0,35	0,16	0,28
0,09	b.d.	b.d.	0,11	b.d.	0,14	b.d.	b.d.
0,32	0,30	0,24	0,24	0,25	0,33	0,39	0,29
19,83	20,09	20,37	20,03	20,52	19,80	20,23	20,06
0,57	0,44	0,27	0,35	0,38	0,45	0,35	0,41
0,12	0,07	0,07	0,06	0,03	0,07	0,13	0,05
99,59	*99,63*	*99,62*	*99,32*	*100,10*	*99,13*	*100,19*	*99,70*
94,41	95,79	97,23	96,57	96,61	95,71	96,27	96,19

4,90	3,81	2,34	3,09	3,20	3,91	3,00	3,55
0,69	0,40	0,42	0,35	0,19	0,39	0,73	0,26
2,053	2,046	2,023	2,040	2,030	2,037	2,040	2,031
0,000	0,006	0,004	0,002	0,000	0,000	0,003	0,000
1,891	1,895	1,924	1,911	1,915	1,914	1,905	1,924
0,000	0,000	0,000	0,000	0,001	0,000	0,000	0,000
0,010	0,007	0,010	0,008	0,009	0,014	0,006	0,011
0,003	0,000	0,000	0,004	0,000	0,000	0,000	0,000
0,022	0,021	0,016	0,017	0,018	0,023	0,027	0,020
0,991	1,003	1,019	1,004	1,022	0,996	1,005	1,001
0,051	0,040	0,025	0,032	0,034	0,041	0,031	0,037
0,007	0,004	0,004	0,004	0,002	0,004	0,008	0,003
5,030	5,022	5,026	5,021	5,030	5,028	5,025	5,027
3,945	*3,941*	*3,947*	*3,950*	*3,944*	*3,951*	*3,945*	*3,955*

44,79	43,54	42,98	43,03	43,93	42,88	45,43	44,40
0,12	0,08	0,07	0,05	0,07	b.d.	b.d.	0,07
33,17	34,73	35,07	35,07	35,10	34,47	33,01	34,24
0,04	b.d.	0,05	0,06	0,11	0,06	b.d.	b.d.
0,61	0,38	0,39	0,39	0,39	0,87	1,11	0,51
b.d.	0,08	b.d.	b.d.	b.d.	b.d.	b.d.	b.d.
0,63	0,36	0,30	0,00	0,32	0,08	0,60	0,31
17,99	19,97	19,91	20,76	19,40	20,04	18,41	19,70
0,78	0,38	0,41	0,05	0,38	0,20	0,63	0,50
0,17	0,09	0,14	0,03	0,13	0,08	0,23	0,07
98,30	*99,60*	*99,31*	*99,44*	*99,83*	*98,68*	*99,42*	*99,80*
91,76	96,21	95,64	99,37	95,87	97,76	92,89	95,20
7,20	3,29	3,55	0,43	3,38	1,75	5,72	4,38
1,03	0,50	0,81	0,20	0,75	0,49	1,39	0,42
2,107	2,034	2,014	2,015	2,041	2,026	2,119	2,066
0,004	0,003	0,002	0,002	0,002	0,000	0,000	0,002
1,839	1,912	1,937	1,936	1,922	1,920	1,815	1,877
0,002	0,000	0,002	0,002	0,004	0,002	0,000	0,000
0,024	0,015	0,015	0,015	0,015	0,034	0,043	0,020
0,000	0,000	0,000	0,000	0,000	0,000	0,000	0,000
0,044	0,025	0,021	0,000	0,022	0,005	0,042	0,021
0,907	0,999	1,000	1,041	0,966	1,014	0,920	0,982
0,071	0,034	0,037	0,004	0,034	0,018	0,057	0,045
0,010	0,005	0,008	0,002	0,008	0,005	0,014	0,004
5,009	5,027	5,037	5,018	5,014	5,025	5,009	5,018
3,947	*3,946*	*3,951*	*3,950*	*3,963*	*3,945*	*3,933*	*3,943*

43,13	43,56	43,87	43,20	43,64	43,46	42,85	43,61
0,03	b.d.	b.d.	b.d.	b.d.	b.d.	b.d.	b.d.
34,74	34,66	34,67	34,15	34,43	34,12	35,12	34,26
b.d.	0,10	b.d.	b.d.	0,23	0,04	b.d.	0,07
0,14	0,12	0,48	0,52	0,30	0,24	0,31	0,26
b.d.	b.d.	b.d.	b.d.	b.d.	b.d.	b.d.	b.d.
0,08	0,12	0,36	0,45	0,22	0,33	0,49	0,24
20,36	20,24	20,04	19,53	20,10	19,64	20,23	19,97
0,32	0,38	0,36	0,45	0,38	0,47	0,41	0,27
0,04	0,08	b.d.	0,15	0,05	0,14	0,14	0,09
98,85	*99,27*	*99,78*	*98,45*	*99,35*	*98,45*	*99,55*	*98,75*
97,00	96,25	96,88	95,17	96,39	95,03	95,71	97,13

2,75	3,29	3,12	3,94	3,31	4,15	3,47	2,33
0,25	0,46	0,00	0,89	0,30	0,82	0,81	0,54

2,028	2,039	2,043	2,041	2,042	2,050	2,005	2,050
0,001	0,000	0,000	0,000	0,000	0,000	0,000	0,000
1,926	1,912	1,903	1,901	1,899	1,897	1,937	1,899
0,000	0,004	0,000	0,000	0,008	0,002	0,000	0,003
0,006	0,005	0,019	0,020	0,012	0,010	0,012	0,010
0,000	0,000	0,000	0,000	0,000	0,000	0,000	0,000
0,006	0,008	0,025	0,032	0,015	0,023	0,034	0,017
1,026	1,015	1,000	0,989	1,008	0,992	1,015	1,006
0,029	0,035	0,032	0,041	0,035	0,043	0,037	0,024
0,003	0,005	0,000	0,009	0,003	0,009	0,009	0,006
5,024	5,023	5,022	5,033	5,023	5,026	5,049	5,014
3,954	*3,951*	*3,946*	*3,942*	*3,942*	*3,948*	*3,942*	*3,949*

43,75	43,82	43,59	43,24	43,79	43,59	43,24	43,79
0,04	b.d.	b.d.	0,15	0,15	b.d.	0,15	0,15
34,59	35,03	34,02	34,29	34,55	34,02	34,29	34,55
b.d.	0,12	0,05	b.d.	0,11	0,05	b.d.	0,11
0,22	0,47	0,37	0,67	0,54	0,37	0,67	0,54
b.d.	0,16	0,11	b.d.	b.d.	0,11	b.d.	b.d.
0,27	0,59	0,29	0,39	0,38	0,29	0,39	0,38
20,13	20,33	20,18	20,20	19,94	20,18	20,20	19,94
0,29	0,45	0,38	0,41	0,54	0,38	0,41	0,54
0,16	0,16	0,13	0,07	b.d.	0,13	0,07	b.d.
99,42	*101,13*	*99,13*	*99,42*	*99,99*	*99,13*	*99,42*	*99,99*
96,58	95,26	95,98	96,05	95,34	95,98	96,05	95,34
2,52	3,83	3,27	3,53	4,66	3,27	3,53	4,66
0,90	0,91	0,74	0,42	0,00	0,74	0,42	0,00
2,044	2,021	2,048	2,028	2,038	2,048	2,028	2,038
0,001	0,000	0,000	0,005	0,005	0,000	0,005	0,005
1,905	1,904	1,883	1,895	1,895	1,883	1,895	1,895
0,000	0,004	0,002	0,000	0,004	0,002	0,000	0,004
0,008	0,018	0,015	0,026	0,021	0,015	0,026	0,021
0,000	0,006	0,005	0,000	0,000	0,005	0,000	0,000
0,019	0,041	0,021	0,027	0,026	0,021	0,027	0,026
1,008	1,005	1,016	1,015	0,994	1,016	1,015	0,994
0,026	0,040	0,035	0,037	0,049	0,035	0,037	0,049
0,009	0,010	0,008	0,004	0,000	0,008	0,004	0,000
5,020	5,050	5,031	5,039	5,032	5,031	5,039	5,032
3,949	*3,925*	*3,931*	*3,924*	*3,933*	*3,931*	*3,924*	*3,933*
43,65	43,60	43,78	43,31	43,73	43,40	43,99	44,04
b.d.	0,07	b.d.	0,08	0,04	b.d.	0,20	0,14
34,70	34,56	34,76	35,26	34,83	34,92	34,90	34,81
b.d.	0,04	b.d.	0,18	b.d.	b.d.	0,03	0,14
0,14	0,29	0,16	0,26	0,24	0,25	0,21	0,22
0,15	b.d.	0,20	b.d.	0,04	0,14	b.d.	b.d.
0,40	0,25	0,13	0,35	0,34	0,40	0,27	0,21
19,88	19,53	20,00	19,90	20,27	20,25	20,05	19,99
0,55	0,41	0,45	0,32	0,45	0,34	0,27	0,41
0,03	0,09	0,09	0,07	b.d.	b.d.	0,08	0,08
99,50	*98,84*	*99,58*	*99,73*	*99,93*	*99,70*	*100,01*	*100,06*
95,05	95,86	95,56	96,78	96,17	97,03	97,17	95,97

4,78	3,61	3,91	2,83	3,83	2,97	2,37	3,55
0,17	0,53	0,53	0,39	0,00	0,00	0,46	0,48
2,040	2,046	2,045	2,018	2,034	2,026	2,041	2,044
0,000	0,003	0,000	0,003	0,002	0,000	0,007	0,005
1,911	1,912	1,914	1,936	1,909	1,921	1,909	1,904
0,000	0,002	0,000	0,007	0,000	0,000	0,001	0,005
0,006	0,011	0,006	0,010	0,009	0,010	0,008	0,009
0,000	0,000	0,000	0,000	0,002	0,000	0,000	0,000
0,028	0,017	0,009	0,024	0,024	0,028	0,018	0,015
0,995	0,982	1,001	0,993	1,010	1,013	0,997	0,994
0,050	0,037	0,041	0,029	0,040	0,031	0,024	0,037
0,002	0,005	0,006	0,004	0,000	0,000	0,005	0,005
5,031	5,016	5,021	5,024	5,030	5,029	5,011	5,017
3,951	*3,958*	*3,959*	*3,954*	*3,943*	*3,947*	*3,950*	*3,948*

43,74	43,41	43,30	43,53	43,72	43,76	44,21	43,56
0,10	0,08	0,10	0,09	0,11	b.d.	0,05	b.d.
34,31	34,31	34,82	34,50	34,69	33,83	33,99	35,21
b.d.	0,18	0,13	b.d.	b.d.	b.d.	0,04	0,21
0,51	0,53	0,60	0,65	0,74	0,55	0,55	0,39
b.d.	b.d.	b.d.	b.d.	b.d.	b.d.	b.d.	b.d.
0,33	0,21	0,35	0,13	0,40	0,39	0,45	0,29
19,75	19,79	20,00	19,86	20,19	19,83	19,60	20,12
0,42	0,39	0,35	0,38	0,53	0,59	0,58	0,44
0,13	0,16	0,07	0,09	0,13	0,19	0,11	0,08
99,29	*99,06*	*99,73*	*99,23*	*100,51*	*99,14*	*99,57*	*100,30*
95,59	95,72	96,52	96,09	94,76	93,88	94,34	95,73
3,64	3,39	3,08	3,36	4,50	5,05	5,04	3,82
0,78	0,90	0,41	0,55	0,74	1,07	0,62	0,45
2,048	2,040	2,022	2,041	2,029	2,056	2,064	2,021
0,003	0,003	0,003	0,003	0,004	0,000	0,002	0,000
1,893	1,900	1,916	1,906	1,898	1,873	1,870	1,925
0,000	0,007	0,005	0,000	0,000	0,000	0,001	0,008
0,020	0,021	0,024	0,026	0,029	0,022	0,021	0,015
0,000	0,000	0,000	0,000	0,000	0,000	0,000	0,000
0,023	0,015	0,025	0,009	0,028	0,027	0,031	0,020
0,991	0,996	1,001	0,998	1,004	0,998	0,980	1,000
0,038	0,035	0,032	0,035	0,048	0,054	0,052	0,040
0,008	0,009	0,004	0,006	0,008	0,011	0,006	0,005
5,025	5,026	5,032	5,023	5,046	5,041	5,028	5,034
3,942	*3,940*	*3,939*	*3,947*	*3,927*	*3,929*	*3,934*	*3,947*

43,57	43,69	43,59	43,73	44,00	43,38	44,03	43,01
b.d.	b.d.	0,05	b.d.	b.d.	0,07	0,03	b.d.
35,08	33,62	34,76	34,78	34,64	34,78	34,25	34,29
0,09	0,11	b.d.	0,09	0,05	0,06	0,04	0,21
0,13	0,48	0,04	0,27	0,09	0,35	0,19	0,34
b.d.	b.d.	0,06	b.d.	0,14	0,03	b.d.	b.d.
0,40	0,65	0,20	0,26	0,19	0,34	0,39	0,40
20,16	19,68	19,99	19,99	20,06	20,05	20,31	19,98
0,44	0,36	0,22	0,33	0,37	0,46	0,48	0,54
0,05	0,07	0,16	0,11	0,10	0,07	0,17	0,10
99,91	*98,65*	*99,08*	*99,56*	*99,63*	*99,59*	*99,89*	*98,86*
95,91	96,40	97,17	96,49	96,25	95,66	95,03	94,79

3,83	3,18	1,90	2,89	3,18	3,96	4,04	4,64
0,26	0,42	0,93	0,62	0,57	0,38	0,93	0,58
2,026	2,059	2,041	2,040	2,052	2,027	2,051	2,027
0,000	0,000	0,002	0,000	0,000	0,002	0,001	0,000
1,923	1,867	1,919	1,912	1,904	1,916	1,880	1,904
0,003	0,004	0,000	0,003	0,002	0,002	0,002	0,008
0,005	0,019	0,002	0,011	0,004	0,014	0,008	0,013
0,000	0,000	0,002	0,000	0,000	0,000	0,000	0,000
0,028	0,046	0,014	0,018	0,013	0,024	0,027	0,028
1,004	0,993	1,003	0,999	1,002	1,004	1,013	1,009
0,040	0,033	0,020	0,030	0,033	0,042	0,043	0,049
0,003	0,004	0,010	0,006	0,006	0,004	0,010	0,006
5,032	5,024	5,012	5,020	5,015	5,034	5,034	5,045
3,949	*3,925*	*3,960*	*3,952*	*3,955*	*3,943*	*3,931*	*3,931*

43,24	43,30	44,00	43,37	43,44	44,19	44,08	44,20
b.d.	0,11	b.d.	0,05	0,17	0,08	0,10	0,17
34,12	34,55	34,77	34,55	34,06	34,82	34,58	34,12
0,05	b.d.	b.d.	0,09	b.d.	b.d.	0,04	0,05
0,35	0,28	0,41	0,58	0,55	b.d.	0,26	0,65
b.d.	0,06	0,15	b.d.	0,11	0,19	b.d.	b.d.
0,41	0,48	0,24	0,11	0,51	0,56	0,22	0,25
19,98	19,80	20,09	20,10	19,78	20,13	20,47	20,29
0,53	0,46	0,48	0,34	0,46	0,51	0,43	0,37
0,09	0,04	0,14	0,09	0,06	0,08	0,24	0,07
98,76	*99,07*	*100,28*	*99,27*	*99,13*	*100,56*	*100,42*	*100,18*
94,97	95,77	95,16	96,57	95,63	95,14	95,04	96,45
4,54	3,99	4,08	2,93	4,01	4,40	3,64	3,15
0,49	0,24	0,76	0,50	0,36	0,46	1,33	0,40
2,038	2,031	2,044	2,034	2,040	2,042	2,044	2,055
0,000	0,004	0,000	0,002	0,006	0,003	0,004	0,006
1,895	1,910	1,903	1,910	1,885	1,896	1,890	1,869
0,002	0,000	0,000	0,003	0,000	0,000	0,002	0,002
0,014	0,011	0,016	0,023	0,021	0,000	0,010	0,025
0,000	0,002	0,000	0,000	0,004	0,007	0,000	0,000
0,029	0,034	0,017	0,008	0,036	0,038	0,015	0,018
1,009	0,995	1,000	1,010	0,995	0,997	1,017	1,010
0,048	0,041	0,043	0,031	0,042	0,046	0,039	0,033
0,005	0,003	0,008	0,005	0,004	0,005	0,014	0,004
5,040	5,032	5,030	5,025	5,034	5,033	5,034	5,022
3,933	*3,942*	*3,947*	*3,944*	*3,926*	*3,937*	*3,933*	*3,924*

43,29	43,76	43,81	42,81	43,73	43,55	43,46	43,39
b.d.	0,10	b.d.	0,09	b.d.	0,05	b.d.	0,04
34,04	34,48	34,82	34,63	34,75	33,90	34,41	34,75
0,06	b.d.	b.d.	0,03	b.d.	0,14	0,16	0,05
0,24	0,15	0,29	0,07	0,23	0,14	0,23	0,24
b.d.	b.d.	b.d.	b.d.	0,11	0,14	b.d.	b.d.
0,23	0,33	0,39	0,29	0,33	0,31	0,36	0,31
20,02	19,80	20,05	20,13	19,72	19,40	19,66	19,83
0,45	0,48	0,47	0,35	0,51	0,44	0,43	0,28
0,08	0,13	0,13	0,11	0,12	0,05	0,09	0,15
98,40	*99,23*	*99,95*	*98,52*	*99,51*	*98,11*	*98,80*	*99,04*
95,69	95,12	95,23	96,33	94,83	95,76	95,67	96,62

3,86	4,13	4,05	3,07	4,47	3,92	3,80	2,49
0,44	0,75	0,71	0,60	0,70	0,32	0,53	0,89

2,046	2,047	2,038	2,021	2,041	2,060	2,043	2,035
0,000	0,004	0,000	0,003	0,000	0,002	0,000	0,001
1,896	1,901	1,908	1,926	1,912	1,890	1,906	1,920
0,002	0,000	0,000	0,001	0,000	0,005	0,006	0,002
0,009	0,006	0,011	0,003	0,009	0,006	0,009	0,009
0,000	0,000	0,000	0,000	0,005	0,000	0,000	0,000
0,016	0,023	0,027	0,021	0,023	0,022	0,025	0,022
1,014	0,992	0,999	1,018	0,986	0,983	0,990	0,996
0,041	0,043	0,043	0,032	0,046	0,040	0,039	0,026
0,005	0,008	0,007	0,006	0,007	0,003	0,006	0,009
5,028	5,024	5,033	5,032	5,030	5,012	5,024	5,020
3,941	*3,948*	*3,946*	*3,947*	*3,953*	*3,951*	*3,949*	*3,955*

43,76	43,43	43,37	43,89	43,38	43,52	43,33	43,95
b.d.	b.d.	b.d.	b.d.	0,13	b.d.	b.d.	b.d.
34,17	34,48	33,96	34,97	34,95	34,67	34,23	34,55
0,09	b.d.	b.d.	b.d.	b.d.	b.d.	0,05	0,03
0,18	0,18	0,27	0,23	0,08	0,00	0,41	0,17
b.d.	b.d.	0,08	b.d.	b.d.	b.d.	b.d.	b.d.
0,13	0,20	0,26	0,24	0,41	0,27	0,41	0,33
19,92	19,49	20,11	19,80	19,90	19,87	20,23	20,04
0,44	0,33	0,52	0,40	0,52	0,42	0,40	0,50
0,10	0,09	0,11	0,05	0,11	0,09	0,12	0,08
98,79	*98,20*	*98,69*	*99,58*	*99,48*	*98,83*	*99,17*	*99,65*
95,63	96,48	94,88	96,26	94,90	95,80	95,92	95,26
3,83	2,97	4,47	3,48	4,50	3,69	3,39	4,29
0,55	0,56	0,65	0,26	0,60	0,51	0,68	0,45
2,057	2,050	2,047	2,044	2,026	2,042	2,035	2,048
0,000	0,000	0,000	0,000	0,005	0,000	0,000	0,000
1,893	1,918	1,889	1,919	1,924	1,918	1,895	1,898
0,003	0,000	0,000	0,000	0,000	0,000	0,002	0,001
0,007	0,007	0,010	0,009	0,003	0,000	0,016	0,006
0,000	0,000	0,000	0,000	0,000	0,000	0,000	0,000
0,009	0,014	0,018	0,017	0,028	0,019	0,029	0,023
1,003	0,985	1,017	0,988	0,995	0,999	1,018	1,001
0,040	0,030	0,048	0,036	0,047	0,039	0,036	0,045
0,006	0,006	0,007	0,003	0,006	0,005	0,007	0,005
5,018	5,010	5,036	5,016	5,034	5,021	5,038	5,027
3,949	*3,967*	*3,936*	*3,963*	*3,949*	*3,960*	*3,930*	*3,946*

43,09	43,36	43,50	43,87	43,20	44,21	43,14	44,36
0,06	b.d.	0,03	b.d.	b.d.	0,13	0,04	b.d.
34,71	34,69	35,48	35,22	34,54	34,75	35,02	33,52
b.d.	0,07	0,18	0,12	0,09	0,05	0,15	0,03
0,36	0,40	0,32	0,27	0,28	0,07	0,34	0,29
b.d.	0,03	b.d.	b.d.	b.d.	0,16	b.d.	0,09
0,35	0,52	0,45	0,36	0,09	0,14	0,36	0,25
19,98	19,94	20,26	20,36	20,53	19,93	20,21	19,18
0,44	0,51	0,37	0,31	0,30	0,53	0,22	0,75
0,05	0,15	0,13	b.d.	0,09	0,08	0,11	b.d.
99,05	*99,67*	*100,71*	*100,51*	*99,12*	*100,05*	*99,58*	*98,47*
95,92	94,79	96,12	97,36	96,91	94,95	97,42	93,35

3,81	4,37	3,17	2,64	2,59	4,57	1,95	6,65
0,27	0,83	0,72	0,00	0,50	0,47	0,63	0,00

2,024	2,026	2,011	2,029	2,030	2,051	2,016	2,089
0,002	0,000	0,001	0,000	0,000	0,005	0,001	0,000
1,921	1,911	1,933	1,919	1,912	1,900	1,929	1,860
0,000	0,002	0,007	0,004	0,004	0,002	0,005	0,001
0,014	0,016	0,012	0,010	0,011	0,003	0,013	0,011
0,000	0,000	0,000	0,000	0,000	0,006	0,000	0,000
0,025	0,036	0,031	0,025	0,006	0,010	0,025	0,018
1,005	0,999	1,003	1,009	1,033	0,991	1,012	0,968
0,040	0,046	0,033	0,027	0,028	0,048	0,020	0,069
0,003	0,009	0,007	0,000	0,005	0,005	0,007	0,000
5,035	5,045	5,039	5,023	5,029	5,020	5,029	5,015
3,945	*3,937*	*3,944*	*3,948*	*3,942*	*3,951*	*3,945*	*3,949*

44,04	43,16	44,19	45,13	44,82	45,15	44,43	44,34
0,11	0,03	0,04	0,08	0,03	b.d.	0,07	b.d.
34,72	34,13	34,38	34,01	34,25	34,46	34,06	34,80
0,13	b.d.	b.d.	0,17	0,07	b.d.	0,09	0,16
0,43	0,35	0,19	0,31	0,22	0,16	0,48	0,18
0,10	0,08	b.d.	b.d.	0,05	0,09	0,03	0,09
0,57	0,28	0,40	0,20	0,36	0,34	0,26	0,48
19,80	19,91	19,25	19,16	19,15	19,51	19,65	19,92
0,56	0,34	0,66	0,71	0,79	0,71	0,48	0,60
0,14	0,17	0,05	0,14	0,13	0,05	0,13	0,08
100,60	*98,44*	*99,16*	*99,93*	*99,87*	*100,47*	*99,66*	*100,66*
94,32	96,08	93,92	92,97	92,39	93,53	95,07	94,36
4,87	2,97	5,79	6,21	6,87	6,17	4,21	5,16
0,81	0,95	0,29	0,82	0,74	0,30	0,72	0,48
2,039	2,040	2,064	2,092	2,080	2,082	2,070	2,047
0,004	0,001	0,001	0,003	0,001	0,000	0,002	0,000
1,894	1,901	1,893	1,858	1,873	1,873	1,871	1,894
0,005	0,000	0,000	0,006	0,003	0,000	0,003	0,006
0,017	0,014	0,007	0,012	0,009	0,006	0,019	0,007
0,000	0,003	0,000	0,000	0,000	0,000	0,001	0,000
0,040	0,020	0,028	0,014	0,025	0,023	0,018	0,033
0,982	1,008	0,963	0,952	0,952	0,964	0,981	0,986
0,051	0,031	0,059	0,064	0,071	0,064	0,043	0,054
0,008	0,010	0,003	0,008	0,008	0,003	0,007	0,005
5,038	5,029	5,019	5,009	5,021	5,015	5,016	5,032
3,932	*3,942*	*3,957*	*3,950*	*3,953*	*3,955*	*3,941*	*3,941*

44,06	42,84	43,92	43,92	44,94	44,98	43,94	46,06
b.d.	b.d.	b.d.	0,14	b.d.	b.d.	b.d.	b.d.
35,16	34,63	34,35	34,81	33,72	33,65	34,34	32,90
0,04	b.d.	b.d.	b.d.	b.d.	0,20	0,14	0,03
0,11	b.d.	0,42	0,43	0,27	0,27	0,38	0,36
0,11	0,05	b.d.	b.d.	b.d.	b.d.	b.d.	0,14
0,33	0,15	0,36	0,32	0,13	0,18	0,46	0,46
20,18	20,26	20,31	20,29	18,90	19,50	20,04	18,87
0,46	0,23	0,46	0,48	0,76	0,82	0,42	0,78
b.d.	0,08	0,08	0,06	0,15	0,08	0,17	0,04
100,44	*98,24*	*99,90*	*100,46*	*98,87*	*99,67*	*99,90*	*99,65*
96,06	97,50	95,64	95,60	92,40	92,52	95,41	92,81

3,94	2,02	3,93	4,06	6,73	7,03	3,66	6,93
0,00	0,48	0,43	0,34	0,87	0,46	0,94	0,26

2,037	2,027	2,046	2,035	2,103	2,093	2,047	2,139
0,000	0,000	0,000	0,005	0,000	0,000	0,000	0,000
1,915	1,931	1,886	1,901	1,859	1,846	1,885	1,800
0,001	0,000	0,000	0,000	0,000	0,007	0,005	0,001
0,004	0,000	0,016	0,017	0,011	0,011	0,015	0,014
0,004	0,000	0,000	0,000	0,000	0,000	0,000	0,000
0,023	0,011	0,025	0,022	0,009	0,012	0,032	0,032
0,999	1,027	1,014	1,007	0,947	0,972	1,000	0,939
0,041	0,021	0,042	0,043	0,069	0,074	0,038	0,070
0,000	0,005	0,005	0,004	0,009	0,005	0,010	0,003
5,025	5,021	5,034	5,033	5,007	5,020	5,032	4,997
3,952	*3,957*	*3,932*	*3,936*	*3,962*	*3,939*	*3,932*	*3,939*

43,90	43,36	42,95	43,71	43,09	43,73	43,77	42,88
b.d.	b.d.	b.d.	b.d.	0,10	b.d.	0,08	0,04
34,64	34,59	34,34	34,51	33,97	34,49	34,14	35,18
b.d.	b.d.	b.d.	0,03	b.d.	0,15	0,04	b.d.
0,22	0,18	0,38	0,20	0,17	0,36	0,25	0,00
b.d.	0,06	b.d.	0,08	0,21	0,14	0,06	0,05
0,37	0,42	0,12	0,33	0,19	0,49	0,47	0,35
19,84	19,90	20,24	19,79	19,90	19,63	19,77	20,13
0,40	0,42	0,39	0,49	0,31	0,60	0,55	0,44
0,11	0,00	0,15	0,12	0,11	0,10	0,05	0,17
99,48	*98,94*	*98,58*	*99,27*	*98,05*	*99,70*	*99,20*	*99,24*
95,87	96,30	95,78	95,05	96,65	94,21	94,95	95,33
3,48	3,70	3,35	4,24	2,72	5,24	4,78	3,73
0,65	0,00	0,87	0,70	0,63	0,56	0,27	0,93
2,048	2,035	2,030	2,046	2,044	2,042	2,051	2,010
0,000	0,000	0,000	0,000	0,003	0,000	0,003	0,001
1,904	1,914	1,913	1,904	1,899	1,898	1,885	1,944
0,000	0,000	0,000	0,001	0,000	0,006	0,001	0,000
0,009	0,007	0,015	0,008	0,007	0,014	0,010	0,000
0,000	0,003	0,000	0,000	0,008	0,000	0,000	0,002
0,025	0,029	0,009	0,023	0,013	0,034	0,033	0,025
0,991	1,001	1,025	0,993	1,011	0,982	0,993	1,011
0,036	0,039	0,036	0,044	0,028	0,055	0,050	0,040
0,007	0,000	0,009	0,007	0,007	0,006	0,003	0,010
5,021	5,027	5,036	5,027	5,021	5,036	5,029	5,042
3,953	*3,949*	*3,943*	*3,950*	*3,943*	*3,940*	*3,936*	*3,953*

43,96	44,06	42,84	43,92	43,92	43,43	43,82	43,43
b.d.	b.d.	b.d.	b.d.	0,14	b.d.	b.d.	b.d.
34,36	35,16	34,63	34,35	34,81	34,62	34,69	35,05
0,10	0,04	b.d.	b.d.	b.d.	b.d.	b.d.	0,16
0,30	0,11	b.d.	0,42	0,43	0,23	0,22	0,22
b.d.	0,11	0,05	b.d.	b.d.	0,15	0,15	b.d.
0,38	0,33	0,15	0,36	0,32	0,32	0,37	0,51
19,92	20,18	20,26	20,31	20,29	20,02	19,81	20,09
0,61	0,46	0,23	0,46	0,48	0,47	0,49	0,41
0,09	b.d.	0,08	0,08	0,06	0,18	b.d.	0,11
99,71	*100,44*	*98,24*	*99,90*	*100,46*	*99,42*	*99,56*	*99,98*
94,29	96,06	97,50	95,64	95,60	94,95	95,71	95,84

5,19	3,94	2,02	3,93	4,06	4,06	4,29	3,56
0,52	0,00	0,48	0,43	0,34	1,00	0,00	0,60
2,049	2,037	2,027	2,046	2,035	2,033	2,043	2,021
0,000	0,000	0,000	0,000	0,005	0,000	0,000	0,000
1,888	1,915	1,931	1,886	1,901	1,910	1,907	1,922
0,004	0,001	0,000	0,000	0,000	0,000	0,000	0,006
0,012	0,004	0,000	0,016	0,017	0,009	0,009	0,008
0,000	0,004	0,000	0,000	0,000	0,006	0,006	0,000
0,026	0,023	0,011	0,025	0,022	0,022	0,026	0,035
0,995	0,999	1,027	1,014	1,007	1,004	0,990	1,001
0,055	0,041	0,021	0,042	0,043	0,043	0,044	0,037
0,006	0,000	0,005	0,005	0,004	0,011	0,000	0,006
5,035	5,025	5,021	5,034	5,033	5,038	5,025	5,037
3,938	*3,952*	*3,957*	*3,932*	*3,936*	*3,943*	*3,950*	*3,943*

43,44	43,41	42,94
b.d.	b.d.	0,11
34,70	34,07	34,60
b.d.	b.d.	b.d.
0,07	0,39	0,23
0,00	0,05	0,00
0,39	0,20	0,16
19,77	19,92	20,31
0,59	0,34	0,25
0,10	0,15	0,06
99,06	*98,52*	*98,66*
94,30	96,19	97,45
5,12	2,98	2,19
0,58	0,84	0,36
2,036	2,050	2,024
0,000	0,000	0,004
1,917	1,896	1,922
0,000	0,000	0,000
0,003	0,015	0,009
0,000	0,000	0,000
0,027	0,014	0,011
0,993	1,008	1,026
0,054	0,031	0,023
0,006	0,009	0,004
5,035	5,022	5,024
3,953	*3,946*	*3,947*

43,50	43,55	43,79	44,06	43,65	43,93	44,22	44,02
b.d.	0,04	b.d.	b.d.	b.d.	b.d.	0,06	0,10
34,45	34,87	35,34	34,73	35,09	34,90	35,42	34,70
0,13	0,10	b.d.	b.d.	b.d.	b.d.	0,15	b.d.
0,12	0,06	0,21	0,26	0,10	0,21	0,13	0,39
b.d.	0,13	0,03	b.d.	0,00	0,08	b.d.	b.d.
0,29	0,45	0,27	0,22	0,51	0,25	0,29	0,39
20,15	20,10	20,45	19,72	20,20	19,95	20,12	19,79
0,31	0,56	0,31	0,42	0,49	0,42	0,21	0,69
0,15	0,15	0,03	0,07	0,03	0,18	0,11	0,16
99,10	*100,01*	*100,43*	*99,47*	*100,07*	*99,91*	*100,71*	*100,24*
96,44	94,39	97,14	95,85	95,60	95,39	97,49	93,20

2,72	4,76	2,66	3,74	4,23	3,60	1,88	5,90
0,84	0,85	0,19	0,41	0,17	1,01	0,63	0,90

2,040	2,026	2,026	2,054	2,027	2,043	2,037	2,042
0,000	0,002	0,000	0,000	0,000	0,000	0,002	0,003
1,904	1,912	1,928	1,908	1,920	1,913	1,922	1,898
0,005	0,004	0,000	0,000	0,000	0,000	0,005	0,000
0,005	0,002	0,008	0,010	0,004	0,008	0,005	0,015
0,000	0,005	0,000	0,000	0,000	0,000	0,000	0,000
0,020	0,031	0,018	0,015	0,035	0,017	0,020	0,027
1,012	1,002	1,014	0,985	1,005	0,994	0,993	0,984
0,029	0,051	0,028	0,038	0,044	0,037	0,019	0,062
0,009	0,009	0,002	0,004	0,002	0,011	0,006	0,009
5,024	5,044	5,025	5,014	5,037	5,024	5,010	5,041
3,944	*3,939*	*3,954*	*3,962*	*3,947*	*3,957*	*3,959*	*3,940*

43,74	43,83	44,33	43,95	43,56	43,63	43,87	43,96
0,04	b.d.	0,04	b.d.	0,07	0,21	0,06	0,08
35,75	34,88	34,85	34,60	34,49	34,96	34,12	34,67
0,11	0,11	0,04	b.d.	b.d.	0,09	b.d.	b.d.
0,20	0,19	0,14	0,37	0,26	0,35	0,24	0,36
b.d.	b.d.	b.d.	0,07	0,07	b.d.	0,10	0,04
0,32	0,08	0,14	0,24	0,28	0,15	0,37	0,49
20,50	20,22	19,95	19,49	20,01	20,07	19,90	19,65
0,27	0,32	0,51	0,43	0,32	0,37	0,37	0,52
0,10	b.d.	0,13	0,06	0,14	b.d.	0,12	0,15
101,02	*99,63*	*100,13*	*99,20*	*99,21*	*99,83*	*99,15*	*99,91*
97,13	97,21	94,91	95,88	96,37	96,80	96,11	94,59

2,33	2,79	4,35	3,79	2,81	3,20	3,21	4,57
0,54	0,00	0,73	0,33	0,81	0,00	0,67	0,85

2,013	2,042	2,054	2,055	2,041	2,031	2,056	2,044
0,001	0,000	0,001	0,000	0,003	0,007	0,002	0,003
1,939	1,915	1,903	1,907	1,905	1,918	1,885	1,900
0,004	0,004	0,001	0,000	0,000	0,003	0,000	0,000
0,008	0,007	0,005	0,014	0,010	0,014	0,010	0,014
0,000	0,000	0,000	0,000	0,003	0,000	0,000	0,002
0,022	0,006	0,010	0,016	0,019	0,010	0,026	0,034
1,011	1,009	0,991	0,977	1,004	1,001	1,000	0,979
0,024	0,029	0,045	0,039	0,029	0,033	0,033	0,047
0,006	0,000	0,008	0,003	0,008	0,000	0,007	0,009
5,028	5,013	5,019	5,012	5,023	5,018	5,019	5,031
3,953	*3,957*	*3,957*	*3,962*	*3,946*	*3,949*	*3,942*	*3,944*

43,38	43,01	43,75	43,17	43,54	43,10	43,36	43,18
b.d.	0,05	b.d.	0,18	0,10	b.d.	0,06	0,07
34,68	34,72	34,22	34,44	34,47	34,02	34,46	34,73
0,12	b.d.	b.d.	b.d.	0,07	0,16	b.d.	b.d.
0,27	0,40	0,15	0,23	0,31	0,30	0,45	0,15
b.d.	b.d.	0,25	0,17	b.d.	0,05	0,04	b.d.
0,43	0,42	0,31	0,11	0,19	0,27	0,38	0,27
19,76	19,95	19,56	19,77	19,94	19,63	19,89	20,28
0,57	0,48	0,45	0,33	0,30	0,33	0,45	0,26
0,15	0,05	0,04	0,14	0,05	0,11	0,07	0,09
99,36	*99,08*	*98,73*	*98,52*	*98,96*	*97,96*	*99,17*	*99,03*
94,26	95,49	95,75	96,32	97,10	96,47	95,67	97,21

4,90	4,20	4,02	2,90	2,63	2,90	3,91	2,29
0,84	0,31	0,23	0,78	0,27	0,63	0,43	0,49

2,031	2,020	2,056	2,039	2,043	2,045	2,035	2,027
0,000	0,002	0,000	0,006	0,003	0,000	0,002	0,002
1,913	1,922	1,896	1,916	1,907	1,902	1,906	1,921
0,005	0,000	0,000	0,000	0,003	0,006	0,000	0,000
0,011	0,016	0,006	0,009	0,012	0,012	0,018	0,006
0,000	0,000	0,010	0,000	0,000	0,002	0,000	0,000
0,030	0,029	0,021	0,008	0,013	0,019	0,026	0,019
0,991	1,004	0,985	1,000	1,002	0,998	1,000	1,020
0,052	0,044	0,041	0,030	0,027	0,030	0,041	0,024
0,009	0,003	0,002	0,008	0,003	0,007	0,004	0,005
5,041	5,040	5,018	5,016	5,014	5,020	5,033	5,025
3,944	*3,942*	*3,952*	*3,955*	*3,950*	*3,947*	*3,941*	*3,948*

42,84	43,71	42,61	43,43
0,08	0,05	b.d.	b.d.
34,50	34,30	34,47	34,62
b.d.	0,08	0,12	b.d.
0,21	0,11	0,23	0,23
0,22	0,03	0,00	0,15
0,41	0,44	0,16	0,32
19,48	19,77	20,07	20,02
0,39	0,45	0,28	0,47
0,06	0,11	0,06	0,18
98,18	*99,05*	*98,01*	*99,42*
96,18	95,42	97,21	94,95

3,48	3,93	2,46	4,06
0,34	0,66	0,33	1,00

2,027	2,049	2,022	2,033
0,003	0,002	0,000	0,000
1,924	1,895	1,928	1,910
0,000	0,003	0,005	0,000
0,008	0,004	0,009	0,009
0,009	0,000	0,000	0,006
0,029	0,031	0,012	0,022
0,988	0,993	1,021	1,004
0,036	0,041	0,026	0,043
0,004	0,007	0,003	0,011
5,027	5,024	5,026	5,038
3,952	*3,944*	*3,951*	*3,943*

Appendix 4B

Pyroxenes

MIL 090070	**Impact melts**						
Oxide Weight Percent							
SiO_2	41,70	51,62	52,31	48,82	52,26	52,35	46,71
TiO_2	0,03	0,98	1,16	1,25	0,51	0,69	0,41
Al_2O_3	24,18	1,80	2,83	11,14	1,63	3,12	12,21
Cr_2O_3	0,12	0,60	0,40	0,50	0,53	0,30	0,18
FeO	12,06	18,64	18,07	8,66	20,64	15,94	17,00
MnO	0,24	0,17	0,51	0,38	0,39	0,33	0,39
MgO	9,46	23,90	23,71	12,88	22,59	22,97	15,34
CaO	13,18	2,21	2,50	17,94	2,87	5,70	7,93
Na_2O	0,33	0,23	0,39	0,34	0,26	0,37	0,32
K_2O	b.d	b.d	b.d	0,04	0,04	0,09	0,08
Total	*101,29*	*100,16*	*101,88*	*101,95*	*101,72*	*101,87*	*100,57*
Mg#	58,29	69,56	70,05	72,61	66,11	71,98	61,66
En	36,80	66,49	66,52	42,05	62,35	63,78	50,16
Fs	26,34	29,10	28,44	15,86	31,96	24,83	31,19
Wo	36,87	4,41	5,04	42,09	5,68	11,38	18,65
Cations per 6 Oxygens							
Si	1,515	1,905	1,893	1,763	1,919	1,892	1,729
Ti	0,001	0,027	0,031	0,034	0,014	0,019	0,011
Al	1,035	0,078	0,121	0,474	0,071	0,133	0,533
Al (IV)	0,485	0,095	0,107	0,237	0,081	0,108	0,271
Al (VI)	0,550	0,000	0,014	0,237	0,000	0,025	0,262
Cr	0,003	0,018	0,012	0,014	0,015	0,009	0,005
Fe	0,367	0,575	0,547	0,262	0,634	0,482	0,526
Mn	0,007	0,005	0,016	0,012	0,012	0,010	0,012
Mg	0,512	1,315	1,279	0,694	1,236	1,238	0,846
Ca	0,513	0,087	0,097	0,694	0,113	0,221	0,315
Na	0,023	0,016	0,028	0,024	0,019	0,026	0,023
K	0,000	0,000	0,000	0,002	0,002	0,004	0,004
Total Cations	3,977	4,044	4,023	3,972	4,045	4,033	4,004
Tet site	*2,000*	*2,000*	*2,000*	*2,000*	*2,000*	*2,000*	*2,000*

Mineral fragments							
Oxide Weight Percent							
SiO_2	48,07	47,23	47,51	47,57	52,13	50,84	51,91
TiO_2	0,82	0,94	0,94	0,92	0,26	0,43	0,39
Al_2O_3	1,76	1,63	1,35	1,39	2,01	1,65	3,36
Cr_2O_3	0,58	0,11	0,35	0,48	0,71	0,84	0,28
FeO	30,12	34,56	34,22	32,45	11,36	17,68	18,96
MnO	0,47	0,59	0,38	0,41	0,13	0,50	0,31

MgO	9,67	7,46	7,39	7,67	15,76	14,46	21,21
CaO	9,55	8,33	9,15	9,55	19,22	14,19	4,40
Na2O	0,21	0,06	0,04	0,10	0,29	0,16	0,28
K2O	0,05	b.d.	b.d.	b.d.	b.d.	b.d.	b.d.
Total	101,29	100,92	101,33	100,54	101,85	100,77	101,09
Mg#	36,39	27,79	27,78	29,63	71,20	59,31	66,60
En	28,91	22,72	22,27	23,42	43,84	41,82	60,59
Fs	50,55	59,04	57,90	55,62	17,73	28,69	30,38
Wo	20,54	18,24	19,83	20,96	38,43	29,50	9,03
Cations per 6 Oxygens							
Si	1,902	1,910	1,913	1,918	1,919	1,926	1,906
Ti	0,024	0,029	0,028	0,028	0,007	0,012	0,011
Al	0,082	0,077	0,064	0,066	0,087	0,074	0,145
Al (IV)	0,098	0,090	0,087	0,082	0,081	0,074	0,094
Al (VI)	0,000	0,000	0,000	0,000	0,006	0,000	0,052
Cr	0,018	0,004	0,011	0,015	0,021	0,025	0,008
Fe	0,997	1,169	1,152	1,094	0,350	0,560	0,582
Mn	0,016	0,020	0,013	0,014	0,004	0,016	0,010
Mg	0,570	0,450	0,443	0,461	0,865	0,817	1,161
Ca	0,405	0,361	0,395	0,412	0,758	0,576	0,173
Na	0,016	0,005	0,003	0,008	0,020	0,012	0,020
K	0,003	0,000	0,000	0,000	0,000	0,000	0,000
Total Cations	4,049	4,037	4,045	4,033	4,030	4,018	4,016
Total tet	*2,000*	*2,000*	*2,000*	*2,000*	*2,000*	*2,000*	*2,000*

51,94	43,27
0,51	3,36
3,23	12,91
0,24	b.d.
20,37	21,24
0,41	0,40
20,66	6,98
4,29	11,79
0,26	0,30
b.d.	0,09
101,91	*100,35*
64,38	36,94
58,74	25,50
32,50	43,54
8,76	30,96
1,904	1,665
0,014	0,097
0,140	0,586
0,096	0,335
0,044	0,251
0,007	0,000
0,625	0,684
0,013	0,013
1,129	0,400
0,168	0,486
0,018	0,022
0,000	0,005
4,018	3,958
2,000	*2,000*

53,36	51,93	51,40	50,73	51,10	50,80	51,37	54,04	53,55
0,67	0,64	0,37	0,70	0,56	0,76	0,61	0,62	0,76
1,87	1,62	1,39	1,39	2,11	1,45	1,59	1,72	1,56
0,44	0,39	0,17	0,29	1,09	0,58	0,50	0,45	0,58
18,62	18,79	24,53	15,46	21,34	15,63	23,16	13,82	13,46
0,21	0,32	0,42	0,49	0,29	0,33	0,44	0,14	0,36

24,33	19,72	19,71	12,27	20,86	12,33	16,67	28,38	28,19
2,20	7,37	2,19	19,49	4,19	19,62	6,95	1,99	2,21
0,29	0,20	0,16	0,07	b.d.	0,14	0,19	0,29	0,16
b.d.	b.d.	b.d.	b.d.	0,03	0,06	0,03	b.d.	b.d.
101,98	100,98	100,33	100,90	101,58	101,70	101,52	101,45	100,84
69,96	65,17	58,88	58,58	63,54	58,44	56,20	78,54	78,87
66,92	55,46	56,24	35,10	58,20	35,03	48,10	75,55	75,50
28,73	29,64	39,27	24,82	33,40	24,91	37,49	20,64	20,23
4,35	14,89	4,49	40,07	8,40	40,06	14,41	3,80	4,26
1,927	1,928	1,943	1,928	1,895	1,918	1,935	1,919	1,915
0,018	0,018	0,011	0,020	0,016	0,021	0,017	0,017	0,020
0,079	0,071	0,062	0,062	0,092	0,065	0,071	0,072	0,066
0,073	0,072	0,057	0,072	0,105	0,082	0,065	0,081	0,085
0,006	0,000	0,005	0,000	0,000	0,000	0,005	0,000	0,000
0,012	0,012	0,005	0,009	0,032	0,017	0,015	0,013	0,016
0,562	0,583	0,775	0,491	0,662	0,494	0,729	0,410	0,403
0,006	0,010	0,013	0,016	0,009	0,011	0,014	0,004	0,011
1,309	1,091	1,110	0,695	1,153	0,694	0,936	1,502	1,502
0,085	0,293	0,089	0,793	0,167	0,794	0,280	0,076	0,085
0,020	0,014	0,012	0,006	0,000	0,011	0,014	0,020	0,011
0,000	0,000	0,000	0,000	0,001	0,003	0,002	0,000	0,000
4,019	4,021	4,019	4,030	4,040	4,044	4,013	4,041	4,048
2,000	*2,000*	*2,000*	*2,000*	*2,000*	*2,000*	*2,000*	*2,000*	*2,000*

53,90	54,13	53,77	52,45	51,18	51,27	51,45	51,42	51,81
0,66	0,72	0,73	0,60	0,32	0,67	0,38	0,37	0,30
1,69	1,91	1,41	2,55	7,68	1,41	2,00	2,09	1,61
0,50	0,68	0,64	0,37	0,13	0,50	0,66	0,64	0,47
13,60	13,22	13,63	18,79	17,13	20,94	19,46	20,06	20,36
0,13	0,16	0,13	0,18	0,50	0,33	0,36	0,36	0,32

28,25	28,01	28,28	24,63	18,72	19,70	19,73	20,30	19,70
2,18	2,21	1,82	1,81	4,86	5,41	6,63	5,95	6,13
0,26	0,10	0,33	0,14	0,29	0,12	0,21	0,24	0,25
b.d.	b.d.	b.d.	b.d.	0,03	b.d.	0,06	0,07	b.d.
101,18	101,14	100,73	101,51	100,83	100,34	100,93	101,51	100,95
78,73	79,06	78,72	70,03	66,08	62,64	64,38	64,34	63,30
75,43	75,66	75,95	67,53	58,83	55,75	55,72	56,66	55,44
20,38	20,04	20,53	28,91	30,20	33,25	30,83	31,41	32,15
4,19	4,30	3,51	3,56	10,97	11,00	13,45	11,94	12,41
1,919	1,922	1,922	1,903	1,864	1,926	1,916	1,906	1,931
0,018	0,019	0,020	0,016	0,009	0,019	0,011	0,010	0,009
0,071	0,080	0,059	0,109	0,330	0,063	0,088	0,091	0,071
0,081	0,078	0,078	0,097	0,136	0,074	0,084	0,094	0,069
0,000	0,002	0,000	0,012	0,194	0,000	0,004	0,000	0,002
0,014	0,019	0,018	0,011	0,004	0,015	0,019	0,019	0,014
0,405	0,393	0,407	0,570	0,522	0,658	0,606	0,622	0,635
0,004	0,005	0,004	0,005	0,016	0,011	0,011	0,011	0,010
1,499	1,483	1,507	1,332	1,016	1,103	1,095	1,122	1,095
0,083	0,084	0,070	0,070	0,190	0,218	0,264	0,236	0,245
0,018	0,007	0,023	0,010	0,020	0,009	0,015	0,018	0,018
0,000	0,000	0,000	0,000	0,001	0,000	0,003	0,003	0,000
4,041	4,012	4,049	4,026	3,971	4,031	4,029	4,041	4,027
2,000	*2,000*	*2,000*	*2,000*	*2,000*	*2,000*	*2,000*	*2,000*	*2,000*

51,75	52,69
0,46	0,19
1,94	1,88
0,72	0,61
20,21	13,70
0,43	0,50

19,98	18,21
5,78	13,66
0,28	0,26
b.d.	b.d.
101,55	101,71
63,79	70,33
56,32	50,99
31,97	21,52
11,72	27,49
1,917	1,932
0,013	0,005
0,085	0,081
0,083	0,068
0,002	0,013
0,021	0,018
0,626	0,420
0,014	0,016
1,103	0,995
0,229	0,537
0,020	0,019
0,000	0,000
4,027	4,023
2,000	*2,000*

Appendix 4C

Olivines

MIL 090070	**Mineral fragments**					
Oxide Weight Percent						
SiO_2	0,31	35,67	35,34	36,11	37,09	0,21
TiO_2	0,81	0,30	0,10	0,07	0,06	2,23
Al_2O_3	54,02	0,99	0,56	0,61	0,55	21,17
Cr_2O_3	7,39	0,06	b.d.	b.d.	0,20	41,24
FeO	23,90	33,69	35,01	31,63	27,01	29,16
MnO	0,27	0,44	0,49	0,18	0,14	0,70
MgO	12,89	29,86	29,16	32,18	36,19	5,88
CaO	0,15	0,24	0,32	0,19	0,33	0,25
Na_2O	b.d.	0,18	0,34	0,47	0,42	0,07
K_2O	b.d.	b.d.	b.d.	b.d.	b.d.	b.d.
Total	*99,74*	*101,42*	*101,32*	*101,44*	*101,99*	*100,92*
Mg#	49,019	61,238	59,752	64,452	70,485	26,453
Fe#	50,981	38,762	40,248	35,548	29,515	73,547
Cations per 4 Oxygens						
Si	0,008	0,970	0,970	0,972	0,970	0,007
Ti	0,017	0,006	0,002	0,001	0,001	0,054
Al	1,748	0,032	0,018	0,019	0,017	0,803
Cr	0,160	0,001	0,000	0,000	0,004	1,050
Fe	0,549	0,766	0,804	0,712	0,591	0,785
Mn	0,006	0,010	0,011	0,004	0,003	0,019
Mg	0,528	1,210	1,194	1,291	1,411	0,282
Ca	0,004	0,007	0,009	0,006	0,009	0,009
Na	0,000	0,010	0,018	0,024	0,021	0,004
Total Cations	3,021	3,012	3,028	3,029	3,029	3,014

35,82
b.d.
0,67
0,03
35,10
0,27
29,27
0,30
0,26
b.d.
101,72
59,781
40,219
0,977
0,000
0,021
0,001
0,801
0,006
1,190
0,009
0,014
3,019